UNIVERSITE MONTPELLIER II
SCIENCES ET TECHNIQUES DU LANGUEDOC

THESE

pour obtenir le grade de

DOCTEUR DE L'UNIVERSITE MONTPELLIER II

Discipline: Physico-Chimie des Matériaux
Ecole Doctorale: Sciences Chimiques et Physiques

Order and Disorder of Relaxor and Ferroelectric Materials: Structural and Vibrational Studies

présentée par

Ali AL-ZEIN

soutenue publiquement le 5 Novembre 2010 devant le Jury composé de:

M. Eric Courtens	Professeur émérite, Université Montpellier II,	Président-Examinateur
M. Roger Cowley	Professeur émérite, University of Oxford,	Rapporteur
M. Jean-Michel Kiat	Directeur de recherche CNRS, SPMS, Paris	Rapporteur
M. Jirka Hlinka	Directeur de recherche, Prague, CR	Examinateur
M. Julien Haines	Directeur de recherche CNRS, ICGM,	Invité
M. Jérôme Rouquette	Chargé de recherche CNRS, ICGM,	Invité
M. Bernard Hehlen	Professeur, Université Montpellier II,	Directeur de thèse
M. Philippe Papet	Professeur, Université Montpellier II,	Directeur de thèse

préparée à l'Institut Charles Gerhardt Montpellier (ICGM)
et "Laboratoire des Colloïdes Verres et Nanomatériaux (LCVN)"

List of Figures

1.1 Simple cubic perovskite unit cell of type ABO_3. 9

1.2 (a) The cubic perovskite in its high symmetry form with no octahedral tilting. (b) Perovskite structure in its low symmetry form with octahedral tilting. The spheres represent the A cations. 10

1.3 Temperature dependence of the dielectric permittivity ϵ and spontaneous polarization P_S for (a) first-order and (b) second-order ferroelectric phase transition. Source: D. Damjanovic [1]. 12

1.4 (a) The six possible directions of the ferroelectric polarization (black arrows) in the tetragonal phase of $BaTiO_3$. (b) Schematic diagram of 180° and 90° domain walls. 13

1.5 The change in the crystallographic symmetry of $BaTiO_3$ at different temperatures. The arrow indicates the spontaneous polarization direction. 14

1.6 Schematic diagram for (a) the cubic phase of $BaTiO_3$ above T_C and (b) the tetragonal phase of $BaTiO_3$ below T_C. The arrow represents the induced spontaneous polarization as the titanium ion shifts from its central position. 14

1.7 Polarization-electric field hysteresis loop. The arrows in the squares indicate the direction of polarization of the material at the indicated fields. 15

1.8 Ideal strain-electric field hysteresis loop. 16

2.1 (a) Formation of polar nanodoamins. (b) The temperature dependence of the soft mode frequency ω_S and the correlation length r_c of ferroelectric material. Source: G. A. Samara [19] 19

2.2 (a) Schematic diagram showing the temperature dependence of the real part of the dielectric pertimittivity measured at different frequencies for a prototypical relaxor. (b) Temperature dependence of the dielectric constant ϵ and its inverse ϵ^{-1} at f = 1 kHz. (c) The polarization-electric field hysteresis loop of a prototypical relaxor $PbMg_{1/3}Nb_{2/3}O_3$ at different temperatures. (d) The variation of the dipolar polarization P_d with temperature. 21

2.3 Deviation of the thermal strain (a), refractive index (b) and the inverse of the dielectric constant (c) from linear behavior near the Burns temperature T_d for PMN relaxor. Panel (a) also shows the decrease of the root-mean square dipole polarization $\sqrt{P_d^2}$ toward zero near T_d. 23

2.4 Temperature dependence of the dielectric permittivity ϵ of $PbMg_{1/3}Nb_{2/3}O_3$ single crystals at various frequencies. Source: V. Bovtun [43]. 24

2.5 Temperature dependence of the cubic cell parameter of $PbMg_{1/3}Nb_{2/3}O_3$. Source: P. Bonneau [40]. 25

2.6 Acoustic emission activity as a function of temperature for $PbMg_{1/3}Nb_{2/3}O_3$ and $PbZn_{1/3}Nb_{2/3}O_3$. Source: B. Dkhil [47]. 25

2.7 Temperature dependence of the lattice parameters of $PbTiO_3$ single crystals. Source: J. Kwapuliński [57]. 27

2.8 (a) X-ray diffraction patterns of $PbTiO_3$ powders showing cubic reflections at 17.7 GPa and tetragonal reflections at 1.4 GPa. (b) Pressure dependence of the lattice parameters of $PbTiO_3$. Source: A. Sani [50]. 27

2.9 Local displacements of Pb and Ti obtained by high-pressure X-ray absorption near-edge spectroscopy measurements. Source: N. Jaouen [61]. 28

2.10 Phase diagram of $Pb(Zr_{1-x}Ti_x)O_3$ showing the monoclinic phase in the morphotropic phase boundary. Source: B. Noheda [62]. 29

2.11 (a) The maximum of the piezoelectric coefficients of $Pb(Zr_{1-x}Ti_x)O_3$ in the morphotropic phase boundary region. (b) The rotation of the polarization vector in the $(1\bar{1}0)$ monoclinic plane between the [100] tetragonal direction and the [111] rhombohedral direction. 29

2.12 (a) The dielectric constant of [111] PZN single crystal as a function of temperature at different frequencies. (b) Diffraction patterns of the (333) Bragg peak of PZN crystals at 300 K and 400 K. Source: A. Lebon [69, 73]. 30

2.13 (a) Neutron powder diffraction pattern of PMT at ambient temperature. Experimental, calculated, and difference profiles are shown. The row of ticks indicate the calculated positions of the diffraction peaks of PMT. Source: S. N. Gvasaliya [74]. (b) Temperature dependence of the dielectric constant of PMT crystals at different frequencies. Source: J.-H. Ko [55]. 31

2.14 (a) The variation of the cubic lattice parameter of PMT as a function of temperature. Source: S. N. Gvasaliya [75]. (b) Temperature dependence of the inverse of the dielectric constant of PMT. Source: Y. L. Wang [78]. . . . 32

3.1 A schematic diagram of an elastic scattering event. 36

3.2 The comparison between the Q dependence of the neutron scattering length b and the X-ray form factor $f(Q)$ for carbon. 37

3.3 The variation of the coherent neutron-scattering length $\bar{b}$ with the atomic number for natural isotopic abundance. 38
3.4 A schematic diagram of the D1B instrument at the ILL. 40
3.5 A schematic top-view of the D20 diffractometer at the ILL. 41
3.6 The experimental setup for high pressure neutron diffraction. (1) Ti-Zr gasket, (2) anvil cell, (3) Paris-Edimburgh press. 41
3.7 The variation of the relative intensity of Bragg reflections as a function of temperature. The major reflection lines were indexed with a pseudocubic symmetry (pc). The unusual ordinate scale cannot be modified in the available software. 45
3.8 Experimental (circles), calculated (red line) and difference (blue line) profiles of $PbTiO_3$ pattern of the tetragonal $P4mm$ phase at 298 K (a) and of the cubic $Pm\bar{3}m$ phase at 778 K (b). The row of ticks indicate the calculated positions of the Bragg peaks of $PbTiO_3$. 46
3.9 Tetragonal structure of $PbTiO_3$. 47
3.10 Temperature dependence of the lattice parameters of $PbTiO_3$. 48
3.11 Temperature dependence of the displacement of the titanium and the oxygen atoms from the centrosymmetric position. 48
3.12 The variation of the spontaneous polarization calculated from Rietveld refined parameters as a function of temperature. 49
3.13 Temperature dependence of the unit cell volume. 50
3.14 The variation of the position of the (111) Bragg peak as a function of temperature. 50
3.15 Experimental (circles), calculated (red line) and difference (blue line) profiles of $PbTiO_3$ pattern of the tetragonal $P4mm$ phase at 0.5 GPa (a), 9.1 GPa (b) and the cubic $Pm\bar{3}m$ phase at 13.6 GPa (c). The upper and lower rows of ticks indicate the calculated positions of the Bragg peaks of $PbTiO_3$ and BN (a,b) or diamond (c), respectively. 52
3.16 The variation of the lattice parameters of $PbTiO_3$ as a function of pressure. The lines represent a fit of the data with a third-order polynomial. 53
3.17 Pressure dependence of (a) the tetragonal distortion c/a and (b) the spontaneous polarization P_S calculated by Rietveld refined parameters. 53
3.18 The variation of c/a - 1 and the square of the spontaneous polarization as a function of pressure. 54
3.19 The variation of the isotropic displacement parameter B as a function of pressure. 54

4.1 Zr K edge X-ray absorption spectrum of $PbZr_{0.52}Ti_{0.48}O_3$ obtained at 3.65 GPa and 300 K. 59

4.2 (a) European Synchrotron Radiation Facility (ESRF), Grenoble. (b) Beamline 29 (BM29). 60
4.3 The experimental setup for high pressure high temperature X-ray absorption experiment in transmission mode coupled with X-ray diffraction. (1) Sintered diamond anvil, (2) boron-epoxy biconical gasket, (3) Paris-Edimburgh press, (4) MAR345 image plate detector, (5) Ion chamber I_0 (incident beam), (6) Ion chamber I_1 (transmitted beam), (7) Oil pump. 60
4.4 The experimental setup for X-ray absorption experiment in fluorescence geometry under electric field (1) Sample holder of PZN single crystal, (2) Electric field generator, (3) Incident X-ray beam, (4) Fluorescent X-ray beam, (5) X-ray detector. 62
4.5 (a) Normalized XAFS spectra obtained at 300 K between 0.9 GPa and 12 GPa, (b) Extracted $\chi(k)$. Both signals are vertically shifted for clarity. . . . 65
4.6 The k^3-weighted EXAFS signals (obtained in the 2-11 Å^{-1} range) are shown at 3.7 GPa (dashed) and 7.0 GPa (full). The Zr-O first coordination shell is extracted using a Hann window in the 1.2-2 Å range. 66
4.7 The k^3-weighted backward Fourier transforms along with the resulting fits (dashed) are shown at 3.7 GPa (a) and 7 GPa (b), respectively. 66
4.8 Pressure behavior of the DWF for the Zr-O atom pairs at 300 K. Values reported in the literature for PZT [114] ($*$) and $BaZrO_3$ [118] ($\circ$) are also included. P_C (the dashed line) corresponds to the paraelectric transition [53]. The dotted line represents the decrease of $\sigma^2_{dyn.}$ as explained in the text. 67
4.9 (a) High-pressure Zr K edge XANES spectra obtained at 300 K. Note the pressure evolution of the PEFS. (b) Experimental and simulated XANES spectra at 1.7 GPa and 7 GPa. In (b), the origin (0) corresponds to the Zr K edge. (c) The non-convoluted and convoluted theoretical PEFS at 1.7 GPa and 7 GPa showing the disappearance of the dipolar contribution at high pressure. 69
4.10 Normalized XAFS spectra obtained at 450 K between 0.8 GPa and 12 GPa. The spectra are vertically shifted for clarity. 71
4.11 The k^3-weighted backward Fourier transforms along with the resulting fits (dashed) are shown at 3.8 GPa (a) and 7.3 GPa (b), respectively. 71
4.12 Pressure behavior of the DWF for the Zr-O atom pairs at 450 K. The calculated value for $BaZrO_3$ ($\circ$) [118] is also included. $\sigma^2_{dyn.}$ (the dotted line) corresponds to a decrease of about 1% per GPa. 72
4.13 High-pressure Zr K edge XANES spectra obtained at 450 K. Note the pressure evolution of the PEFS. 73
4.14 Normalized XAFS spectra at Zn K edge (a) and Nb K edge (b). The signals are vertically shifted for clarity. 75

4.15 Extracted EXAFS spectra $\chi(k)$ in k^3 space at Zn K edge (a) and Nb K edge (b). The signals are vertically shifted for clarity. 76
4.16 The k^3-weighted EXAFS signals (obtained in the 2-11 Å^{-1} range) are shown for unpoled 0 kV/cm and poled 8 kV/cm Zn (a) and Nb (b) K edge XAFS spectra. The Zn-O and Nb-O first coordination shell is extracted using a Hann window in the 1.2-2.2 Å and 1.1-2.1 Å range, respectively. 77
4.17 The k^3-weighted EXAFS signals (obtained in the 2-11 Å^{-1} range) are shown for poled 0 kV/cm and poled 6 kV/cm Nb K edge XAFS spectra. The Nb-O first coordination shell is extracted using a Hann window in the 1.1-2.1 Å range. 77
4.18 The k^3-weighted backward Fourier transforms along with the resulting fits (dashed) are shown for unpoled 0.47 kV/cm (a) and poled 6 kV/cm (b) Zn K edge XAFS spectra, respectively. 78
4.19 The k^3-weighted backward Fourier transforms along with the resulting fits (dashed) are shown for unpoled 0 kV/cm (a) and poled 4 kV/cm (b) Nb K edge XAFS spectra, respectively. 78
4.20 The variation of the DWF for the Zn-O (a) and Nb-O (b) atom pairs as a function of the applied electric field. 79
4.21 Shematic diagram for $PbZn_{1/3}Nb_{2/3}O_3$ showing the centrosymmetric-like Zn atom (a) and the distorted Nb atom (b). 80

5.1 The Stokes (a) and anti-Stokes (b) hyper-Raman scattering energy-conservation diagrams. 86
5.2 The theoretical dispersion curve of the complex refractive index of an isotropic medium in the zero damping limit. 91
5.3 Schematic diagram of the HRS setup at the LCVN in 90° scattering (a), near-forward scattering (b), and backscattering geometry (c). The conservation of the linear momentum and the polarization analysis process in near-forward scattering and backscattering geometry are shown in the lower parts of (b) and (c) respectively. 93
5.4 High temperature HRS set-up in backscattering geometry. (1) Lens L_1, (2) Lens L_2, (3) Linkam furnace, (4) Lens L_3, (5) sem-rock filter, (6) entrance of the spectrometer. 94
5.5 A schematic diagram showing the reflection of the incident beam on the back face of the sample. 95
5.6 (a) HRS spectra of $PbMg_{1/3}Nb_{2/3}O_3$ crystal measured at different positions of the scattering volume in backscattering. (b) The normalized intensity of the LO2 and LO3 modes of PMN as a function of the depth inside the 1 mm sample. The red line corresponds to a fit with equation (5.33). 96

5.7 The normalized intensity of the LO2 and LO3 modes of PMN in backscattering as a function of the depth in 1 mm (full symbols) and 4 mm (open symbols) sample. The red and blue lines are fits using equations (5.33) and (5.34) respectively. The inset shows the HRS spectra obtained near the front face of the 4 mm sample where the LO intensity is minimum. 98

6.1 Eigen-displacements (normal coordinates) of (a) Last, (b) Slater, (c) Axe and (d) the non-polar F_{2u} zone-center modes in lead-based perovskites. . . . 100

6.2 Raman spectra of $PbMg_{1/3}Nb_{2/3}O_3$ crystal at various temperatures. Source: O. Svitelskiy [149]. 100

6.3 (a) INS spectra measured at the zone center at $Q = (2, 0, 0)$ from 1100 K (above T_d) down to 600 K (near T_d). (b) Temperature dependence of A_1 frequency obtained from the INS data of Refs. [146, 159] and IR of Ref. [160].101

6.4 Spectra of the imaginary part of the permittivity (top panel) and of the calculated imaginary part of the inverse permittivity (lower panel). Solid line corresponds to the effective macroscopic permittivity ϵ_{eff}, dashed and dotted lines correspond to the $\epsilon_\perp$ and $\epsilon_\parallel$ components of the local permittivity, respectively [153]. 102

6.5 $q \parallel [001]$. 104

6.6 Room-temperature polarized HRS spectra in relative units taken in different backscattering geometries (a) sample A with $q \parallel (001)$, (b) sample B with $q \parallel (110)$, and (c) sample C with $q \parallel (111)$. 107

6.7 (a) HRS spectra of PMN taken in $z''(x''y')\bar{z}''$ geometry at various temperatures. (b) Different spectra normalized to the top of the F_{2u} mode. The inset shows the temperature dependence of the frequency of the F_{2u} mode. . 108

6.8 Details of HRS spectra 1, 8 and 12 from Figure 6.6 in the spectral region around the F_{2u} band. Insets show DHO fits of TO2 and U bands after subtraction of the background signal. 110

6.9 Adjustments of room-temperature spectra in the vicinity of the F_{2u} band to a superposition of predefined TO2 and F_{2u} band profiles, as explained in the text. For clarity, the background is removed and the spectra denoted 12 and 3 are translated vertically by 10 and 5 intensity units, respectively. Dashed lines show individual components corresponding to TO2 and the F_{2u} vibrations, the thin full line is the resulting fit. 112

6.10 Unpolarized (V+H) HRS spectra of PMN at 748 K compared with INS data at 750 K taken from Ref. [173] (•). 114

6.11 Temperature evolution of unpolarized HRS spectra of (a) [001] PMN and (b) [111] PMN crystals. 115

6.12 473 K (a) and 423 K (b) [001] PMN spectra together with the instrumental function (green line). 116

6.13 VV (left) and VH (right) hyper-Raman spectra of [001] PMN at various temperatures fitted to the model described in the text (red full lines). Green dashed and blue dash-dotted lines show DHO components corresponding to the E_1 and the A_1 modes, respectively. 116

6.14 The fitting (red lines) of the Stokes part of unpolarized hyper-Raman spectra of [111] PMN. Blue and green lines show DHO components corresponding to the E_1 and the A_1 modes, respectively. 117

6.15 VV (left) and VH (right) hyper-Raman spectra of [111] PMN at 773 K, 673 K and 573 K with the fitting of the Stokes part shown in red. Blue and green lines show DHO components corresponding to the E_1 and the A_1 modes, respectively. 118

6.16 (a) Temperature dependence of E_1 and A_1 frequencies ω_0 and damping (in the inset) obtained from [001] PMN data compared to the INS data of Refs. [146, 159] and IR of Ref. [160]. The lower line (E_1) corresponds to a fit with a Cochran law. (b) Temperature dependence of the E_1 mode frequencies ω_0, $\omega_{\rm rel}$, ω', and ω'', defined in the text. (c) Temperature dependence of E_1 and A_1 frequencies ω_0 and damping (in the inset) obtained from [111] PMN data. (d) Temperature dependence of the E_1 mode frequencies ω_0, $\omega_{\rm rel}$, ω', and ω''. The lines in (b), (c) and (d) stand for Cochran-like laws $\omega^2 \propto (T - T_0)$. . . 119

6.17 473 K (a) and 423 K (b) spectra of [111] PMN together with the resulting fit (red lines) using a flat background, a gaussian, a lorentzian, and a DHO. Dashed grey, blue and green lines show individual components corresponding to the SHG, the E_1 mode and the A_1 mode respectively. For clarity, insets show the figure in log scale. 121

6.18 (a) and (b) show the polarization ratio ρ of the normalized HRS intensities of the E_1 and A_1 components, respectively. The lines are guides for the eyes. Insets show $I_N(VV)$ (full symbols) and $I_N(VH)$ (open symbols) for the two components separately. 122

6.19 The polarization ratio ρ of the normalized HRS intensities of the E_1 and A_1 components, respectively. The inset shows the VV and 5.6×VH spectra at 673 K emphasizing that both E_1 and A_1 modes have the same depolarization ratio. 123

6.20 The polarization ratio ρ of the normalized HRS intensities of the A_1 (a) and E_1 (b) components obtained along $z(x'x')\bar{z}$ and $z(x'y')\bar{z}$ directions with $q \parallel [001]$. Insets show both $I_N(VV)$ and $I_N(VH)$ for the two components. . . 124

6.21 Unpolarized HRS spectra of PMT at various temperatures. 125

6.22 Temperature dependence of E_1 and A_1 frequencies ω_0 and damping (in the inset) obtained from PMT data. The open triangles represent the variation of ω_{rel}. (b) Temperature dependence of the E_1 mode frequencies ω_0, ω', and ω'', defined in the text. The lines are Cochran-like laws $\omega^2 \propto (T - T_0)$. . . . 125
6.23 HRS spectra of PMN (a), PMT (b) and PZN (c) at various temperatures. Experiments were performed in forward-scattering except for the high temperature PMT spectra which were collected in backscattering geometry. . . . 128
6.24 Temperature dependence of the frequency ω (a) and the linewidth (b) of the LO3 mode. The inset shows the fitting of the LO3 mode using a lorentzian function with a gaussian function for the tail. 129
6.25 Temperature dependence of LO2 in (a) PMN (forward-scattering, high resolution) and (b) PMT (spectra reproduced from Figure 6.23). For sake of clarity, the spectra are normalized on top of low-frequency component. . . . 130
6.26 (a) PMN spectrum at 723 K (top) and at 230 K (bottom). (b) PMT spectra at 623 K (top) and at 373 K (bottom). The red line is fit resulting from the model described in the text. Dashed lines show the individual contributions corresponding to the E_1 and A_1 components. 130
6.27 Temperature dependence of the E_1 (a) and A_1 (b) frequencies together with $\Delta\omega = \omega(A_1) - \omega(E_1)$ (c) for both PMN and PMT. The dashed lines are guides for the eyes. 131
6.28 Temperature dependence of the E_1 and A_1 (a) and $\Delta\omega = \omega(A_1) - \omega(E_1)$ (b) for PZN. The inset shows the evolution of the A_1 component near T_m. 132
6.29 Temperature dependence of the frequency of the E_1-component of LO1 in PMN. The inset shows the HRS spectra at three different temperatures surrounding $T_f \approx 220$ K. 133
6.30 Temperature dependence of the frequency of the E_1-component of the LO1 mode of PMT (a), PMN (b) and PZN (c). 134
6.31 The SHG (elastic contribution in HRS) as a function of temperature in PMN (a) and PZN (b) emphasizing a sharp maximum at $T_f \approx 385$ K in the latter. The inset shows the hysteresis behavior of the SHG signal in PZN. 135
6.32 The full set of HRS vibrations in PMN (a) and PMT (b). 136
6.33 Temperature dependence of the inverse of the dielectric constant in PMN. The circles represents the values of $1/\epsilon$ calculated from the HRS polar modes. 138
6.34 (a) Polarized HRS and RS spectra of [001] PMN crystal. (b) Unpolarized HRS and RS spectra of [001] PMT crystal. 139

List of Tables

2.1 Type and characteristic temperatures for each of our five samples. T_C is used for normal ferroelectrics and T_f for relaxors. 26

6.1 HRS symmetry selection rules indicating normalized relative intensities of F_{1u} and F_{2u} modes in a $Pm\bar{3}m$ symmetry crystal in various backscattering geometries describing the general conditions for first-order HRS. 105

6.2 HRS symmetry selection rules indicating normalized relative intensities of F_{1u} and F_{2u} modes in a $Pm\bar{3}m$ symmetry crystal in various backscattering geometries for the case of *fully symmetric* HRS tensors ($b = b'$ and $c = c'$) as a function of $\eta = a/b$. 106

6.3 Values of frequencies ω_0 and damping parameters Γ (defined in equation (6.4) and, in case of F_{2u} mode, in equation (6.5)), as obtained from fits to data shown in the Figure 6.8. 111

6.4 Frequencies and damping parameters of PMN and PMT modes obtained from HRS spectra at room temperature. The PMN parameters are compared with the corresponding values obtained from the fit of the IR reflectivity spectra [153]. 137

6.5 Frequencies and damping parameters of the E_1 and A_1 modes of the TO1 doublet of PMN obtained from HRS spectra at different temperatures. . . . 138

Contents

Introduction **1**

I Ferroelectrics and Relaxors **5**

1 Properties of Ferroelectric Materials **7**

1.1 Introduction . . . 7

1.2 Ferroelectricity and Perovskite Structure . . . 8

1.2.1 Symmetry of materials . . . 8

1.2.2 Simple and complex perovskites . . . 8

1.2.3 Distortions in perovskites . . . 10

1.2.4 Stability of perovskite structure . . . 11

1.3 Ferroelectric Materials . . . 11

1.3.1 Ferroelectric transitions . . . 11

1.3.2 Ferroelectric domains and polarization switching . . . 13

1.3.3 Polarization-electric field hysteresis loop . . . 14

1.3.4 Strain-electric field hysteresis loop . . . 16

2 Relaxors and Complex Perovskites **19**

2.1 Normal Ceramics and Single Crystal Relaxors . . . 19

2.1.1 Relaxors and polar nanodomains . . . 19

2.1.2 General properties of relaxors . . . 20

2.1.3 Evidences for polar nanodomains in relaxors below T_d: the case of $PbMg_{1/3}Nb_{2/3}O_3$ . . . 22

2.2 Specific Properties of Complex Perovskites . . . 26

2.2.1 $PbTiO_3$ . . . 26

2.2.2 $Pb(Zr_{1-x}Ti_x)O_3$ . . . 28

2.2.3 $PbZn_{1/3}Nb_{2/3}O_3$ . . . 30

2.2.4 $PbMg_{1/3}Ta_{2/3}O_3$ . . . 31

II Structural Investigations of Lead-based Perovskites 33

3 Neutron Diffraction Study of the Ferroelectric-Paraelectric Phase Transition in $PbTiO_3$ 35

3.1 Neutron Powder Diffraction . . . 35
3.1.1 Theoretical background . . . 35
3.1.2 Experimental procedure . . . 39
3.1.3 Rietveld refinement . . . 42
3.2 Neutron Diffraction from $PbTiO_3$ . . . 43
3.2.1 Introduction . . . 43
3.2.2 High temperature experiment . . . 45
3.2.3 High pressure experiment . . . 51
3.2.4 Conclusion . . . 55

4 Local Structure of $PbZr_{0.52}Ti_{0.48}O_3$ and $PbZn_{1/3}Nb_{2/3}O_3$ 57

4.1 X-ray Absorption Fine Structure . . . 57
4.1.1 Definition . . . 57
4.1.2 X-ray absorption spectrum . . . 58
4.1.3 Performing the experiments . . . 59
4.1.4 Analysis of the data . . . 62
4.2 Zr K Edge XAFS Study of PZT . . . 64
4.2.1 Introduction . . . 64
4.2.2 Results and discussion . . . 65
4.2.3 Conclusion . . . 72
4.3 Probing the Giant Piezoelectric Effect in PZN . . . 73
4.3.1 Introduction . . . 73
4.3.2 Results and discussion . . . 74
4.3.3 Conclusion . . . 81

III Lattice Dynamics of Lead-based Relaxors 83

5 Hyper-Raman Scattering 85

5.1 Theory and Experimental Technique . . . 85
5.1.1 Optical spectroscopy . . . 85
5.1.2 Phenomenological treatment of HRS . . . 86
5.1.3 Lattice dynamics of polar modes . . . 87
5.1.4 Hyper-Raman scattering cross-section . . . 90
5.1.5 Experimental . . . 92
5.2 LO Modes in Backscattering Geometry . . . 95

6 Hyper-Raman Scattering of Typical Ferroelectric Relaxors **99**
6.1 Introduction . . . 99
6.2 F_{2u} Mode of PMN . . . 102
6.2.1 Theoretical background . . . 103
6.2.2 Experimental . . . 105
6.2.3 HRS spectra . . . 106
6.2.4 Mode assignment . . . 109
6.2.5 Conclusion . . . 113
6.3 Soft Mode . . . 113
6.3.1 PMN . . . 113
6.3.2 PMT . . . 124
6.3.3 Conclusion . . . 126
6.4 LO Modes . . . 127
6.4.1 LO3 . . . 127
6.4.2 LO2 . . . 129
6.4.3 LO1 . . . 132
6.4.4 Conclusion . . . 134
6.5 Summary of HRS modes . . . 136
6.5.1 Assignment of the modes . . . 136
6.5.2 Relation to dielectric properties . . . 137
6.5.3 Comparison with Raman . . . 139

Conclusions and Perspectives **141**

Appendix **145**
A High-Tempertaure Neutron Diffraction of $PbZr_{0.52}Ti_{0.48}O_3$ . . . 145
B Hyper-Raman Selection Rules in Cubic Relaxors: Detailed Calculations . . . 146

Publications **151**

Bibliography **153**

Introduction

The discovery of piezoelectricity in 1880 opened a new field of experimental and theoretical research. This property is present in crystalline structures that lack a center of symmetry and the piezoelectric materials convert mechanical energy into electrical energy and vice-versa. Although quartz is up to the present the most used piezoelectric material for electronic applications, lead-based ferroelectric perovskites are known to have the largest piezoelectric coefficients and electromechanical coupling. These materials exhibit a net spontaneous polarization even in the absence of an external electric field which can be modulated by applying an electric field or mechanical stress. These ferroelectrics include mainly the lead zirconate titanate $PbZr_{1-x}Ti_xO_3$ with $0.45 < x < 0.52$ (*i.e.* compositions in the morphotropic phase boundary region), which is the most widely used piezoelectric material in technological applications such as electromechanical transducers, actuators, motors, sensors, capacitors of very high capacitance, 3D memories in new microelectromechanical systems (MEMS), micro- and nano- positioning devices, etc. Moreover, the complex lead perovskite solid-solution relaxors $PbMg_{1/3}Nb_{2/3}O_3$-$PbTiO_3$ (PMN-PT) and $PbZn_{1/3}Nb_{2/3}O_3$-$PbTiO_3$ (PZN-PT) which are characterized by huge electromechanical coupling have great potential for new generations of technological materials. The exceptional characteristics of these lead-based materials encourage us to study the physical properties of the $PbZr_{0.52}Ti_{0.48}O_3$ ceramic as well as $PbTiO_3$ (PT), $PbMg_{1/3}Nb_{2/3}O_3$ (PMN), and $PbZn_{1/3}Nb_{2/3}O_3$ (PZN) which serve as the essential parent materials for PZN-PT and PMN-PT.

Most of the widely used relaxors are complex oxide perovskites with two different cations, B' and B'', occupying the B-site of the ABO_3 lattice. The random substitution of B' and B'' gives rise locally to a strong chemical and positional disorder. Therefore, the local structure of most relaxors is different from their average structure. Upon cooling, the nucleation of randomly oriented polar nanoregions (PNRs) starts near a singular temperature known as Burns temperature T_d. This is accompanied with a transformation from a paraelectric phase to ergodic relaxor state. However, the absence of charge compensation between the ions of B' and B'' leads to the appearance of very strong local electric fields. It is these random fields together with the strong structural disorder which probably prevent for a long range order. It is believed that all the physical properties of relaxors are governed by the dynamics of the PNRs. Below T_d, the motion of the PNRs slows down until they are completely frozen below a temperature T_f, where there is a transition to a nonergodic state. Similar kind of nonergodicity is a characteristic of a dipole glass phase. The existence in relaxors of an equilibrium phase transition into a low-temperature glassy phase is one of the most interesting hypotheses which have been intensively discussed. The dielectric constant exhibits a strong diffuse behavior characterized by a temperature and frequency dependent

maximum. This maximum occurs at a temperature T_m which does not correspond to a structural phase transition from paraelectric to ferroelectric state similar to the Curie point T_C in normal ferroelectrics.

In spite of the numerous works that have been published, the lack in the clear understanding of the size distribution, the roughness of the boundaries, the shape anisotropy, the distribution of the associated dipolar moments, and the dynamics of these PNRs limit the further advancement for using relaxors in technological applications. Indeed, it is very difficult to access the nano-scale structure of these disordered systems using the usual structural and spectroscopic tools.

The experiments described in this manuscript were performed by neutron diffraction, X-ray absorption fine structure (XAFS), and hyper-Raman scattering (HRS). Owing to its favorable static structure factor and its sensitivity to oxygen atoms, the first is the technique of choice to refine the average crystalline symmetry of oxide perovskites. The second probe the first coordination shells of a given atom and is thus very sensitive to the local order or disorder. The third one, hyper-Raman scattering, is a non-linear optical spectroscopy and probe the vibrations. It is very sensitive to polar modes, but interestingly has been only very little exploited in complex perovskites. In this thesis work the materials were studied as a function of temperature, pressure, and under applied electric field. The manuscript is divided into three parts:

Part I introduces the definitions and the common properties of ferroelectric materials including the structural and the crystal symmetry conditions for ferroelectricity. The types of phase transitions which take place upon temperature and the effects of an applied electric field such as polarization switching and the hysteresis loop are also described. In chapter 2, the general properties of relaxors as compared to those of normal ferroelectrics are discussed. The experimental evidences for the presence of polar nanodomains in relaxors below the Burns temperature are shown for the prototypical relaxor system, PMN. Finally, the main physical properties of the materials studied in this work are briefly summarized.

In Part II, neutron diffraction and XAFS were used to study the structural properties of three lead-based perovskites in function of temperature, pressure and applied electric field. In chapter 3, we introduce the main properties of neutrons and list the advantages of neutron diffraction experiments compared to X-rays. The chapter continues with a short description of the experimental setups. Then, the neutron diffraction results of the ferroelectric-paraelectric phase transitions in lead titanate PT as a function of pressure and temperature are discussed. Chapter 4 concerns the XAFS experiments performed on the European Synchrotron at the ESRF (Grenoble). The first part briefly introduces XAFS,

and discusses its ability for probing the local structure of complex ferroelectric materials. After a short description of the experimental setup, the results of $PbZr_{0.52}Ti_{0.48}O_3$ in function of temperature and pressure and of PZN under electric field are summarized, and their consequences in term of local order are discussed.

The third part concerns the HRS from three model lead-based relaxors, (PMN, $PbMg_{1/3}Ta_{2/3}O_3$ (PMT) and PZN). All the experiments were performed on single crystal samples. The basics of HRS and the experimental setup are presented in chapter 5. A discussion about the activity of the longitudinal modes (LO) in backscattering is also included. Chapter 6 presents the experimental results. It is divided into five sections. Section 1, gives a brief overview of the literature data on the vibrations in these materials, obtained by Raman scattering, infrared reflectivity, and inelastic neutron scattering. The next section summarizes the detailed spectroscopy of the non-polar silent mode of PMN, including polarization analysis, and wave vector dependence of the intensities. The temperature dependence of the soft mode measured in PMN and PMT down to very low frequency is discussed in section 3. The behavior of the three polar LO modes in PMN, PMT, and PZN are shown in section 4. Finally, a summary of all the hyper-Raman active modes, a comparison with the dielectric properties and with the Raman spectra is given in the last section.

Part I

Ferroelectrics and Relaxors

Chapter 1

Properties of Ferroelectric Materials

1.1 Introduction

Dielectric materials of large permittivity are predominantly characterized by ionic bonds. When an electric field $\vec{E}$ is applied, positive charges are attracted to the cathode and negative charges are attracted to the anode due to the electrostatic interaction. This charge distribution generates electric dipole moments and this phenomenon is known as the *polarization* of dielectrics by an electric field. The induced polarization $\vec{P}$ is the sum of the electric dipole moments per unit volume. The total stored charge per unit surface of material is known as the dielectric displacement $\left|\vec{D}\right|$ where the vector $\vec{D}$ is [1]:

$$\vec{D} = \epsilon_0 \vec{E} + \vec{P} \tag{1.1}$$

where ϵ_0 is the dielectric permittivity of vacuum.

A dielectric material is referred to as a *piezoelectric* material if it can be polarized, in addition to an electric field, by the application of a *mechanical stress*. The appearance of a charge density when a mechanical stress is applied is known as the *direct* piezoelectric effect, while the deformation (expansion or contraction) of a material by an applied electric field is known as the *converse* piezoelectric effect.

A *Pyroelectric* material exhibits polarization even in the absence of an external electric field. This polarization is called a spontaneous polarization $\vec{P}_S$. The change of the spontaneous polarization vector with temperature T defines the pyroelectric effect [1]:

$$\vec{p} = \frac{\partial \vec{P}_S}{\partial T} \tag{1.2}$$

where $\vec{p}$ (C m^{-2} K^{-1}) is the vector of pyroelectric coefficients. All pyroelectric materials are piezoelectric.

If the direction of the spontaneous polarization of a pyroelectric material can be reoriented (switched) by the application of an external electric field, this material is called a *ferroelectric* [2]. It is clear that all ferroelectric materials are pyroelectric. In a similar manner, a material is said to be *ferroelastic* if the spontaneous strain can be switched when a mechanical stress is applied. In general, ferroelectric and ferroelastic behaviors are highly coupled.

1.2 Ferroelectricity and Perovskite Structure

The crystalline structure of a material affects its properties. Some properties (such as dielectric permittivity, elastic compliance) are present in all materials while other properties (such as pyroelectricity and piezoelectricity) are present only in materials of certain symmetries. According to Neuman's principle, it is known that the symmetry elements of any physical property of a crystal must include all the symmetry elements of the point group of the crystal. This means that the value of any physical property of a cystal should not change when it is subjected to a symmetry element of this crystal [3].

1.2.1 Symmetry of materials

According to crystal symmetry, crystals can be divided into 32 point groups (crystal classes). 11 of these classes have a center of symmetry. Centrosymmetric crystalline structures do not possess any polar properties even when an electric field is applied. Of course, the electric field will produce a strain but this strain is unchanged on the reversal of the electric field. This is known as *electrostriction* property and occurs naturally in all substances [4]. Among the other 21 non-centrosymmetric groups, 20 groups can exhibit polarity when a stress is applied. These 20 groups are piezoelectric. Among those, 10 point groups (1, 2, m, mm2, 4, 4mm, 3, 3m, 6, and 6mm) have a unique polar axis and display a spontaneous polarization [5]. Such classes are the pyroelectric (polar) classes. In some pyroelectric classes, the spontaneous polarization can be switched when an electric field is applied and thus possess the ferroelectric properties.

1.2.2 Simple and complex perovskites

There are many types of crystals that show ferroelectric properties but the best known since over 60 years probably belong to the perovskite family of general formula ABO_3 [6, 7, 8, 9]. In addition to ferroelectricity, compounds of this family exhibit many other

physical properties such as ferroelasticity [10], superconductivity [11, 12, 13], magnetoresistance [14], dielectric properties [15], ferro/antiferro-magnetism [16], multiferroic properties [17].

The ideal perovskite oxide structure is cubic, with space group symmetry $Pm\bar{3}m$. It is probably one of the simplest examples of structure containing two different cations [18]. The cubic perovskite structure is shown in Figure 1.1 where the A atoms are at the corners of the cube, the B atoms are at the center of the cube and the oxygens at the center of the faces. The perovskite lattice usually consists of small B cations at the center of the oxygen octahedra, and larger A cations which are 12 fold coordinated by oxygen.

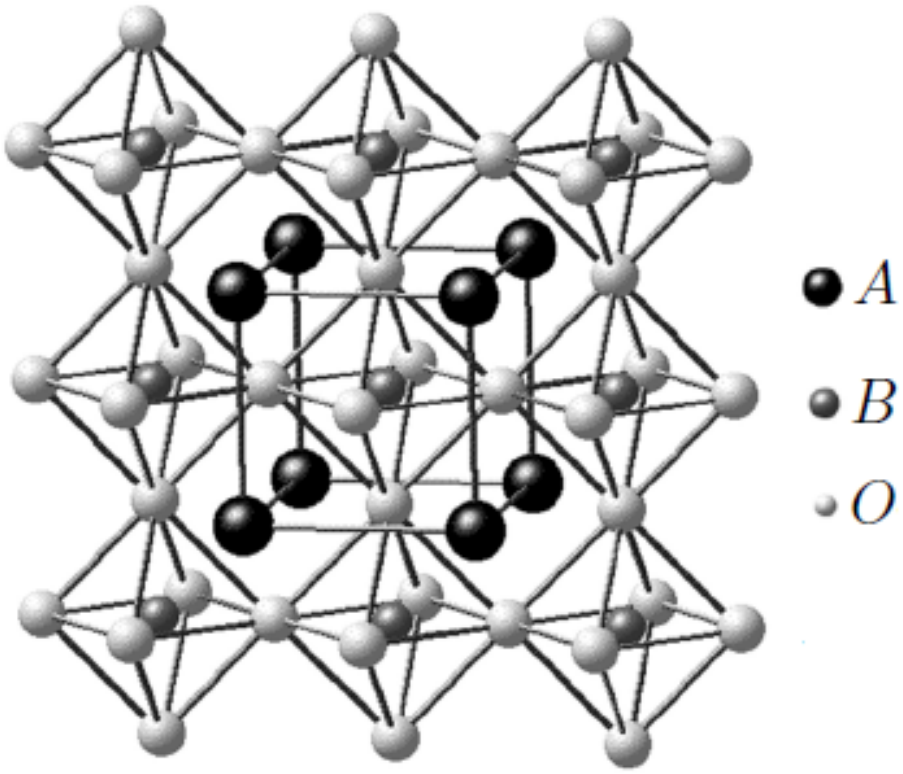


Figure 1.1: Simple cubic perovskite unit cell of type ABO_3.

There also exists perovskite-type crystals where the A-site and/or the B-site are occupied by more than one cation. This leads to another type of materials known as complex or double perovskite structure. Complex perovskite structure has a general formula $AA'BB'O_3$. Complex perovskites show many new physical properties that do not appear in simple perovskites, in particular the relaxor effect [19] which is the main topic of this work.

1.2.3 Distortions in perovskites

Owing to the relative sizes of the cations A and B, different types of distortions occur in simple cubic perovskite structures leading to a reduction in symmetry. The three distortions identified by Megaw [18] are:

i- Distortions of the octahedral units (Jahn-Teller distortion).

ii- B-cation displacements relative to the oxygen octahedra, leading to either a ferroelectric (if all the B atoms move in the same direction with irreducible representation Γ_4^-) or antiferroelectric (if the B atoms move in opposite directions with irreducible representation M_3^-) structure.

iii- The tilting of the octahedra relative to one another [20, 21]. This is the most common distortion of perovskites (Figure 1.2). The titling takes place if the A atom is too small for the large 12-fold site, thus adjacent octahedra tilt in opposite senses about one or more of their symmetry axes, maintaining both regularity of the octahedra (approximately) and their corner connectivity (strictly) [22]. Such tilting increases the size of the unit cell and reduces the size of the A-site while leaving the environment of the B-cation essentially unchanged [22]. The tilt of two adjacent octahedra is always out-of-phase in the plane perpendicular to the rotation axis, but can be either in-phase or out-of-phase for successive octahedra along the axis. The former leads to a structure with an irreducible representation M_3^+ while the irreducible representation of the latter is R_4^+.

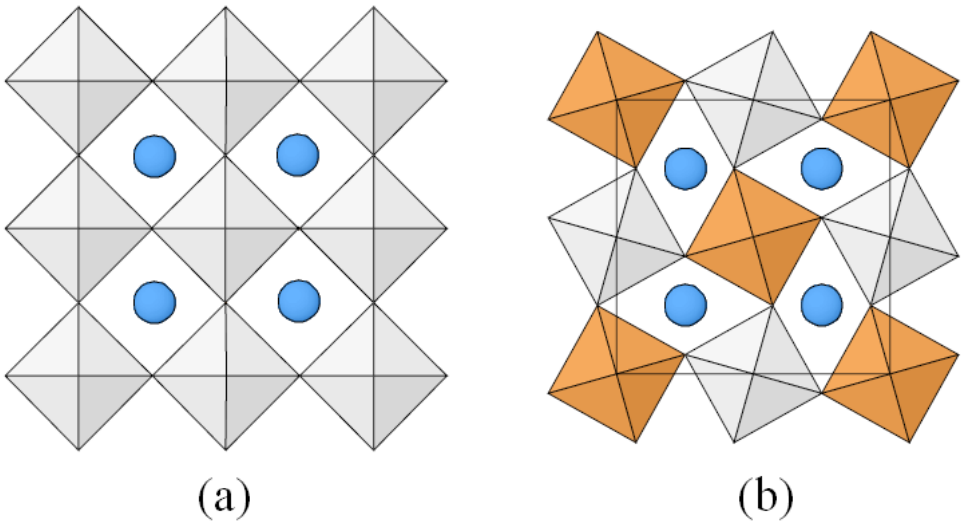


Figure 1.2: (a) The cubic perovskite in its high symmetry form with no octahedral tilting. (b) Perovskite structure in its low symmetry form with octahedral tilting. The spheres represent the A cations.

Each of these distortions can occur separately or in combination, leading to a great variety of different structural modifications depending on the sizes, the bonding character and the ordering of these different cations occupying the A or B sites.

1.2.4 Stability of perovskite structure

The octahedral tilting distortion was first examined by Goldschmidt in 1926 [23]. In order to determine the stability of perovskite phases, Goldschmidt defined the tolerance factor t as follows

$$t = \frac{(R_A + R_X)}{\sqrt{2}(R_B + R_X)} \tag{1.3}$$

where R_A, R_B and R_X are the ionic radii of the A-site and B-site cations and the X-site anion respectively in an ABX_3 perovskite. In the case of complex perovskites, the average ionic radius of the ions occupying each site is considered.

The deviation of t from unity measures the degree of distortion of a perovskite from the ideal cubic structure. The ideal cubic perovskite $SrTiO_3$ has $t = 1.00$, $R_A = 1.44$ Å, $R_B = 0.605$ Å, and $R_X = 1.40$ Å. Stable perovskite structures have values approximately $0.78 < t < 1.05$ [24]. The relation between the value of the tolerance factor t and the symmetry has been determined through experiments. The symmetry is hexagonal when t ranges between 1 and 1.13, cubic for $0.89 < t < 1$ [25, 26] and orthorhombic for $0.75 < t < 0.89$. The phase of tilting also depends on the tolerance factor. Reaney *et al.* [24] showed that at room temperature perovskites with $0.985 < t < 1.06$ are expected to have untilted structures. Perovskites with $0.964 < t < 0.985$ are usually tilted in antiphase and perovskites with $t < 0.964$ are expected to show in-phase and antiphase tilting.

1.3 Ferroelectric Materials

1.3.1 Ferroelectric transitions

The magnitude of the net spontaneous polarization of a ferroelectric material decreases when increasing temperature or pressure. Above a critical temperature T_C (and a critical pressure P_C), the spontaneous polarization disappears and a phase transition from ferroelectric state (polar) to a paraelectric state (non-polar) takes place. This transition can be defined from a structural point of view as a phase transition from a non-centrosymmetric to a centrosymmetric structure [2]. For most ferroelectrics, the paraelectric state is the highest symmetry phase compatible with the ferroelectric structure which is known as the prototype phase.

The structural phase transition from paraelectric to ferroelectric phase is due to the displacement of both cations occupying the A and B sites in the perovskite. This transition usually leads to strong anomalies in the dielectric, elastic, thermal and other properties of the material [2] and is accompanied by changes in the dimensions of the crystal unit cell. In most cases, this transition should be associated with the condensation of a low frequency vibrational mode (soft-mode) at the Brillouin zone-center [2, 27].

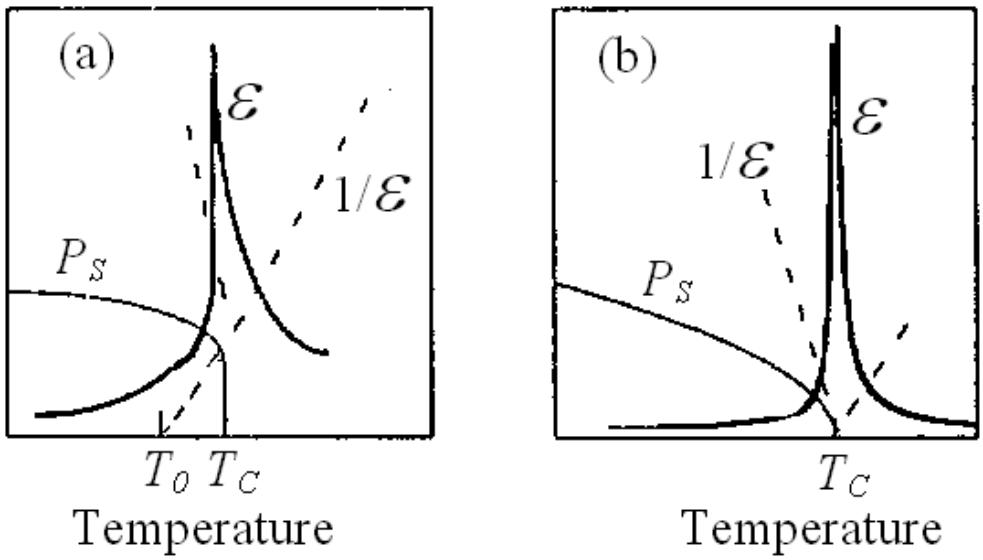


Figure 1.3: Temperature dependence of the dielectric permittivity ϵ and spontaneous polarization P_S for (a) first-order and (b) second-order ferroelectric phase transition. Source: D. Damjanovic [1].

Ferroelectric transitions are classified into first-order and second-order phase transitions. The spontaneous polarization (Figure 1.3(a)) and crystal structure of first-order ferroelectric are characterized by sudden (discontinuous) changes at the phase transition temperature where a metastable phase appears while the second-order phase transition is characterized by continuous changes in the spontaneous polarization (Figure 1.3(b)) and crystal structure at the phase transition temperature.

For ceramic ferroelectrics, the change in the lattice structure will be associated with a sharp peak in the dielectric constant at T_C. In the paraelectric phase above T_C, the dielectric constant ϵ decreases with temperature according to the Curie-Weiss law (shown in Figure 1.3)

$$\epsilon = \frac{C}{T - T_0} \tag{1.4}$$

where C is the Curie constant and T_0 is the Curie-Weiss temperature. It is important to know that for a second order phase transition $T_0 = T_C$ while for a first order phase transition $T_0 < T_C$ as shown in Figure 1.3.

1.3.2 Ferroelectric domains and polarization switching

Ceramic ferroelectrics consist of large number of randomly oriented grains. A grain is made of ferroelectric domains (symmetry-related variants) and the domain itself is composed of number of unit cells. In each domain, the spontaneous polarization is uniformly oriented and its direction is determined by the symmetry of the material [28]. For example, the six variants are equivalent in a cubic cell while they are different in a tetragonal phase as shown in Figure 1.4(a). Since the domains are energetically identical, it is possible to switch one domain to another by suitable applied electric field. The permanent alignment of different domains by a strong applied electric field is known as poling.

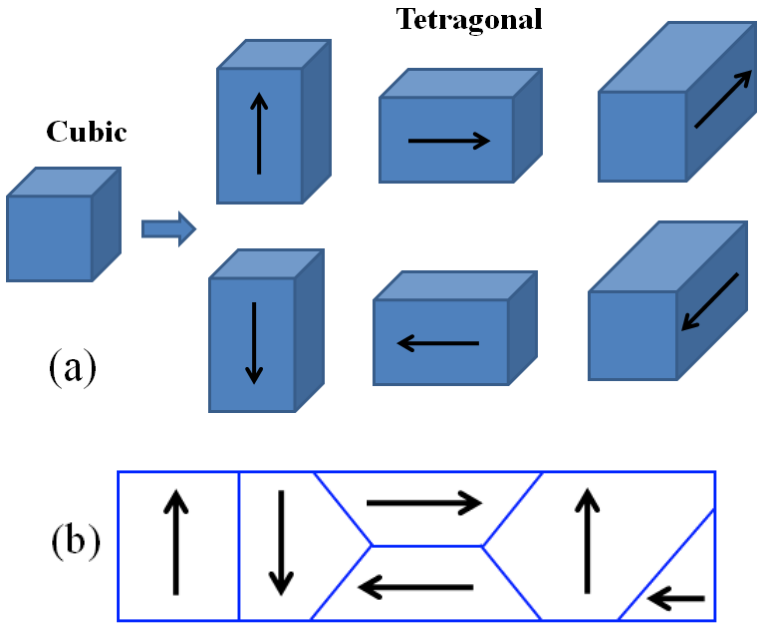


Figure 1.4: (a) The six possible directions of the ferroelectric polarization (black arrows) in the tetragonal phase of $BaTiO_3$. (b) Schematic diagram of 180° and 90° domain walls.

Domains are separated by domain walls. The width of a domain wall is of few nanometers or less [29]. In a tetragonal ferroelectric phase, the angles between two domains are either 90° or 180°, whereas they are 71°, 109°, or 180° in a rhombohedral phase. 180° domain walls separate domains with oppositely oriented polarization while 90° domain walls separate perpendicular domains. The 180° and 90° domain walls are schematically shown in Figure 1.4(b). Ferroelectric domains form to minimize the electrostatic energy of depolarizing fields and the elastic energy associated with mechanical constrains to which the material is subjected when it is cooled down through the paraelectric-ferroelectric phase transition [2, 30, 31].

Let us take the prototypical perovskite, barium titanate ($BaTiO_3$) [32, 33], as an example. Figure 1.5 shows various crystalline phases of $BaTiO_3$ at different temperatures. It is paraelectric (no net spontaneous polarization) with cubic phase at high temperature,

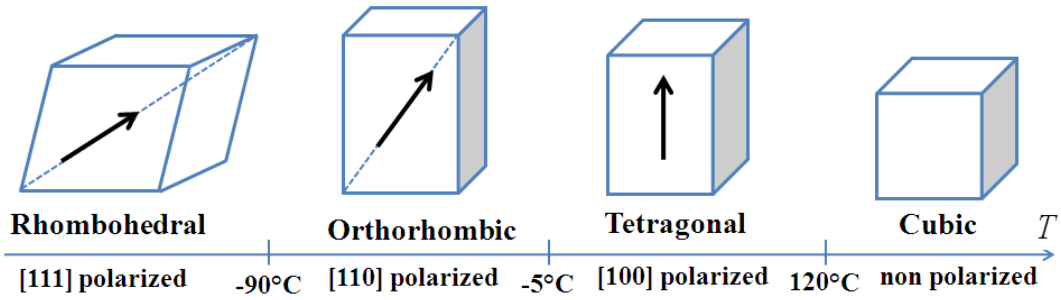


Figure 1.5: The change in the crystallographic symmetry of $BaTiO_3$ at different temperatures. The arrow indicates the spontaneous polarization direction.

tetragonal and [100] polarized below its Curie temperature (T_C = 120°C), orthorhombic and [110] polarized below 5°C, and [111] polarized rhombohedral below -90°C. Figure 1.6 shows the crystal structures of $BaTiO_3$ in both cubic and tetragonal phases. As shown in the figure, when $BaTiO_3$ is cooled down through the Curie temperature, both the Ba and Ti atoms shift upward from their lattices relatively to the negatively charged oxygens, generating a spontaneous polarization (net dipole moment per unit volume). This shift breaks the cubic symmetry into a tetragonal phase and results in six symmetry-related and crystallographically-equivalent polar axes (Figure 1.4).

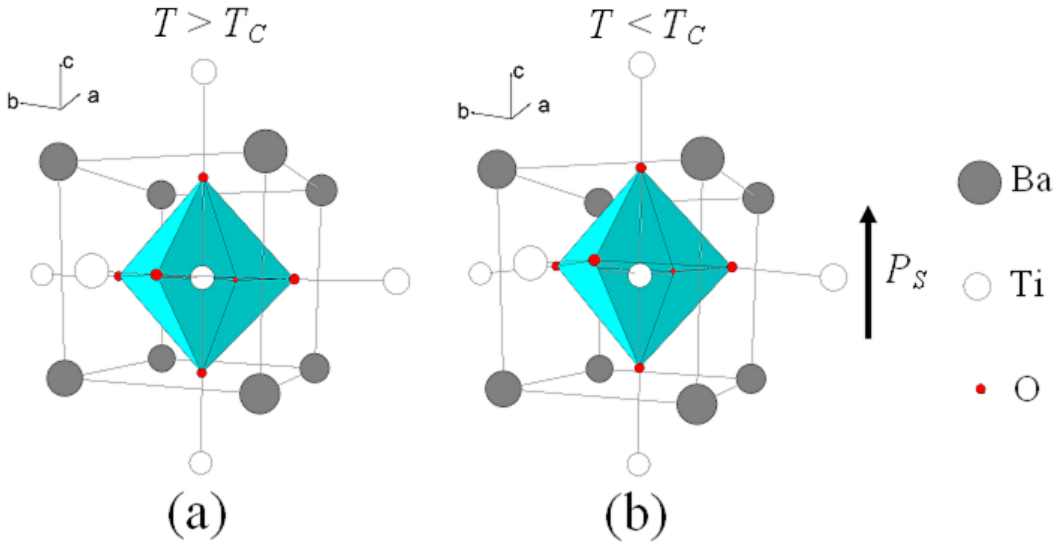


Figure 1.6: Schematic diagram for (a) the cubic phase of $BaTiO_3$ above T_C and (b) the tetragonal phase of $BaTiO_3$ below T_C. The arrow represents the induced spontaneous polarization as the titanium ion shifts from its central position.

1.3.3 Polarization-electric field hysteresis loop

The effect of polarization switching by an external electric field can be clearly seen in the universal hysteresis behavior of ferroelectric materials. Figure 1.7 shows the polarization-electric field hysteresis loop of a typical polydomain ferroelectric material.

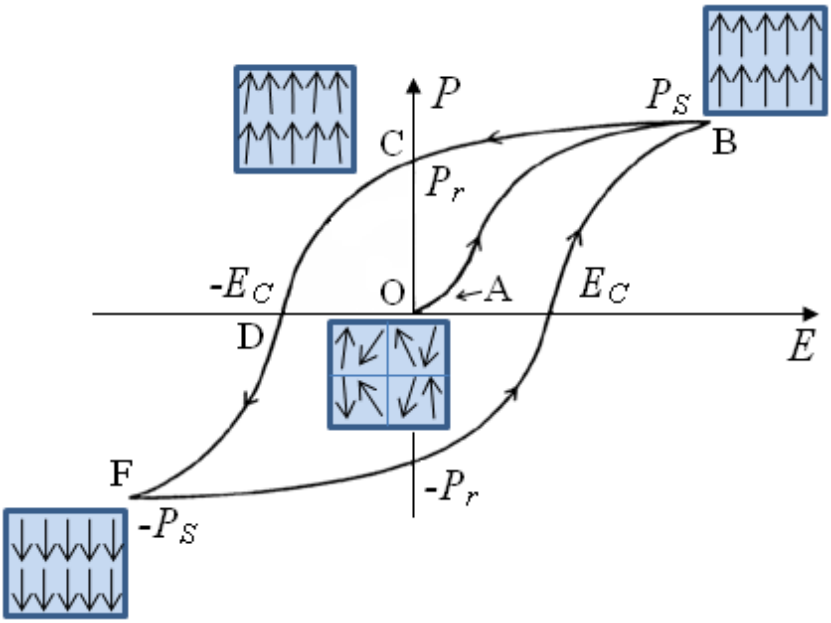


Figure 1.7: Polarization-electric field hysteresis loop. The arrows in the squares indicate the direction of polarization of the material at the indicated fields.

The net polarization of an unpolarized ferroelectric material is almost zero. When a dc electric field is applied, the polarization starts to increase linearly with the applied field, according to the equation $P_i = \epsilon_0 \chi_{ij} E_j$ [1] where χ_{ij} is the second-rank tensor known as the dielectric susceptibility of the material. The segment OA in Figure 1.7 shows this linear region where no polarization switching of unfavorable domains takes place due to small amplitude of the applied field. Increasing the applied field will start polarization switching of the unfavorable domains (domains with the direction of the spontaneous polarization different from the applied field) till all the domains are aligned with the field. The relation of the polarization and the electric field is nonlinear in this region (segment AB in Figure 1.7). At this point, if the field is further increased the polarization remains constant. When the electric field returns to zero, some domains will back-switch but the polarization will not go back to zero (point C). The amount of the switchable polarization at zero electric field is called the remanent polarization, P_r. To go back to zero polarization, the applied field should be reversed (point D). The strength of the electric field that brings the polarization back to zero is known as coercive field, E_C. If the electric field is increased more in the reversed direction, opposite alignment of the domains will take place (point F). To complete the cycle, the field will be reduced back to zero and then reversed again. The value of the coercive field is not fixed [30] because if a smaller value of the field will be applied over very long time the polarization switching takes place.

The value of the maximum remanent polarization $(P_r)_{max}$ depends on the number of domain states. For a ferroelectric with 180° domain walls only, the maximum remanent polarization $(P_r)_{max}$ is just $0.25\,P_S$. For a tetragonal phase with six domains, $(P_r)_{max}$

$= 0.83\,P_S$. For a rhombohedral phase with eight domains, $(P_r)_{max} = 0.87\,P_S$. For an orthorhombic phase with twelve domains, $(P_r)_{max} = 0.91\,P_S$ [34, 35]. These are the values corresponding to the reorientation of all the available domains. Higher values of $(P_r)_{max}$ have been found in some new systems.

1.3.4 Strain-electric field hysteresis loop

In addition to induced polarization, an applied electric field can change the dimensions of a ferroelectric material. The linear relation between the strain x_{ij} and the applied electric field E is given by the converse piezoelectric equation [1]:

$$x_{ij} = d_{kij} E_k, \tag{1.5}$$

where d_{kij} is the converse piezoelectric coefficient.

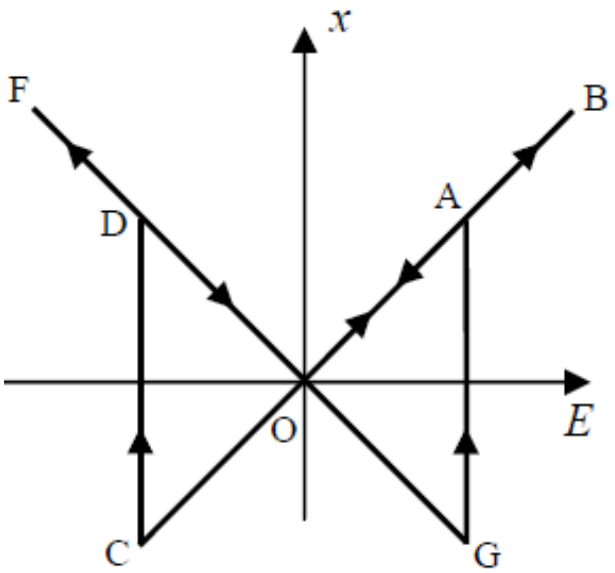


Figure 1.8: Ideal strain-electric field hysteresis loop.

The polarization switching, the movement of domain walls and the strain created by a dc applied electric field will give another hysteresis loop known as strain-electric field hysteresis loop (electromechanical hysteresis loop). The ideal electromechanical loop is schematically shown in Figure 1.8. With no applied electric field, the strain of a material is zero (point O). When a dc field parallel to the spontaneous polarization is applied, the lattice expands and the strain increases (segment OA) according to equation (1.5) till it reaches its maximum at point B. At point B, the strain goes back to zero on decreasing the field back to zero (from B to O). Now if the field is increased in the opposite direction (antiparallel to P_S), the lattice starts to contract and the strain is negative (point C). At C, the large negative field will switch the direction of the polarization (the field and P_S are now parallel again) and the strain will be positive (point D). According to equation (1.5), d_{kij} transforms to $-d_{kij}$. If the field continues to increase in the negative direction,

the strain will increase more till it reaches its maximum at point F. The strain decreases again to zero at point O as the field goes back to zero. At G, the applied positive field will switch the polarization and the strain is reversed to be positive (point A) where the cycle is completed. The strain-field curve is linear everywhere except at the two switching points C and G. In reality, the electromechanical hysteresis loop has a butterfly shape because the switching of non-180° domains makes a significant change in the dimensions of the sample.

Chapter 2

Relaxors and Complex Perovskites

2.1 Normal Ceramics and Single Crystal Relaxors

2.1.1 Relaxors and polar nanodomains

Relaxor ferroelectrics [19, 36, 37] are characterized by broad frequency-dependent peaks of the dielectric constant with a maximum at a temperature T_m that does not correspond to a structural phase transition from paraelectric to ferroelectric state like in normal ferroelectrics. Relaxors can be grown as single crystals and they have higher values of electromechanical and piezoelectric coefficients compared to ferroelectric ceramics owing to the absence of grain boundaries.

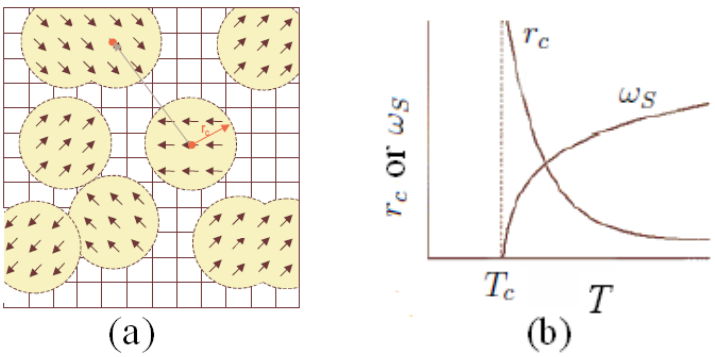


Figure 2.1: (a) Formation of polar nanodoamins. (b) The temperature dependence of the soft mode frequency ω_S and the correlation length r_c of ferroelectric material. Source: G. A. Samara [19]

The chemical substitution in a perovskite can lead to the formation of dipolar impurities owing to the chemical or positional disorder. These dipolar entities on a given lattice site in highly polarizable hosts polarize the regions around them leading to the formation of polar nanodomains (Figure 2.1(a)). The size of these polar nanodomains can be estimated by the temperature-dependent correlation length, r_c, at that site [19]. For a ferroelectric

material, the correlation length is inversely proportional to the soft mode frequency, ω_S [37]. Figure 2.1(b) shows that, at high temperature, r_c and thus the nanodomains are relatively small. With decreasing T, r_c increases and neighboring domains can merge to form larger polar domains (Figure 2.1(a)). If the concentration of the dipoles, n_d, is ultimately high, the domains will percolate the whole sample and form a static, long-range ordered ferroelectric state at $T < T_C$. On the other hand, if n_d is not large enough, the domains will not induce a ferroelectric state; rather, a dynamic 'slowing down' of the dipolar fluctuations within each domain occurs at $T < T_m$ leading at T_f to a glass-like relaxor state [37].

At very high temperatures, thermal fluctuations are large and all relaxors are in the paraelectric state. Upon cooling, the appearance of small polar nanodomains takes place near what is called the Burns temperature (T_d), and the relaxor enters into the ergodic relaxor state [38]. This transformation is not accompanied by a change in crystal structure that can be detected by X-rays and neutron Bragg diffraction peaks because of the extremely small size of these polar regions. The evidence for the existence of the polar nanodomains near T_d far above T_m will be discussed in section 2.1.3. Near T_d, the polar nanodomains are mobile but their dynamics start slowing down when the temperature is decreased toward the temperature T_f where the freezing of polar nanodomains takes place and the relaxor enters in the nonergodic state [38]. The complicated dynamics of these polar nanodomains give rise to a frequency dispersion in the dielectric constant with a maximum T_m greater than T_f. Because of this dispersion, relaxors are known as "ferroelectrics with a diffuse phase transition". The application of a large electric field is able to locally align the polarization leading to larger nanodomains. In this case, the nonergodic state is transformed into long range ferroelectric state. This is known as field-induced nano-to-macrodomain transition [19].

2.1.2 General properties of relaxors

In the literature, different particular temperatures are used to define the relaxor state. But, the Burns temperature T_d [39], the dynamic transition temperature (that corresponds to the broad frequency-dependent peak of the dielectric constant) T_m, and the freezing temperature T_f are the best known three singular temperatures. It is clear that all the main physical properties of relaxors are related to the dynamical behavior of the polar nanodomains that nucleate near T_d, that is far above T_m [19]. The most important properties of a relaxor are shown in Figure 2.2 and can be summarized as follows:

i- Very broad $\epsilon(T)$ peak that shifts to higher temperatures with increasing frequency (Figure 2.2(a)) in contrary to the sharp narrow frequency-independent peak that characterizes a normal ferroelectric (Figure 1.3). The strong frequency dispersion in $\epsilon(T)$ seen

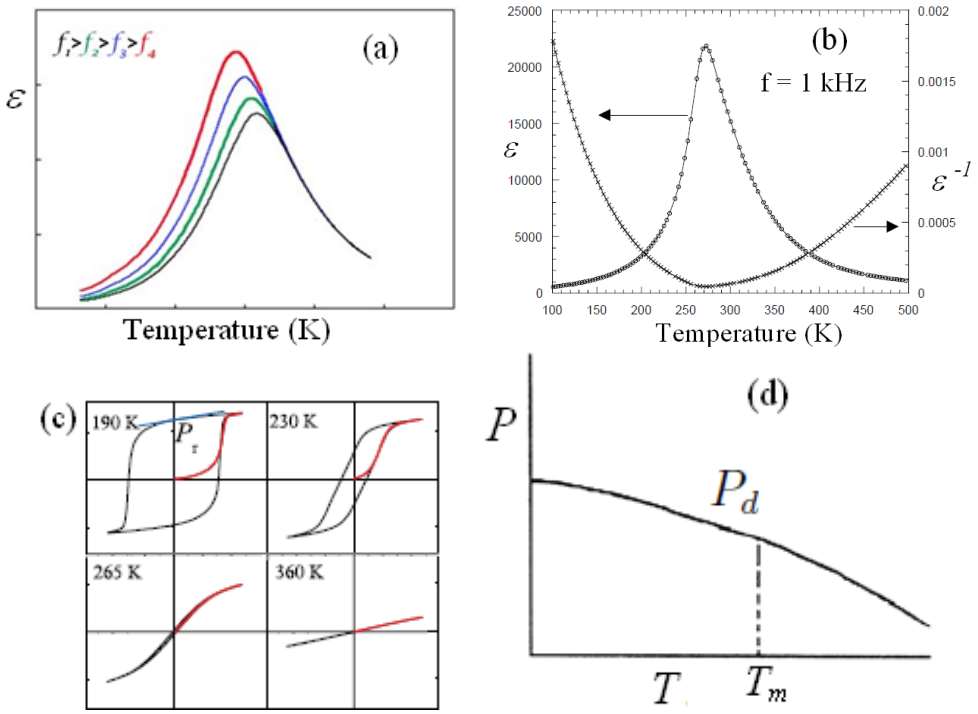


Figure 2.2: (a) Schematic diagram showing the temperature dependence of the real part of the dielectric pertimittivity measured at different frequencies for a prototypical relaxor. (b) Temperature dependence of the dielectric constant ϵ and its inverse ϵ^{-1} at f = 1 kHz. (c) The polarization-electric field hysteresis loop of a prototypical relaxor $PbMg_{1/3}Nb_{2/3}O_3$ at different temperatures. (d) The variation of the dipolar polarization P_d with temperature.

below T_m is due to the slowing down of dipolar fluctuations in the polar nanodomains. This dispersion can be also seen above T_m in the imaginary part of the dielectric constant [19].

ii- The dielectric constant of a relaxor does not follow the Curie-Weiss law (equation 1.4) as for normal ferroelectric (Figure 1.3) except may be well above T_d (Figure 2.2(b)).

iii- At temperatures below T_f, the polarization-electric field loop of a relaxor (left top panel of Figure 2.2(c)) is similar to that of a normal ferroelectric (Figure 1.7). As the temperature increases, both the remanent polarization P_r and the coercive field E_C start to decrease gradually till they become zero above T_m (Figure 2.2(c)). This behavior is not seen in normal ferroelectric, characterized by macro-size domains, where a sudden disappearance of its hysteresis loop takes place above its Curie temperature T_C. Near T_m and for high applied electric field, the nanodomains of a relaxor can be oriented with the field leading to large induced polarization. When the field is removed, most of these domains recover their random orientation leading to a very small remanent polarization P_r.

iv- The dipolar polarization P_d (defined below) does not go to zero at T_m (Figure 2.2(d) as it does for the remanent and the saturation polarization (Figure 1.3) of a normal ferro-

electric that goes to zero near the Curie temperature T_C. The non-zero value of P_d above T_m arises from the persistence of the nanodomains up to $\sim T_d$.

2.1.3 Evidences for polar nanodomains in relaxors below T_d: the case of $PbMg_{1/3}Nb_{2/3}O_3$

Lead magnesium niobate $PbMg_{1/3}Nb_{2/3}O_3$ (PMN) is a typical representative of ferroelectric relaxors. PMN, like most other important relaxors, crystallizes in perovskite structure. It is the random distribution of the Mg^{2+} and Nb^{5+} cations that occupy the B-site and the "off-centering" of the A and/or B cations that lead to the creation of polar nanoregions (PNRs), lowering the symmetry at the local scale. This ensures that the anomalous behavior of many physical properties of PMN that appear near the Burns temperature T_d is due to the nucleation of these randomly oriented ferroelectric clusters (polar nanoregions). However, the refinement of X-ray and neutron diffraction patterns reveals that PMN remains cubic on the average with no structural phase transition down to 5 K [40]. The presence of an electric field that exceeds a threshold value can induce a ferroelectric phase transition in the vicinity of the freezing temperature $T_f = 220$ K [41].

The formation of polar nanodomains near T_d translates into the deviation of the thermal expansion [42] and the refractive index [39] from their standard linear behavior. Both depend on the square of the dipolar polarization, P_d^2, which is a more appropriate quantity than P_d to characterize the polarization state in a relaxor. Indeed, while P_d is always null on the average ($\sum P_d$), owing to the lack of long range polar order, the sum of P_d^2, $\sum P_d^2$, becomes non-zero as far as a static local polarization develops in the material.

The temperature dependence of the thermal strain for the relaxor PMN can be seen in Figure 2.3(a). For a cubic perovskite, the axial thermal strain, x_{11}, above T_m is given by [42]

$$x_{11} = \frac{l_T - l_0}{l_0} = \alpha(T - T_0) + \frac{1}{3}(Q_{11} + 2Q_{12})P_d^2, \tag{2.1}$$

where l_T is the sample length at temperature T, l_0 is the initial length at temperature T_0. α is the linear coefficient of thermal expansion and Q_{11} and Q_{12} are electrostrictive coefficients. Figure 2.3(a) shows that the thermal strain follows the usual linear behavior (the first term on the right-hand side of equation (2.1)) above T_d (top panel of Figure 2.3(a)), and deviates from linearity for $T \leq T_d$ when P_d locally becomes non-zero (the second term on the right-hand side of equation (2.1)).

A similar deviation from the linear behavior can be seen in the temperature dependence of the refractive index n of PMN (Figure 2.3(b)) [39]. It is known that the refractive index of a normal ferroelectric changes linearly with temperature and starts to deviate

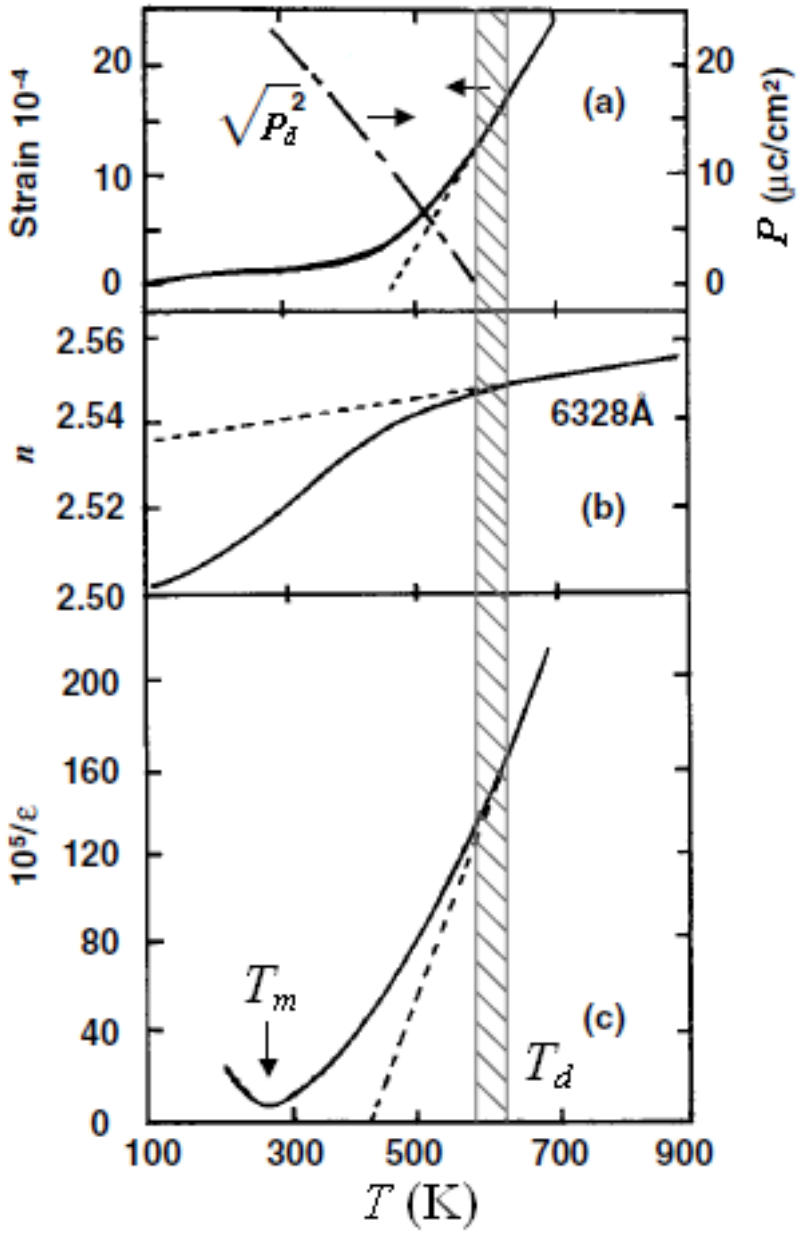


Figure 2.3: Deviation of the thermal strain (a), refractive index (b) and the inverse of the dielectric constant (c) from linear behavior near the Burns temperature T_d for PMN relaxor. Panel (a) also shows the decrease of the root-mean square dipole polarization $\sqrt{P_d^2}$ toward zero near T_d.

from linearity near the Curie temperature T_C. As the temperature decreases below T_C, the deviation increases owing to the phase changes from paraelectric to ferroelectric state and the appearance of spontaneous polarization. However, for relaxors, Burns and Dacol observed deviations from linearity well above T_m. Figure 2.3(b) shows that for a PMN relaxor, the deviation starts near $T_d \approx 620$ K, far from $T_m \approx 270$ K. These deviations can be quantitatively described as [39]

$$\Delta n = \frac{\Delta n_{||} + 2\Delta n_{\perp}}{3} = -\frac{(n^0)^3}{2}\left[\frac{g_{33} + 2g_{13}}{3}\right] P_d^2, \tag{2.2}$$

where $\Delta n_{||}$ and $\Delta n_{\perp}$ are the changes in the parallel and perpendicular components of n, respectively, n^0 is the refractive index at zero polarization, represented by the dashed straight line in Figure 2.3(b), while g_{33} and g_{13} are the electro-optic coefficients [3].

The temperature behaviors of the strain and the refractive index show the first evidence for the formation of polar nanodomains in relaxor at a temperature T_d much higher than the one corresponding to the maximum of the dielectric constant, T_m.

Figure 2.4 shows the temperature dependence of the dielectric permittivity ϵ of PMN single crystals at various frequencies between 3×10^{-3} Hz and 4.2×10^{11} Hz [43]. A typical relaxor behavior with a frequency-dependent peak that moves toward high temperature on increasing the frequency is seen. This dielectric dispersion takes place over a broad temperature region of several hundreds of degrees with a maximum in the vicinity of $T_m = 270$ K at 10 kHz. Similar relaxor behavior was also reported for PMN ceramics and PMN thin films. A comparison of dielectric data obtained for single crystal, ceramics and thin films shows only quantitative, but not qualitative differences [43].

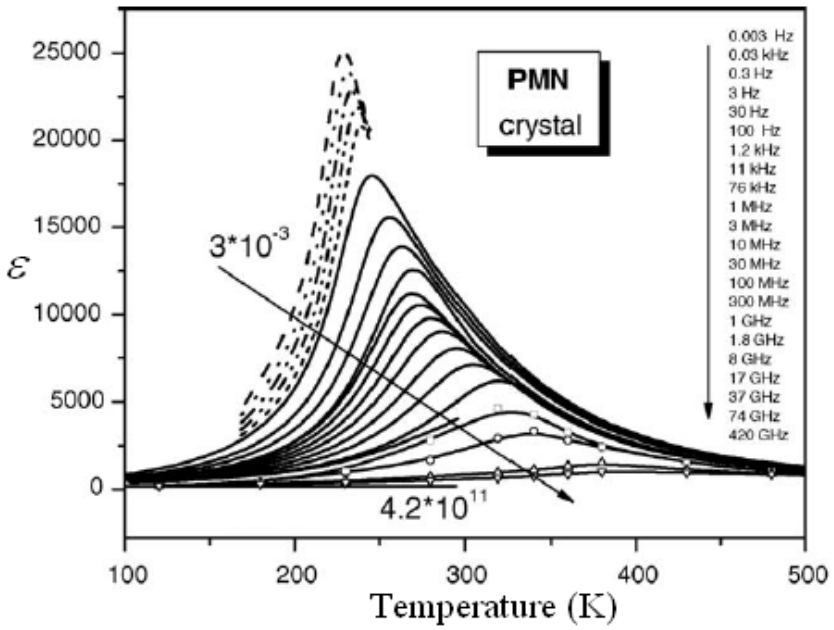


Figure 2.4: Temperature dependence of the dielectric permittivity ϵ of $PbMg_{1/3}Nb_{2/3}O_3$ single crystals at various frequencies. Source: V. Bovtun [43].

Further evidence for the presence of polar nanodomains far above T_m is clearly seen in the temperature dependence of the inverse of the dielectric constant ϵ^{-1} of PMN (Figure 2.3(c)) [44]. It is clear that ϵ^{-1} follows the Curie Weiss law (equation 1.4) in the high temperature region (paraelectric phase) above T_d, while large deviation from this law appear near T_d. This deviation increases on cooling because the size of the polar nanodomains and their correlations increase.

The temperature dependence of the cubic lattice parameter a (Figure 2.5) of PMN shows a clear deviation from its linear behavior near 600 K [40]. This deviation is similar to the

deviation of the thermal strain, refractive index and the inverse of the dielectric constant (Figure 2.3) that takes place near the Burns temperature T_d. This provides another way to estimate T_d.

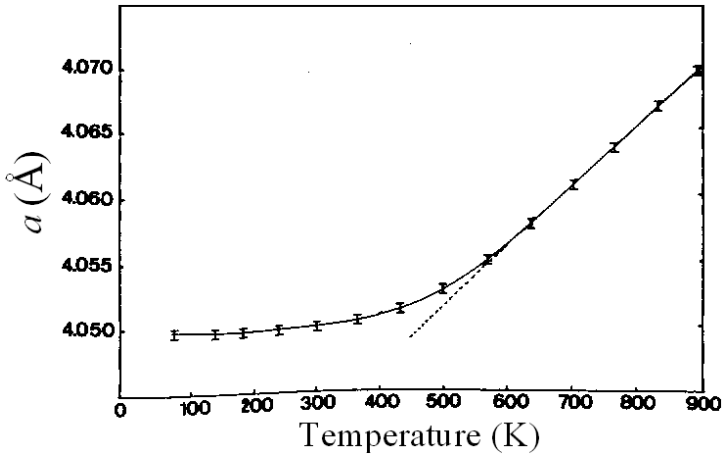


Figure 2.5: Temperature dependence of the cubic cell parameter of $PbMg_{1/3}Nb_{2/3}O_3$. Source: P. Bonneau [40].

Recently, the acoustic emission (AE) method appears as a technique which can be used to investigate different phase transitions in ferroelectric materials. AE is attributed to a sudden release of stored elastic energy. The appearance of AE signals in ferroelectrics can be related to the spontaneous formation of microcracks, the discontinuous motion of domain walls clamped by structural defects or the instantaneous formation of a domain wall of finite size [45]. It is highly sensitive not only to structural changes which occur in

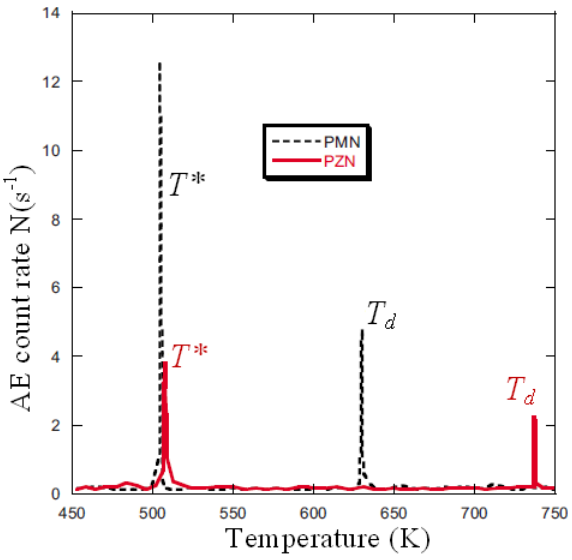


Figure 2.6: Acoustic emission activity as a function of temperature for $PbMg_{1/3}Nb_{2/3}O_3$ and $PbZn_{1/3}Nb_{2/3}O_3$. Source: B. Dkhil [47].

normal ferroelectrics near T_C [46] but also to relatively small structural changes in relaxors

[45, 47, 48]. This can be clearly seen in Figure 2.6, where two AE signals that appear around 500 and 630 K for PMN and 500 and 740 K for PZN. The signals near 630 K and 740 K corresponds to the Burns temperature T_d of PMN and PZN respectively, thus providing AE as a very accurate tool to determine the value of T_d in relaxors. The other signal that appears around 500 K for both PMN and PZN is related to another singular temperature in relaxors known as T^*. T^* corresponds to a local phase transition where static polar nanoclusters start to appear. In other words, it is only at this temperature that the polar nanodomains, that start to nucleate near T_d and considered to be dynamic, start to become static at a nanoscale.

2.2 Specific Properties of Complex Perovskites

One very interesting aspect of relaxor science, which turns out to be a difficulty for the understanding of their physical properties, is that these systems have very marked specific properties in addition to universal ones. For example, materials of the family $AB'B''O_3$ can or can not show a relaxor behavior, some remain cubic down to the lowest temperature (like PMN) while others can exhibit more complex phase diagrams including or not morphotropic phases as defined below,....

Table 2.1: Type and characteristic temperatures for each of our five samples. T_C is used for normal ferroelectrics and T_f for relaxors.

Sample	abbreviation	(K)	T_m (K)	T_d (K)	type
$PbTiO_3$	PT	$T_C = 763$			single crystal
$PbZr_{0.52}Ti_{0.48}O_3$	PZT	$T_C = 664$			ceramic*
$PbMg_{1/3}Nb_{2/3}O_3$	PMN	$T_f = 210$	270	630	single crystal
$PbZn_{1/3}Nb_{2/3}O_3$	PZN	$T_f = 385$	410	740	single crystal
$PbMg_{1/3}Ta_{2/3}O_3$	PMT		170	420 or 570	single crystal

* PZT single crystals have been grown recently in the Department of Chemistry and 4D LABS, Simon Fraser University, Burnaby, British Columbia, Canada [49].

In this part, we summarize the main specific properties of the materials which are studied in this thesis. These samples include the simple perovskite $PbTiO_3$ [50] and four complex perovskites $PbZr_{0.52}Ti_{0.48}O_3$ [51, 52, 53, 54], $PbMg_{1/3}Nb_{2/3}O_3$ [39] (discussed in the previous section), $PbZn_{1/3}Nb_{2/3}O_3$ [39] and $PbMg_{1/3}Ta_{2/3}O_3$ [55] of $AB'B''O_3$ structure. The values of the characteristic temperatures for each of these materials and their types are shown in Table 2.1.

2.2.1 $PbTiO_3$

Lead titanate $PbTiO_3$ (PT) is a classical example of ferroelectric perovskites. It has a cubic structure at high temperature, like most perovskite materials. It exhibits a first-

order displacive paraelectric-ferroelectric phase transition to a tetragonal structure below its Curie temperature $T_C = 763$ K [56] which is considered among the highest for ferroelectric perovskites. This phase transition produces a tetragonal c axis below T_C (Figure 2.7) in case of PT single crystals [57]. X-ray absorption spectroscopy [58] shows that both Pb and Ti atoms are displaced from their positions well above the transition temperature T_C revealing in addition a non-negligible order-disorder character of this transition.

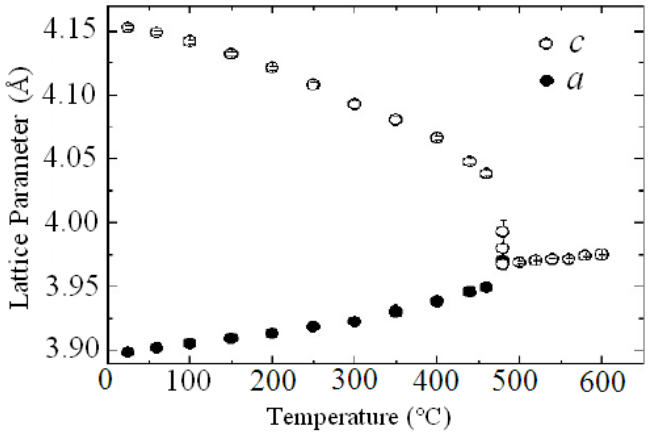


Figure 2.7: Temperature dependence of the lattice parameters of $PbTiO_3$ single crystals. Source: J. Kwapuliński [57].

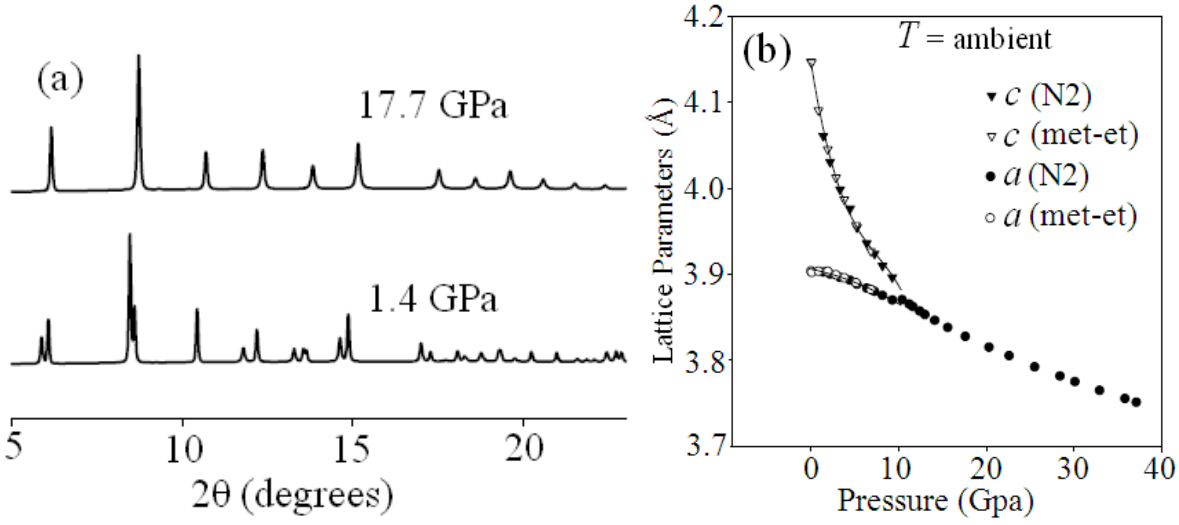


Figure 2.8: (a) X-ray diffraction patterns of $PbTiO_3$ powders showing cubic reflections at 17.7 GPa and tetragonal reflections at 1.4 GPa. (b) Pressure dependence of the lattice parameters of $PbTiO_3$. Source: A. Sani [50].

In the P-T phase diagram, PT also exhibits a cubic to tetragonal phase transition at a pressure P_C and room temperature. The structural changes are clearly visible in the powder diffraction patterns (Figure 2.8(a)), and P_C is obtained from the behavior of the lattice parameters as a function of pressure shown in Figure 2.8(b) [50]. This apparently

continuous phase transition takes place near about 12 GPa, a value in good agreement with that obtained from Raman spectroscopy [59]. A recent high pressure study of PT refined this value to $P_C = 13$ GPa [60]. Jaouen *et al.* [61] checked the nature of the high-pressure phase transition of PT powders at the local scale by using high-pressure Ti K edge X-ray absorption near-edge spectroscopy (XANES). Figure 2.9 shows the deviation of Ti and Pb cations from their cubic sites under pressure. The remaining displacement of the Ti atoms above the critical pressure clearly indicates that, similarly to the transition at T_C, an order-disorder component is also present in this pressure-induced phase transition.

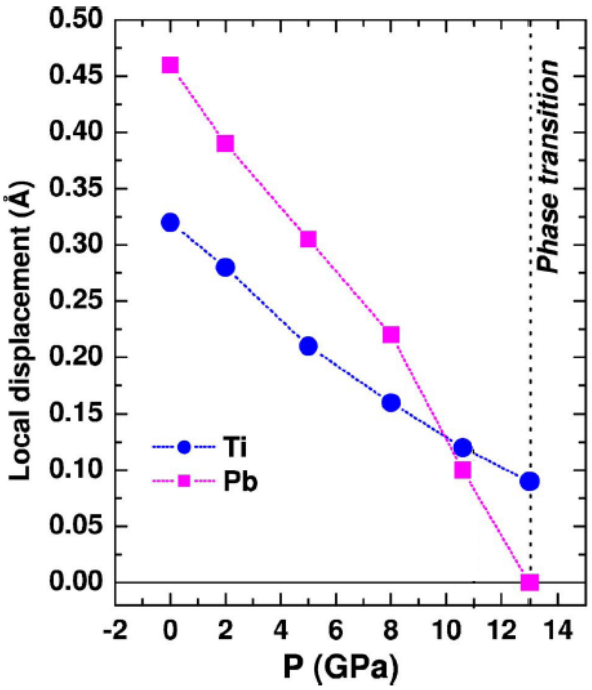


Figure 2.9: Local displacements of Pb and Ti obtained by high-pressure X-ray absorption near-edge spectroscopy measurements. Source: N. Jaouen [61].

2.2.2 $Pb(Zr_{1-x}Ti_x)O_3$

Lead zirconate titanate $Pb(Zr_{1-x}Ti_x)O_3$ (PZT) is a solid solution of lead zirconate ($PbZrO_3$) and lead titanate ($PbTiO_3$). At room temperature, $PbZrO_3$ is in an orthorhombic antiferroelectric phase while $PbTiO_3$ is in a tetragonal ferroelectric phase. PZT is a complex perovskite where the B-site is randomly occupied with Ti^{4+} and Zr^{4+} cations.

The temperature composition phase diagram of PZT is shown in Figure 2.10 [62]. In the paraelectric phase (above $T_C \approx 664$ K), PZT has a cubic structure. Upon decreasing the temperature below T_C, the Ti-rich compositions transform into a tetragonal phase (space group $P4mm$) with polarization along the [001] direction and the Zr-rich compositions transform into a rhombohedral phase (space group $R3c$) with polarization along the

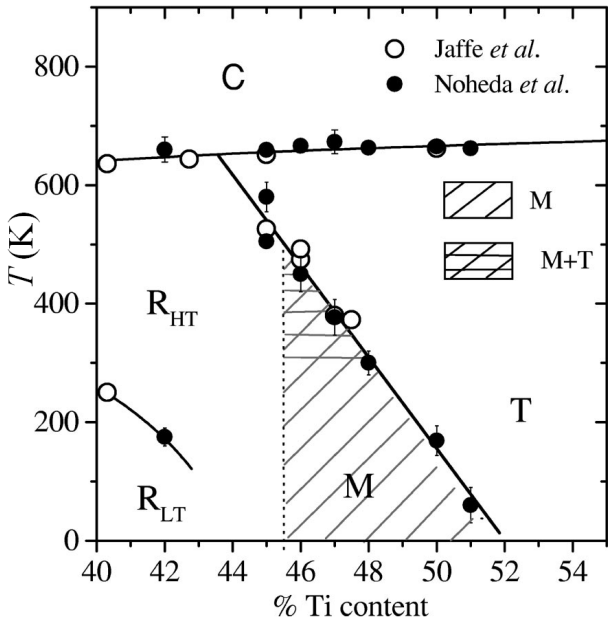


Figure 2.10: Phase diagram of $Pb(Zr_{1-x}Ti_x)O_3$ showing the monoclinic phase in the morphotropic phase boundary. Source: B. Noheda [62].

[111] direction. Both phases are ferroelectric and are separated by what is known as a morphotropic phase boundary (MPB) region [63] that appears as a narrow triangle in the phase diagram. It is in this zone that the material exhibits the most remarkable dielectric and piezoelectric properties. For a long time, it was believed that both tetragonal and rhombohedral phases occur simultaneously in the MPB but in 2000, Noheda *et al.* showed that there is an intermediate monoclinic phase of space group Cm in this composition range ($0.45 < x < 0.52$) [51, 64, 65]. There is an abrupt change in lattice constants [51] upon

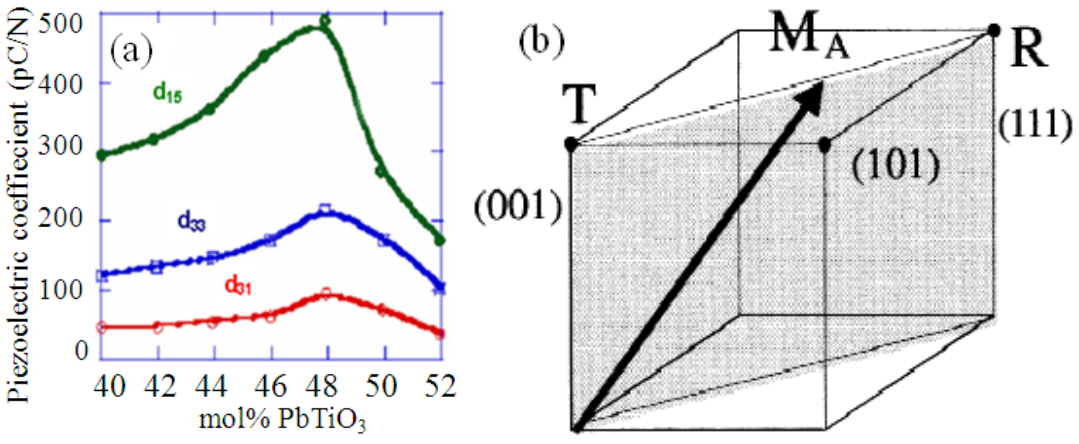


Figure 2.11: (a) The maximum of the piezoelectric coefficients of $Pb(Zr_{1-x}Ti_x)O_3$ in the morphotropic phase boundary region. (b) The rotation of the polarization vector in the $(1\bar{1}0)$ monoclinic plane between the [100] tetragonal direction and the [111] rhombohedral direction.

approaching the MPB region. Also, the dielectric constants, the remanent polarization, and the piezoelectric coefficients (Figure 2.11(a)) exhibit an anomalous peak. It was pro-

posed that the anomalous properties near the MPB are due to the continuous rotation of the polarization axis in the $(1\bar{1}0)$ monoclinic plane, from the [100] tetragonal direction to the [111] rhombohedral direction as the Ti content decreases [66]. This rotation process is shown in Figure 2.11(b) . First principle calculations by Bellaiche *et al.* [67] and by Fu and Cohen [36] show that it is this rotation which is at the origin of the very high values of the piezoelectric coefficients. The maximum polarization in the MPB region is due to the easy reorientation of domains. It is known that for a monoclinic phase, there are 24 domain states [68]. So, in the MPB region, there are 24 available directions with equal free energy along which the polarization may be reoriented leading to a large remanent polarization.

2.2.3 $PbZn_{1/3}Nb_{2/3}O_3$

Lead zinc niobate $PbZn_{1/3}Nb_{2/3}O_3$ (PZN) is another prototypical relaxor. Figure 2.12(a) shows the temperature dependence of the dielectric constant at different frequencies of PZN single crystals along the [111] direction. A typical relaxor behavior can be seen with $T_m \approx$ 410 K [69]. Upon cooling, a sharp phase transition can be induced near 390 K if an electric field is applied along [111] direction [70]. The anomaly in the temperature dependence of the dielectric constant at 390 K together with the disappearance of the dielectric dispersion below 390 K show that this phase transition is established with a macroscopic ferroelectric order.

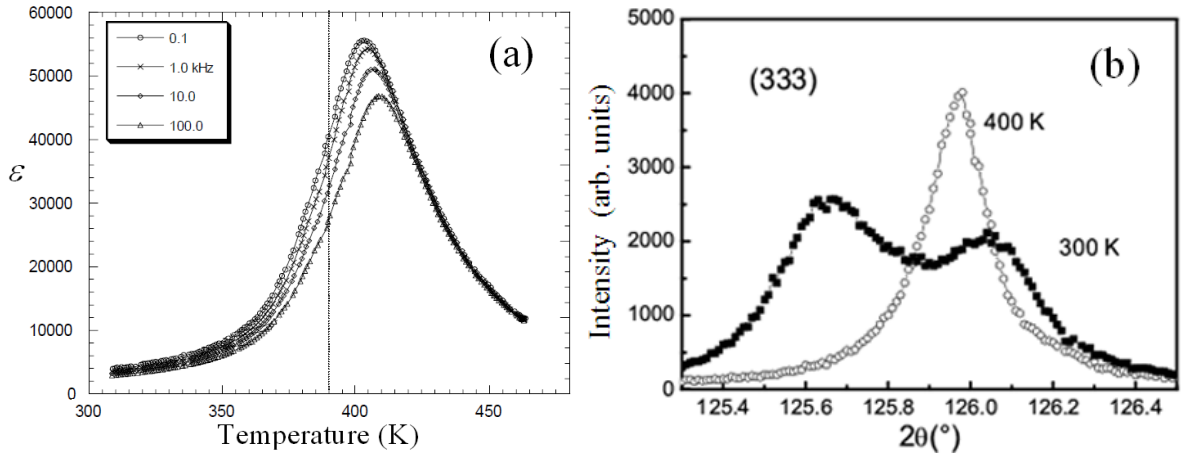


Figure 2.12: (a) The dielectric constant of [111] PZN single crystal as a function of temperature at different frequencies. (b) Diffraction patterns of the (333) Bragg peak of PZN crystals at 300 K and 400 K. Source: A. Lebon [69, 73].

Contrary to PMN, a spontaneous phase transition from a cubic to a rhombohedral phase occurs in PZN within the temperature range corresponding to the maximum of $\epsilon(T)$. It was first stated that this transition takes place around 410 K [71, 72], but a recent high-resolution X-ray diffraction study on PZN single crystals shows that this transition is diffuse and spreads over the temperature range between 385 K and 325 K with a full establishment

of the rhombohedral phase below 325 K [73]. At 300 K, a clear splitting of the (333) Bragg peak is observed (Figure 2.12(b)).

2.2.4 $PbMg_{1/3}Ta_{2/3}O_3$

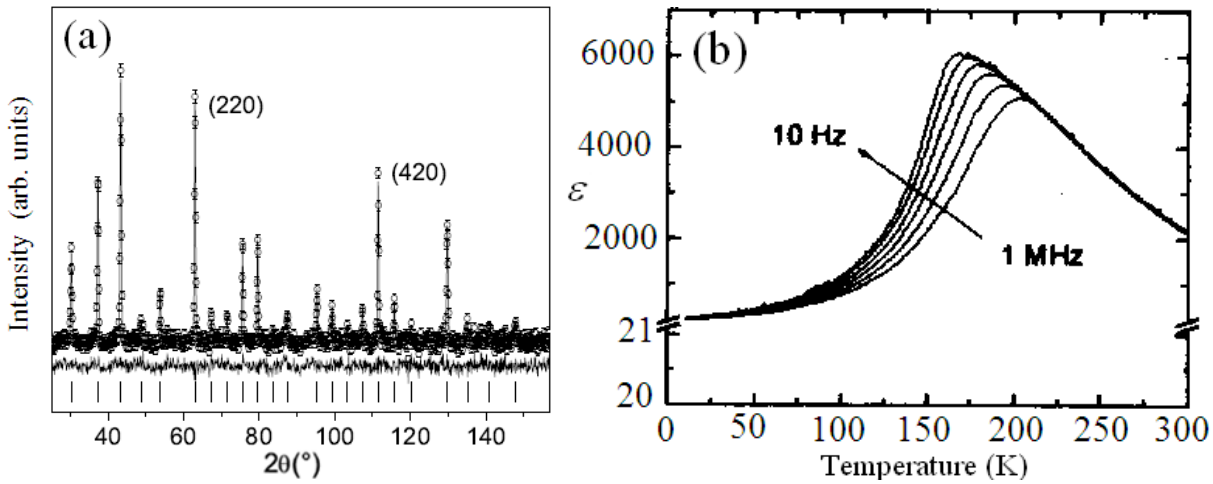


Figure 2.13: (a) Neutron powder diffraction pattern of PMT at ambient temperature. Experimental, calculated, and difference profiles are shown. The row of ticks indicate the calculated positions of the diffraction peaks of PMT. Source: S. N. Gvasaliya [74]. (b) Temperature dependence of the dielectric constant of PMT crystals at different frequencies. Source: J.-H. Ko [55].

At ambient conditions, lead magnesium tantalate $PbMg_{1/3}Ta_{2/3}O_3$ (PMT) possesses an average cubic structure of $Pm\bar{3}m$ space group with a lattice parameter $a = 4.04$ Å [74]. This can be seen in Figure 2.13(a) where a neutron powder diffraction pattern of PMT at ambient temperature [74] together with the calculated profiles obtained from Rietveld refinement using $Pm\bar{3}m$ space group and the corresponding difference profiles are shown. High-temperature neutron powder diffraction experiment [75] of PMT revealed that there is no structural phase transition in the temperature range from 1.5 K (far below $T_m \approx 170$ K) to 730 K, which is similar to the case of PMN. Howerever, in contrast to PMN, the PMT crystals remain cubic even if an external electric field is applied [75]. Similar to PMN and PZN, the PMT crystals exhibit the usual relaxor behavior also with a $T_m \approx 170$ K at 10 kHz (Figure 2.13(b) [55]).

It is noted in the literature that the Burns temperature T_d of PMT is about 570 K. This value was obtained from a comparative Brillouin scattering experiment between PMT [55] and PMN [76, 77], since the temperature dependence of the refractive index of PMT was never measured. But, is Brillouin scattering an appropriate way to determine T_d? On the other hand, both the lattice parameter a (Figure 2.14(a) [75]) and the inverse of the dielectric constant ϵ^{-1} (Figure 2.14(b) [78]) of PMT show a deviation from their linear

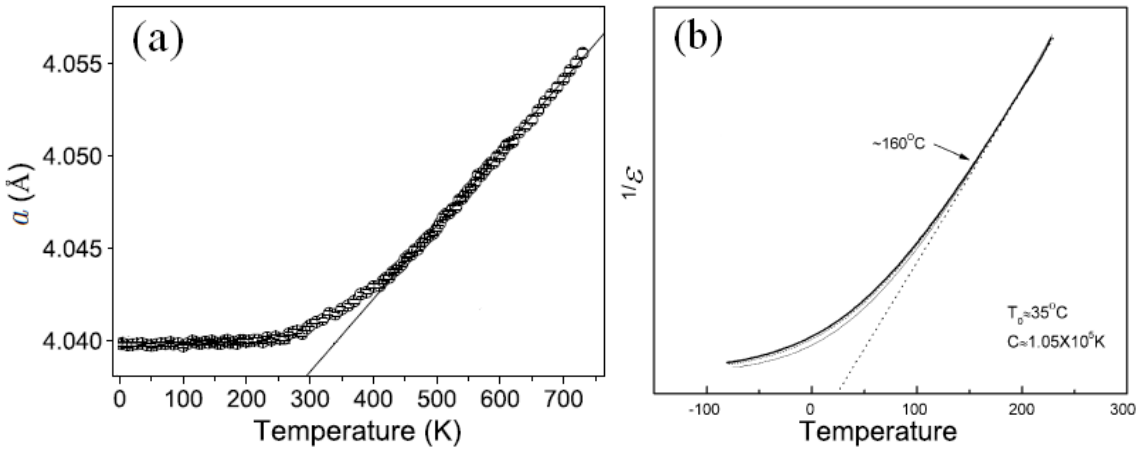


Figure 2.14: (a) The variation of the cubic lattice parameter of PMT as a function of temperature. Source: S. N. Gvasaliya [75]. (b) Temperature dependence of the inverse of the dielectric constant of PMT. Source: Y. L. Wang [78].

behavior around 420 K. And as it was explained before in the case of PMN, the temperature obtained by these quantities corresponds to the Burns temperature of PMN. So it seems to us that the value of T_d of PMT remains questionable.

Part II

Structural Investigations of Lead-based Perovskites

Chapter 3

Neutron Diffraction Study of the Ferroelectric-Paraelectric Phase Transition in $PbTiO_3$

3.1 Neutron Powder Diffraction

Diffraction methods provide one of the most powerful techniques to probe the mean position of atoms in the unit cells (Bragg peaks) of a crystalline material as well as slight chemical or positional disorder around their means (diffuse scattering). Diffraction experiments can be performed using electrons, X-rays, or neutrons and each type has its advantages and disadvantages. Although X-ray diffraction is considered as an extremely powerful technique owing to the very intense X-ray sources that are used nowadays (especially synchrotron sources), it is sometimes worth complementing these data by those obtained with neutron diffraction. This is particularly true in lead-based oxide perovskites where X-rays are mostly sensitive to lead atoms while neutrons see both lead and oxygen atoms. In this thesis, high-pressure and high-temperature neutron powder-diffraction experiments were used to determine the crystal structure of $PbTiO_3$ and in particular to measure the cation and anion shifts at the origin of the spontaneous polarization (P_S). It is thus possible to determine the pressure and temperature dependence of P_S and the resulting phase transitions in P and T space.

3.1.1 Theoretical background

Neutrons are subatomic particles that are found in the atomic nucleus. They have no electrical charge, a mass almost equal to the mass of the proton, a nuclear spin that equals 1/2, and a magnetic moment. For diffraction experiments, neutrons can be generated in two main ways. The fission of a heavy nucleus, typically ^{235}U, in a nuclear research reactor is the first method of generating neutrons. The use of a spallation source, where a heavy

metal target is bombarded with high energy protons generated by a particle accelerator, is the second way that can be used to generate neutrons. The energy of the ejected neutrons by these two methods is too high to be immediately used in a diffraction experiment. The produced neutrons are passed through a moderator such as heavy water in order to be thermalized. Thermal neutrons are slower because their energy is reduced and consequently their wavelength λ is increased, from de Broglie relationship $\lambda = h/mv$, to the order of 1 - 2 Å. These values are of the same order of magnitude as the diameter of the atoms [79], leading to a high efficiency of the diffraction process.

In a neutron diffraction experiment [79, 80, 81], the incident neutron is characterized by its wave vector $\vec{k}_i$ and its energy E_i, and the scattered neutron is characterized by its wave vector $\vec{k}_f$ and energy E_f. There is no energy transfer during this elastic scattering process, *i.e.* $E_i = E_f$, and the scattering vector is $\vec{Q} = \vec{k}_i - \vec{k}_f$ with $k_i = k_f$ (Figure 3.1). Applying the cosine rule, we find that $Q = 2k_i \sin\theta = 4\pi \sin\theta/\lambda_i$ where 2θ is the scattering angle and λ_i is the incident wavelength.

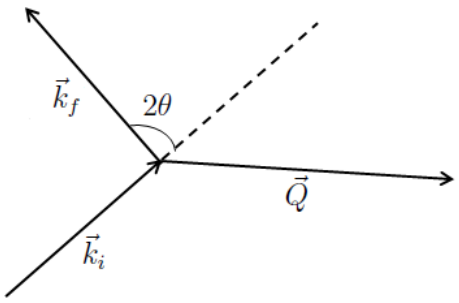


Figure 3.1: A schematic diagram of an elastic scattering event.

The nature of the interaction of X-rays and neutrons with the sample is completely different. Neutrons interact with atomic nuclei via the very short range nuclear force (Fermi pseudo-potential). Since the diameter of the atomic nucleus (of order 10^{-15} m) is much smaller than the wavelength of the thermal neutrons (of order 10^{-10} m), this scattering process is isotropic and is characterized by a scattering length b which is of the order of the size of the nucleus [79]. This scattering length b is a measure of the strength of the interaction between the incident neutron and the atom. It is a constant (independent of Q) which only depends on the nature of the atom. On the other hand, since X-rays interact with electrons, the X-ray scattering process is not isotropic owing to the space distribution of the electrons and it is characterized by a form factor $f(Q)$ whose intensity decreases as the scattering vector Q increases. The form factor $f(Q)$ is defined as the Fourier transform of the average density of the electrons surrounding the nucleus. The Q dependence of b and $f(Q)$ for carbon, for example, are shown in Figure 3.2 [81].

It is known that the forward scattering value of $f(Q)$ increases linearly with the atomic

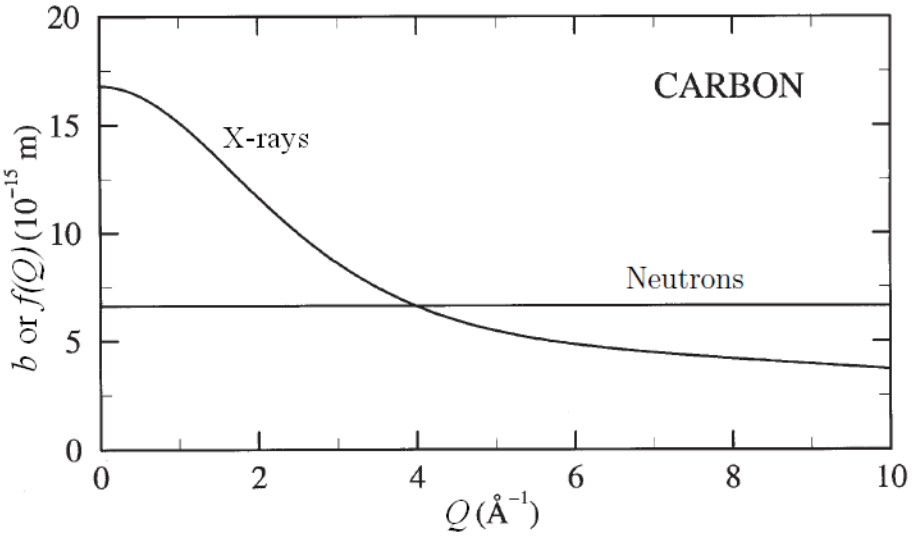


Figure 3.2: The comparison between the Q dependence of the neutron scattering length b and the X-ray form factor $f(Q)$ for carbon.

number Z [79, 81], while for the neutron-scattering length b there is no clear relationship between the variation of b and the atomic number Z as seen in Figure 3.3. Owing to this irregular behavior of b, neutrons can be used to distinguish between atoms that are close to one another in the periodic table. Also it can be used to detect light atoms in the presence of heavy atoms which is impossible in X-rays. Neutrons play an important role also to distinguish between different isotopes because the neutron-nucleus scattering length depends on the isotope and not on the number of electrons as for $f(Q)$ in X-ray experiments. In this thesis for example, neutron diffraction was used for the study of lead perovskites because the oxygen positions can be refined with great accuracy which is not possible with X-rays owing to the very low X-ray scattering factor of oxygen compared to that of lead.

To measure the intensity of the reflections in the diffraction pattern, it is necessary to calculate the double differential cross-section $\frac{d^2\sigma}{d\Omega dE}$ of the neutron-matter interaction. From perturbation theory, $\frac{d^2\sigma}{d\Omega dE}$ is given by [80]:

$$\frac{d^2\sigma}{d\Omega dE} = \left[\frac{m}{2\pi\hbar^2}\right]^2 \frac{k_f}{k_i} \sum_{n_0} p(n_0) \sum_{n_1} \left|\langle k_f s_f n_1 \left|V\right| k_i s_i n_0\rangle\right|^2 \delta(\epsilon_1 - \epsilon_0 - \hbar\omega) \qquad (3.1)$$

the indices i and f are used for the incident and final neutrons while the indices 0 and 1 are used for the initial and final states of the sample, ϵ is the energy of the sample, E is the energy of the neutron and s is its spin-state. The first sum runs over all initial states n_0 of the system each occurring with a probability $p(n_0)$ while the second sum runs over all final states n_1 of the system. The matrix element $\langle ....\rangle$ is between the initial state of the total system given by n_0, $\vec{k}_i$, s_i and the final state of the total system given by n_1, $\vec{k}_f$, s_f.

For nuclear scattering, the neutron-nucleus interaction can be written in terms of the

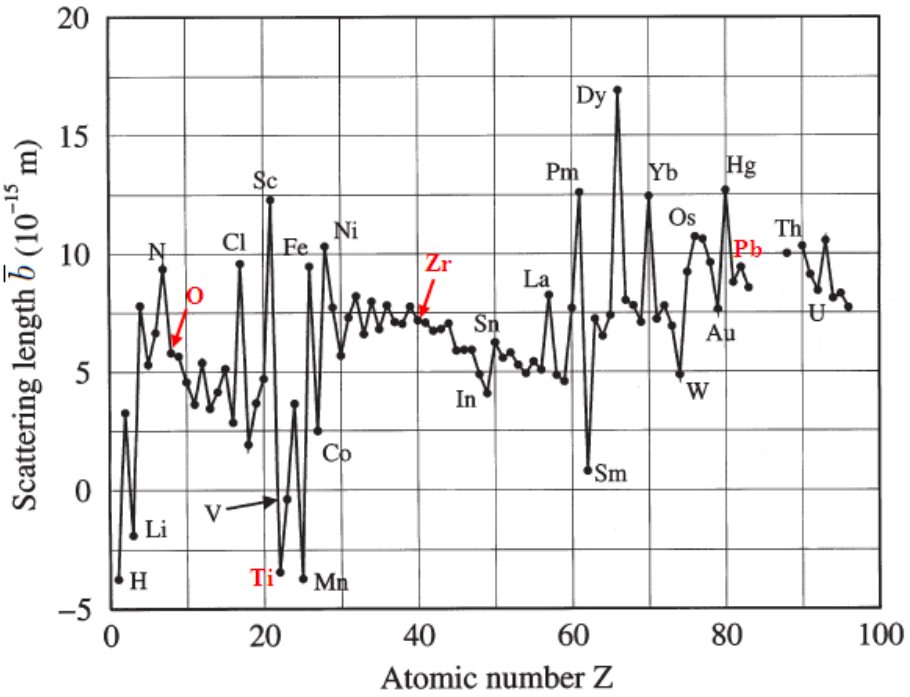


Figure 3.3: The variation of the coherent neutron-scattering length $\bar{b}$ with the atomic number for natural isotopic abundance.

Fermi pseudo-potential such as [80]:

$$V(\vec{r}) = \frac{2\pi\hbar^2}{m} \sum_j b_j \delta(\vec{r} - \vec{r_j}) \tag{3.2}$$

where $\vec{r_j} = x_j\vec{a} + y_j\vec{b} + z_j\vec{c}$ is the position of nucleus j in real space $(\vec{a}, \vec{b}, \vec{c})$ and b_j its scattering length.

Inserting the definition of V in equation 3.1 gives [80]:

$$\frac{d^2\sigma}{d\Omega dE} = \frac{k_f}{k_i} \sum_{n_0} p(n_0) \sum_{n_1} \left| \left\langle n_1 \left| \sum_j b_j e^{i\vec{Q}.\vec{r_j}} \right| n_0 \right\rangle \right|^2 \delta(\epsilon_1 - \epsilon_0 - \hbar\omega) \tag{3.3}$$

where $\vec{Q} = h\vec{a}^* + k\vec{b}^* + l\vec{c}^*$ is the scattering vector in reciprocal space $(\vec{a}^*, \vec{b}^*, \vec{c}^*)$.

After some treatment, $\frac{d^2\sigma}{d\Omega dE}$ for mono-atomic systems can be written as [79, 80]

$$\frac{d^2\sigma}{d\Omega dE} = \frac{k_f}{k_i} \sum_{j,j'} \overline{b_j{}^* b_{j'}} S(\vec{Q}, \omega) \tag{3.4}$$

where $S(\vec{Q}, \omega)$ is the scattering function or the one-phonon dynamic structure factor.

If $j = j' \Rightarrow \overline{b_j{}^* b_{j'}} = \overline{b^2}$, and if $j \neq j' \Rightarrow \overline{b_j{}^* b_{j'}} = \overline{b_j^*}.\overline{b_{j'}} = \bar{b}^2$. Accordingly, $\frac{d^2\sigma}{d\Omega dE}$ can be seperated into a coherent and an incoherent term as:

$$\frac{d^2\sigma}{d\Omega dE} = \frac{k_f}{k_i}\overline{b}^2 S_{coh}(\vec{Q},\omega) + \frac{k_f}{k_i}(\overline{b^2} - \overline{b}^2)S_{inc}(\vec{Q},\omega), \tag{3.5}$$

The coherent term in equation (3.5) describes the correlation between different particles in the sample, while the incoherent term which is called an auto-correlation function describes the motion of one particle.

It is useful here to define a quantity called the structure factor $F(\vec{Q})$ (sometimes written F_{hkl}) where $S_{coh}(\vec{Q},\omega) \propto \left|F(\vec{Q},\omega)\right|^2$. This structure factor is given by:

$$F_{hkl} = \sum_j e^{-W_j}\overline{b}_j e^{2i\pi\vec{Q}.\vec{r}_j} = \sum_j e^{-W_j}\overline{b}_j e^{2i\pi(hx_j+ky_j+lz_j)}, \tag{3.6}$$

e^{-W_j} is called the Debye-Waller factor (different from σ_i^2 in EXAFS expression) that takes into account the thermal vibrations of the atoms and is given by $e^{-W_j} = e^{-B_j\frac{sin^2\theta}{\lambda^2}}$ where B_j is the isotropic displacement parameter of the vibration.

The scattered intensity I_{hkl} of a reflection hkl is proportional to the square of the structure factor F_{hkl} of this reflection [81]:

$$I_{hkl} \propto \left|F_{hkl}\right|^2, \tag{3.7}$$

3.1.2 Experimental procedure

High temperature experiment

This experiment was performed on the CRG beamline D1B at the Institut Laue-Langevin (ILL) in Grenoble. D1B is a two-axis spectrometer dedicated to diffraction experiments requesting a high neutron flux. A (002) pyrolytic graphite monochromator was used to provide a neutron beam with wavelength $\lambda = 2.52$ Å and a flux of 6.5×10^6 s^{-1} cm^{-2} at the sample position. D1B is equipped with 3He/Xe position-sensitive detector composed of a system of multi-electrodes with 400 cells, which span a 2θ range of 80° [82]. A schematic diagram of D1B instrument is shown in Figure 3.4. This high-temperature neutron diffraction experiment was performed to investigate the temperature behavior of $PbTiO_3$ close to the ferroelectric-paraelectric phase transition.

High pressure experiment

The experiment was performed on D20 at the Institut Laue-Langevin (ILL) in Grenoble. This neutron diffractometer is characterized by a high neutron flux (10^8 s^{-1} cm^{-2}) at the sample position and a curved position sensitive detector (PSD) [83, 84] which allows the simultaneous detection of the scattered neutrons with a scattering range of 153.6°. A

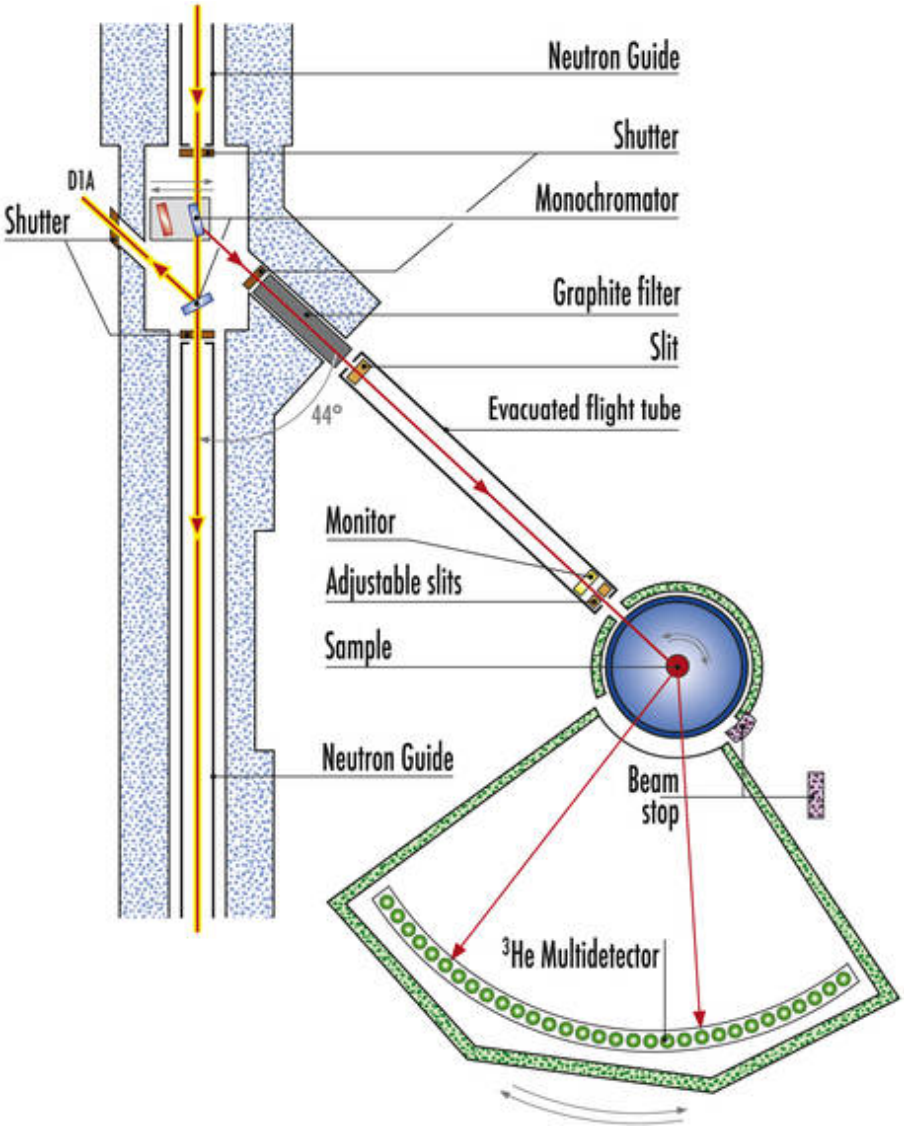


Figure 3.4: A schematic diagram of the D1B instrument at the ILL.

schematic diagram of D20 instrument can be seen in Figure 3.5.

To perform our high-pressure experiment (Figure 3.6), a Paris-Edinburgh press equipped with boron nitride anvils was used for pressures below 12 GPa, while another Paris-Edinburgh press equipped with double-toroidal sintered diamond anvils was used for pressures up to 18 GPa. A finely ground powder of $PbTiO_3$ was placed in an encapsulated Ti-Zr null scattering gasket with deuterated 4:1 methanol:ethanol as a pressure transmitting medium. The pressure was estimated based on the pressure-volume data of $PbTiO_3$ obtained from X-ray diffraction [85]. Neutron-diffraction data was collected in transmission mode (with windows for collimation) each 2 GPa. A (200) Cu monochromator was used to give a neutron beam with wavelength $\lambda = 1.54$ Å.

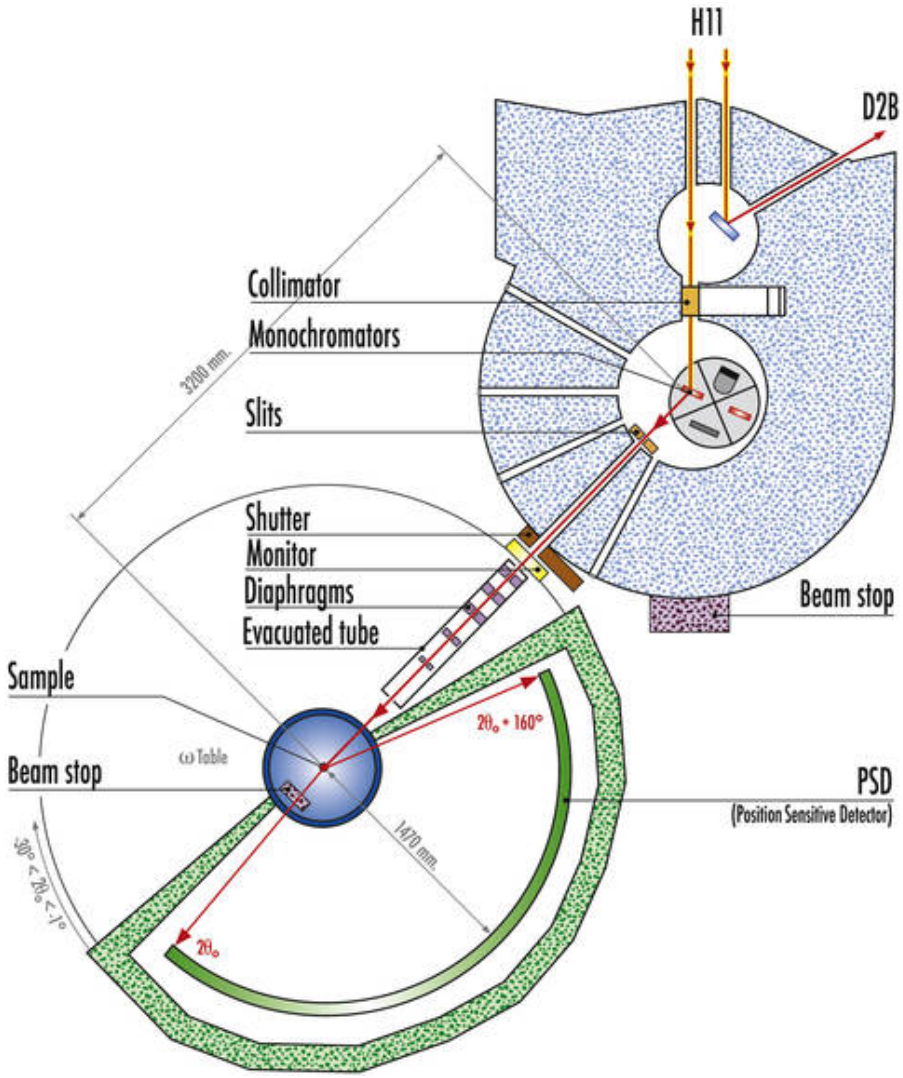


Figure 3.5: A schematic top-view of the D20 diffractometer at the ILL.



Figure 3.6: The experimental setup for high pressure neutron diffraction. (1) Ti-Zr gasket, (2) anvil cell, (3) Paris-Edimburgh press.

3.1.3 Rietveld refinement

The Rietveld refinement is the method used to analyse diffraction patterns. The idea is to fit the parameters of a proposed model to the measured profile, and thereby obtain the optimal crystallographic structure of the material under study [86]. There are many softwares that can be used to perform the refinement. In this thesis, the FullProf program [87] was used to refine the diffraction patterns.

The experimental powder diffraction pattern is usually given as (T_i, y_{io}, σ_i), where T_i is the scattering variable, y_{io} is the observed intensity, and σ_i is the standard deviation of the profile intensity. As mentioned before, the aim of the refinement is to minimize the difference between a calculated model y_{ic} and the observed pattern y_{io}. The function to be minimized in the Rietveld method is [87]:

$$\chi^2 = \sum_i w_i \{y_{io} - y_{ic}\}^2 \tag{3.8}$$

with $w_i = \frac{1}{\sigma_i^2}$, where σ_i^2 is the variance of the observation y_{io}.

The calculated profile in a Rietveld method can be modeled as follows:

$$y_{ic} = bg_i + \sum_\phi S_\phi \sum_h I_{\phi,h}\ \Omega(T_i - T_{\phi,h}) \tag{3.9}$$

where bg_i is the background intensity, S_ϕ is the scale factor of the phase ϕ, $I_{\phi,h}$ is the calculated integrated intensity which is proportional to the square of the structure factor (the vector h labels the Bragg reflections), and Ω is the reflection profile function that models both instrumental and sample effects.

From equation 3.9, it is clear that the first step of a refinement procedure is to define the appropriate phases, to calculate the background, and to choose the suitable profile function. The corresponding symmetry phases are defined according to literature data (experiments or simulation works) and also to experimental details (for example, additional phases arising from the gasket and the anvil cell). The background was calculated by a linear interpolation of 30 to 40 selected points in the diffraction patters. "Gaussian" functions were used for high temperature diffraction patterns while "Thompson-Cox-Hastings (TCH) pseudo-Voigt" functions were assumed for high pressure patterns.

In a Rietveld method, the model parameters that should be refined can be divided into two categories [81, 86]:

1. The instrumental parameters that are determined by the experimental apparatus. These include the zero-shift coefficient, the background parameters, the peak shape parameters (usually we refine the FWHM parameters of the chosen function).

2. The sample parameters which depend on the structure of the studied material. These include the unit cell parameters, the atomic positions, the site occupancies, and the displacement parameters. The unit cell parameters, in combination with the diffractometer zero-shift, determine the peak positions in the diffraction pattern. The atomic positions, the displacement parameters and the site occupancies are used to determine the calculated integrated intensities.

It is impossible to refine all these parameters from the beginning. In general, it is better to refine a small number of parameters first and then increase the number of parameters as the refinement progresses.

After the refinement of all the parameters, it is then necessary to judge the quality of the refinement. The agreement between observed and calculated profiles is measured by a set of factors that include the reduced chi-square χ^2_v, the profile factor R_p, the weighted profile factor R_{wp} and the expected weighted profile factor R_{exp}. These factors are defined as follows [87]:

$$\chi^2_v = \frac{\chi^2}{n-p} \tag{3.10}$$

where n is the number of observations and p is the number of refined parameters.

$$R_p = 100\frac{\sum_i |y_{io} - y_{ic}|}{\sum_i y_{io}} \tag{3.11}$$

$$R_{wp} = 100\left[\frac{\sum_i w_i |y_{io} - y_{ic}|^2}{\sum_i w_i y_{io}^2}\right]^{1/2} \tag{3.12}$$

$$R_{exp} = 100\left[\frac{n-p}{\sum_i w_i y_{io}^2}\right]^{1/2} \tag{3.13}$$

Ideally, the lowest possible values of these factors will give the best fitting. But, it is also important to check the obtained values of the instrumental and sample parameters and to be sure that these values have physical meaning. Another thing that can be judged is the difference plot between the diffraction pattern and the fitted model.

3.2 Neutron Diffraction from $PbTiO_3$

3.2.1 Introduction

The paraelectric (cubic) to ferroelectric (tetragonal) phase transition in $PbTiO_3$ occurring at $T_C \approx 763\,\mathrm{K}$ [56] had been considered for a long time as a text-book example of a

purely displacive phase order transition. The weakly first-order transition is associated with a well-defined zone center soft mode [88]. About fifteen years ago, the EXAFS observation of distortions of the Pb and Ti ions from the ideal cubic structure in the paraelectric cubic phase raised the issue of an additional order-disorder component at T_C [58]. This led to a renewed interest in this prototypical material, first owing to fundamental motivations, but also because $PbTiO_3$ is the parent compound of the lead-based complex perovskites, including relaxors.

The pressure phase diagram is even more under discussion. The effect of pressure on materials exhibiting displacive ferroelectric transition was first studied by Samara *et al.* [89]. It was found that hydrostatic pressure reduces ferroelectricity, decreasing the value of the ferroelecric-paraelectric (*F-P*) transition temperature T_C. In $PbTiO_3$, Raman [90] and X-ray diffraction [50] results reveal that T_C reduces from 763 K at P_{atm} to 300 K at about 12 GPa. The latter phase transition was considered to be displacive and second order [50, 90]. However, some questions remains debated such as the symmetry of the soft mode [90, 91], as well as the space group of the high pressure (> 12 GPa) paraelectric phase.

Recently, experimental and theoretical investigations at high pressure have renewed the interest in the ferroelectric behavior of $PbTiO_3$. Numerical simulations supported by experiments performed by Kornev *et al.* [92] have confirmed that pressure reduces ferroelectricity as already demonstrated by Samara [89], but reveal that increasing the pressure above a critical value ($\sim$ 30 GPa) produces an enhancement of ferroelectricity in $PbTiO_3$ perovskites. This is explained in [92] as being due to a balance between long-range Coulomb ionic interactions and short-range electronic effects. While the former favor ferroelectricity at low pressures and the latter suppress it, this role is reversed at sufficiently high pressures. These expectations motivated new high pressure investigations, in particular X-ray diffraction where a splitting of the {*h00*} and {*hh0*} Bragg peak has been observed above $\sim$ 20 GPa. This transition-like feature associates with the appearance of new vibrational bands in the Raman spectra [60]. These authors concluded that there is a succession of at least three distinct phases, ferroelectric below 13 GPa, antiferrodistorsive from 20 to 45 GPa, and re-entrant ferroelectric above 45 GPa. However, this interpretation remains debated.

The pressure-temperature *P-T* phase diagram of $PbTiO_3$ is clearly more complicated than previously anticipated. Its understanding seems crucial in particular because $PbTiO_3$ is the end-member of $PbZr_{1-x}Ti_xO_3$, the most widely used current piezoelectric material in modern technological applications. It also serves as the essential parent material for the complex solid solutions $PbMg_{1/3}Nb_{2/3}O_3$-$PbTiO_3$ (PMN-PT) and $PbZn_{1/3}Nb_{2/3}O_3$-$PbTiO_3$ (PZN-PT) which are characterized by huge electromechanical coupling and have great potential for new generations of technological materials. This motivated us to perform

neutron diffraction experiments. Neutron diffraction is particularly useful to investigate the *F-P* phase transition in *P-T* space of oxides. The understanding of the *P-T* phase diagram of a prototype perovskite material $PbTiO_3$ is important from a fundamental point of view. In particular, above 12 GPa where some doubt on whether the space group is $Pm\bar{3}m$. Neutron diffraction is particularly sensitive to distortions from cubic symmetry owing to the strong scattering of oxygen, thus allowing detection of the phase transitions involving BO_6 octahedral tilting or polar displacements.

3.2.2 High temperature experiment

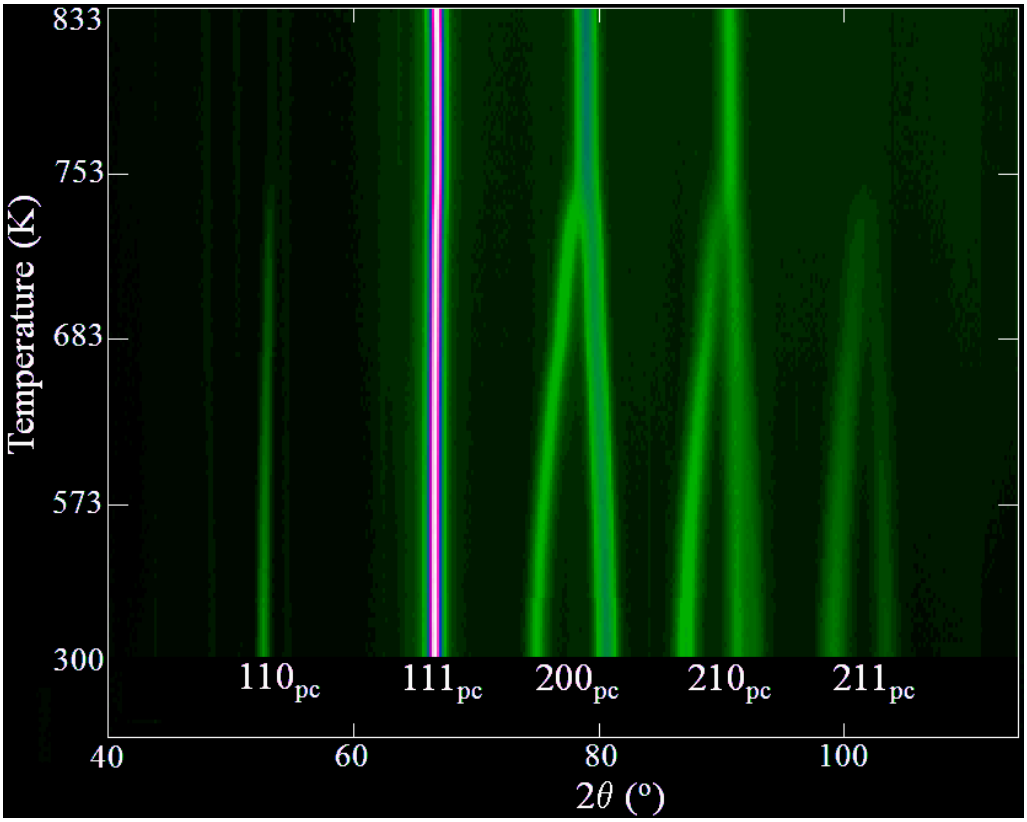


Figure 3.7: The variation of the relative intensity of Bragg reflections as a function of temperature. The major reflection lines were indexed with a pseudocubic symmetry (pc). The unusual ordinate scale cannot be modified in the available software.

A finely ground powder of commercial $PbTiO_3$ with grain size of few μm was used in this experiment. The sample was placed in a vanadium capsule. A neutron beam of wavelength $\lambda = 2.52$ Å was used. Figure 3.7 shows the coalescence of different pseudocubic reflections into a single reflection near the *F-P* transition temperature T_C. In addition, the diffraction patterns contain specific reflections, (*h, k, 2l*) for h and k odd, characteristic of polar shifts, which disappear above T_C. Figures 3.8(a) and 3.8(b) show the observed and calculated neutron diffraction patterns at 298 K and 778 K, respectively. The structural refinement of the patterns was achieved by the Rietveld method using the software Fullprof [87]. At

298 K, the $P4mm$ tetragonal phase (Figure 3.9) was used with the origin at the Pb site, that is Pb at 1a(0,0,0), Ti at 1b(1/2, 1/2, 1/2 + z(Ti)), O(1) at 1b(1/2, 1/2, z(O(1))) and O(2) at 2c(1/2, 0, 1/2 + z(O(2))). The $Pm\bar{3}m$ cubic phase was suitable to refine the pattern at 778 K, with Pb at 1a(0,0,0), Ti at 1b(1/2, 1/2, 1/2) and O at 3c(1/2, 1/2, 0). Gaussian profile function proved to be appropriate to fit the experimental pattern. The

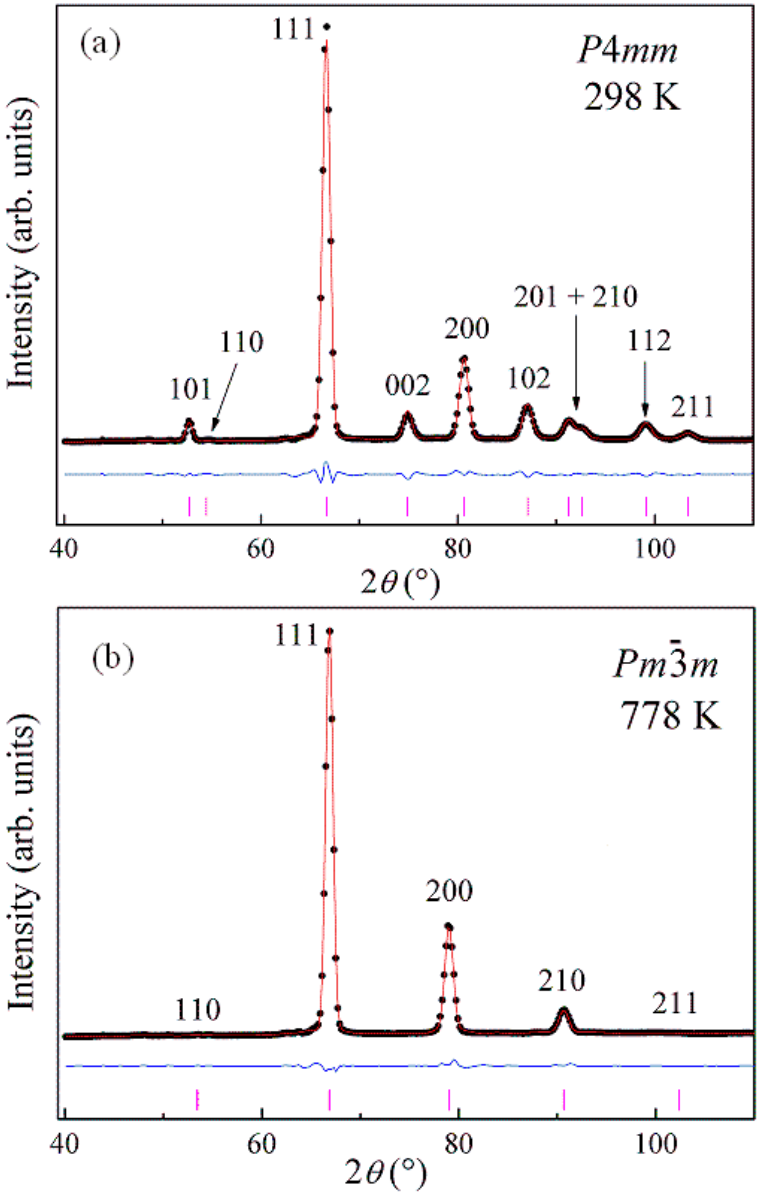


Figure 3.8: Experimental (circles), calculated (red line) and difference (blue line) profiles of $PbTiO_3$ pattern of the tetragonal $P4mm$ phase at 298 K (a) and of the cubic $Pm\bar{3}m$ phase at 778 K (b). The row of ticks indicate the calculated positions of the Bragg peaks of $PbTiO_3$.

overall isotropic displacement parameter B was taken into account during this refinement in view of the low d-spacing ($\lambda = 2.52$ Å and 2θ range = 80^o) of the measured patterns. For high temperature patterns (*i.e.* 50 K before the phase transition), B was fixed to the values obtained by linear extrapolation of the values measured at lower temperature.

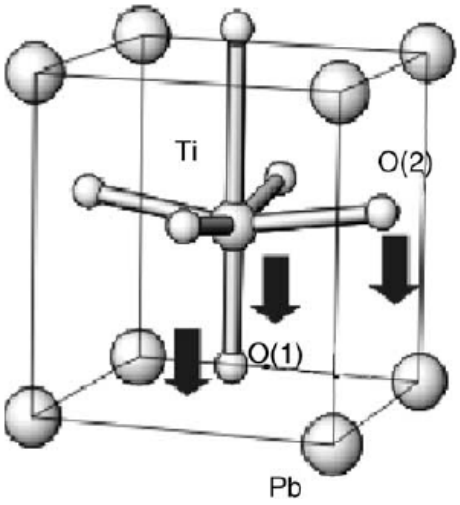


Figure 3.9: Tetragonal structure of $PbTiO_3$.

The intensity of diffraction peaks can be calculated using equations (3.6) and (3.7) which relate the scattered intensity I_{hkl} of a reflection hkl to the structure factor F_{hkl} of this reflection.

$$I_{hkl} \propto |F_{hkl}|^2 \tag{3.14}$$

with

$$F_{hkl} = \sum_j e^{-W_j} \bar{b}_j \left[\cos 2\pi(hx_j + ky_j + lz_j) + i \sin 2\pi(hx_j + ky_j + lz_j)\right]. \tag{3.15}$$

For a centrosymmetric structure, the imaginary part (sine term) vanishes for all reflections and the structure factor has only real terms.

We now calculate the structure factor of the (*h, k, 2l*) reflections with h and k odd, near the *F-P* transition where the atoms occupy the positions defined by the crystal structure. For these reflections, equation (3.15) gives $F_{hkl} \propto b_A + b_B - b_O$. In the case of $PbTiO_3$, the neutron scattering lengths of Pb, Ti and O are: b_{Pb} = 9.405 fm, b_{Ti} = -3.438 fm and b_O = 5.803 fm, so that

$$F_{hkl} \propto b_{Pb} + b_{Ti} - b_O = 9.405 - 3.438 - 5.803 = 0.164.$$

The experimental data (Figures 3.7) reflects this small value of F_{hkl} through the behavior of the 110_{pc} and 211_{pc} reflections whose intensity, proportional to F^2_{hkl}, becomes almost zero above 753 K. It can be concluded that the progressive disappearance of these polar reflections is due to the anti-phase scattering of A (Pb), B (Ti) and O atoms. A similar behavior has been observed in the case of $PbZr_{0.52}Ti_{0.48}O_3$ (Appendix A) where the intensity of the even-even-odd, (*2h, 2k, l*) with l odd, reflections starts vanishing near T_C = 664 K owing to the anti-phase values of the scattering lengths of the cations occupying the B-site.

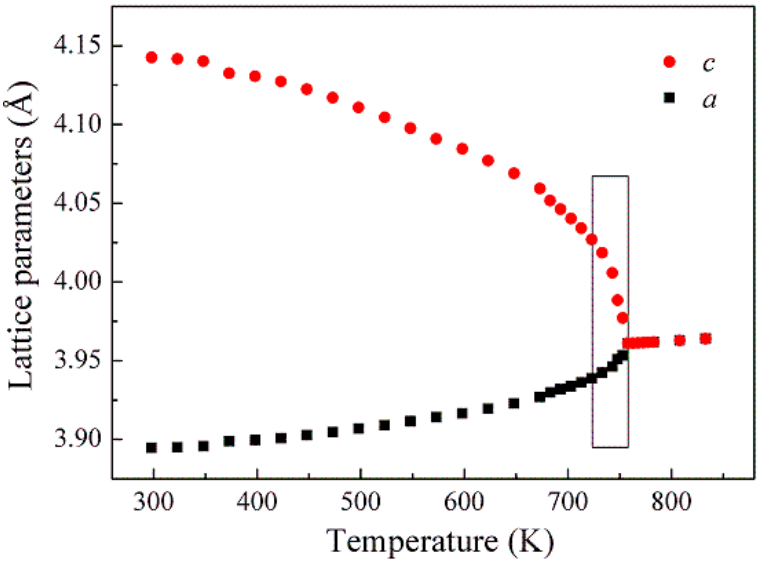


Figure 3.10: Temperature dependence of the lattice parameters of $PbTiO_3$.

The variation of the observed lattice parameters in function of temperature is shown in Figure 3.10. The experimental error bars are smaller than the symbol size. The observations seem to suggest that the transition is continuous. We attribute this to the large electrostriction which is likely to produce different deformations in different grains, depending on their surface strains. An accurate determination of a and c is thus not possible near T_C, within the rectangle in Figure 3.10. As the temperature increases, the a axis increases while the c axis decreases in quantitative agreement with previous results of X-ray powder diffraction [56] and single crystal [57] experiments. Figure 3.11 shows the atomic positions

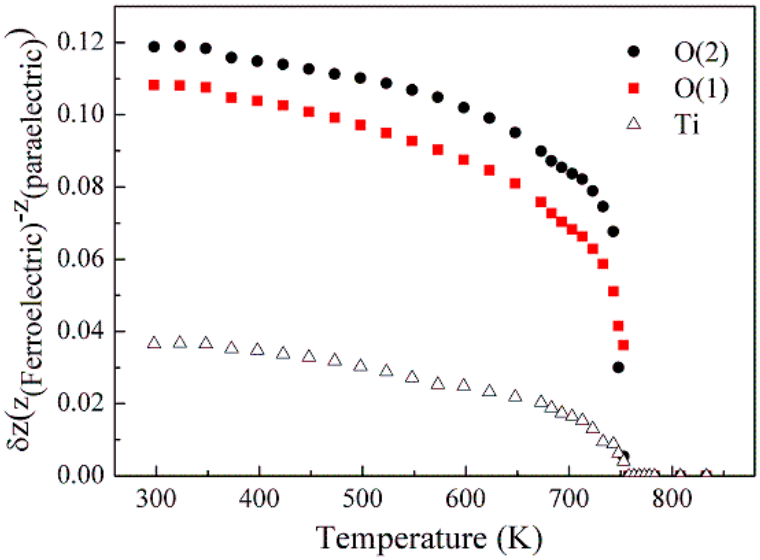


Figure 3.11: Temperature dependence of the displacement of the titanium and the oxygen atoms from the centrosymmetric position.

of Ti, O(1) and O(2) in the tetragonal phase with respect to their centosymmetric position in the paraelectric phase. All these parameters vanish more or less discontinuously at the

F-P transition point indicating that the oxygen and titanium atoms are on the average in $Pm\bar{3}$m positions above 760 K.

In such tetragonal-to-cubic phase transition, two order parameters can be taken into account: the spontaneous polarization P_S and the spontaneous strain η_S. According to group theory [93], this transition has a ferroelectric proper order parameter (P_S) and a ferroeleastic improper order parameter (usually defined as the c/a ratio). In this case, neutron diffraction gives accurate values of P_S owing to the refinement of the atomic positions of the oxygen atoms which is hardly accessible with X-rays.

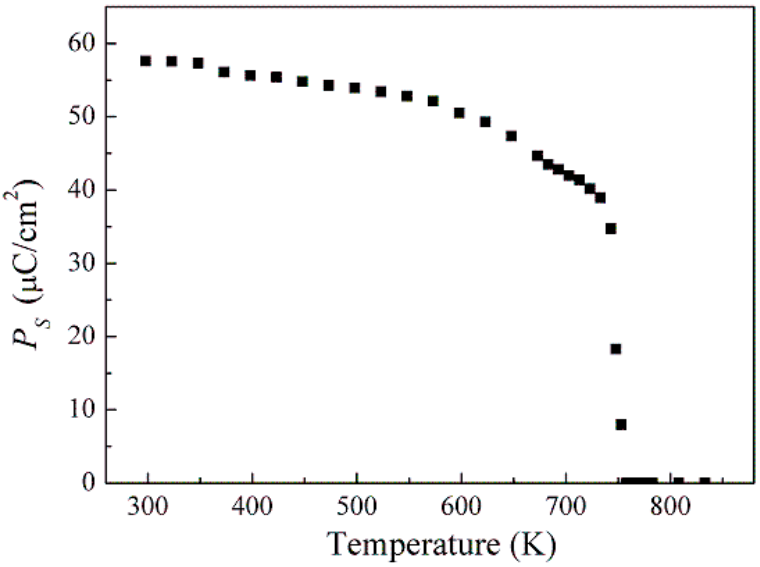


Figure 3.12: The variation of the spontaneous polarization calculated from Rietveld refined parameters as a function of temperature.

The structural data together with the atomic positions can be used to calculate the spontaneous polarization P_S in the tetragonal phase. If electronic polarization and domain contributions are neglected, the spontaneous polarization can be calculated using the following relation [94]:

$$P_S \approx \frac{1}{V} \sum_i q_i r_i \tag{3.16}$$

where r_i is the position of the ith ion carrying a point charge q_i and V is the volume of the unit cell.

The variation of the spontaneous polarization as a function of temperature is shown in Figure 3.12. The calculation of equation 3.16 was done with the nominal charges q_i. The value of P_S obtained at room temperature (57.6 μm/cm^2) is in perfect agreement with the value 57 μm/cm^2 obtained by pyroelectric measurements [95]. P_S decreases on heating

indicating a tendency toward a paraelectric state and becomes zero near $T_C \approx 760\,K$ where the $Pm\bar{3}$m-symmetry cubic phase is reached. It is clear from Figure 3.12 that the temperature behavior of P_S exhibits a rapid jump near T_C, consistent with the first-order nature of the transition.

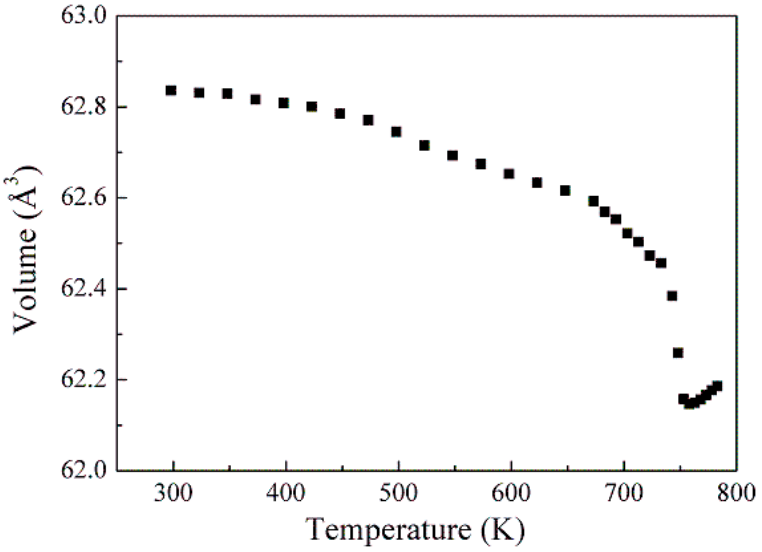


Figure 3.13: Temperature dependence of the unit cell volume.

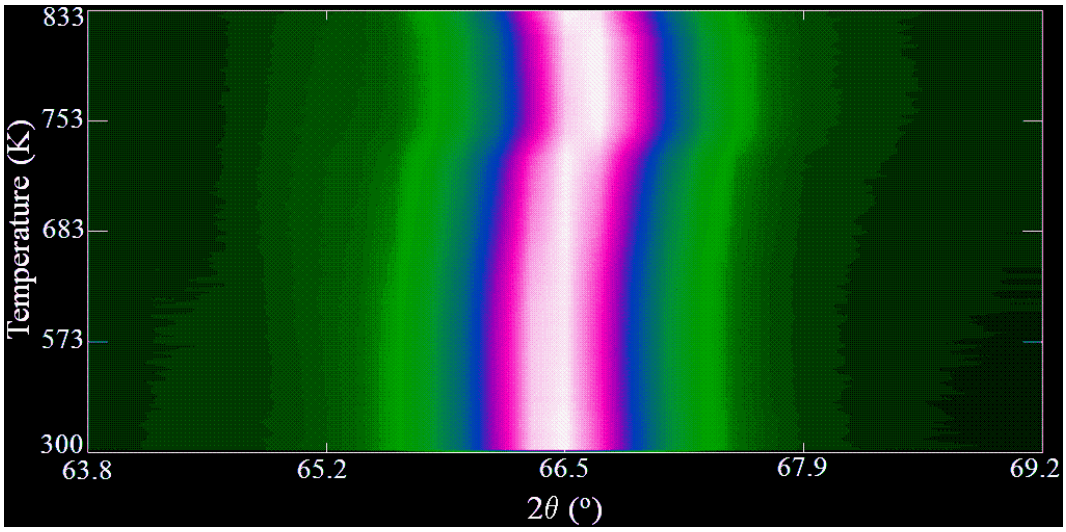


Figure 3.14: The variation of the position of the (111) Bragg peak as a function of temperature.

For non-polar materials, the volume V usually increases with temperature. In the case of $PbTiO_3$ (Figure 3.13), like in most of ferroelectric materials, the opposite applies. This negative thermal expansion below T_C is directly related to the polarization which increases on cooling, inducing a dilatation greater than the normal contraction effect. In the cubic region above T_C where the polarization becomes zero, V shows a normal expansion behavior

with temperature. The behavior of V in the tetragonal phase can also be observed on the shift of the (111) reflection toward higher diffraction angles on heating. The step-like behavior of that reflection is another indication of the first order nature of the transition (Figure 3.14).

3.2.3 High pressure experiment

To study the effect of high pressure on the structure of lead titanate, a neutron diffraction experiment was performed on D20 at the ILL using a monochromatic neutron beam with wavelength $\lambda = 1.54$ Å. Figure 3.15 shows the obtained diffraction patterns at 0.5 GPa, 9.1 GPa and 13.6 GPa. Boron nitride anvils were used for pressures below 12 GPa while higher pressure values required sintered diamond anvils. In that case, the intensity of diamond peaks is very large compared to those of $PbTiO_3$ (Figure 3.15(c)). A clear phase transition is observed above $\sim$ 13 GPa. It is important to note that the reflection width remains constant with pressure indicating good hydrostatic conditions.

To extract the lattice parameters, the atomic positions, and the isotropic displacement parameter B at different pressure points, structural refinement using the Rietveld method was performed with the help of the software Fullprof [87]. $PbTiO_3$ and BN or diamond (depending on the pressure cell) phases were included in the refinement for pressure points below and above 12 GPa, respectively. Thompson-Cox-Hastings (TCH) pseudo-Voigt functions were used to fit the experimental patterns. At 0.5 GPa and 9.1 GPa (Figures 3.15(a) and 3.15(b)), the fit was performed using the $P4mm$ tetragonal structure with the origin at the Pb site, while the $Pm\bar{3}m$ cubic structure gives the best refined pattern at 13.6 GPa (Figure 3.15(c)).

The variation of the lattice parameters with pressure is shown in Figure 3.16. a slightly increases up to $\sim$ 1.8 GPa and then decreases at higher pressures. This is in agreement with previous experiments [50]. The incease of the a parameter is due to the competition between compression (decrease in a owing to hydrostatic compression) and η_S (increase in a owing to the reduction in the tetragonal distortion). As expected, $PbTiO_3$ is more compressible along the polarization axis c than in the perpendicular plane. Both a and c have been fitted by a third-order polynomial in P. From the variation of these parameters, we obtain the value of the critical pressure $P_C \approx 12.3$ GPa at which $a = c$. This value is in good agreement with P_C obtained from X-ray [50, 60] and Raman [90].

The tetragonal distortion c/a and the spontaneous polarization P_S extracted from the Rietveld refinement are shown in Figure 3.17. On this basis, it is difficult to have a conclusion about the nature (first or second order) of the transition. It is thus interesting to

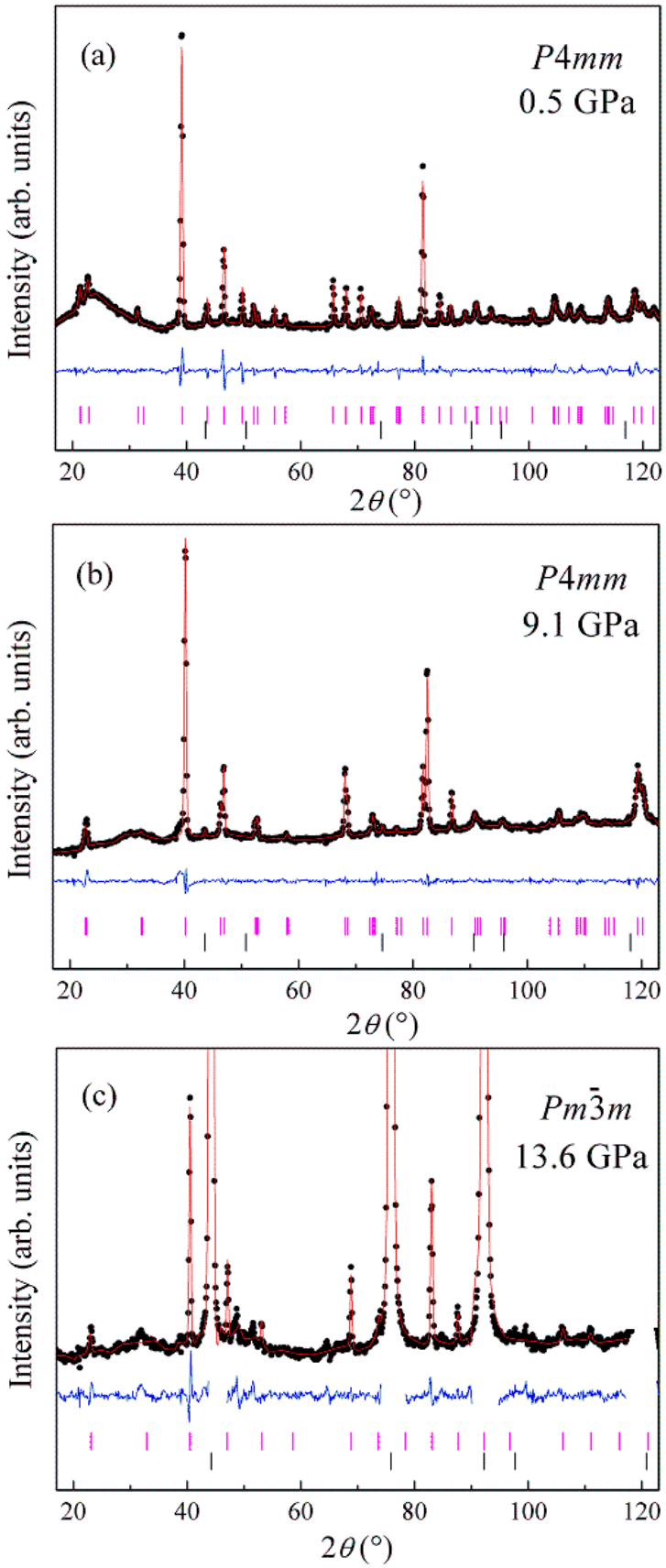


Figure 3.15: Experimental (circles), calculated (red line) and difference (blue line) profiles of $PbTiO_3$ pattern of the tetragonal $P4mm$ phase at 0.5 GPa (a), 9.1 GPa (b) and the cubic $Pm\bar{3}m$ phase at 13.6 GPa (c). The upper and lower rows of ticks indicate the calculated positions of the Bragg peaks of $PbTiO_3$ and BN (a,b) or diamond (c), respectively.

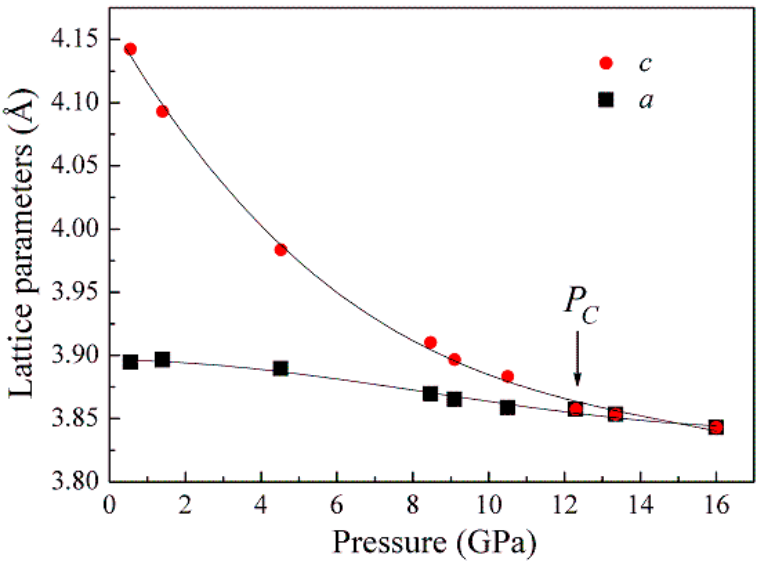


Figure 3.16: The variation of the lattice parameters of $PbTiO_3$ as a function of pressure. The lines represent a fit of the data with a third-order polynomial.

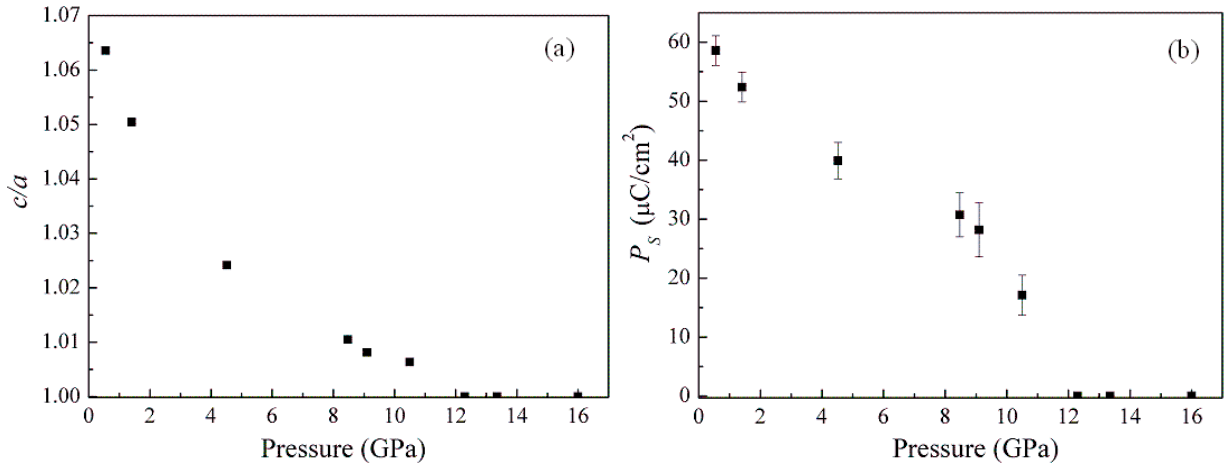


Figure 3.17: Pressure dependence of (a) the tetragonal distortion c/a and (b) the spontaneous polarization P_S calculated by Rietveld refined parameters.

compare P_S^2 with the deformation $c/a - 1$ (Figure 3.18) close to the transition. Although a linear fit is possible, the number of experimental points and the accuracy of the results do not allow making a conclusion concerning the order of the phase transition.

The isotropic displacement parameter B for both Pb and O were obtained only for patterns below 12 GPa. For higher pressures, the strong reduction of the sample volume prevented for such an analysis. The temperature dependence of B for both Pb and O is shown in Figure 3.19. The accuracy on the extracted B-values for the Ti-atom are poor and they are thus not shown.

The isotropic displacement parameter B contains two contributions: a dynamic and

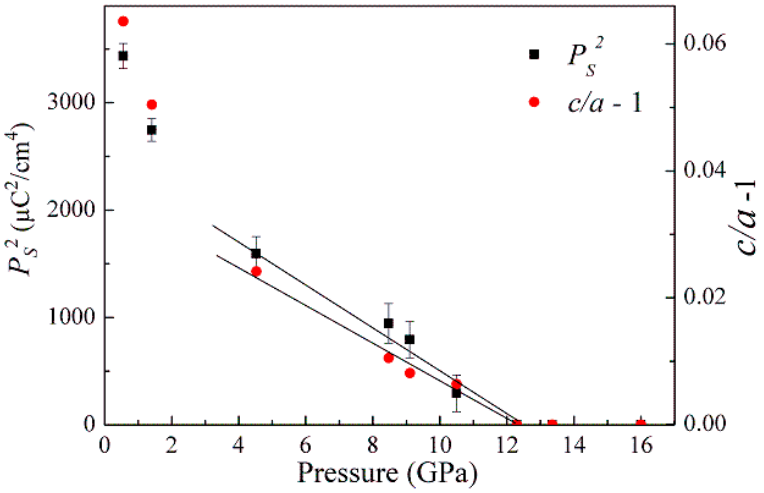


Figure 3.18: The variation of c/a - 1 and the square of the spontaneous polarization as a function of pressure.

a static one. They are linked to the local thermal vibrations and to the local structural distortions, respectively. It is known that the oxygen atoms should have no static distortions under pressure so that B_{O} in Figure 3.19 only reflects the pressure dependence of the vibrational part. However, B_{Pb} which contains both static and dynamic contributions is greater than B_{O}. This can be attributed to the presence of static disorder at the A-site absent in the O_6 octahedra. Although one expects the dynamical contribution to slightly decrease with pressure [96] (see B_{O}), the fast decrease of B_{Pb} probably indicates that pressure reduces the static disorder for the Pb-atoms till P_C.

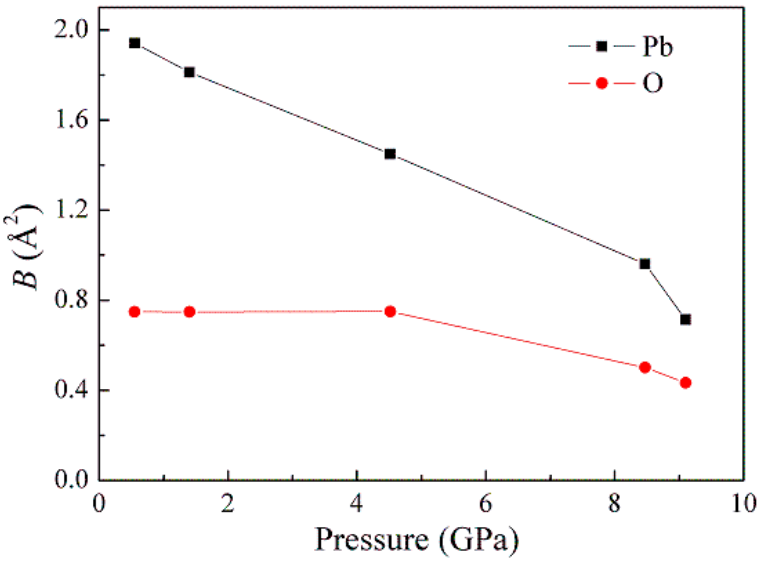


Figure 3.19: The variation of the isotropic displacement parameter B as a function of pressure.

3.2.4 Conclusion

The ferroelectric phase transition of $PbTiO_3$ has been investigated by neutron diffraction in function of temperature and pressure. This technique offers an interesting alternative to X-rays for the measurement of spontaneous polarization in lead-based ferroelectric oxides, in particular near phase transitions. In $PbTiO_3$, the F-P transition at $T_C \approx 763\,\mathrm{K}$ and ambient pressure is accompanied by the disappearance of particular reflections. The progressive disappearance of these reflections is due to the anti-phase scattering of Pb, Ti and O atoms. At high pressure, the comparison of P_S^2 and $c/a - 1$ shows that a ferroelectric-paralectric phase transition takes place near $P_C \approx 12.3$ GPa in agreement with previous literature data [50, 60, 90]. Structure refinements confirm that the high pressure phase is cubic with space group $Pm\bar{3}m$. This apparently contradicts the presence of first order Raman signal [60, 97], forbidden by symmetry selection rules. However, this Raman signal possibly originates from local distortions inside the TiO_6 octahedra which remains above P_C. This is further supported by X-ray absorption results which show that the disorder of Ti persists in the cubic phase [61].

Chapter 4

Local Structure of $PbZr_{0.52}Ti_{0.48}O_3$ and $PbZn_{1/3}Nb_{2/3}O_3$

4.1 X-ray Absorption Fine Structure

4.1.1 Definition

X-ray Absorption Fine Structure (XAFS) spectroscopy is an atomic probe that is used to study the local structure around selected atomic species. Important information can be obtained when XAFS (a short-range order technique) is combined with other complementary techniques like X-ray diffraction (a long-range order technique). The data that can be obtained from a XAFS spectrum are very incisive and unique [98].

XAFS is produced by the scattering of the ejected photoelectron by its environment. This scattering is represented by weak oscillations that appear on $\mu(E)$ beyond the absorption edge of the atom under study. Here E is the energy of the incident X-ray photons and the absorption coefficient is $\mu(E)$. The absorption edge results from the quantum-mechanical transition of a particular atomic core-orbital electron to the free or unoccupied continuum levels [99]. This transition from an initial state ψ_i (with an X-ray, a core electron and no photo-electron) with energy E_i to a final state ψ_f (with no X-ray, a core hole and a photo-electron) with energy E_f corresponds to the X-ray absorption coefficient $\mu(E)$ and it is described in the one-electron approximation of Fermi's Golden Rule [80]:

$$\mu(E) \propto \sum_f |\langle \psi_f | H | \psi_i \rangle|^2 \, \delta(E_f - E_i - \hbar\omega) \tag{4.1}$$

where H is the Hamiltonian describing the interaction of X-rays with electrons and its first term can be approximated in perturbation theory as $H_1 = \frac{e}{mc}\vec{p}.\vec{A}$. $\vec{p}$ is the momentum operator and $\vec{A}$ is the vector potential of the incident electromagnetic field. The oscillatory wiggles contain precise information about the local atomic structure around the atom that

absorbed the X-ray. Thanks to synchrotron X-ray sources and to the advances in the theoretical treatment of the absorption spectra, it is nowadays possible to access quantitative understanding of the local environment of the probed atom.

XAFS spectroscopy in transmission geometry is used here to study the effect of high-pressure and high-temperature on Zr atom in PZT ceramic compounds and its role in the ferroelectric-paraelectric phase transition at the atomic scale. Additionally, the effect of applied external electric field on the piezoelectric properties of a model ferroelectric relaxor (PZN) at different absorption edges is studied using XAFS in fluorescence geometry.

4.1.2 X-ray absorption spectrum

The variation of the absorption coefficient as a function of the photon energy E shows three general features [98] (Figure 4.1): (1) as the energy increases the X-ray absorption intensity shows an overall decrease. This is related to the quantum-mechanical phenomenon of X-ray absorption by atoms, as described by Fermi's "golden rule"; (2) the sudden appearance of sharp jumps step function called the absorption edge. These edges occur when the incident X-ray energy is equal to the binding energy of an inner-shell electron; and (3) the presence of a series of weak wiggles or oscillatory structure which correspond to the XAFS region. The signal in this region contains detailed structural information about the absorption atom and its neighbors.

The XAFS spectrum can be defined as the normalized, oscillatory part of the X-ray absorption above a given absorption edge, i.e. [99]

$$\chi(E) = [\mu(E) - \mu_0(E)]/\Delta\mu_0 \tag{4.2}$$

where $\mu(E)$ is the measured absorption coefficient, $\mu_0(E)$ is the smoothly varying atomic-like background absorption (may include contributions from other edges), and $\Delta\mu_0$ is a normalization factor that arises from the net increase in the total atomic background absorption at the studied edge. This normalization factor is usually equal to the magnitude of the jump at the absorption edge.

According to Figure 4.1, a typical XAFS spectrum can be divided into three regions that contain related, but slightly different information about an element's local coordination and chemical state. These regions are known as:

i- Pre-edge Fine Structure (PEFS): PEFS region [100] appears before the main rise of the absorption edge and in some cases it provides valuable information on the local structure

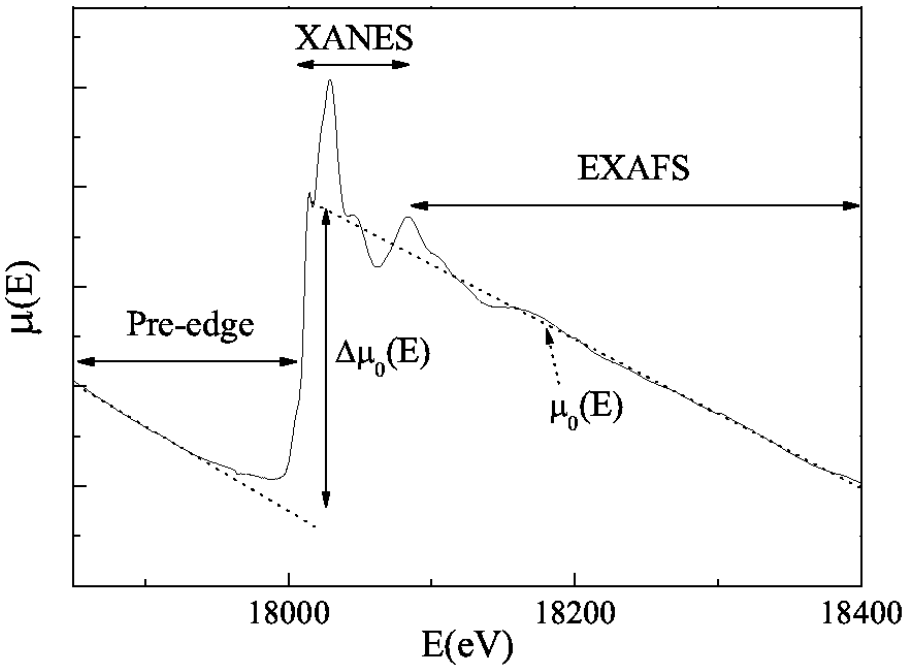


Figure 4.1: Zr K edge X-ray absorption spectrum of $PbZr_{0.52}Ti_{0.48}O_3$ obtained at 3.65 GPa and 300 K.

of the atom in question.

ii- X-ray Absorption Near-Edge Spectroscopy (XANES): within 30 eV of the main absorption edge. The spectral shape in the near-edge region is determined by electron correlation and density of states effects (multiple scattering of the photo-electron). It gives mainly information about the electronic properties of the absorbing atom and it is sensitive to oxidation state and coordination chemistry [99].

iii- Extended X-ray Absorption Fine Structure (EXAFS): is the region of weak oscillatory wiggles beyond 30 eV above the absorption edge. This fine structure contains precise information about the local atomic structure around the atom that absorbed the X-ray and it is used to determine the distance, coordination number and species of the neighbors of the absorbing atom. EXAFS region is the result of the single scattering of the ejected photo-electron from the absorbing atom and its neighbor atoms.

4.1.3 Performing the experiments

Characteristics of Beamline 29 at ESRF

Our experiments have been performed at beamline 29 (BM29) [101] at the European Synchrotron Radiation Facility (ESRF) (Figure 4.2). BM29 is a standard XAFS beamline characterised by a bending magnet source that gives reasonable X-ray flux with different monochromators Si(111), Si(220), Si(311) and Si(511) crystal pairs in order to cover a wide

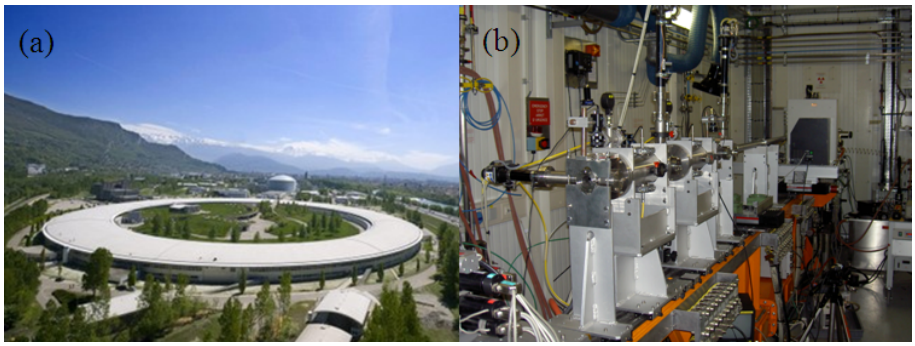


Figure 4.2: (a) European Synchrotron Radiation Facility (ESRF), Grenoble. (b) Beamline 29 (BM29).

operational energy range (4 keV to 74 keV). This energy range is sufficient for K-edge studies of elements in the range $22 < Z < 76$ and L-edges for $Z > 76$. This beamline is characterized by high energy resolution, high spectral signal to noise ratio (7×10^4), high beam stability and reasonable X-ray flux over the whole operational energy range.

High pressure High temperature XAFS for PZT

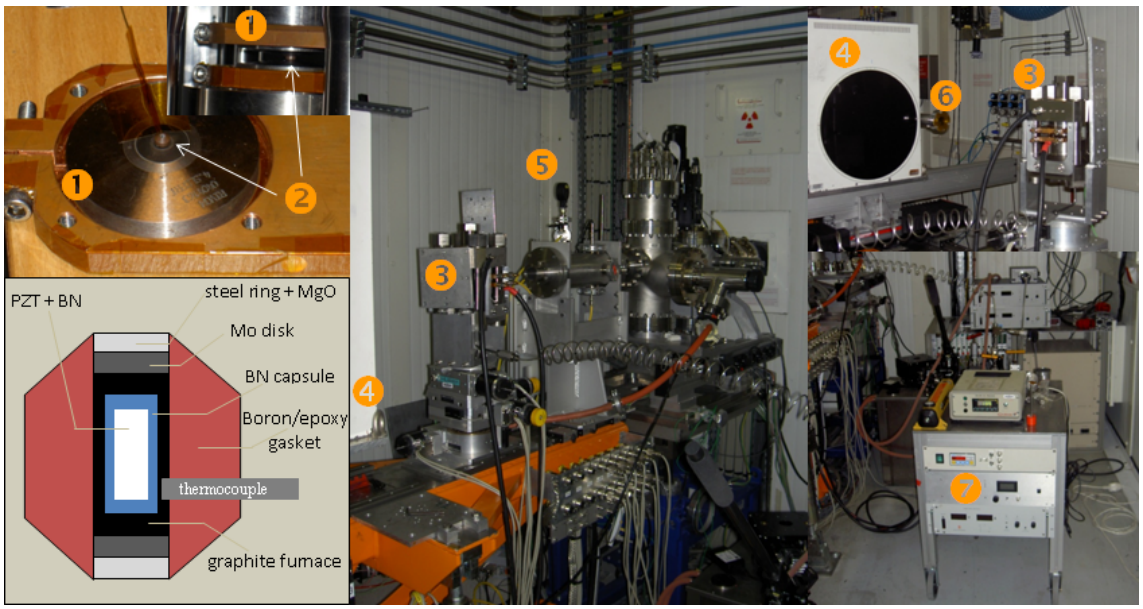


Figure 4.3: The experimental setup for high pressure high temperature X-ray absorption experiment in transmission mode coupled with X-ray diffraction. (1) Sintered diamond anvil, (2) boron-epoxy biconical gasket, (3) Paris-Edimburgh press, (4) MAR345 image plate detector, (5) Ion chamber I_0 (incident beam), (6) Ion chamber I_1 (transmitted beam), (7) Oil pump.

Zr K edge measurements (17998 eV) at high pressure and high temperature were performed in transmission geometry. (Figure 4.3). A (311) Si monochromator with a resolution of 0.5 eV was used. A Paris-Edinburgh press, equipped with sintered diamond anvils were coupled with 5 mm boron-epoxy biconical gaskets with a high X-ray transmission in the

selected energy range. A finely ground powder of $PbZr_{0.52}Ti_{0.48}O_3$ was mixed with boron nitride used as light element matrix and known to be chemically inert to the materials, in order to have the appropriate sample thickness for XAS measurements. The sample-matrix mixture was pelleted to a cylindrical shape, inserted into boron nitride capsule itself inserted in a graphite furnace and finally placed into the pressure gasket. Note that the use of boron nitride capsule was necessary in order to avoid the reduction of PZT by graphite at high temperature. The Mo disk was used to have electrical contact between the furnace and the anvil assured also by the steel ring on the top. The MgO inside the steel ring was used for thermal insulation. In order to characterize the sample and to measure the P and T data, a monochromatic beam (20 keV) was impinged onto the sample and the diffraction rings from the sample were intercepted by a MAR345 image plate detector mounted in an offset position. This in-situ diffraction measurement has also enabled us to check the tetragonal distortion of PZT in the P-T space. The pressure was measured using the equation of state of BN. The temperature was read from a thermocouple located in contact with the sample. XAS data were collected in transmission mode each 1-2 GPa along 3 isotherms (300 K, 450 K and 650 K). Beer-Lambert law was used to measure the linear absorption coefficient μ as a function of energy at each pressure point with

$$I(E) = I_0(E)e^{-\mu x} \tag{4.3}$$

where $I_0(E)$ is the intensity of the incident beam measured by the ion chamber I_0, $I(E)$ is the intensity of the transmitted beam measured by the ion chamber I_1, and x is the thickness of the sample.

XAFS under electric field for PZN

Zn K edge (9659 eV) and Nb K edge (18986 eV) measurements under electric field were performed in fluorescence geometry at beamline BM29 of the European Synchrotron Radiation Facility (Figure 4.4). $PbZn_{1/3}Nb_{2/3}O_3$ (PZN) [001] oriented single crystals with gold electrodes sputtered on both faces (a few nanometers) were used. A DC voltage was applied on these electrodes to produce an electric field up to 8 kV/cm. XAS data was collected in fluorescence mode owing to the strong absorption of PZN samples. Platelets of finely ground powder of PZN and boron nitride (light element matrix) with different thicknesses (depending on the studied absorption edge) were used as reference materials. XAFS measurements in transmission mode were performed on these reference samples before performing fluorescence measurements at each absorption edge. In case of fluorescence, the energy dependence of the linear absorption coefficient μ is given by

$$\mu(E) \propto I_f/I_0 \tag{4.4}$$

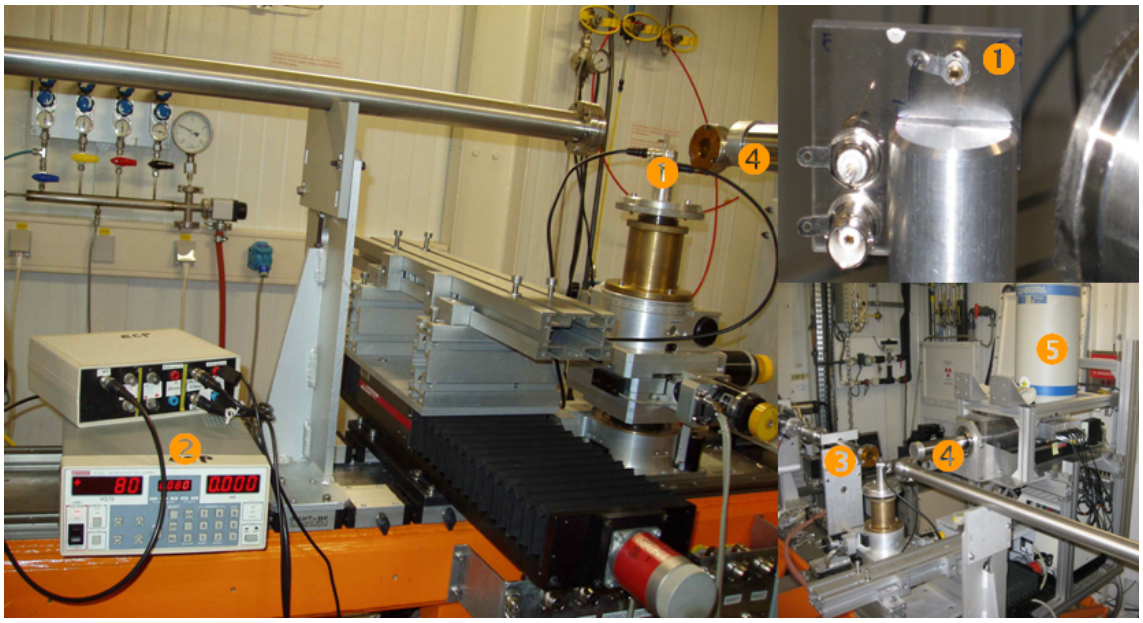


Figure 4.4: The experimental setup for X-ray absorption experiment in fluorescence geometry under electric field (1) Sample holder of PZN single crystal, (2) Electric field generator, (3) Incident X-ray beam, (4) Fluorescent X-ray beam, (5) X-ray detector.

where I_f is the intensity of the fluorescent beam and $I_0(E)$ is the intensity of the incident beam.

4.1.4 Analysis of the data

EXAFS

The EXAFS data analysis is the same for both transmission and fluorescence geometry measurements. It was performed using the IFEFFIT package [102]. This analysis is divided into two main parts. The first one is the reduction of the raw data and the second is the theoretical modeling in order to have quantitative values. The procedure develops as follows:

1. Conversion of the measured intensities into $\mu(E)$ and, if necessary, make instrumental corrections such as detector dead-time losses and remove the monochromator glitches.

2. Removal of a smooth pre-edge background that contains the instrumental background and contributions of other absorption edges.

3. Selection of the energy threshold E_0 which is usually equal to the energy corresponding to the maximum of $\mu(E)$, and normalize the spectrum to unit edge step.

4. Removal of a smooth post-edge background $\mu_0(E)$. A simple cubic spline function is usually used, but it is necessary to take care that the chosen function will not remove the XAFS oscillations themselves.

5. Transformatin of the spectrum into k-space where k is the wave-vector given by $k = \sqrt{2m(E - E_0)/\hbar^2}$ to obtain $\chi(k)$.

6. Fourier transformation of $\chi(k)$ into R-space, choose a suitable window to isolate the needed region of $\chi(R)$ in order to produce single shell amplitude and phase and then back-Fourier transform the weighted $\chi(R)$ into the k-space.

7. Defining a structural model in order to calculate the interatomic distance (distance to the neighboring atoms) R_i, the coordination number (number of neighboring atoms at distance R_i) N_i, the Debye-Waller factor σ_i^2, and the photoelectron energy shift ΔE_0 using the EXAFS expression (equation 4.5) and the already known values of $A_i(k)$, $\delta_c(k)$ and $\phi_i(k)$. During the fitting, S_0^2 is kept fixed.

$$\chi(k) = -S_0^2 \sum_i \frac{N_i A_i(k)}{kR_i^2} e^{-2k^2\sigma_i^2} e^{-2R_i/\lambda(k)} \times \sin[2kR_i + 2\delta_c(k) + \phi_i(k)], \qquad (4.5)$$

where $A_i(k)$ is the effective scattering amplitude and $\lambda(k)$ is the energy-dependent photoelectron mean-free path. S_0^2 is an overall amplitude factor, close to 1, which accounts for many-electron effects in the excited central atom. $\delta_c(k)$ and $\phi_i(k)$ are phase shifts associated with the electron propagating into and out the potentials of the absorbing site and scattering sites, respectively. σ_i^2 is the standard deviation of the R_i distance distribution. σ_i^2 contains two contributions: a thermal dynamic contribution that takes into account the vibrational local disorder and a static contribution that takes into account small structural disorder.

XANES and Pre-edge

At low photoelectron energy, single scattering or path expansion are not sufficient to simulate the experiments. Better techniques, such as the full multiple scattering theory are thus required. For the XANES part of the spectra we used the FDMNES code2 [103] using the finite difference method with the full multiple scattering theory. This theory works within the muffin-tin approximation on the potential shape, but it is more tractable with large systems. The PEFS are caused by the unoccupied p and d states of the B atoms in the perovskite [104]. For an absorbing atom out of a center of symmetry, an increased dipolar contribution associated with the hybridization of the d and p states appears in the intensity at the pre-edge. The intensity of this p-d peak is a direct measurement of the polar shift. In the centrosymmetric paraelectric form, this dipolar contribution disappears and only the quadrupolar contribution is observed.

4.2 Zr *K* Edge XAFS Study of PZT

4.2.1 Introduction

Understanding the physical behavior of a material at the atomic scale has always presented a great challenge to condensed matter physicists and materials scientists. The effort to elucidate the role played by Zr/Ti atoms which are at the origin of the polar displacements in ferroelectric $PbZr_{0.52}Ti_{0.48}O_3$ (PZT) is a prime example of such a challenge [105, 106, 107]. Ferroelectric perovskites of general formula ABO_3 exhibit a ferroelectric - paraelectric (F-P) phase transition at a critical temperature T_C (and a critical pressure P_C). The origin of the large dielectric susceptibility and piezoelectric properties in these highly polarizable ferroelectric perovskites is due to the cooperative displacement of the B cations, *i.e.* the Zr/Ti atoms in our case, from the center of symmetry of their octahedral sites below T_C (and P_C). These spontaneous displacements create local dipoles that are aligned parallel to one another leading to macroscopic dipole moment by application of an electric field E.

PZT is widely used in technological applications owing to its high piezo-ferro electric properties. The particular composition $x = 0.48$ in the $Pb(Zr_{1-x}Ti_x)O_3$ solid solution exhibits the highest electromechanical response. It is generally called the Morphotropic Phase Boundary (MPB) [51, 63]. Above $T_C = 664$ K, PZT is cubic with a Pb atom at each corner of the cubic cell, the Ti/Zr atoms in the center, and the oxygen atoms at the face centers. Upon decreasing temperature, both Pb and Ti/Zr move along the pseudocubic [001] direction giving rise to the tetragonal form. As PZT is a ferroic material, it exhibits domain configurations (elastic and electric) which make the understanding of these compounds much more complex. Different scales should be considered: between the atomic scale (individual polar displacements) and the macroscopic scale (macroscopic piezoelectric effect), the mesoscopic scale is governed by the domain wall motion.

High piezoelectric properties of PZT, PMN, and PZN are structurally linked to strong disorder which can be characterized by the presence of diffuse scattering [53, 108, 109] in diffraction experiments and by nanosized domains [110]. In this X-ray absorption fine structure (XAFS) study, and owing to the experimental technique used, we focus on the characterization of the Zr-polar displacements at the atomic scale. Since the only difference between $PbTiO_3$ end-member (d_{33}= 35 pC/N) [111] and $PbZr_{0.52}Ti_{0.48}O_3$ (d_{33}= 520 pC/N) [112] is the presence of zirconium, we focus our study on the role of the Zr atom in PZT solid solutions to understand this difference in the piezoelectric constants. The $3d^0/4d^0$ state of the Ti/Zr atoms can give an insight on the local shifts at the center of the oxygen octahedron. Zr^{4+} and Ti^{4+} have ionic radii of 0.72 Å and 0.605 Å respectively [113]. One therefore expects a much more pronounced off-center shift of the smaller Ti-atoms in their

oxygen-octahedron cage in comparison to the larger Zr-atoms. This scenario is confirmed based on XAFS [114] and Pair Distribution Function measurements [115]; the Ti off-center displacement is experimentally found to be about 0.2-0.3 Å, while Zr is found to have either a small shift (0.07 Å) [114] or no shift [115]. Additionally, although the Zr-shift is found to be both temperature and composition independent [100, 114], the Ti-shifts appear to have a disorder component as a function of temperature [58] and pressure [61] which is unusual for these ferroelectric displacive-type transitions [116].

4.2.2 Results and discussion

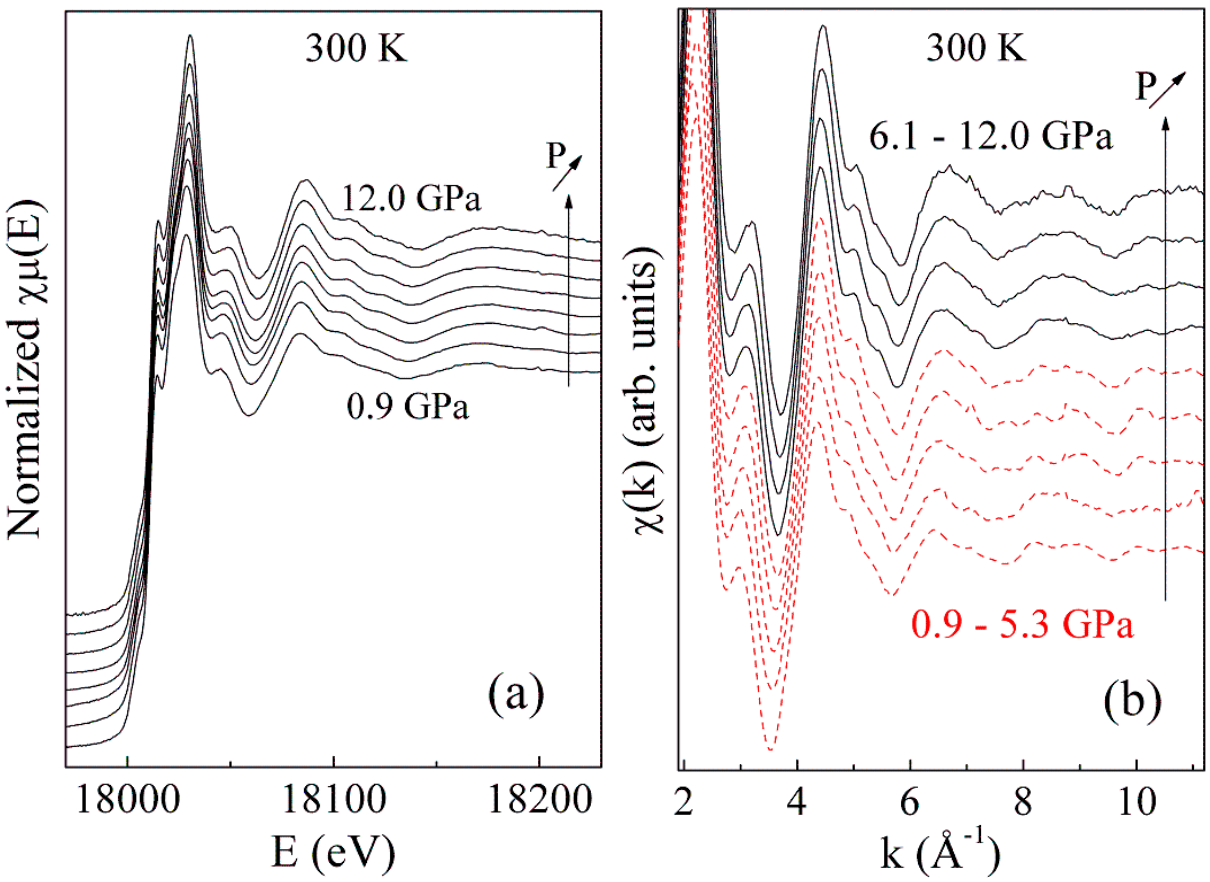


Figure 4.5: (a) Normalized XAFS spectra obtained at 300 K between 0.9 GPa and 12 GPa, (b) Extracted $\chi(k)$. Both signals are vertically shifted for clarity.

High quality, high-pressure XAFS data of PZT were normalized to the jump at the absorption edge. A small effect of pressure on the Zr K edge (17998 eV) spectra is seen, Figure 4.5(a). The extracted $\chi(k)$ spectra, Figure 4.5(b), give evidence above 6.1 GPa for the disappearance of some high frequency contributions: in particular the split features between $k = 6$ Å^{-1} and $k = 7.5$ Å^{-1} and between $k = 8$ Å^{-1} and $k = 10$ Å^{-1} merge into two single oscillations. Based on these data, there appears to be a low pressure behavior below ~ 6.1 GPa, and a high pressure behavior above this value.

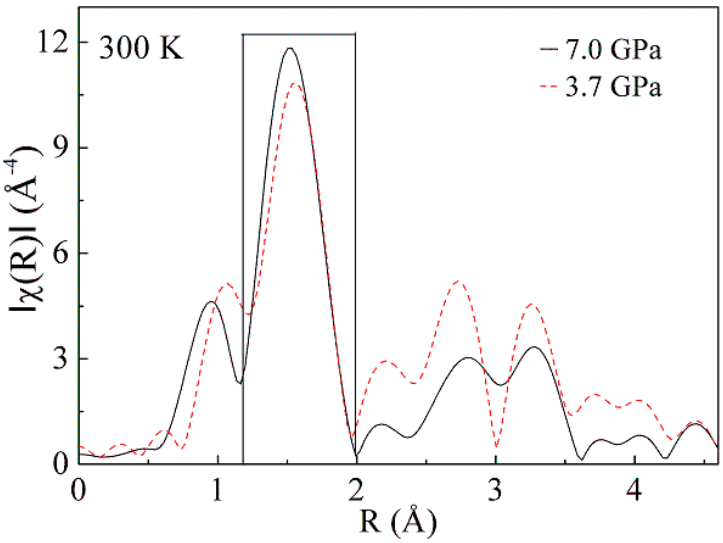


Figure 4.6: The k^3-weighted EXAFS signals (obtained in the 2-11 Å^{-1} range) are shown at 3.7 GPa (dashed) and 7.0 GPa (full). The Zr-O first coordination shell is extracted using a Hann window in the 1.2-2 Å range.

In Figure 4.6, we show the Fourier transforms of the EXAFS signal at 3.7 GPa and 7.0 GPa. The first peak near 1 Å is non-physical. The peak in the Hann window can be correlated with the radial distribution function around the photoabsorber. At 7.0 GPa, the maximum of the peak is shifted with respect to that at 3.7 GPa indicating a weak contraction of the Zr-O distance. In addition, the peak amplitude at 7.0 GPa is higher. Nevertheless, the shape of the first peak in the Fourier transform is a Gaussian at all pres-

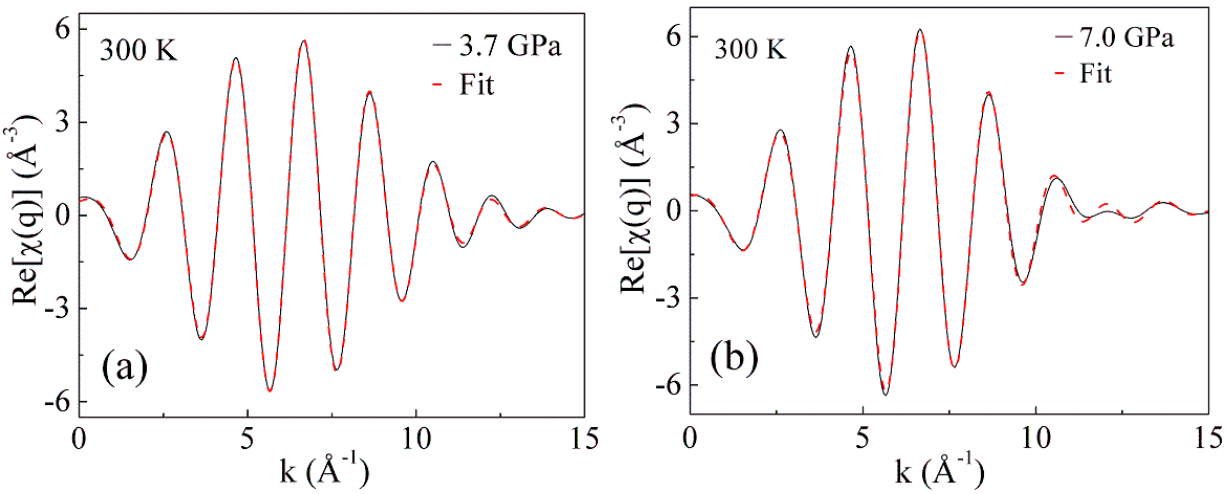


Figure 4.7: The k^3-weighted backward Fourier transforms along with the resulting fits (dashed) are shown at 3.7 GPa (a) and 7 GPa (b), respectively.

sures which allows the use of the same structural model given by six oxygen atoms as first neighbours at the same distance. The fitting is done in q space isolating the Zr-O peak of the Fourier transform and back transforming it in q space using a standard procedure. A symmetric distribution of bond distances is used, characterized by the following structural

parameters: R (average bond distance), σ^2 (relative mean square displacement or EXAFS DWF: $\exp(-2\sigma^2k^2)$), and the number of neighbours which is kept fixed at six. Figures 4.7(a) and 4.7(b) show the Zr-O atom pair-distribution function, *i.e.* the back Fourier transform, in the k^3-weighted space along with the best fit calculation obtained at 3.7 GPa and 7 GPa. The experimental data are correctly reproduced within the pressure range of investigation.

Figure 4.8 shows the pressure behavior of the experimental σ^2 for the Zr-O atom pairs at 300 K; σ^2 accounts for the relative mean square displacement of the Zr-O distance and contains two contributions: a thermal ($\sigma^2_{dyn.}$) and a structural ($\sigma^2_{stat.}$) contribution linked to the local vibrational dynamics and the local structural distortions, respectively. One can first note that the fitted ambient value is perfectly consistent with that reported in the literature [114] (the open star). Additionally, a noticeable decrease of σ^2 can be observed with increasing pressure with a change in the trend at $\sim$ 7 GPa.

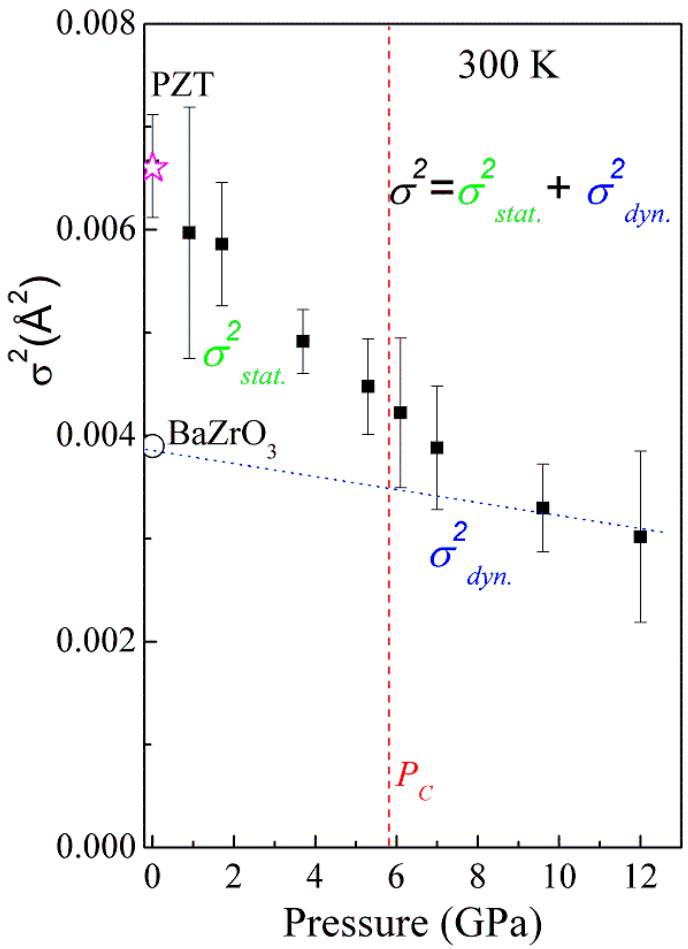


Figure 4.8: Pressure behavior of the DWF for the Zr-O atom pairs at 300 K. Values reported in the literature for PZT [114] (∗) and $BaZrO_3$ [118] (∘) are also included. P_C (the dashed line) corresponds to the paraelectric transition [53]. The dotted line represents the decrease of $\sigma^2_{dyn.}$ as explained in the text.

We compared these data with the σ^2 of centrosymmetric Zr-based oxide compounds. Since the $PbZrO_3$ end-member is antiferroelectric, it has antiphase polar displacements. Additionally, it was found that its structure is disordered with two substructure components related by a shear of c/2 [117]. In our study, $BaZrO_3$ (BZ) was chosen because the Zr-atoms are known to be perfectly in the center of the oxygen octahedra over the whole pressure-temperature range [118], implying that the σ^2 in BZ is only dependent on the thermal vibrations (θ_E = 606 K) as it does not contain a static contribution [119]. Note that other centrosymmetric Zr-based oxide materials (for example, ZrW_2O_8 [119]) also exhibit similar values of σ^2.

The behavior of $\sigma^2_{dyn.}$(BZ) at a fixed temperature (300 K) can be expected to smoothly decrease upon increasing pressure. This decreasing behaviour of $\sigma^2_{dyn.}$(dotted line in Figure 4.8) can be estimated using the equivalent isotropic temperature factors of the B atom reported in a high pressure single crystal diffraction study [120] of $GdFeO_3$, a centrosymmetric perovskite (no static disorder) which exhibits no phase transition in the pressure range of interest. The pressure dependence of $\sigma^2_{dyn.}$ corresponds to a decrease of about 1% per GPa [120]. At ambient conditions, we observe that σ^2 of PZT is higher than that of BZ. This can be attributed to the presence of static disorder in PZT, which is absent in BZ. At high pressure, the $\sigma^2_{dyn.}$ of BZ perfectly fits the high pressure values of σ^2 for PZT indicating that pressure eliminates the static disorder for the Zr-atoms of PZT above 7 GPa and that the only contribution to the EXAFS DWF is dynamic above this pressure. Based on previous studies, we already identified the F-P phase transition of PZT at 5-6 GPa [53], Figure 4.8 (P_C: dashed line). This transition can be related to the change of slope of σ^2 for the Zr-O bond. In the low pressure regime, σ^2 contains the static and dynamic contributions while in the high pressure regime only the dynamic part contributes to the σ^2. This implies that $\sigma^2_{stat.}$ of PZT is due to a small random Zr off-center displacement in the oxygen-octahedron cage, which produces a small polarization. This Zr-shift can be roughly estimated to be $\sqrt{0.0067 - 0.003} \cong 0.06$ Å. The excess of $\sigma^2_{stat.}$ appears at pressures above P_C suggesting that disorder persists few GPa above the transition, as it has already been reported for Ti-shifts in P-T space [58, 61]. Finally, between 0 and 12 GPa we find a contraction of the Zr-O distances of $\sim$ 0.01 Å.

We now discuss the XANES part of the spectra. The p-d peak, linked to the dipole transition, is expected to disappear at the ferroelectric-paraelectric transition as in $PbTiO_3$. However, it is difficult to observe this effect in PZT [100] at the Zr K edge owing to the large Zr K hole width ($\gamma_K(Zr) \approx 3.84$ eV) as compared to that of the Ti K edge in $PbTiO_3$ ($\gamma_K(Ti) \approx 0.8$ eV). The very weak variation of $\sigma^2_{dyn.}$ in this high-pressure experiment enables to distinguish a smooth, but observable decrease in the PEFS intensity in the 0.9 GPa - 6.1 GPa pressure range, as shown in Figure 4.9(a). Above 6.1 GPa, the PEFS spectra

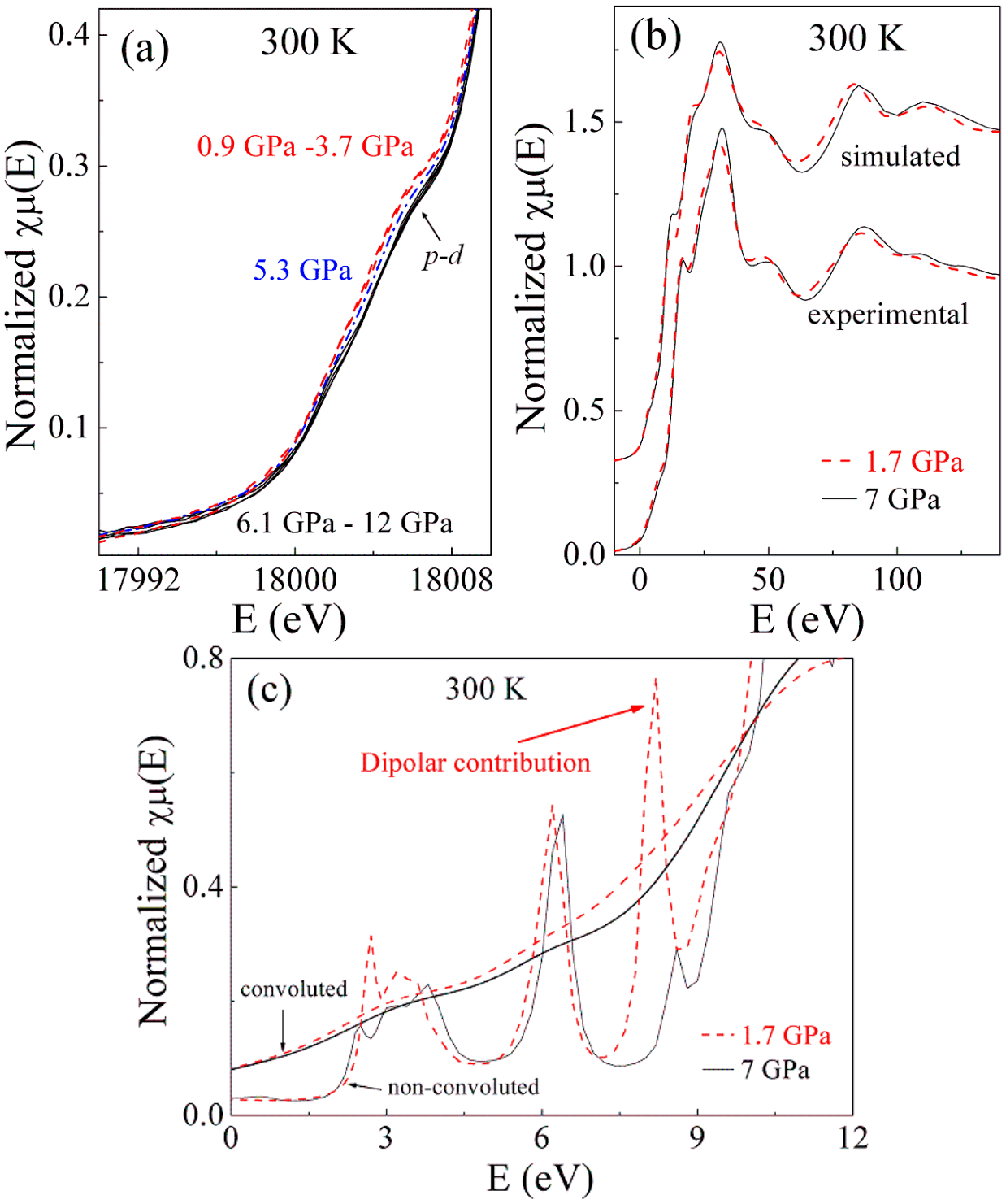


Figure 4.9: (a) High-pressure Zr K edge XANES spectra obtained at 300 K. Note the pressure evolution of the PEFS. (b) Experimental and simulated XANES spectra at 1.7 GPa and 7 GPa. In (b), the origin (0) corresponds to the Zr K edge. (c) The non-convoluted and convoluted theoretical PEFS at 1.7 GPa and 7 GPa showing the disappearance of the dipolar contribution at high pressure.

overlap almost perfectly. The critical pressure for the change in behavior, *i.e.* 6.1 GPa, is roughly consistent with the results described above, Figures 4.5(b) and 4.8. In order to determine the origin of the change in the behavior in the XANES spectra, we performed full multiple scattering calculations. Based on structural data obtained from neutron diffraction [53], an excited atom embedded in a 10 Å-cluster is used to simulate the XANES spectra in the ferroelectric and paraelectric state. In the ferroelectric state, a Zr-displacement of 0.06 Å from the symmetric position is kept fixed consistent with the EXAFS results. The theoretical spectra are convoluted with the combined Zr K hole width, the photoelectron width, and the experimental resolution. Figure 4.9(b) shows the experimental and simulated XANES spectra obtained at 1.7 GPa and 7 GPa, which are consistent with long range polar and non-polar states, respectively. All the features are correctly reproduced starting from the more intense white line in the paraelectric state, centered at 30 eV, to the well-known shift to higher energy of the XANES spectrum at high pressure. However, the convolution with the large Zr K hole width hides the structure at low energy. We illustrate in Figure 4.9(c), the non-convoluted and convoluted spectra at 1.7 GPa and 7 GPa. It is here clearly possible to identify the dipolar contribution in the low-pressure spectrum at about 8.2 eV due to the breaking of the inversion symmetry induced by the small Zr-shift from its symmetric position. At high pressure in the paraelectric state, *i.e.* 7 GPa, only the quadrupolar contribution for which intensities are only very weakly affected by the Zr-shift can be observed. Therefore contrary to what was expected, these simulations confirm that even a small Zr-shift can be observed in the PEFS signal. This confirms that XAFS measurements are a perfect probe of local polar displacements. Note that for the EXAFS analysis mentioned above, the small Zr-shift can only be observed in the high-pressure measurements at constant temperature. As stated previously, the thermal vibrations in our case are almost constant thereby making the interpretation considerably easier.

Normalized high-pressure XAFS spectra of PZT obtained at 450 K can be seen in Figure 4.10. The shape of the contributions becomes different above $\sim$ 5.5 GPa. Figures 4.11(a) and 4.11(b) show the Zr-O atom pair-distribution function, *i.e.* the back Fourier transform, in the k^3-weighted space along with the best fit calculation obtained at 3.8 GPa and 7.3 GPa. The experimental data are correctly reproduced within the pressure range of investigation. Figure 4.12 shows the pressure behavior of the experimental σ^2 for the Zr-O atom pairs at 450 K. As observed at ambient temperature, a noticeable decrease of σ^2 can be observed with increasing pressure followed by a plateau at higher pressures. The extrapolated value of σ^2 in BZ at 450K is plotted (θ_E = 606 K) [119]. As in Figure 4.8, the $\sigma^2_{dyn.}$ estimate of BZ (dotted line) fits with the values of σ^2 for PZT at high pressure giving an additional evidence that pressure eliminates the static disorder for the Zr-O bond in PZT above 5 GPa. The only contribution to the EXAFS Debye-Waller factor above this pressure is dynamic. As observed previously, $\sigma^2_{stat.}$ of PZT comes from a small random Zr

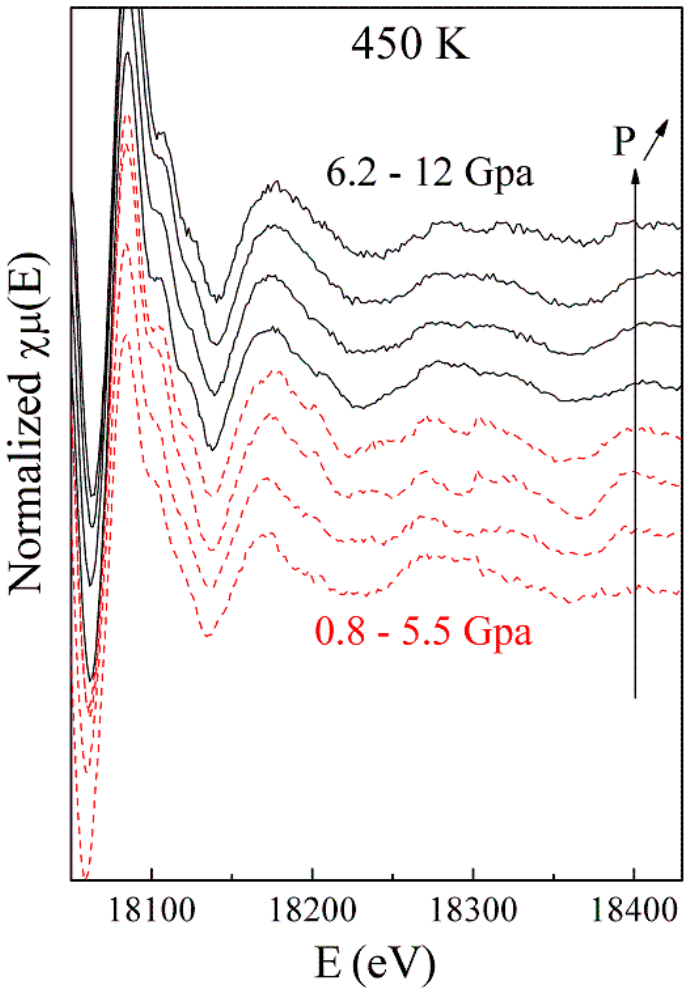


Figure 4.10: Normalized XAFS spectra obtained at 450 K between 0.8 GPa and 12 GPa. The spectra are vertically shifted for clarity.

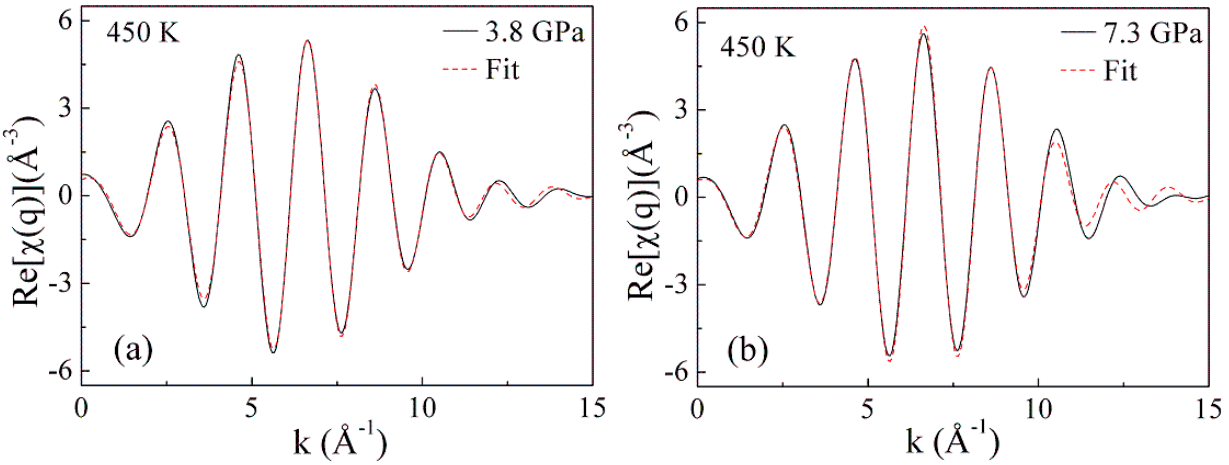


Figure 4.11: The k^3-weighted backward Fourier transforms along with the resulting fits (dashed) are shown at 3.8 GPa (a) and 7.3 GPa (b), respectively.

off-center displacement in the oxygen octahedron cage which produces a small polarization. This finding is supported by the high-pressure XANES spectra obtained at 450 K, Figure 4.13. It is possible to distinguish a smooth decrease in the PEFS intensity in the 0.9 GPa - 5.7 GPa pressure range. Above 5.7 GPa, the PEFS spectra overlap almost perfectly indicating the disappearance of the dipolar contribution as shown by the full multiple scattering calculations mentioned above.

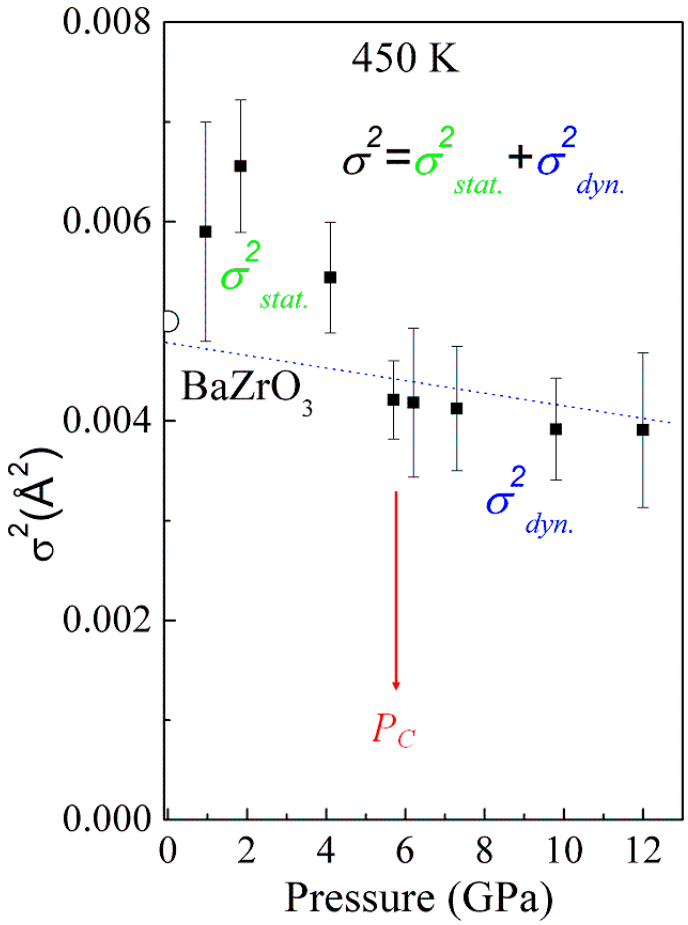


Figure 4.12: Pressure behavior of the DWF for the Zr-O atom pairs at 450 K. The calculated value for $BaZrO_3$ (○) [118] is also included. $\sigma^2_{dyn.}$ (the dotted line) corresponds to a decrease of about 1% per GPa.

4.2.3 Conclusion

In conclusion, the pressure induced F-P transition in PZT has been investigated by XAFS at the Zr K edge. The first coordination shell of the Zr atom can be reproduced assuming a cubic environment inside a ZrO_6 octahedra. This supports previous results showing that in mixed perovskites, the polarization mainly originates from the off-center of the small atom (Ti in PZT) of the B-site. While the larger one (Zr in PZT) is very close to its centered position. The peaking of the ZrO_6 cage with pressure leads to a reduction of the Zr-O

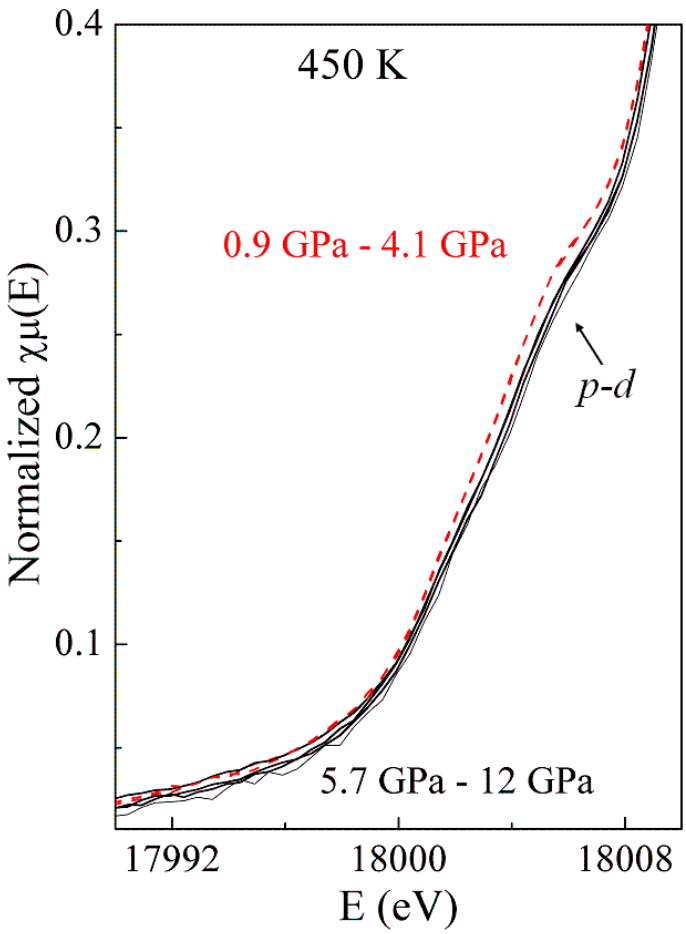


Figure 4.13: High-pressure Zr K edge XANES spectra obtained at 450 K. Note the pressure evolution of the PEFS.

distance of ~ 0.01 Å. The corresponding decrease of the static contribution of σ^2_{Zr} suggests that pressure induces an ordering in the Zr atoms. The F-P transition is clearly observed by a change of slope in the σ^2_{Zr} pressure dependence. We find $P_C \approx$ 6-7 GPa at 300 K and $P_C \approx 5$ GPa at 450 K. This transition translates into the disappearance of the dipolar contribution in the PEFS, as well as a small decrease of the amplitude of the p-d peak.

4.3 Probing the Giant Piezoelectric Effect in PZN

4.3.1 Introduction

A XAFS experiment under dc electric field has been performed to study the polarization at the B-site in a single crystal of PZN. It was commonly believed that PZN undergoes a paraelectric (cubic) to a disordered ferroelectric (rhombohedral) phase transition at the freezing temperature $T_f \approx 385$ K [73] slightly below its T_m. However, high-energy X-ray diffraction experiments performed in Shirane's group around 2003 [121, 122] suggested that the transition at T_f would only take place on the outer layer of the sample (10 to 50 μm), while the structure in the bulk would remain cubic (X-phase) over a wide temperature range

($15\,\mathrm{K} < T < 750\,\mathrm{K}$). A recent neutron-diffraction study [123] disclaimed the above interpretation showing that the cubic-rhombohedral phase transition occurs in both thin and thick PZN powders (143 μm and 1-2 mm grain size). Later on, Lebon *et al.* [124] showed that tetragonal and rhombohedral ferroelectric phases (*i.e.*, long-range order) could be induced under a dc electric field applied along [001]- and [111]-directions respectively. This study shows that the [001]-direction is most favorable for inducing a ferroelectric phase in the temperature range of the dielectric anomaly and it is the preferable direction for the shift of a large fraction of Nb ions under electric field.

It is known that PNRs associate with large local lattice distortions from the average structure. Diffuse scattering is one of the techniques that can be used to directly probe the local inhomogeneities. Different studies of PZN showed that the diffuse scattering intensities coming from the PNRs increase upon cooling and persist into the low-temperature phase below T_f. However, a recent high-energy X-ray diffuse scattering experiment [125] revealed that the short-range polar order (*i.e.*, diffuse scattering intensity) was not suppressed under an electric field applied along the [111] direction which suggests a competition between short-range and long-range order in these materials.

As stated before, [001] is the most favorable direction for inducing a ferroelectric phase and the direction for which PZN exhibits giant electromechanical coupling (k_{33}) (~ 0.85 compared to ~ 0.38 along [111]-direction) and ultrahigh piezoelectric coefficient (d_{33}) ($\sim$ 1100 pC/N compared to ~ 80 pC/N along [111]-direction) with a relatively modest applied electric field [126]. Unfortunately, no local structure study has been performed to explain the effect of the external field along the [001] direction. The aim of this study is to probe the polar displacements of PZN at the atomic scale by another short-range order technique, X-ray absorption fine structure (XAFS) spectroscopy. Owing to the above, we decided to investigate these ferroelectric local distortions with an applied electric field along the [001] direction. We believe this could help to understand which atom(s) predominantly gives rise to the polarization *i*) in the moderate and *ii*) high $\vec{\mathrm{E}}$ regime and give information on the possible electric-field induced order in this material.

4.3.2 Results and discussion

Because of the large absorption coeffieceint of Pb atoms in the PZN single crystals, XAFS data are collected in fluorescence mode at both the Zn K edge (9659 eV) and the Nb K edge (18986 eV). It is known that the $\mu(E)$ measured in fluorescence is the ratio of the signals on the fluorescence and incident ion chambers, but this is only true in the limit of very thin or very dilute samples [102]. For thick samples, the penetration depth of the incident beam changes with $\mu(E)$. It diminishes when the oscillatory part wiggles up and increases

when the oscillatory part wiggles down. This effect leads to an apparent attenuation of the oscillatory structure in the raw data. Hence, the self-absorption correction constitutes an essential step during data analysis. To avoid any correction mistakes, we checked that the XAFS spectrum of a platelet of finely ground powder of PZN and boron nitride measured in transmission geometry gives similar results as the fluorescence spectrum of our thick PZN single crystal.

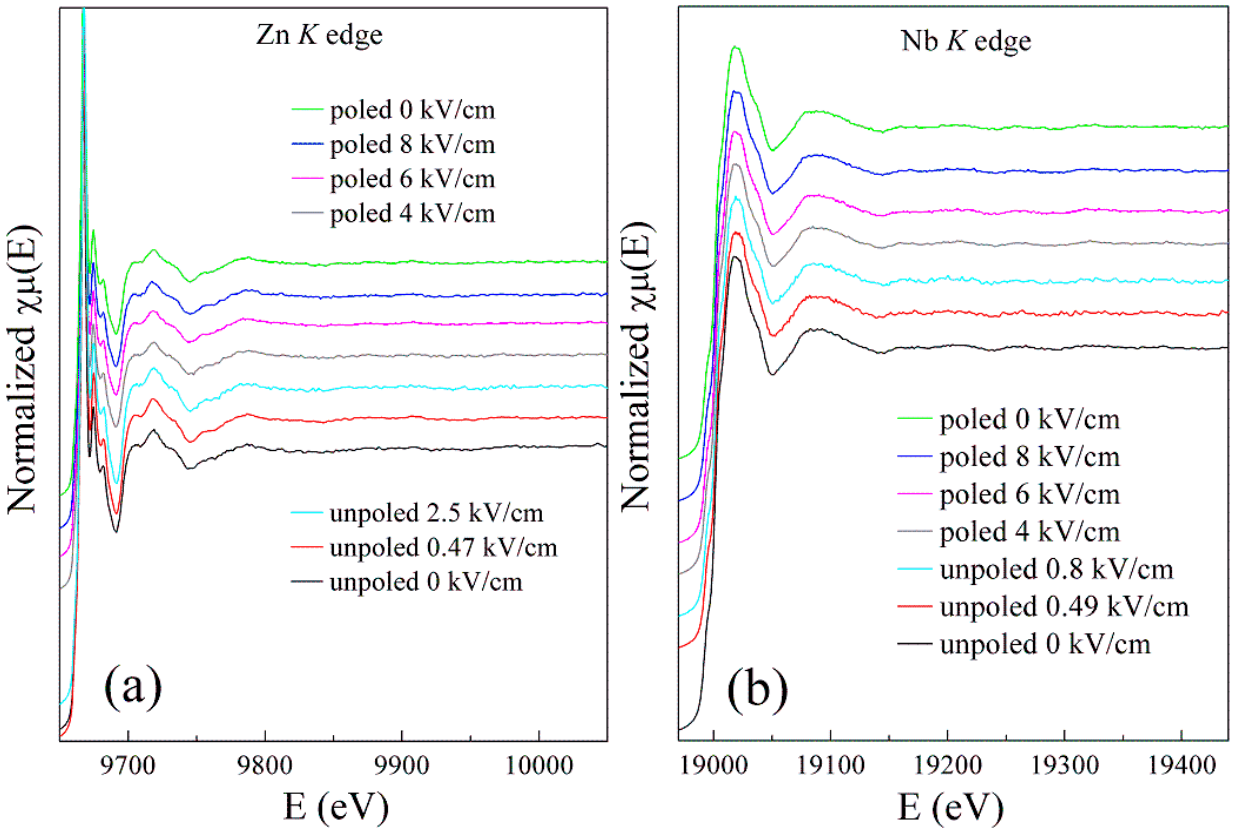


Figure 4.14: Normalized XAFS spectra at Zn K edge (a) and Nb K edge (b). The signals are vertically shifted for clarity.

Figures 4.14(a) and 4.14(b) show the data at the Zn K edge and the Nb K edge, respectively, normalized to the jump at the absorption edge at different values of the applied dc electric field (E_{dc}). The data has been corrected to the self-absorption approximation which affects the amplitude of XAFS spectra measured in fluorescence mode as explained above. No clear difference can be seen between the spectra of the unpoled sample with low values of the applied E_{dc} and the spectra of the poled sample with high E_{dc} values.

The EXAFS signal $\chi(k)$ was obtained after subtracting the embedded-atom absorption background from the measured absorption coefficients and normalizing by the edge step using the IFEFFIT package [102]. The corresponding curves at Zn K edge and Nb K edge are shown in Figures 4.15(a) and 4.15(b), respectively. Again, the shape of the spectra are

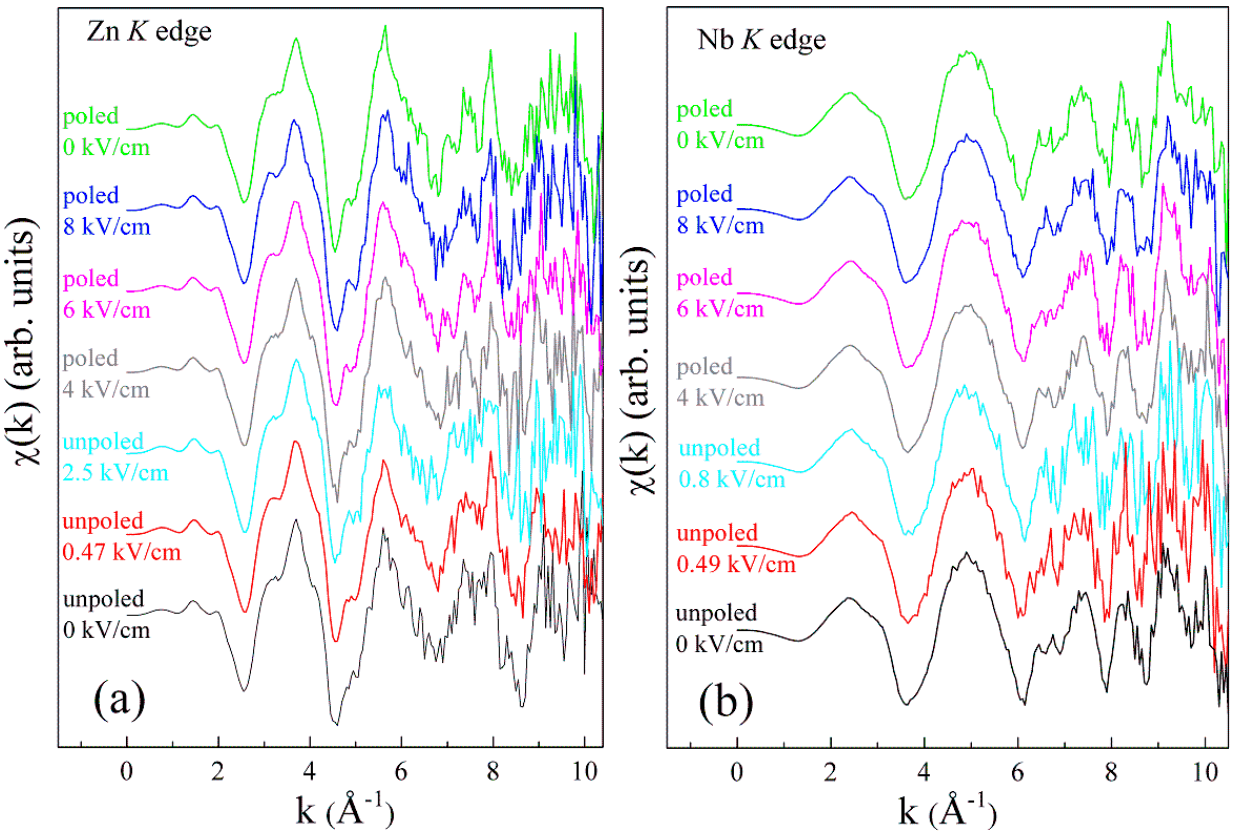


Figure 4.15: Extracted EXAFS spectra $\chi(k)$ in k^3 space at Zn K edge (a) and Nb K edge (b). The signals are vertically shifted for clarity.

very similar indicating that the local alignment of the polarization of different nanodomains by the poling process has no big effect on the individual reflections of the EXAFS signature. It is worth noting that no changes are expected in the XANES and the pre-edge regions in this system especially the p-d peak which is caused by mixing of unoccupied p and d states of the B atom, because the d orbital of the Zn atom is fully occupied (d^{10} state) and Nb K hole width is large (γ_K(Nb) $\approx$ 4.14 eV).

A complete analysis of the first coordination shell of both Zn- and Nb-atom for the PZN single crystals has been performed at different values of E_{dc}. The EXAFS signal was Fourier transformed using a Hann window in the k range of 2-11 Å^{-1}. The resulting curves for unpoled 0 kV/cm and poled 8 kV/cm Zn and Nb K edge spectra are shown in Figure 4.16. The main contribution to the EXAFS signal is the first peak (at $R \approx 1.6$ Å for the Zn spectra) which can be correlated with the radial distribution function around the photoabsorber and the two peaks centered near 1.4 Å and 1.9 Å for the Nb spectra. Figure 4.16(a) shows that the maximum of the peak of the Zn poled 8 kV/cm sample is up-shifted with respect to that of the unpoled sample which in addition has a smaller peak amplitude. On the contrary, the comparison of the unpoled and poled Nb spectra (Figure 4.16(b)) shows that the peak maximum of the 8 kV/cm Nb poled sample is shifted to lower values. This

indicates a change in the local structure between the unpoled and poled samples and therefore, a difference in the values of the corresponding Debye-Waller factors (DWF) should be expected. This also emphasizes that the effect of the applied field is really efficient, that is not screened by a possible surface-charges effect induced by the incident X-ray beam. On the contrary, the peaks of the EXAFS signal of the poled Nb spectra at both 0 kV/cm and 6 kV/cm are almost similar (Figure 4.17).

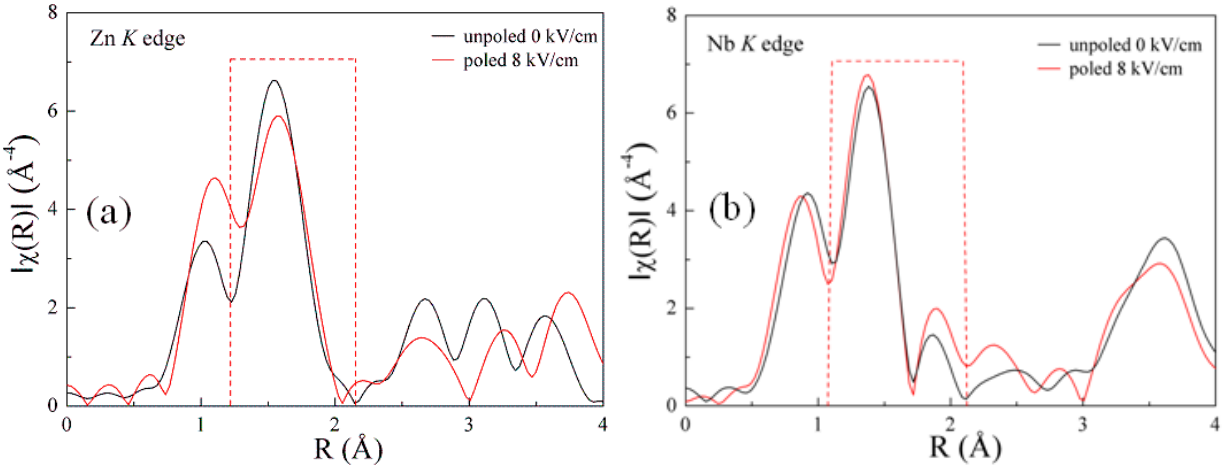


Figure 4.16: The k^3-weighted EXAFS signals (obtained in the 2-11 Å^{-1} range) are shown for unpoled 0 kV/cm and poled 8 kV/cm Zn (a) and Nb (b) K edge XAFS spectra. The Zn-O and Nb-O first coordination shell is extracted using a Hann window in the 1.2-2.2 Å and 1.1-2.1 Å range, respectively.

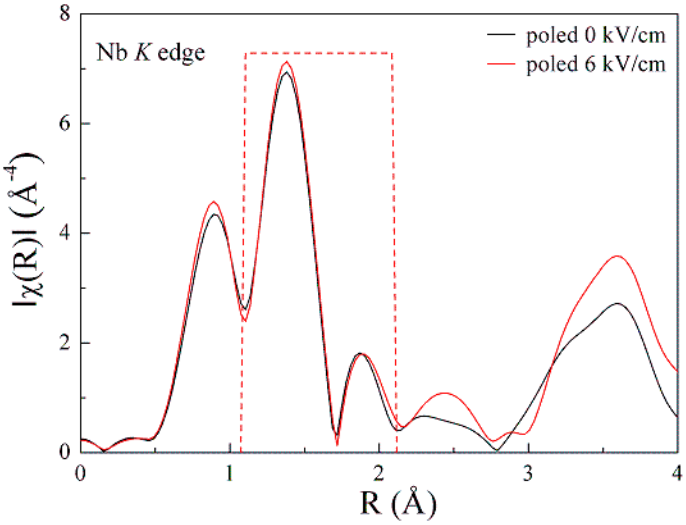


Figure 4.17: The k^3-weighted EXAFS signals (obtained in the 2-11 Å^{-1} range) are shown for poled 0 kV/cm and poled 6 kV/cm Nb K edge XAFS spectra. The Nb-O first coordination shell is extracted using a Hann window in the 1.1-2.1 Å range.

Since the shape of the first peak of the Fourier transform is a Gaussian for all the Zn spectra, the same structural model given by six oxygen atoms as first neighbors at the same

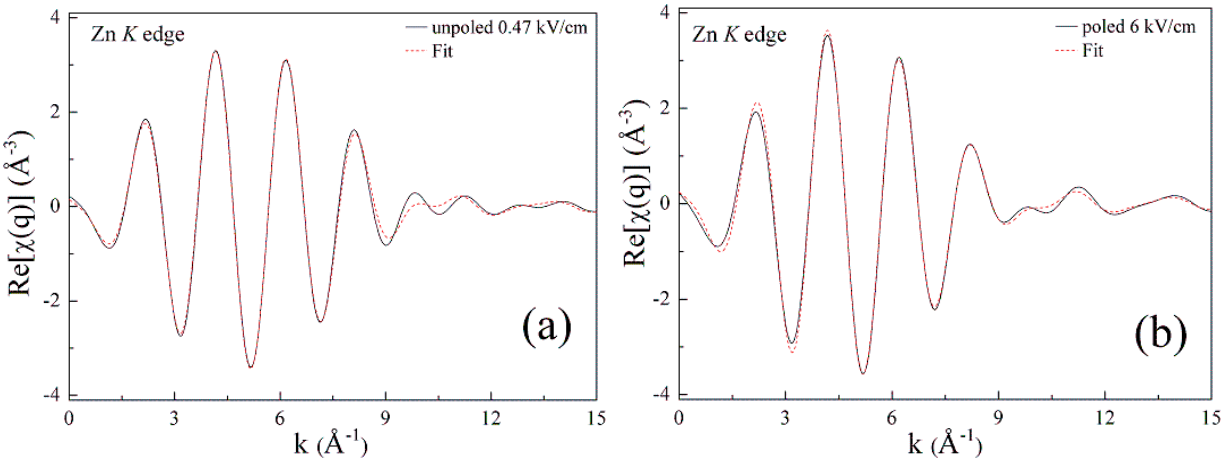


Figure 4.18: The k^3-weighted backward Fourier transforms along with the resulting fits (dashed) are shown for unpoled 0.47 kV/cm (a) and poled 6 kV/cm (b) Zn K edge XAFS spectra, respectively.

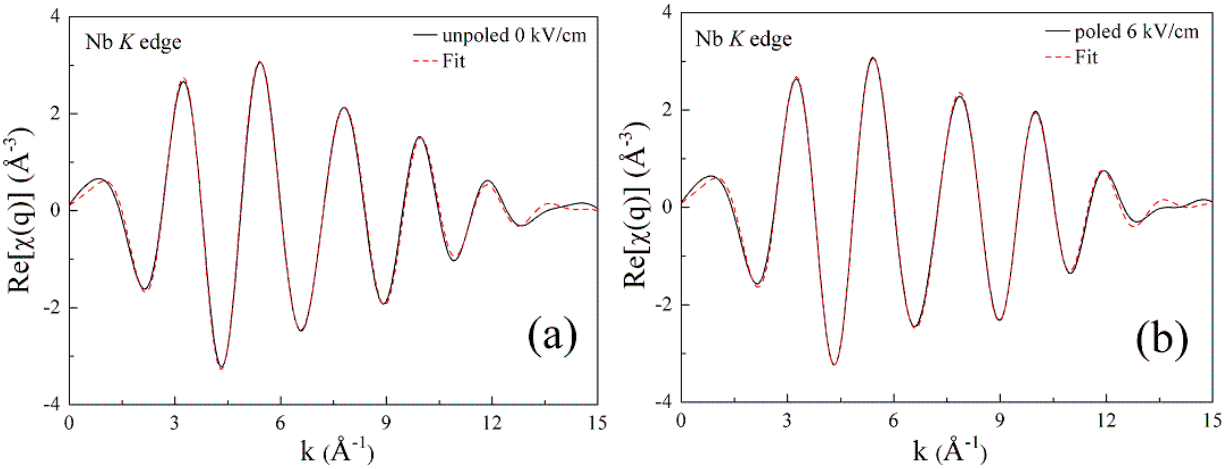


Figure 4.19: The k^3-weighted backward Fourier transforms along with the resulting fits (dashed) are shown for unpoled 0 kV/cm (a) and poled 4 kV/cm (b) Nb K edge XAFS spectra, respectively.

distance has been used. A symmetric distribution of bond distances is used, characterized by the following structural parameters: R (average bond distance), σ^2 (relative mean square displacement of the Zn-O or Nb-O bond), and the number of neighbors which is kept fixed at six. For Nb, a structural model given by six oxygen atoms as first neighbors with a tetragonal distortion, due to presence of an asymmetry on the main peak in the selected frequency range, has been used to fit the data. Two Nb-O distances R_1 and R_2 are taken into account with four oxygen atoms at R_1 and two oxygen atoms at R_2. The fitting is done in q space isolating the Zn-O and the Nb-O peak of the Fourier transform and back transforming in q space using a standard procedure. Figures 4.18(a) and 4.18(b) show the Zn-O atom pair distribution function, *i.e.* the backward Fourier transform, in the k^3-weighted space along with the best fit calculation for unpoled 0.47 kV/cm and poled 6 kV/cm samples, respectively. The corresponding Nb-O atom pair distribution function

with the fit for unpoled 0 kV/cm and poled 4 kV/cm Nb K edge XAFS spectra are shown in Figures 4.19(a) and 4.19(b), respectively.

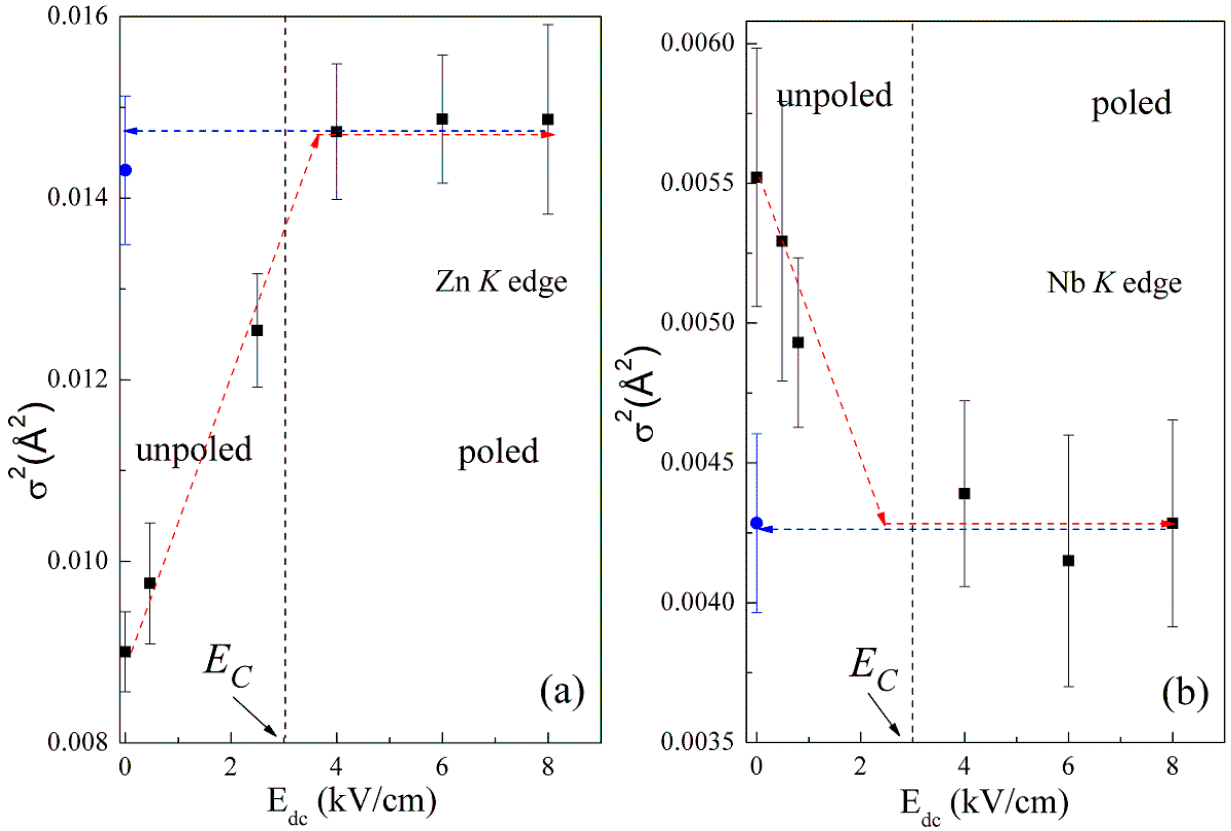


Figure 4.20: The variation of the DWF for the Zn-O (a) and Nb-O (b) atom pairs as a function of the applied electric field.

Figures 4.20(a) and 4.20(b) show the variation of the extracted DWF for Zn-O and Nb-O atom pairs as a function of E_{dc}, respectively. The average Zn-O distance is 2.07 Å and the two Nb-O distances are 1.94 and 2.14 Å. For PMN, two Nb-O bond lengths of 1.95 and 2.16 Å were also observed [127]. As stated before, σ^2 contains two contributions: a thermal ($\sigma^2_{dyn.}$) and a structural ($\sigma^2_{stat.}$) contribution. The experiment has been performed at fixed temperature (room temperature), meaning that the thermal contribution $\sigma^2_{dyn.}$ linked to the local vibrational dynamics should be almost constant and the evolution in the measured values of σ^2 correspond to the static part of the DWF which is related to the local structural distortions.

As the field increases, σ^2_{Zn} starts to increase till it becomes almost constant above the coercive field ($E_C \approx 3$ kV/cm [126, 124]). When the applied E_{dc} is removed, σ^2_{Zn} does not go back to its original value. On the contrary, σ^2_{Nb} decreases upon increasing the applied field, then it attains a constant value above E_C. These opposite behaviors of σ^2_{Zn} and σ^2_{Nb} at least for the values of the applied E_{dc} below E_C can be attributed to the difference in the size of the two atoms. The ionic radius of Nb^{5+} (0.64 Å) [113] is smaller than that of Zn^{2+} (0.74 Å)

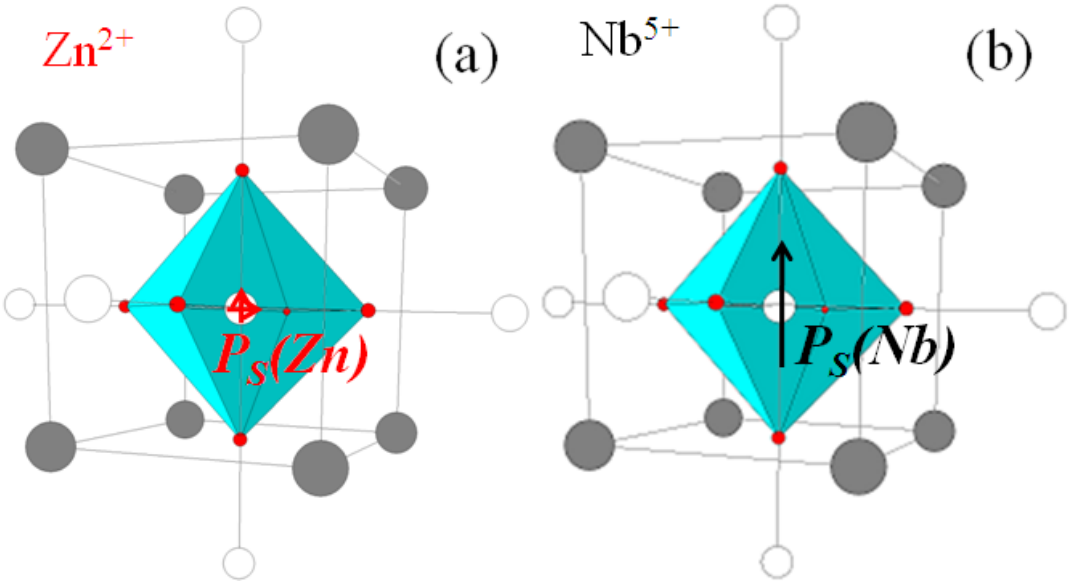


Figure 4.21: Shematic diagram for $PbZn_{1/3}Nb_{2/3}O_3$ showing the centrosymmetric-like Zn atom (a) and the distorted Nb atom (b).

[113]. The unpoled PZN sample at zero field has no *macroscopic* spontaneous polarization P_S. The small Nb atom is off-centered with a large *local* polarization P_{Nb} (Figure 4.21(b)) owing to the strong polar Nb-O dipole while the larger Zn atom which is almost centered produce a smaller polarization P_{Zn} (Figure 4.21(a)). The applied field causes a shift in the Zn-O distances toward higher values (Figure 4.16) meaning that the distortion of the ZnO_6 octahedra increases. Within a cubic model, this translates into an increase in the corresponding values of σ^2_{Zn} (Figure 4.20(a)). Comparing PZT under pressure and PZN under electric field, it is thus tempting to relate σ^2 of the large cation occupying the B-site to the distortion of the oxygen-octahedra. σ^2 increases as the distortion increases, and vice-versa. The distortion of BO_6 octahedra suggests that another mechanism related to a possible small off-centering of the large atom, which was not taken into account in our model, could also be involved. The alignment of the local Nb-O dipoles is mainly responsible for the macroscopic spontaneous polarization P_S. The orientation of the dipoles causes the decrease in the values of σ^2_{Nb} (Figure 4.20(b)). A sketch of the alignment mechanism of the Nb-O dipoles and the corresponding increase in P_S under an external electric field has been shown in Figure 1.7. Above E_C where the polarization reaches its saturation, σ^2 has almost a constant value owing to the alignment of all the unfavorable nanodomains along the direction of the applied electric field. When the field is removed, σ^2 does not go back to its original value. This is related to the remanent polarization. Its zero field value is almost similar to that of reached for applied field above E_C because the remanent polarization is almost equal to the saturation polarization (refer to the hysteresis loop of a ferroelectric relaxor at temperatures below T_f (Figure 2.2)).

4.3.3 Conclusion

XAFS measurement in function of applied dc electric field was performed to study the local B-site distortion in PZN relaxor. As the applied field increases below E_C, the Debye-Waller factor $\sigma^2(Zn)$ of the large Zn atom increases while $\sigma^2(Nb)$ of the small Nb atom decreases. The increase of $\sigma^2(Zn)$ is related to the distortion of the ZnO_6 octahedra. The decrease in the values of σ^2_{Nb} is due to the alignment of the strong Nb-O dipoles with the field.

Part III

Lattice Dynamics of Lead-based Relaxors

Chapter 5

Hyper-Raman Scattering

5.1 Theory and Experimental Technique

There exists several experimental tools which probe the vibrations in solids. The most common are inelastic neutron scattering (INS) and inelastic light spectroscopies (Raman scattering and infrared absorption). Inelastic light scattering in crystals is characterized by very stringent selection rules. For example, for high symmetry structures, there exists a rule of mutual exclusion between Raman scattering (RS) and infrared absorption (IR). Modes active in RS are not in IR, and vice versa. This contrast in the activity of the modes is often very useful to describe the nature (*e.g.* symmetry) of the vibrations.

Hyper-Raman scattering (HRS) is a less conventional technique, mostly because it was very difficult to operate until several years. Though, owing to the specificity of its selection rules, it appears to be a very powerful tool which nicely complement RS and IR [128, 129]. This is even truer in partially disordered and amorphous materials, where the structural disorder (partially) lifts the crystalline selection rules, and for the study of low-lying vibrations such as the polar ferroelectric soft modes which are difficult to access using IR [130, 131, 132].

5.1.1 Optical spectroscopy

The space-time dependent polarization P_{ind} induced in a material irradiated by a laser with an incident electric field $E \propto e^{-i\omega t}$ is given by:

$$\vec{P}_{ind} = \vec{P}^{(1)} + \vec{P}^{(2)} + \ldots = \alpha\vec{E} + \frac{1}{2}\beta\vec{E}\vec{E} + \ldots \tag{5.1}$$

where α and β are the first- and second-order polarizability tensors respectively. The total polarization of the material is $\vec{P} = \vec{P}^{(0)} + \vec{P}_{ind}$, where $\vec{P}^{(0)} = \vec{\mu}$ is the permanent dipole moment of the material. The modulation of the polarizabilities by the vibrational modes of normal coordinate Q leads to the modulation of $\vec{P}$. For a given mode η, we can define

the infrared dipole moment, and the Raman and the hyper-Raman polarizability tensors as $\vec{\mu}^{\eta} = [\partial\vec{\mu}/\partial Q_{\eta}]$, $\alpha^{\eta} = [\partial\alpha/\partial Q_{\eta}]$ and $\beta^{\eta} = [\partial\beta/\partial Q_{\eta}]$, respectively.

5.1.2 Phenomenological treatment of HRS

The HRS intensity relates to the space and time fluctuations of the first non-linear term in the expansion of the electrical polarization (equation (5.1)) $P_i^{(2)} \propto \beta_{ijk}E_jE_k$. In other words, HRS is a three photon process where two incident photons produce one scattered photon after interaction with an elementary excitation in the material (*e.g.* vibration or relaxation motions).

The dependence of the hyperpolarizability tensor on the normal coordinate Q_{η} can be written as follows:

$$\beta_{ijk} = \beta^0_{ijk} + (\partial\beta_{ijk}/\partial Q_{\eta})_0 Q_{\eta} + \ldots, \tag{5.2}$$

where β^0_{ijk} is a time-independent term producing the second harmonic generation (SHG) and $R^{\eta}_{ijk} = \partial\beta_{ijk}/\partial Q_{\eta}$ is the hyper-Raman tensor of the mode η.

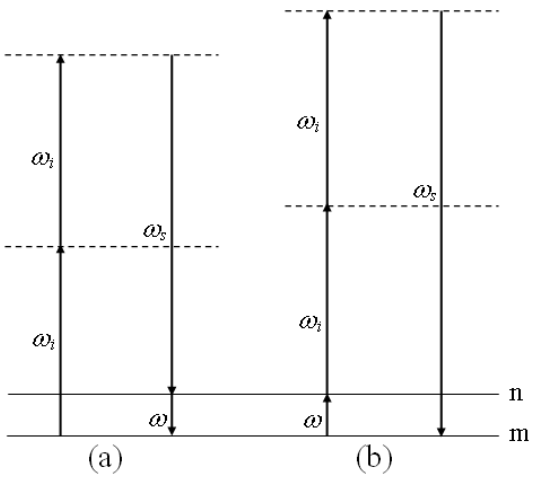


Figure 5.1: The Stokes (a) and anti-Stokes (b) hyper-Raman scattering energy-conservation diagrams.

For an incident electric field $\vec{E} = \vec{E}_0 \cos\omega_i t$ and an harmonic motion of the normal coordinate $Q = Q_0 \cos\omega t$, $P_i^{(2)}$ develops [128]:

$$\begin{aligned} P_i^{(2)} = {} & \tfrac{1}{4}\beta^0_{ijk}E_{0j}E_{0k} + \tfrac{1}{4}\beta^0_{ijk}E_{0j}E_{0k}\cos 2\omega_i t + \tfrac{1}{4}(\partial\beta_{ijk}/\partial Q_{\eta})_0 Q_{0\eta}E_{0j}E_{0k}\cos\omega t + \\ & \tfrac{1}{8}(\partial\beta_{ijk}/\partial Q_{\eta})_0 Q_{0\eta}E_{0j}E_{0k}\cos(2\omega_i - \omega)t + \tfrac{1}{8}(\partial\beta_{ijk}/\partial Q_{\eta})_0 Q_{0\eta}E_{0j}E_{0k}\cos(2\omega_i + \omega)t, \end{aligned} \tag{5.3}$$

The hyper-Rayleigh scattering of frequency $2\omega_i$ is represented by the second term in equation (5.3), while the Stokes and anti-Stokes HRS are represented by the fourth and the fifth terms respectively. The energy-conservation diagrams of the hyper-Raman Stokes scattering at frequency $2\omega_i - \omega$ (fourth term) and the hyper-Raman anti-Stokes scattering

at frequency $2\omega_i + \omega$ (fifth term) are shown in Figure 5.1. For HRS, the law of conservation of energy relates the incident frequency ω_i, the scattered frequency ω_s and the vibrational frequency ω while momentum conservation relates the incident wave-vector $\vec{k}_i$, the scattered wave-vector $\vec{k}_s$ and the phonon wave-vector $\vec{q}$ as follows

$$\begin{cases} 2\omega_i = \omega_s \pm \omega \\ 2\vec{k}_i = \vec{k}_s \pm \vec{q} \end{cases} \tag{5.4}$$

5.1.3 Lattice dynamics of polar modes

Assume an external force $F(t)$ which couples to the amplitude $W(\vec{r})$ of the excitation whose power spectrum is investigated. The Fourier transform of $F(t)$, $F(\omega)$, relates to the average of the Fourier component $W(\vec{q},\omega)$ by [133]:

$$W(\vec{q},\omega) = T(\vec{q},\omega)F(\omega), \tag{5.5}$$

where $T(\vec{q},\omega)$ is called the linear response function. In this equation, $F(t)$ and $W(r)$ are "conjugated" so that $F(t)W(r)$ has the dimension of an energy density. Thus $F(\omega)$ does not in general have the dimension of force; it is regarded as generalized force. If the perturbation $F(\omega)$ originates from an incident electric field $\vec{E}$, then W associates with the electrical polarization $\vec{P}$, and $T(\vec{q},\omega)$ is either the first-order susceptibility $\chi^{(1)}$ (Raman scattering), or the second-order susceptibility $\chi^{(2)}$ (hyper-Raman scattering).

The fluctuation dissipation theorem proved in Landau and Lifshitz [134] relates the scattering cross-section to the imaginary part of the response function:

$$\langle W^*(\vec{q})W(\vec{q})\rangle_\omega = \frac{\hbar}{\pi}\left[n(\omega)+1\right]\mathrm{Im}\ T(\vec{q},\omega). \tag{5.6}$$

The brackets $\langle ... \rangle_\omega$ defines the power spectrum of W. Following the notation of Hayes and Loudon [133], we have:

$$\langle W^*(\vec{q})W(\vec{q})\rangle_\omega \delta(\omega-\omega') = \langle W^*(\vec{q},\omega)W(\vec{q},\omega')\rangle\,, \tag{5.7}$$

where the average is taken over the probability distribution at thermal equilibrium. The two quantities in the brackets in the right-hand side of equation (5.7) are independent random variables whose phases take all values between 0 and 2π. Their product therefore has a zero average except in the case $\omega = \omega'$. The Bose-Einstein factor $[n(\omega)+1]$ in equation (5.6) is replaced by $n(\omega)$ for the anti-Stokes scattering with:

$$n(\omega) = \frac{1}{e^{\frac{\hbar\omega}{k_B T}} - 1}, \tag{5.8}$$

where k_B is Boltzmann's constant.

A simple illustration of the calculation of a linear response function is provided by a molecular vibration σ of amplitude W_σ, natural frequency ω_σ and damping Γ_σ. In that case, the equation of motion writes:

$$\ddot{W}_\sigma + \Gamma_\sigma \dot{W}_\sigma + \omega_\sigma^2 W_\sigma = f(\omega) \tag{5.9}$$

For N identical molecules in the scattering medium, the generalized force $F(\omega)$ writes

$$F(\omega) = N f(\omega), \tag{5.10}$$

and $T(\vec{q}, \omega)$ takes the form of a damped harmonic oscillator:

$$T(\vec{q}, \omega) = \frac{1}{N(\omega_\sigma^2 - \omega^2 - i\omega\Gamma_\sigma)}, \tag{5.11}$$

Thus:

$$\text{Im } T(\vec{q}, \omega) = \frac{\omega\Gamma_\sigma}{N\left[(\omega_\sigma^2 - \omega^2)^2 + \omega^2\Gamma_\sigma^2\right]}. \tag{5.12}$$

The dielectric properties of a polar crystal are described by its linear (and non-linear) susceptibility χ which determines the polarization according to:

$$P_i = \epsilon_0 \chi_{ij}(\omega) E_j + ... \tag{5.13}$$

where ϵ_0 is the permittivity of vacuum.

The total polarization in the crystal separates into an ionic and an electronic contribution. For an applied electric field of frequency ω, the harmonic oscillator equation is similar to equation (5.9) with a force induced on the oscillator of the form $F_i(\omega) = Z_\sigma \xi_{i,\sigma} E_i$, where Z_σ is the effective charge of the normal mode σ, and $\vec{\xi}_\sigma$ is a unit vector parallel to the polarization generated by the mode of amplitude W_σ.

If ω is in the vicinity of the vibrational frequencies, that is well below the frequency of all electronic transitions, the frequency dependence of the dielectric constant only arises from that of the total ionic polarization, $P_{i,ion} = \sum_\sigma Z_\sigma \xi_{i,\sigma} W_\sigma / V_0$, where V_0 is the unit-cell volume:

$$\epsilon_i = \epsilon_{i,\infty} + \sum_\sigma \frac{Z_\sigma^2 \xi_{i,\sigma} r / \epsilon_0 V_0}{\omega_\sigma^2 - \omega^2 - i\omega\Gamma_\sigma}, \tag{5.14}$$

However, polar modes produce a lattice polarization which in turn generate a macroscopic electric field. With $\vec{E}$ henceforth taken to represent the macroscopic electric field of the polar modes, the equation of motion (5.9) continues to hold, but with a different expression for the term in the right hand side. This term can be obtained considering that

both $\vec{E}$ and $\vec{P}$ should satisfy Maxwell's equations.

Using the constitutive relations between $\vec{E}$ and $\vec{P}$, the equation of motion in the absence of damping transforms into:

$$\ddot{W}_\sigma + \omega_\sigma^2 W_\sigma = -\frac{Z_\sigma(\vec{q}.\vec{\xi_\sigma}) \sum_\tau Z_\tau(\vec{q}.\vec{\xi_\tau}) W_\tau}{\epsilon_0 V_0 \left(\epsilon_{x,\infty} q_x^2 + \epsilon_{y,\infty} q_y^2 + \epsilon_{z,\infty} q_z^2\right)}, \tag{5.15}$$

where the sum is over all polar modes τ .

This equation shows that non-polar modes ($Z_\sigma = 0$) and transverse modes ($\vec{q}.\vec{\xi_\tau} = 0$) have no associated macroscopic electric field; the right-hand side of equation (5.15) is zero and the ω_σ give the correct vibrational frequencies. The right-hand side of equation (5.15) is non-zero for polar modes ($Z_\sigma \neq 0$) that are not transverse ($\vec{q}.\vec{\xi_\tau} \neq 0$). In this case, the macroscopic electric field associated with such modes couples with their normal coordinates. For example, for a scattering experiment along a general wave vector direction, the right-hand side of equation (5.15) couples modes whose polarization vectors point along all three of the principal axes, producing excitations of mixed symmetry character.

Another situation leading to a coupling between the macroscopic electric field and the normal coordinates arises from the scattering by longitudinal optic (LO) vibration. To illustrate the consequence of the effect of the macroscopic electric field on LO modes, we will consider the simple situation of a cubic crystal. For any direction of the wave vector of a three-fold degenerated polar mode, it is possible to choose two of the polarization vector $\vec{\xi}_\sigma$ perpendicular to $\vec{q}$ and the third $\vec{\xi}_\sigma$ parallel to $\vec{q}$.

As shown above, the two transverse modes have a frequency ω_σ determined by the standard lattice-dynamic calculations, but that of the LO of any trio is changed by the associated macroscopic electric field. For a cubic crystal having a single three-fold polar mode, the dielectric constant has an isotropic form:

$$\epsilon = \epsilon_\infty + \frac{Z^2/\epsilon_0 V_0}{\omega_{\mathrm{T}}^2 - \omega^2 - i\omega\Gamma_{\mathrm{T}}}, \tag{5.16}$$

where ω_{T} is the frequency of the TO mode.

In the absence of damping, the frequency of the LO component is given by the Lyddane-Sachs-Teller relation[1]:

$$\omega_{\mathrm{L}} = \left(\frac{\epsilon(0)}{\epsilon_\infty}\right)^{1/2} \omega_{\mathrm{T}}, \tag{5.17}$$

[1]For LO modes ($\vec{q} \parallel \vec{\xi}_\sigma$)of cubic crystals, the Fresnel equation derived from the Maxwell's equations applied to $\vec{P}$ and $\vec{E}$ simply reduces to $\epsilon = 0$ ($cq >>> \omega$).

where $\epsilon(0)$ is the zero-frequency value of the relative permittivity. The equation of motion (5.15) for longitudinal mode takes the form:

$$\ddot{W} + \omega_{\mathrm{T}}^2 W = -\frac{Z^2 W}{\epsilon_0 V_0 \epsilon_\infty} = Z E_{macroscopic} \tag{5.18}$$

leading to

$$\omega_{\mathrm{L}}^2 = \omega_{\mathrm{T}}^2 + \frac{Z^2}{\epsilon_0 V_0 \epsilon_\infty}, \tag{5.19}$$

The relative permittivity can thus be written in the compact form:

$$\epsilon = \epsilon_\infty \left\{ 1 + \frac{\omega_{\mathrm{L}}^2 - \omega_{\mathrm{T}}^2}{\omega_{\mathrm{T}}^2 - \omega^2 - i\omega\Gamma_{\mathrm{T}}} \right\}, \tag{5.20}$$

The effect of the macroscopic electric field is thus to lift the group-theoretical degeneracy of polar modes, producing a non-degenerate longitudinal vibration which lies at a higher frequency than the doubly degenerate transverse vibration.

Similar arguments apply to crystals having more than one polar-mode triplet. Each polar vibration splits into a transverse doublet and a longitudinal singlet. According to Cochran and Cowley [135], the LST relation (equation (5.17)) generalizes to:

$$\prod_{\mathrm{L}} \omega_{\mathrm{L}}^2 = \frac{\epsilon(0)}{\epsilon_\infty} \prod_{\mathrm{T}} \omega_{\mathrm{T}}^2, \tag{5.21}$$

all polar modes being included in the products. The relative permittivity in the zero damping limits becomes:

$$\epsilon = \epsilon_\infty \frac{\prod_{\mathrm{L}} (\omega_{\mathrm{L}}^2 - \omega^2)}{\prod_{\mathrm{T}} (\omega_{\mathrm{T}}^2 - \omega^2)}, \tag{5.22}$$

a form that shows that the longitudinal frequencies associate with zeros in $\epsilon(\omega)$, while the transverse frequencies correspond to poles in the undamped limit. This can be seen from the variation of the real part η and the imaginary part κ of the complex refractive index $n = \eta - i\kappa$ as a function of ω (Figure 5.2).

5.1.4 Hyper-Raman scattering cross-section

The spectral HRS efficiency S_{HR} (also known as the differential scattering cross-section per unit volume) for a phonon mode can be written as [130, 131]

$$S_{HR} = \left(\frac{\omega_S}{c}\right)^4 \frac{V}{(4\pi\epsilon_0)^2} \frac{\left\langle \left| \vec{e}.\vec{P}^{NL} \right|^2 \right\rangle_{\omega_s}}{\left| \vec{E}_L \right|^2}, \tag{5.23}$$

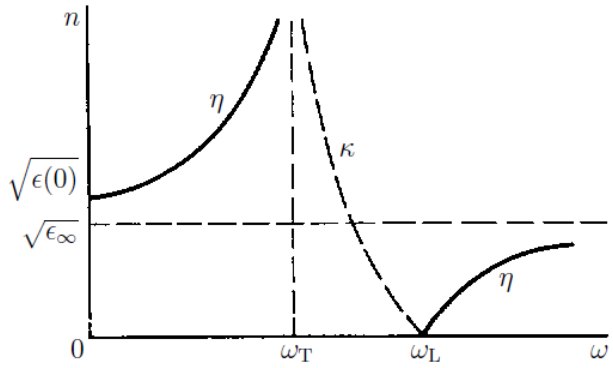


Figure 5.2: The theoretical dispersion curve of the complex refractive index of an isotropic medium in the zero damping limit.

where ω_S is the outgoing photon frequency, c is the speed of light in vacuum, V is the scattering volume, $\vec{P}^{NL}$ is the nonlinear polarization representing the source of the scattered light, $\vec{e}$ is a unit vector along the scattered field, and $\vec{E}_L$ is the amplitude of the electric field of the incident laser radiation. The term in brackets denotes the power spectrum of $\vec{P}^{NL}$, as defined in equation (5.7).

For the case of one-phonon scattering, $\vec{P}^{NL}$ is given by [130]

$$\vec{P}^{NL} = \frac{1}{2}\sum_{j,k}\left(\sum_{\eta}(\partial\beta_{ijk}/\partial Q_\eta)Q_\eta + \sum_{m}(\partial\beta_{ijk}/\partial E_m)E_m\right)(E_L)_j(E_L)_k, \tag{5.24}$$

where $\vec{E}$ is the electric field associated with the longitudinal optical phonons.

Combining equations (5.23) and (5.24), keeping in mind that $\partial\beta_{ijk}/\partial Q_\eta$ is the HRS tensor, we can write the differential scattering cross-section per unit volume S_{HR} by a phonon mode as [132]

$$S_{HR} = I_L\frac{2\pi}{c\sqrt{\epsilon_\infty}}\frac{1}{(4\pi\epsilon_0)^2}\left(\frac{\omega_S}{c}\right)^4\frac{V}{N}\frac{\hbar}{2\omega}[n(\omega)+1]Y(\omega)R^2, \tag{5.25}$$

with

$$R^2 = \sum_{\delta}|e_i^S R_{ijk}^{\delta} e_j^L e_k^L|^2, \tag{5.26}$$

where I_L is the exciting laser intensity (power flux), N is the number of unit cells within the scattering volume V, ω is the frequency shift related to the incident frequency ω_i and the scattered frequency ω_S through $\omega = 2\omega_i - \omega_S$, $\sqrt{\epsilon_\infty}$ is the refractive index near ω_i, $n(\omega)$ stands for the Bose-Einstein population number and $Y(\omega)$ for a normalized response function of the phonon mode under consideration.

The factor R^2 defined in equation (5.26) describes the dependence of S_{HR} on the scattering geometry described by the cartesian components of polarization vectors of the incident

(Laser) and detected (Scattered) photons $\vec{e}^L$, $\vec{e}^S$. The summation index δ distinguishes independent eigenvectors in case of degenerate modes, and R^δ_{ijk} stands for the elements of the so-called HRS tensor of third rank associated with given phonons.

The HRS tensor of a TO phonon can be written as the derivative of the second-order or second-harmonic-generation susceptibility $\chi^{(2)}$ with respect to the normal coordinate Q;

$$R^\delta = \frac{\partial \chi^{(2)}}{\partial Q^\delta} \tag{5.27}$$

For F_{1u} symmetry, the TO phonons are doubly degenerate. δ distinguishes two displacement directions perpendicular to the phonon wave vector $\vec{q}$ as determined by the scattering geometry. The transformation from Q^δ to displacements Q^m parallel to the cubic axes m is provided by directional cosines according to:

$$R^\delta = \sum_{m=1}^{3} R^m \frac{\partial Q^m}{\partial Q^\delta} = R^x \frac{\partial Q^x}{\partial Q^\delta} + R^y \frac{\partial Q^y}{\partial Q^\delta} + R^z \frac{\partial Q^z}{\partial Q^\delta} \tag{5.28}$$

For LO phonons, there is the electro-optic contribution in addition to the deformation-potential contribution. So, the HRS tensor is given by:

$$R^\delta = \frac{\partial \chi^{(2)}}{\partial Q^\delta} + \frac{4\pi N}{\epsilon(\infty) V} Z^L \frac{\partial \chi^{(2)}}{\partial E^\delta} \tag{5.29}$$

In this case, δ indicates the direction of $\vec{q}$, $\vec{E}$ is the macroscopic electric field associated with the LO phonons, $\epsilon(\infty)$ the electronic part of the infrared dielectric function, and Z^L the longitudinal effective charge.

5.1.5 Experimental

HRS experiments are not widely used mainly because the weak HRS efficiency is about 10^6 times weaker than the Raman scattering efficiency. It is only in the last ten years that several recent instrumental advances such as high power pulsed lasers, multichannel photo-counting devices, and large aperture and aberration corrected optical design have opened up the possibility for many new HRS investigations.

Our experiments were performed using a new generation setup, constructed at the "Laboratoire des Colloïdes Verres et Nanomatériaux (LCVN)". It combines high luminosity and high resolution [136, 137, 138]. The optical design is shown in Figure 5.3. The hyper-Raman spectrum is excited by a diode pumped Q-switched Nd-doped yttrium aluminum garnet laser emitting at the wavelength $\lambda = 1.064$ μm. The repetition rates are between 1 Hz and 50 kHz with pulse widths of $\sim$ 30 ns. The incident beam is focused on the sample

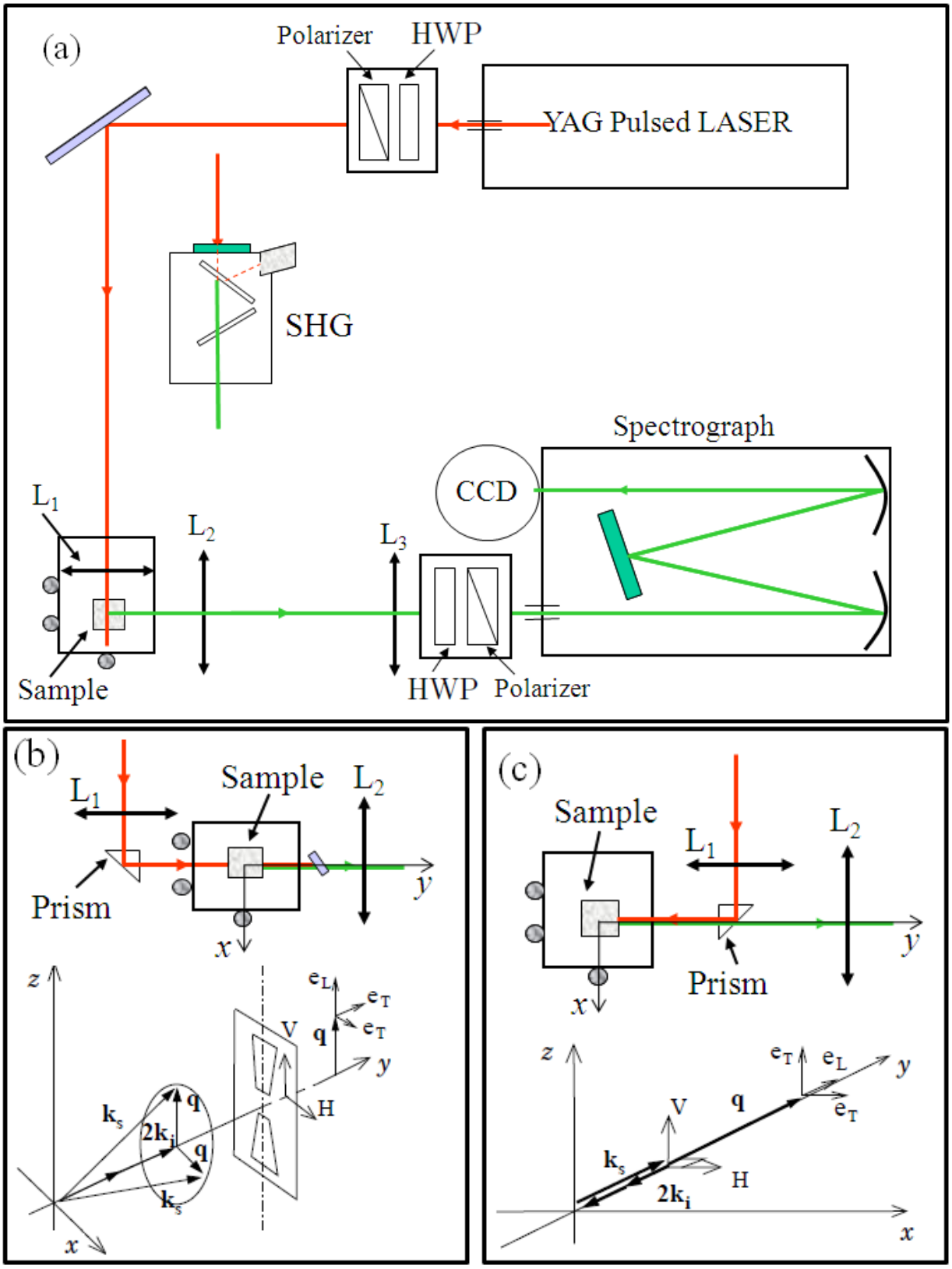


Figure 5.3: Schematic diagram of the HRS setup at the LCVN in 90° scattering (a), near-forward scattering (b), and backscattering geometry (c). The conservation of the linear momentum and the polarization analysis process in near-forward scattering and backscattering geometry are shown in the lower parts of (b) and (c) respectively.

with a lens L_1 of focal length $f_1 = 47$ mm leading to a waist diameter of a few tens of micrometers (~ 20 μm). The scattered light is collected by a photo-objective lens L_2 ($f_2 = 50$ mm) of numerical aperture $N_A = 0.45$ followed by another lens L_3 of focal length $f_3 = 230$ mm. The usual scattering geometries are either 90° scattering (Figure 5.3(a)), near-forward scattering (Figure 5.3(b)) or backscattering (Figure 5.3(c)). The HRS spectra are analyzed with a $f/5.6$ Jobin-Yvon FHR-640 single-grating diffractometer of focal length $f = 640$ mm and detected with a nitrogen-cooled charge-coupled-device camera (CCD) with 2048×512 pixels. Two different gratings with 600 grooves/mm and 1800 grooves/mm can be used. The first one gives a resolution of ~ 6 cm^{-1} [full width at half maximum (FWHM)] using an entrance slit of 100 μm. The grating with 1800 grooves/mm is used for high resolution experiments. It gives a spectral resolution of ~ 2 cm^{-1} (FWHM) for a 100 μm entrance slit.

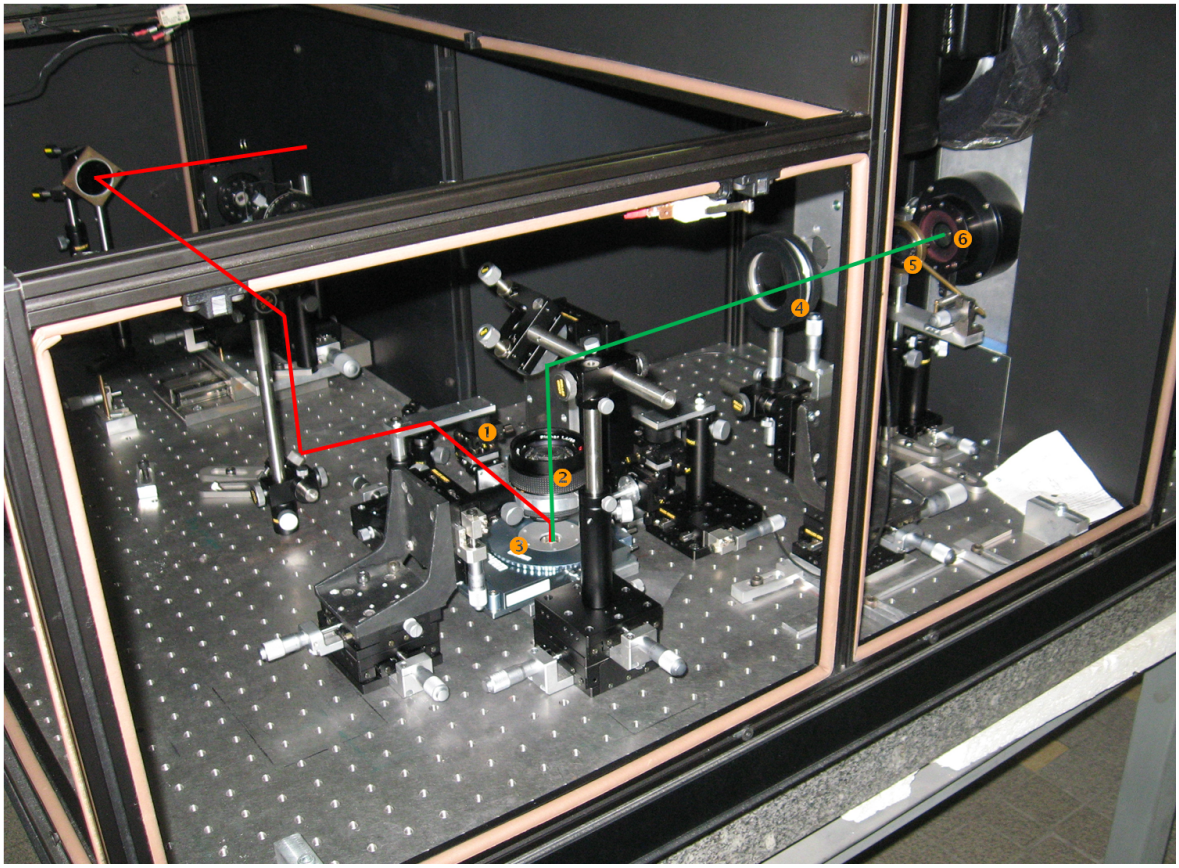


Figure 5.4: High temperature HRS set-up in backscattering geometry. (1) Lens L_1, (2) Lens L_2, (3) Linkam furnace, (4) Lens L_3, (5) sem-rock filter, (6) entrance of the spectrometer.

In a standard experiment, the incident peak power is kept slightly below the optical damage threshold of the sample, which for most of our ferroelectric samples was about 2 kW. The incident light can be polarized vertically (V) or horizontally (H) using a Glan-Thomson polarizer while its intensity is regulated with a $\lambda/2$ half-wave plate (HWP) placed before the polarizer. An equivalent system, composed of a $\lambda/2$ broadband HWP followed by a Glan-Thomson polarizer inserted before the entrance of the spectrometer, can be used to

select the polarization of the scattered light along V or H. Provided the peaks are well defined, this optical set-up allows polarization measurements with a precision greater than 1%.

The insertion of a second harmonic generator (BBO crystal) followed by an IR absorbing filter in the incident beam gives the second-harmonic green light with $\lambda = 0.532\ \mu$m, thus opening the possibility of performing Raman experiments with the same setup. In the case of Raman experiments or HRS experiments in samples with a strong hyper-Rayleigh signal, it is possible to filter the strong elastic line using a band-pass filter (Sem-Rock) with a transmission band of $\sim 80\,\mathrm{cm}^{-1}$.

Temperature dependent measurements can be also performed. Two hot stages (a Linkam THMS600 for $75\,K < T < 850\,K$ and a Linkam THM1500 for $75\,K < T < 1700\,K$) and one cryostat (Microstat Oxford Instrument for $4\,K < T < 300\,K$) are available. The THMS600 mounted in the spectrometer in the backscattering geometry is shown in Figure 5.4. This device gives a temperature stability of $\pm 1\,$K.

5.2 LO Modes in Backscattering Geometry

HRS experiments [136, 139, 140, 141] performed on mixed lead-based perovskite-ferroelectric single crystals show the appearance of LO modes in backscattering with the wave-vector $\vec{q}$ ([001], [110]) where they should be inactive. The observed intensity of the LO modes in PMN [141] and PZT [140] is much higher than that measured in TiO_2 [142] and in $SrTiO_3$ for backscattering resonant HRS experiments [143]. The excess HRS intensity of the LO modes thus appears to be a phenomenon inherent to PMN and related materials.

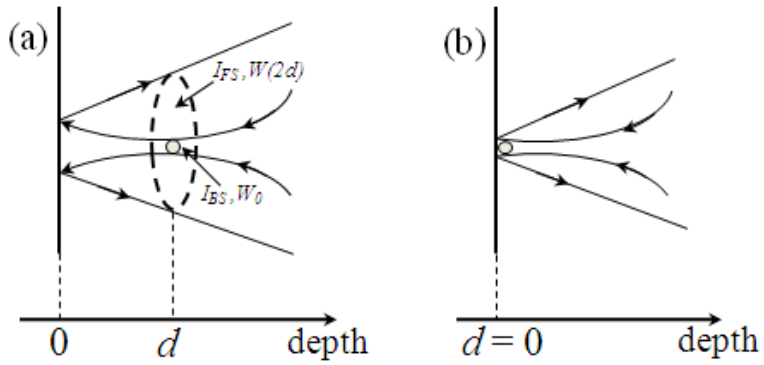


Figure 5.5: A schematic diagram showing the reflection of the incident beam on the back face of the sample.

A possible origin for this excess could be a forward scattering process arising from the reflection of the incident beam on the back face of the sample as sketched in Figure 5.5. Indeed the refractive index of PMN is very high, $n \approx 2.5$ and it leads to a reflectivity R

of about 18% at normal incidence. Since the scattering from LOs in near-forward is very efficient, this additional contribution could naturally explain the unexpected LO intensities observed in backscattering.

In order to clarify this issue, we decided to measure the LO activity in function of the position of the scattering volume in the sample. The experiment has been performed in a 1 mm thick sample with a large surface of 4×4 mm^2 perpendicular to $\vec{k}_i$, thus preventing possible scattering artifacts arising from the side faces. The two strongest peaks around 400 and 700 cm^{-1} in Figure 5.6(a) correspond to the LO2 and LO3 modes, respectively. The peak at ~ 248 cm^{-1} will be discussed in the next chapter. It has been assigned to the "silent" F_{2u} vibration. As a non-polar excitation, its intensity is expected to be the same in forward and backscattering and it is thus possible to normalize all the spectra on the top of this band. Doing so, one clearly observes a strong increase of the intensity when the scattering volume approaches the back face of the sample (Figure 5.6(b)). This is the situation where the flux collected by the spectrometer coming from the forward process (Figure 5.5(b)) is maximum and therefore supports the assumption of an additional contribution to the backscattering HRS arising from a near-forward scattering.

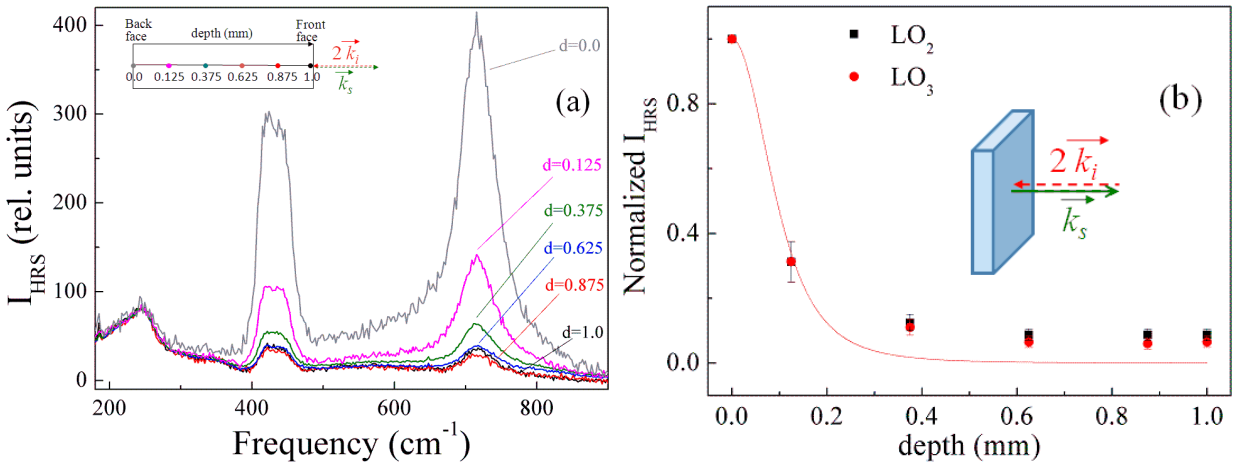


Figure 5.6: (a) HRS spectra of $PbMg_{1/3}Nb_{2/3}O_3$ crystal measured at different positions of the scattering volume in backscattering. (b) The normalized intensity of the LO2 and LO3 modes of PMN as a function of the depth inside the 1 mm sample. The red line corresponds to a fit with equation (5.33).

It is possible to evaluate this parasitic contribution. Assuming that the image of the beam waist completely passes through the slit of the spectrometer, the HRS intensity can be written as [128]:

$$I \sim \beta^2 \frac{I_0^2}{S^2} V \approx \beta^2 I_0^2 \frac{L}{S}, \tag{5.30}$$

where β is the hyperpolarizability, I_0 is the incident intensity and V is the scattering volume with $V \approx LS$. L and S are the depth of the field and the section of the beam waist

respectively. At the beam waist, W_0, both L and S are proportional to W_0^2 so that

$$I \propto \beta^2 I_0^2, \tag{5.31}$$

The dependence of the spot diameter $W(z)$ of a focused beam as a function of the distance z is given by [144]:

$$W^2(z) = W_0^2 \left(1 + \left(\frac{\lambda z}{\pi W_0^2}\right)^2\right), \tag{5.32}$$

where λ is the wavelength of the incident beam.

Using equations (5.31) and (5.32) and looking at Figure 5.5, one sees that the HRS intensity ratio $\frac{I_{FS}}{I_{BS}}$ between forward at $W(z) = W(2d)$ and backscattering at W_0 simply writes:

$$\frac{I_{FS}}{I_{BS}} = \left(\frac{S_{BS}}{RS_{FS}}\right)^2 = \left(\frac{W_0^2}{RW^2(2d)}\right)^2 = \frac{1}{R^2\left[1 + \left(\frac{2\lambda d}{\pi W_0^2}\right)^2\right]^2}, \tag{5.33}$$

where R is the reflectivity of the back face.

The red line in Figure 5.6(b) shows the results of a fit with equation (5.33). For high values of d, the LO intensity is larger than the value predicted by this model. We have complemented these data by HRS along [110] in a sample of 4 mm depth but with thin surface (1×4 mm^2) perpendicular to the incident beam. The two series of data are coupled in Figure 5.7. Owing to a lower quality of the back face in the second sample, the second set of data has been scaled to the first one. The result of the fit confirms that equation (5.33) cannot account for the LO intensities far from the back face of the sample. To reproduce this effect, we have introduced a constant value b to the intensity given in equation (5.33) and a normalization factor a, leading to

$$\frac{I_{FS}}{I_{BS}} = a \times \left[\frac{1}{R^2\left[1 + \left(\frac{2\lambda d}{\pi W_0^2}\right)^2\right]^2} + b\right], \tag{5.34}$$

The modified expression gives a much better agreement (blue line in Figure 5.7) and brings us to the conclusion that although a part of the LO mode backscattering intensity may actually arise from events involving a near-forward HRS scattering induced by the reflection of the incident beam on the back face of the sample, still the existence of an intrinsic phenomenon that lifts selection rules for HRS by LO modes is presumably active [141].

It could naturally originate from a departure of the local structure from cubic symmetry. In that case, the wave-vector $\vec{q}$ is no longer parallel to [110] but integrates over arbitrary directions of the nano-crystallites, thus allowing HRS by LOs in backscattering. Even for the situation where the LOs are the weakest, their intensity is still much stronger than that of the TO2 and TO3 and prevents clear observation of the TOs at least in PMN (inset of Figure 5.7).

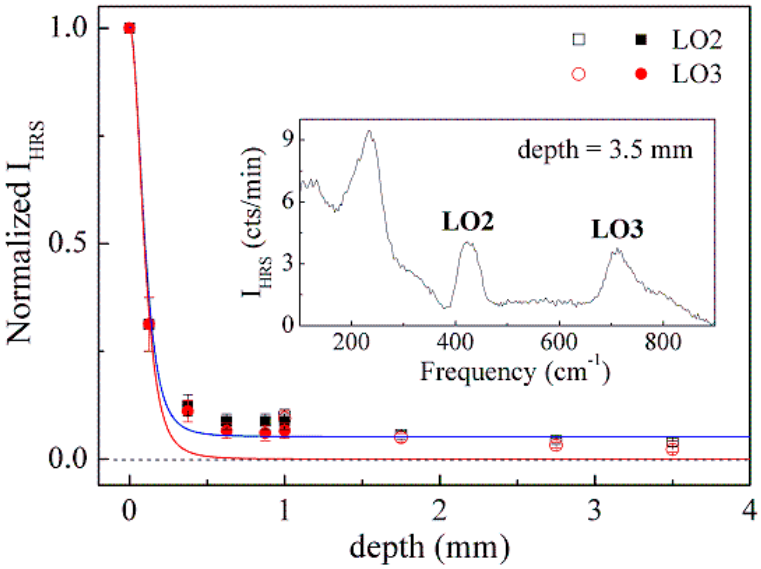


Figure 5.7: The normalized intensity of the LO2 and LO3 modes of PMN in backscattering as a function of the depth in 1 mm (full symbols) and 4 mm (open symbols) sample. The red and blue lines are fits using equations (5.33) and (5.34) respectively. The inset shows the HRS spectra obtained near the front face of the 4 mm sample where the LO intensity is minimum.

Chapter 6

Hyper-Raman Scattering of Typical Ferroelectric Relaxors

6.1 Introduction

The lattice dynamics of ferroelectric relaxors is still the subject of many theoretical and experimental investigations. In addition to the usual structural techniques, spectroscopic methods sensitive to vibrational modes are widely used to elucidate phase transition mechanisms. Numerous studies have been already performed using inelastic neutron scattering (INS) [145, 146, 147, 148], Raman scattering (RS) [149, 150, 151, 152] and infrared reflectivity (IR) [153, 154, 155]. Owing to the local disorder, it is not possible yet to disentangle the numerous vibrational bands observed in the inelastic scattering spectra of relaxors. For example, PMN has an average cubic structure with $Pm\bar{3}m$ space group. The irreducible representation of the modes is written:

$$3F_{1u} + F_{2u}, \tag{6.1}$$

where the triply degenerated F_{1u}-symmetry vibrations are polar and the triply degenerated F_{2u}-symmetry mode is non-polar and involves only the oxygen atoms. The eigenvectors of the vibrations are represented in Figure 6.1. The three F_{1u} vibrations are referred as 'Last', 'Slater' and 'Axe'. In classical ferroelectrics, the lowest frequency mode (soft mode) is either the Slater mode ($BaTiO_3$, $SrTiO_3$, $KNbO_3$) or the Last mode (lead-based perovskites), and it is generally the Last mode in lead-based relaxors. Following the selection rules of the $Pm\bar{3}m$ space group, all these modes are inactive in RS. On the contrary, the Raman spectra of PMN exhibits a series of broad bands associated with the first-order scattering (Figure 6.2) which clearly arise from the local vibrations of the randomly distorted structure. The quantitative interpretation of the experimental data usually requires taking into account the short- or medium-range inhomogeneities of the structure, associated for example with B-site "chemical" ordering and/or the "polar nanoregions" PNR. The Raman spectra have also been reported by many other groups [156, 157, 158] but still the interpretation of the

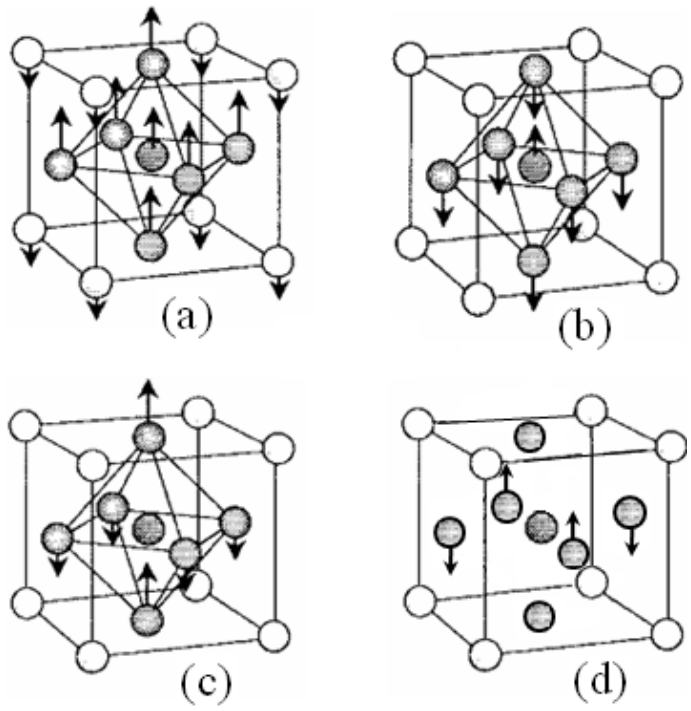


Figure 6.1: Eigen-displacements (normal coordinates) of (a) Last, (b) Slater, (c) Axe and (d) the non-polar F_{2u} zone-center modes in lead-based perovskites.

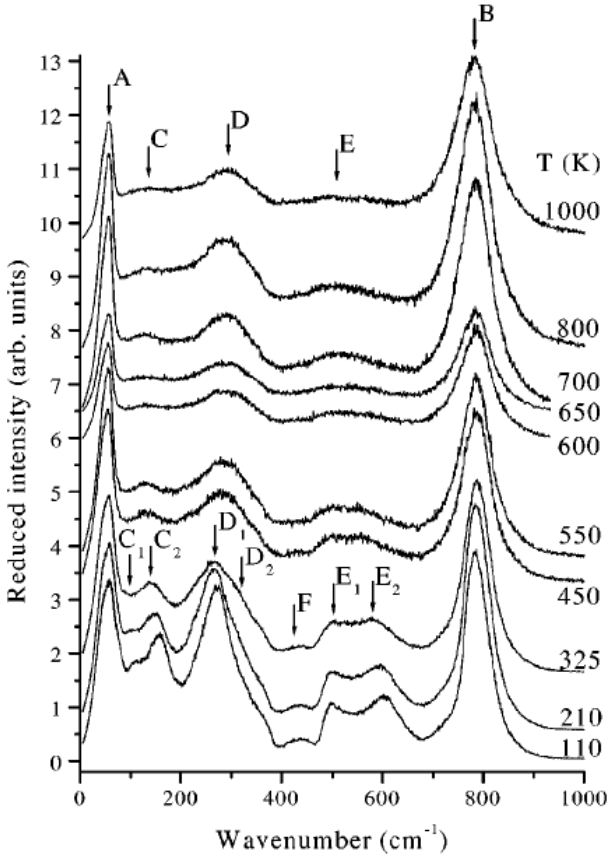


Figure 6.2: Raman spectra of $PbMg_{1/3}Nb_{2/3}O_3$ crystal at various temperatures. Source: O. Svitelskiy [149].

different spectral lines is not unique owing to the site disorder, the presence of chemically ordered regions, and the off-center ionic displacements. It is worth noting that the appearance of the Raman lines up to very high temperature [149] is an evidence of the persistence of this local disorder well above the Burns temperature T_d.

INS experiments are used to study the "soft" phonon branch related to the lowest frequency transverse optic TO mode. It gave the first evidence that these modes woe softening at intermediate temperatures [146, 159] (Figure 6.3). This dynamical behavior of the low frequency modes has also been observed by far-infrared spectroscopy [160, 161]. The results on the vibration of lowest frequency observed in INS and far-IR on PMN are summarized in Figure 6.3(b). However the strong anharmonic effects, the coupling with acoustic modes, and the diffuse scattering contributions complicate the analysis of the soft-mode. Finally, IR spectroscopy probes polar modes only. It was shown that the IR reflectivity spectra of PMN in the phonon-frequency region can be interpreted as due to the three F_{1u} modes. A splitting of the polar F_{1u} modes into E_1 and A_1 vibrations was observed, and explained as due to the local dielectric anisotropy, most likely associated with local polar order [153] (Figure 6.4).

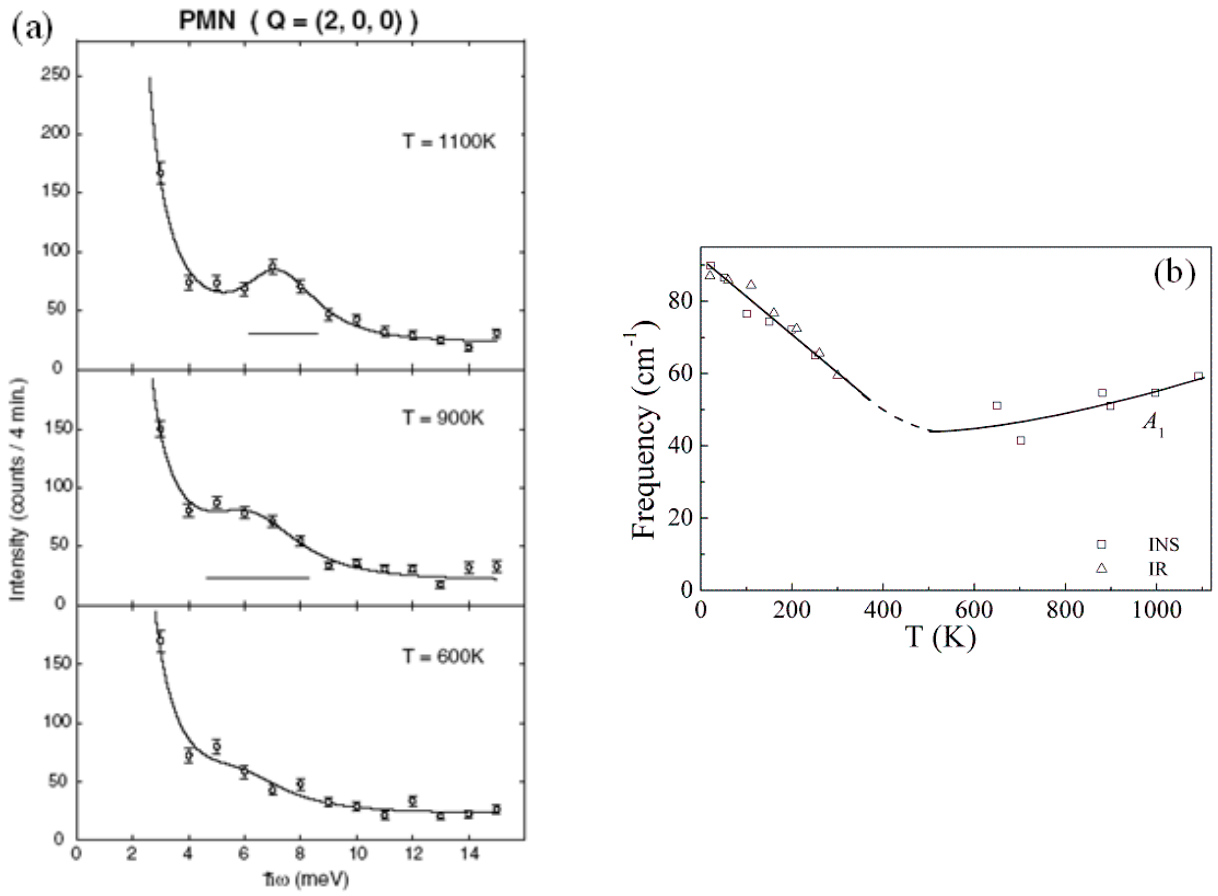


Figure 6.3: (a) INS spectra measured at the zone center at $Q = (2, 0, 0)$ from 1100 K (above T_d) down to 600 K (near T_d). (b) Temperature dependence of A_1 frequency obtained from the INS data of Refs. [146, 159] and IR of Ref. [160].

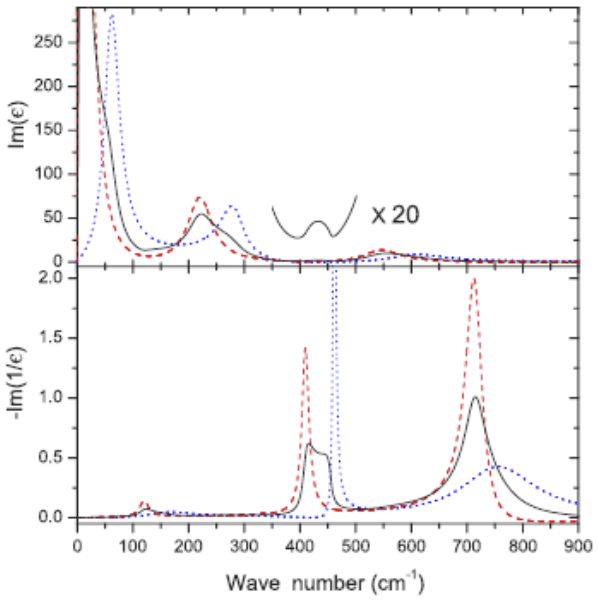


Figure 6.4: Spectra of the imaginary part of the permittivity (top panel) and of the calculated imaginary part of the inverse permittivity (lower panel). Solid line corresponds to the effective macroscopic permittivity ϵ_{eff}, dashed and dotted lines correspond to the $\epsilon_{\perp}$ and $\epsilon_{\parallel}$ components of the local permittivity, respectively [153].

In this work, hyper-Raman scattering (HRS) is used to study phonons in the ferroelectric relaxors PMN, PMT, and PZN. HRS constitutes a powerful experimental tool that can probe polar and non-polar excitations and that gives details about the spectral shape down to frequencies of a few cm^{-1}. These unique characteristics provide an alternative way to study the behavior of the vibrational spectra of relaxors in function of temperature, especially for the low frequency soft-modes.

6.2 F_{2u} Mode of PMN

The $3\,F_{1u} + 1\,F_{2u}$ zone-center optic modes of the parent $Pm\bar{3}m$ cubic group of PMN are not allowed in first-order Raman spectra. Infrared spectroscopy allows the study of the F_{1u} modes, but not of the "silent" nonpolar F_{2u} mode. On the other hand, all of these modes are allowed by symmetry in first-order HRS [139].

The silent F_{2u} mode being non-polar, it has no LO-TO splitting and the electro-optic mechanism does not contribute to its strength in HRS spectra. In a previous HRS study of pure PMN, Hehlen *et al.* [141] have indeed found a vibrational mode at a frequency near $250\,\text{cm}^{-1}$ and with depolarization ratio that conforms to the F_{2u} symmetry. To confirm our assignment and verify the applicability of the symmetry selection rules, we recorded a number of polarized HRS spectra in various geometries designed to probe independently phonon modes propagating along [001], [110] and [111] crystallographic directions.

The F_{2u} mode is unique as its eigenvector corresponds solely to the bending of oxygen octahedra [139]. Since no cation displacements are involved, changes in its frequency with temperature or B-site substitutions must be related to a change in force constants, as the eigenvector and effective mass remain preserved. Interestingly, recent HRS measurements in $Pb(Mg_{1/3}Nb_{2/3})_{0.73}Ti_{0.27}O_3$ (PMN-27PT) suggested that the F_{2u} mode might drastically soften [139] near $T_0 = 570\,K$, which is close to the Burns temperature T_d [39, 162, 163]. It was then speculated that the competing F_{2u} order parameter can contribute to the suppression of long-range polar order in relaxors [139]. The two characteristic temperatures above the temperature of the dielectric anomaly T_m in PMN are T^* and T_d, which should be near 500 K and 630 K respectively. Therefore, we carried out high temperature measurements with the aim to follow the frequency of the F_{2u} vibrational mode in PMN up to the Burns temperature.

6.2.1 Theoretical background

In the case of cubic $Pm\bar{3}m$ crystal symmetry, the elements of the F_{1u}-mode HRS tensor can be written using the standard abbreviated notation ($a = R^x_{111}, b = R^x_{122}, b' = R^x_{212}$) as [132, 136]

$$\begin{aligned} R^x(F_{1u}) &= \begin{pmatrix} a & b & b & 0 & 0 & 0 \\ 0 & 0 & 0 & 0 & 0 & b' \\ 0 & 0 & 0 & 0 & b' & 0 \end{pmatrix}, \\ R^y(F_{1u}) &= \begin{pmatrix} 0 & 0 & 0 & 0 & 0 & b' \\ b & a & b & 0 & 0 & 0 \\ 0 & 0 & 0 & b' & 0 & 0, \end{pmatrix}, \\ R^z(F_{1u}) &= \begin{pmatrix} 0 & 0 & 0 & 0 & b' & 0 \\ 0 & 0 & 0 & b' & 0 & 0 \\ b & b & a & 0 & 0 & 0 \end{pmatrix}. \end{aligned} \tag{6.2}$$

Similarly, the HRS tensor of the silent F_{2u} phonon mode reads ($c = R^x_{122}, c' = R^x_{212}$)

$$\begin{aligned} R^x(F_{2u}) &= \begin{pmatrix} 0 & c & -c & 0 & 0 & 0 \\ 0 & 0 & 0 & 0 & 0 & c' \\ 0 & 0 & 0 & 0 & -c' & 0 \end{pmatrix}, \\ R^y(F_{2u}) &= \begin{pmatrix} 0 & 0 & 0 & 0 & 0 & -c' \\ -c & 0 & c & 0 & 0 & 0 \\ 0 & 0 & 0 & c' & 0 & 0, \end{pmatrix}, \\ R^z(F_{2u}) &= \begin{pmatrix} 0 & 0 & 0 & 0 & c' & 0 \\ 0 & 0 & 0 & -c' & 0 & 0 \\ c & -c & 0 & 0 & 0 & 0 \end{pmatrix}. \end{aligned} \tag{6.3}$$

The cartesian reference system assumed in equations (6.2) and (6.3) is the one associated with the cubic crystallographic axes x, y, z, and also the matrices R^x, R^y, R^z for the F_{1u} mode corresponding to the components associated with the dipolar moment along the x, y, z, respectively [132]. Owing to the LO-TO splitting of F_{1u} polar modes, it is usually necessary to consider separately the tensors describing the LO mode and the tensors belonging to the TO-mode doublet. The corresponding tensors are calculated from those of equation (6.2) using directional cosines of the phonon wave vector as shown for example in Ref [132]. To describe the various scattering geometries, we use the usual Porto notation $a(bc)d$ where a and b stand for the propagation and polarization directions of the two incident photons, and d and c stand for the outgoing photon propagation and polarization directions. According to equations (5.29), (6.2), and (6.3), we show below the calculation of $R^2_{TO}(F_{1u})$, $R^2_{LO}(F_{1u})$ and $R^2(F_{2u})$ in the case of $z(xx)\bar{z}$, that is with $q \parallel [001]$. The calculation of R^2 for other polarization geometries is detailed in Appendix B.

For the case, $q \parallel [001]$

$$\begin{cases} \vec{e}_{TO1} \parallel [100] \Rightarrow R^{e_{TO1}} = R^x; \\ \vec{e}_{TO2} \parallel [010] \Rightarrow R^{e_{TO2}} = R^y; \end{cases}$$

$$\Rightarrow R^2_{TO} = |e^S R^x e^L e^L|^2 + |e^S R^y e^L e^L|^2$$

and $\vec{e}_{LO} \parallel [001] \Rightarrow R^{e_{LO}} = R^z$;
$\Rightarrow R^2_{LO} = |e^S R^z e^L e^L|^2$

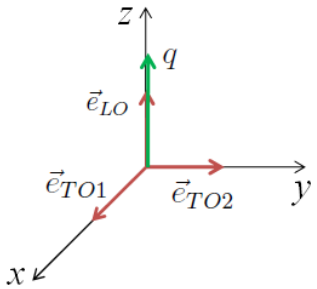


Figure 6.5: $q \parallel [001]$.

For $z(xx)\bar{z}$, $e^S = e^L = [100]$.

$$R^2_{TO}(F_{1u}) = \left| \begin{pmatrix} 1 \\ 0 \\ 0 \end{pmatrix} R^x \begin{pmatrix} 1 \\ 0 \\ 0 \end{pmatrix} \begin{pmatrix} 1 \\ 0 \\ 0 \end{pmatrix} \right|^2 + \left| \begin{pmatrix} 1 \\ 0 \\ 0 \end{pmatrix} R^y \begin{pmatrix} 1 \\ 0 \\ 0 \end{pmatrix} \begin{pmatrix} 1 \\ 0 \\ 0 \end{pmatrix} \right|^2 = (R^x_{111})^2 + (R^y_{111})^2 = a^2$$

$$R^2_{LO}(F_{1u}) = \left| \begin{pmatrix} 1 \\ 0 \\ 0 \end{pmatrix} R^z \begin{pmatrix} 1 \\ 0 \\ 0 \end{pmatrix} \begin{pmatrix} 1 \\ 0 \\ 0 \end{pmatrix} \right|^2 = (R^z_{111})^2 = 0$$

$$R^2(F_{2u}) = \left| \begin{pmatrix} 1 \\ 0 \\ 0 \end{pmatrix} (R^x) \begin{pmatrix} 1 \\ 0 \\ 0 \end{pmatrix} \begin{pmatrix} 1 \\ 0 \\ 0 \end{pmatrix} \right|^2 + \left| \begin{pmatrix} 1 \\ 0 \\ 0 \end{pmatrix} (R^y) \begin{pmatrix} 1 \\ 0 \\ 0 \end{pmatrix} \begin{pmatrix} 1 \\ 0 \\ 0 \end{pmatrix} \right|^2$$
$$+ \left| \begin{pmatrix} 1 \\ 0 \\ 0 \end{pmatrix} (R^z) \begin{pmatrix} 1 \\ 0 \\ 0 \end{pmatrix} \begin{pmatrix} 1 \\ 0 \\ 0 \end{pmatrix} \right|^2 = 0$$

In consequence, TOs are active through the a tensor element while both the LOs and the F_{2u} are inactive.

Explicit values of the R^2 factor for the F_{1u} and F_{2u} modes in a range of scattering geometries accessible in our experimental conditions are summarized in Table 6.1. High symmetry axes exploited in the experiment are denoted as follows: $x \parallel [100]$, $y \parallel [010]$, $z \parallel [001]$, $x' \parallel [110]$, $y' \parallel [1\bar{1}0]$, $x'' \parallel [11\bar{2}]$, $z'' \parallel [111]$.

Table 6.1: HRS symmetry selection rules indicating normalized relative intensities of F_{1u} and F_{2u} modes in a $Pm\bar{3}m$ symmetry crystal in various backscattering geometries describing the general conditions for first-order HRS.

	Scat. geometry		General case		
Sample ($\mathbf{q}$)	No.	symbol	$R^2_{\mathrm{TO}}(F_{1u})$	$R^2_{\mathrm{LO}}(F_{1u})$	$R^2(F_{2u})$
	1	$z(xx)\bar{z}$	a^2	0	0
A	2	$z(x'x')\bar{z}$	$(\frac{a+b+2b'}{2})^2$	0	$\frac{1}{4}(c+2c')^2$
$\mathbf{q}\parallel(001)$	3	$z(xy)\bar{z}$	b^2	0	c^2
	4	$z(x'y')\bar{z}$	$(\frac{a+b-2b'}{2})^2$	0	$\frac{1}{4}(c-2c')^2$
	5	$x'(zz)\bar{x'}$	a^2	0	0
B	6	$x'(y'y')\bar{x'}$	$(\frac{a+b+2b'}{2})^2$	0	$\frac{1}{4}(c+2c')^2$
$\mathbf{q}\parallel(110)$	7	$x'(zy')\bar{x'}$	b^2	0	c^2
	8	$x'(y'z)\bar{x'}$	b^2	0	0
	9	$z''(y'y')\bar{z''}$	$(\frac{a+b+2b'}{2})^2$	0	$\frac{1}{4}(c+2c')^2$
C	10	$z''(x''x'')\bar{z''}$	$(\frac{a+b+2b'}{2})^2$	$\frac{1}{2}(\frac{a-b-2b'}{3})^2$	$\frac{1}{12}(c+2c')^2$
$\mathbf{q}\parallel(111)$	11	$z''(y'x'')\bar{z''}$	$(\frac{a+5b-2b'}{6})^2$	$\frac{1}{2}(\frac{a-b-2b'}{3})^2$	$\frac{1}{12}(c-2c')^2$
	12	$z''(x''y')\bar{z''}$	$(\frac{a+5b-2b'}{6})^2$	0	$c'^2+\frac{c^2}{4}+\frac{cc'}{3}$

In the usual case when electronic transition frequencies are high with respect to phonon and laser frequencies, HRS tensors are fully symmetric so that $b = b'$ and $c = c'$ [131]. In this case, the expressions for R^2 reduce to those summarized in Table 6.2. For the sake of convenience, we tabulated the values normalized by $(R^x_{122})^2/12$, denoting $\eta = a/b$ in the case of the F_{1u} tensor. In this case, the expected relative intensities in different geometries for a given species can be more easily appreciated (it should be kept in mind here that a and b in the case of LO modes are different from those for TO modes due to the strong electro-optic contribution to LO mode HRS tensors).

6.2.2 Experimental

We use commercially available PMN single crystals grown at Shanghai Institute of Ceramics. All samples are transparent, $\sim 1\,\mathrm{mm}$ thick plates of 7x7 mm^2, both-side polished.

Table 6.2: HRS symmetry selection rules indicating normalized relative intensities of F_{1u} and F_{2u} modes in a $Pm\bar{3}m$ symmetry crystal in various backscattering geometries for the case of *fully symmetric* HRS tensors ($b = b'$ and $c = c'$) as a function of $\eta = a/b$.

	Scat. geometry		Fully symmetric case		
Sample (**q**)	No.	symbol	$\frac{12}{b^2}R^2_{TO}(F_{1u})$	$\frac{12}{b^2}R^2_{LO}(F_{1u})$	$\frac{12}{c^2}R^2(F_{2u})$
A **q**$\|\|$(001)	1	$z(xx)\bar{z}$	$12\eta^2$	0	0
	2	$z(x'x')\bar{z}$	$27(1+\frac{\eta}{3})^2$	0	27
	3	$z(xy)\bar{z}$	12	0	12
	4	$z(x'y')\bar{z}$	$3(1-\eta)^2$	0	3
B **q**$\|\|$(110)	5	$x'(zz)\bar{x'}$	$12\eta^2$	0	0
	6	$x'(y'y')\bar{x'}$	$27(1+\frac{\eta}{3})^2$	0	27
	7	$x'(zy')\bar{x'}$	12	0	12
	8	$x'(y'z)\bar{x'}$	12	0	0
C **q**$\|\|$(111)	9	$z''(y'y')\bar{z''}$	$27(1+\frac{\eta}{3})^2$	0	27
	10	$z''(x''x'')\bar{z''}$	$27(1+\frac{\eta}{3})^2$	$6(1-\frac{\eta}{3})^2$	9
	11	$z''(y'x'')\bar{z''}$	$3(1+\frac{\eta}{3})^2$	$6(1-\frac{\eta}{3})^2$	1
	12	$z''(x''y')\bar{z''}$	$3(1+\frac{\eta}{3})^2$	0	19

The crystallographic orientation of the direction normal to the surface in samples A, B and C is (001), (110) and (111), respectively. Prior to the HRS experiments, the orientation of the crystallographic axes was verified on all samples by X-ray diffraction.

The HRS is measured with the apparatus described in chapter 5. Our as-received samples exhibit significant hyper-Rayleigh scattering. This strong elastic line is filtered by a Notch filter of $\sim 150\,\mathrm{cm}^{-1}$ half width at half maximum. The HRS spectra are corrected by the transmission of the Notch, which was independently measured using a white-light source. This procedure allows reliable inelastic intensities measurements down to $\sim 130\,\mathrm{cm}^{-1}$. However, owing to the very fast increase of the transmission function, the elastic contribution can slightly change depending on the setting. This is the reason why, in the next section, we prefer to show the HRS intensities I_{HRS} without reduction by the Bose-Einstein factor.

6.2.3 HRS spectra

Figure 6.6 shows a set of polarized spectra obtained in various backscattering geometries using our three platelets A, B, and C, with the incident and scattered beams perpendicular to the large surface, hence probing phonons with wavevectors q $\|$(001), (110), and (111), respectively. For a given sample, it is also possible to change the orientation of the incident light polarization with respect to the crystallographic axes by rotating the sample around q, *e.g.* by 45° for sample A and 90° for samples B and C. Consequently, four spectra per

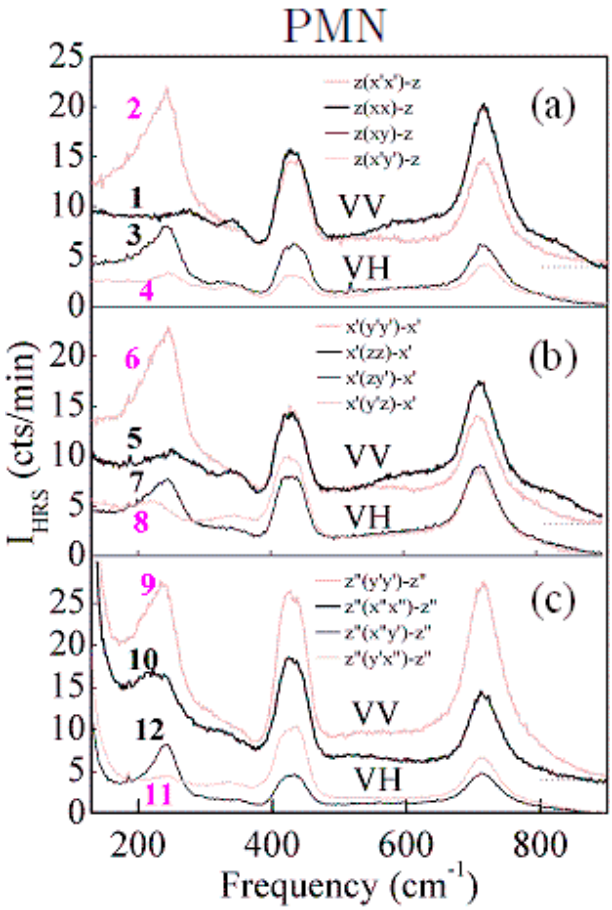


Figure 6.6: Room-temperature polarized HRS spectra in relative units taken in different backscattering geometries (a) sample A with $q \parallel(001)$, (b) sample B with $q \parallel(110)$, and (c) sample C with $q \parallel(111)$.

sample appear in Figure 6.6. Sample B was measured immediately after sample A with the utmost care to maintain identical experimental conditions. Unfortunately, the orientation of the Notch filter slightly changed for sample C, thus explaining the stronger elastic tail at low frequencies. However we estimate that the error on the relative inelastic intensities remains below 10%.

The strong peaks near 400 and 700 cm^{-1} correspond to the LO2 and LO3 modes, respectively. According to Table 6.2, the LO modes should not appear in the spectra taken from samples A and B. The appearance of LO modes in backscattering geometry was discussed in the previous chapter. The F_{2u} vibrational mode is located near 250 cm^{-1} [141], and it is clearly seen *e.g.* in spectrum 2 of Figure 6.6(a), corresponding to the $z(x'x')\bar{z}$ geometry. The mode is also seen in $z(xy)\bar{z}$ (VH) spectrum 3, but not in the $z(xx)\bar{z}$ (VV) spectrum 1, in full agreement with the F_{2u} general selection rules shown in Table 6.2. Such a complete extinction was not observed before [141], possibly owing either to some structural imperfections or the presence of differently oriented grains in the previously studied PMN crystal. The present experiment allows to estimate the relative intensities of the F_{2u} mode

in different geometries. For example, the F_{2u} intensities in spectra 2 and 6 are almost equal, in agreement with Table 6.2, and the same holds for spectra 3 and 7. Moreover, the ratio of the F_{2u} intensities in spectra 2 and 3 of Figure 6.6(a) is slightly larger than 2, which implies that $c' \approx c$ (see Table 6.2), *i.e.* that the usual case of a fully symmetric HRS tensor (last column of Table 6.2) seems to apply here. In principle, the relations discussed so far would also hold true for the F_{1u}-TO modes, if by chance the absolute value of element a were much smaller than that of b ($\eta \approx 0$). Nevertheless, F_{1u}(TO) and F_{2u} modes can be distinguished with the help of spectrum 8. Indeed, according to Table 6.2, the F_{1u}(TO) mode intensity in spectrum 8 should be identical to that of spectra 3 and 7, while for the F_{2u} mode, no intensity is expected in spectrum 8. Thus, comparison of spectrum 8 with 7 or 3 confirms that the mode at 250 cm^{-1} is indeed the anticipated F_{2u} mode.

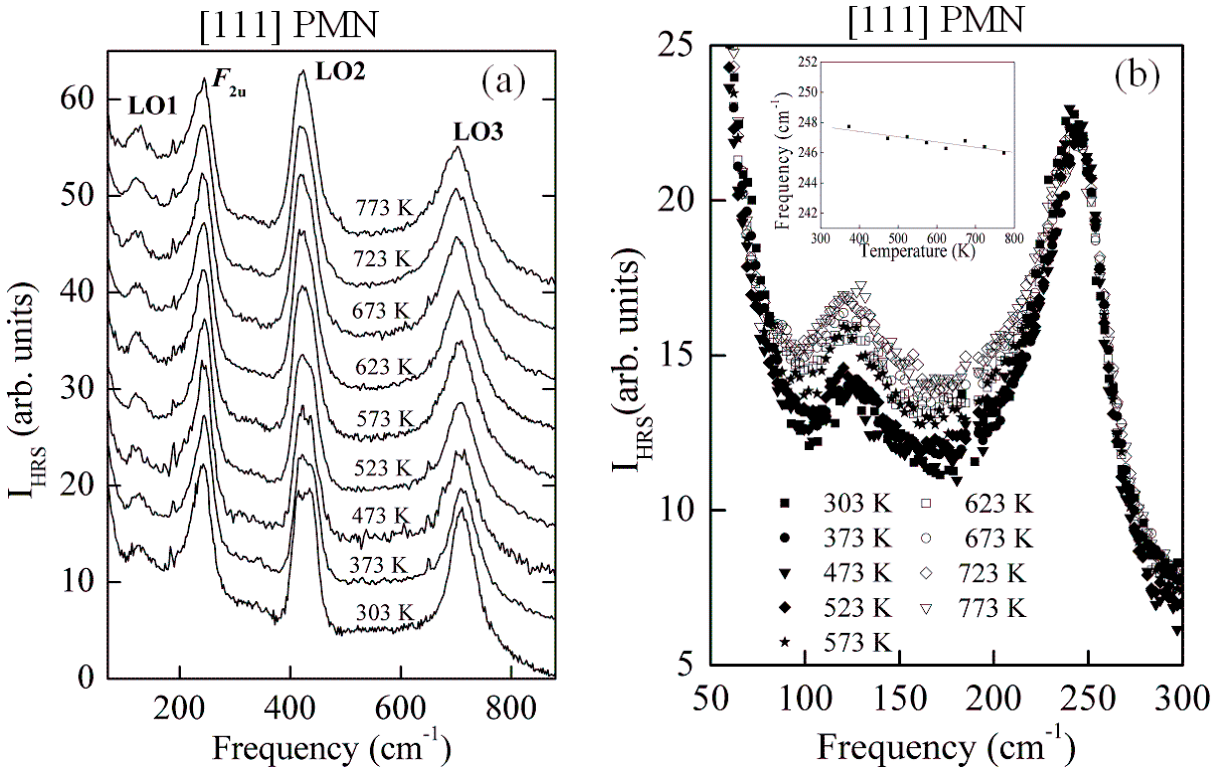


Figure 6.7: (a) HRS spectra of PMN taken in $z''(x''y')\bar{z}''$ geometry at various temperatures. (b) Different spectra normalized to the top of the F_{2u} mode. The inset shows the temperature dependence of the frequency of the F_{2u} mode.

For the high temperature measurements, we selected the $z''(x''y')\bar{z}''$ (VH) geometry (sample C, spectrum 12) because, according to Table 6.2, the F_{2u} *vs* F_{1u}(TO) intensity ratio is expected to be sufficiently large to allow neglecting the TO2 contributions. Measurements are done in a single cooling sequence. The spectra are shown in Figure 6.7(a). In each spectrum, three LO bands and the F_{2u} band are clearly seen. The splitting of LO2 seems to disappear at temperatures above T_d, which might indicate some change in the local polarization ordering. However, the F_{2u} mode does not appear to be affected by heating above T^* and T_d.

The absence of F_{2u}-mode softening (Figure 6.7(b)) towards the Burns temperature in PMN strongly indicates that the hypothetical relation between the softening of the F_{2u} mode and the Burns temperature [139] is very unlikely. Indeed, the Burns temperature is known to be rather insensitive to the Ti content in PMN-PT compounds. As the F_{2u}-mode eigenvector involves only the bending vibrations of the oxygen skeleton, and it also implies that its frequency should not so drastically depend on the Ti content in PMN-PT compounds.

In fact, we rather expect that the analogous F_{2u} mode in PMN-27PT has almost identical frequency as in the PMN crystal. If so, the soft modes observed in the HRS experiment on PMN-27PT [139] do not correspond to the F_{2u} mode so far considered: these soft modes are either not F_{2u} modes at all or at least they have completely different eigenvectors. Therefore, it becomes highly interesting to analyze the low frequency part of the HRS spectrum also in PMN. A detailed study of the low frequency soft modes in PMN and PMT is shown in the next section.

6.2.4 Mode assignment

The spectra in Figure 6.6 show some other features not discussed so far. For example, the spectra 1 and 5 have a pronounced peak near 340 cm^{-1} that was earlier [141, 153, 164] assigned to the fourth F_{1u} mode of the $Fm\bar{3}m$ clusters of partial 1:1 occupational order on B-sites, deduced from (1/2 1/2 1/2) diffuse reflections in diffraction experiments. This mode primarily corresponds to the antiparallel vibrations of neighboring B-site cations (B-B beating) [164, 165]. The LO-TO splitting of this weak B-B mode is certainly small with respect to the apparent width. From the comparison of B-B *vs* LO2 relative intensity in our HRS and in Im[$1/\epsilon$] spectra from Ref. [153], we infer that the B-B mode contributes here mainly through its anomalous scattering LO component.

Spectra 1 and 5 also show broad features near 800, 550 and 270 cm^{-1}, rather close to the main bands observed in Raman scattering [149, 166, 167, 168]. Such "background" spectra could eventually arise from Raman scattering generated by the second harmonic signal, similarly as it was observed for example in PZT [140]. However, a calibration of the Raman and hyper-Raman relative intensities reveals that in our PMN samples, such a contamination should not exceed 0.2 cts/mn (at the frequencies of the main Raman bands) which implies that it is negligible in the HRS spectra shown here. However, since there are no first-order Raman active modes in PMN except for those activated by short-range order, the shape of the Raman spectra of PMN can probably be understood as originating from a weighted phonon density of states. Obviously, the same short-range order may in principle introduce a similar density-of-state like component in the HRS spectra.

On top of these contributions, one should expect HRS by the principal F_{1u}(TO) modes. Judging from the corresponding spectrum of Im[ϵ] obtained from IR spectroscopy [153], one can expect a strong scattering by a soft TO1 mode below 100 cm^{-1} (region inaccessible in this experiment), a TO2 band located near 225 cm^{-1} and a weak TO3 band located near 550 cm^{-1}. Based on this correspondence, we expect that the weak mode observed near 225 cm^{-1} in the spectrum 8 of Figure 6.6 is actually due to TO2.

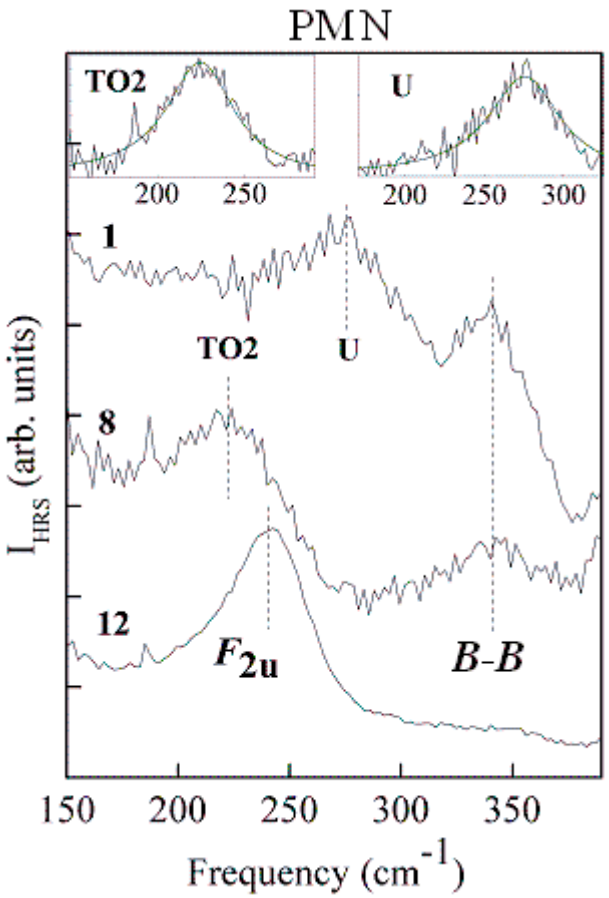


Figure 6.8: Details of HRS spectra 1, 8 and 12 from Figure 6.6 in the spectral region around the F_{2u} band. Insets show DHO fits of TO2 and U bands after subtraction of the background signal.

In summary, it seems that the F_{2u} band in spectra of Figure 6.6 is approximately overlapping with two other bands: the TO2 band at 225 cm^{-1} and the so far unassigned band U at 275 cm^{-1}. As LO2 is clearly splitted, one might also expect a splitting of TO2 also. In this case, the U mode could correspond to the second component of the TO2. Therefore, a simple fitting procedure was applied here in order to get a more quantitative estimate of these contributions. At first we considered only the spectra 1, 8 and 12, where these three bands seem to contribute rather separately (see Figure 6.8), in order to extract their individual spectral responses. The fitting function is the damped harmonic oscillator (DHO)

response multiplied by the Bose-Einstein factor

$$I(\omega) = I_0 \frac{\Gamma \omega \omega_0^2}{(\omega^2 - \omega_0^2)^2 + \Gamma^2 \omega_0^2} \times [n(\omega) + 1] \ , \tag{6.4}$$

plus a straight-line sloping background. The good fitting agreement for the TO2 and U bands is shown in the insets of Figure 6.8.

For the F_{2u} band shown in spectrum 12 of Figure 6.8, a single DHO formula cannot reproduce its asymmetric spectral lineshape, so we rather use the Breit-Wigner-Fano (BWF) formula [169, 170]

$$I_{F_{2u}}(\omega) = I_0 \frac{\left(1 + \dfrac{\omega - \omega_0}{\alpha\gamma}\right)^2}{1 + \left(\dfrac{\omega - \omega_0}{\gamma}\right)^2} \times [n(\omega) + 1] \quad , \tag{6.5}$$

where ω_0 is the peak frequency, I_0 the peak intensity, and α a coefficient relating to the degree of asymmetry of the line. For $1/\alpha \to 0$, the profile reduces to a simple lorentzian with full width at half maximum $\Gamma = 2\gamma$. The fitting results for the position and linewidth of the TO2, U, F_{2u}, as well as of the nearby B-B vibration are listed in Table 6.3.

Table 6.3: Values of frequencies ω_0 and damping parameters Γ (defined in equation (6.4) and, in case of F_{2u} mode, in equation (6.5)), as obtained from fits to data shown in the Figure 6.8.

	TO2	U	F_{2u}	B-B
ω_0 (cm^{-1})	224	274	247	340
Γ (cm^{-1})	47	55.3	40	47.1

The asymmetric shape of F_{2u} may originate from inhomogeneous broadening, for example owing to the B-site disorder, which certainly modifies the stiffness of the inequivalent oxygen octahedra. However, the apparent asymmetry can also be effectively increased by the contribution of the TO2 mode. Indeed, even in spectrum 12, where the F_{2u} band clearly exhibits the weakest apparent width, a small but finite contribution of the TO2 mode is expected according to Table 6.2. Therefore, in the second step all spectra were adjusted to a linear combination of the same DHO and BWF functions, with their widths and frequencies fixed according to Table 6.3, thus leaving adjustable only the individual intensities and the asymmetry parameter α. It turned out that all spectra could be adjusted in this way using $\alpha \simeq 7 \pm 2$.

The good quality of such fits for several representative spectra is shown in Figure 6.9. For those, the U component around $274\,\mathrm{cm}^{-1}$ appears very weak relatively to the F_{2u} band,

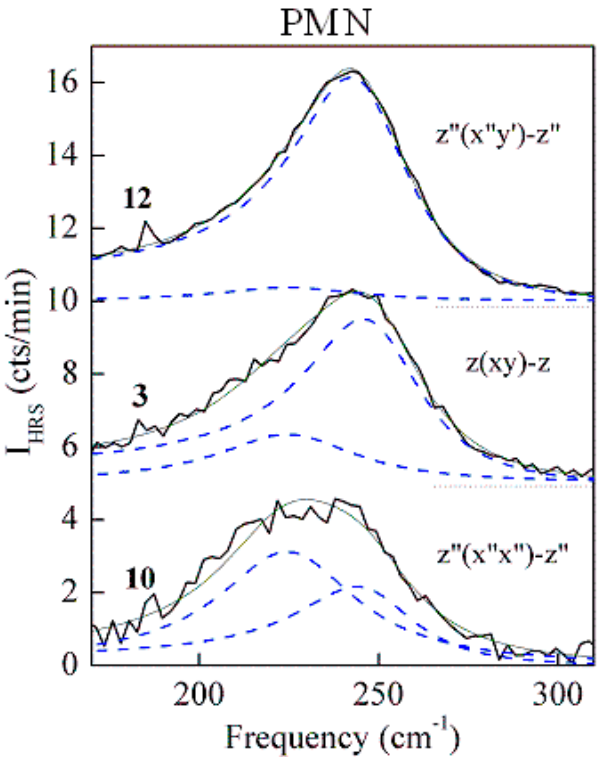


Figure 6.9: Adjustments of room-temperature spectra in the vicinity of the F_{2u} band to a superposition of predefined TO2 and F_{2u} band profiles, as explained in the text. For clarity, the background is removed and the spectra denoted 12 and 3 are translated vertically by 10 and 5 intensity units, respectively. Dashed lines show individual components corresponding to TO2 and the F_{2u} vibrations, the thin full line is the resulting fit.

so the fits only account for the F_{1u}(TO2) and F_{2u} vibrations. Resulting mode intensities can be scaled by a common factor in order to facilitate comparison with the numbers given in Table 6.2. Normalization of the F_{2u}-intensity from the fit to the $z''(x''y')\bar{z}''$ spectrum to the value of 19, gives the values 14 ± 1.5 and 6.7 ± 1 for the F_{2u}-intensities in spectra 3 and 10 ($z(xy)\bar{z}$ and $z''(x''x'')\bar{z}''$), respectively. These numbers are in a reasonably good agreement with those derived in the 3-rd and 10-th lines of Table 6.2, emphasizing that the F_{2u} mode rather follows the selection rules for a fully symmetric HRS cubic tensor (c=c'). Similarly, the normalization of the F_{1u}(TO2) intensity in the spectrum 10 ($z''(x''x'')\bar{z}''$) to the value of 27 leads to the values 11.6 ± 4 and 3 ± 3 for the spectra 3 and 12 ($z(xy)\bar{z}$ and $z''(x''y')\bar{z}]''$), respectively. These numbers are also in good agreement with the predictions of Table 6.2 for any reasonably small value of η. Thus, these results support our assignment of the 225 cm^{-1} band to a F_{1u}(TO) vibration. In principle, η^2 can be evaluated for example from the experimental ratio $I_{z(xx)\bar{z}}/I_{z(xy)\bar{z}}$. Our data indicate that η is probably smaller than 1/5, *i.e.* $b > 5a$ for the TO2 mode.

6.2.5 Conclusion

In conclusion, we derived tables of relative HRS intensities in a number of high symmetry backscattering geometries for the HRS-active optic modes of the $Pm\bar{3}m$ cubic perovskites. Performing the corresponding set of HRS experiments on high quality PMN single crystals, it is found that the $250\,\mathrm{cm}^{-1}$ band fully obeys the symmetry requirements for the silent F_{2u} vibration, and that its HRS tensor is nearly symmetric. The spectral lineshape of the F_{2u} mode is found to be slightly asymmetric, with a BWF asymmetry parameter of about 7 and damping parameter of about $40\,\mathrm{cm}^{-1}$ at room temperature. The crystal was heated well above the Burns temperature but no significant changes in the F_{2u} mode behavior were observed. In addition, several other modes are characterized. In particular, the F_{1u}(TO2) band near $225\,\mathrm{cm}^{-1}$ is also found in good agreement with the predicted HRS intensity ratios for different scattering geometries. The B-B mode corresponding to the antiparallel vibrations of neighboring B-site cations is clearly observed at ~ 340 cm^{-1}.

In general, small structural inhomogeneities are not expected to alter significantly the scattering-intensity ratios for the regular zone-center optic modes of the average structure. These conditions are experimentally verified in the present case for both the F_{2u} and F_{1u}(TO2) modes of the relaxor PMN. Thus, we conclude that HRS is a promising tool for studying the $Pm\bar{3}m$ (O_h^1) zone center modes in weakly disordered complex cubic perovskites, including lead-based relaxors.

6.3 Soft Mode

6.3.1 PMN

Introduction

The zone-center polar soft mode, a hallmark of every displacive ferroelectric phase transition, has already been studied in PMN by most possible techniques, including Raman scattering [149, 171]. A partially soft excitation with a low and strongly temperature dependent frequency was first identified by inelastic-neutron scattering (INS) investigations [145, 146, 159], but only above T_d and below T_f (Figure 6.3(a) and 6.3(b)). The same mode was then also seen by IR reflectivity and transmission spectroscopy experiments in crystals at low temperatures [160] (Figure 6.3(b)) and in thin films even up to the Burns temperature [161]. The nature of this mode in the intermediate "waterfall" region between T_f and T_d in bulk has been strongly debated. The INS spectra were compatible with the presence of an overdamped zone-center soft-mode, but the data did not allow a unique determination of its frequency and damping parameter [172].

At the same time, the presence of another mode was pointed out [145, 173], at least above T_d. That mode showed a Cochran law $\omega_0^2 \propto (T - T_0)$ but with $T_0 \approx 0\,\mathrm{K}$ [159] or even negative [173] above T_d, while $T_0 \approx +400\,\mathrm{K}$ is expected from the high-temperature Curie-Weiss law [44]. Indeed, PMN should behave as a conventional ferroelectric above T_d and the dielectric permittivity should thus be determined mostly by a corresponding soft polar excitation. In fact, the INS spectra could alternatively be fitted to a two-mode model considering an additional, so-called quasioptic mode, having a frequency as low as $\sim 12\,\mathrm{cm}^{-1}$ at 880 K and $T_0 \approx +340\,\mathrm{K}$ above T_d. That fit was clearly not unique since a single DHO model worked equally well [159]. Later on, an additional polar excitation, originally denoted as a "central mode", was observed by a separate dielectric loss peak at about $20\,\mathrm{cm}^{-1}$ in IR and THz spectroscopy. It was proposed that the two polar excitations could correspond to the soft mode fluctuations parallel and perpendicular to the local field, respectively [153]. Therefore, the two polar modes (the partially soft mode and the central mode) were tentatively denoted as A_1 and E_1 components of the TO1 soft mode [153]. However, the E_1 "central mode" could not be followed above T_d by the IR technique because of the strong absorption in the far-IR region.

Hyper-Raman scattering (HRS) provides an interesting alternative to study the vibrations in ferroelectric-type materials and in particular the paraelectric soft modes [174]. The advantage of HRS for the measurement of soft modes is apparent from Figure 6.10 where the low frequency part of the HRS spectrum of PMN is compared to a zone-center INS spectrum [146, 173]. In the latter, the leakage of the elastic scattering and of the scattering by acoustic phonons considerably limits the observations at low frequencies. On the opposite, the very good instrumental resolution combined with a very weak second harmonic generation (SHG) signal above T^* (narrow band at $\omega = 0$ in Figure 6.10), allows measurements of polar modes by HRS down to a few cm^{-1}.

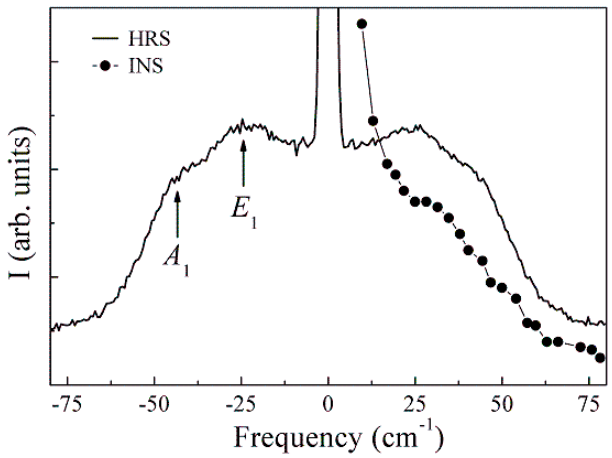


Figure 6.10: Unpolarized (V+H) HRS spectra of PMN at 748 K compared with INS data at 750 K taken from Ref. [173] (•).

Experimental

HRS experiments were performed using the setup described in chapter 5. The sample is a 1 mm thick platelet of PMN single crystal grown at Shanghai Institute of Ceramics, with [001] (z-axis) normal to the surface. It was mounted in a hot stage with the [100] (x) and [010] (y) crystallographic axes parallel to the horizontal (H) and vertical (V) direction, respectively. The data were collected in the backscattering geometry with $q \parallel [001]$. VV spectra thus correspond to a $z(yy)\bar{z}$ scattering geometry and VH spectra to $z(xy)\bar{z}$. A 1800 grooves/mm grating and a 150 μm entrance slit provide a resolution of $\sim 3\,\mathrm{cm}^{-1}$. Cooling and heating rates did not exceed 10 K/min with stabilization within $\sim \pm 1$ K. The same experiment was repeated using another sample of PMN single crystal with [111] (z-axis) normal to the surface and the [$1\bar{1}0$] (x) and [$11\bar{2}$] (y) crystallographic axes parallel to the horizontal (H) and vertical (V) direction, respectively.

Results and Discussion

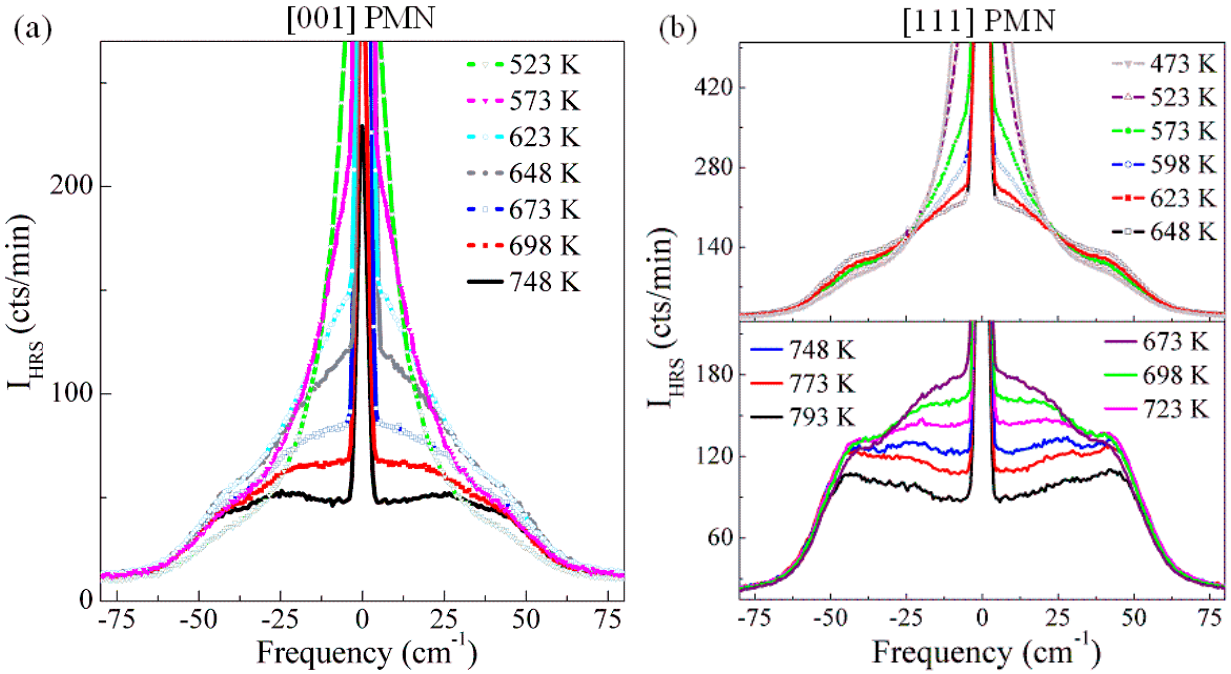


Figure 6.11: Temperature evolution of unpolarized HRS spectra of (a) [001] PMN and (b) [111] PMN crystals.

Figure 6.11 shows a series of HRS spectra measured between 520 K and 750 K on the [001] sample and between 473 K and 800 K on the [111] sample without polarization analysis in the frequency region where the F_{1u}(TO1) mode is expected to contribute. Clearly, there are two bands over the investigated temperature interval. The upper-frequency band peaks near $45\,\mathrm{cm}^{-1}$ at all temperatures while the lower-frequency band exhibits a clear soft-mode behavior on cooling. Around T_d, it transforms into a gradually narrowing quasi-elastic-like feature which then merges with the more and more intense SHG elastic scattering around

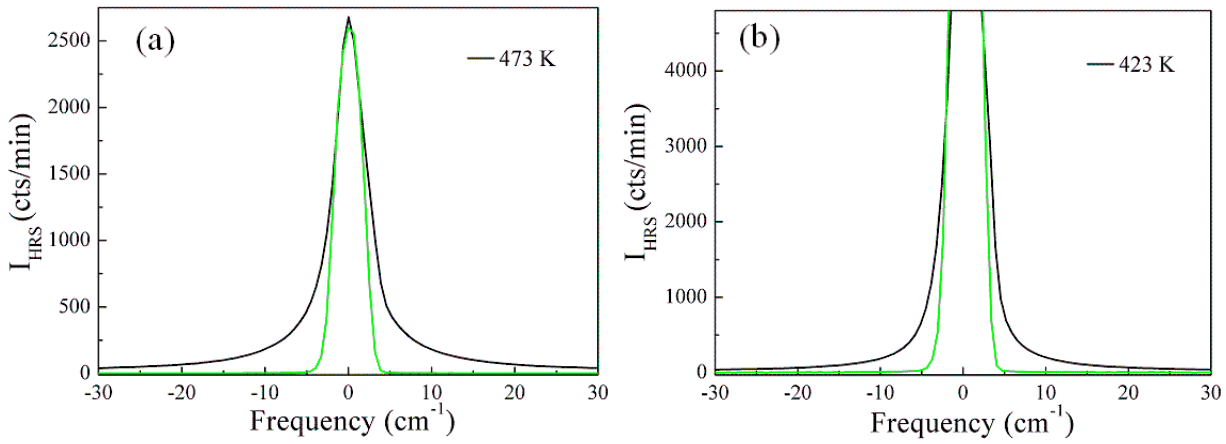


Figure 6.12: 473 K (a) and 423 K (b) [001] PMN spectra together with the instrumental function (green line).

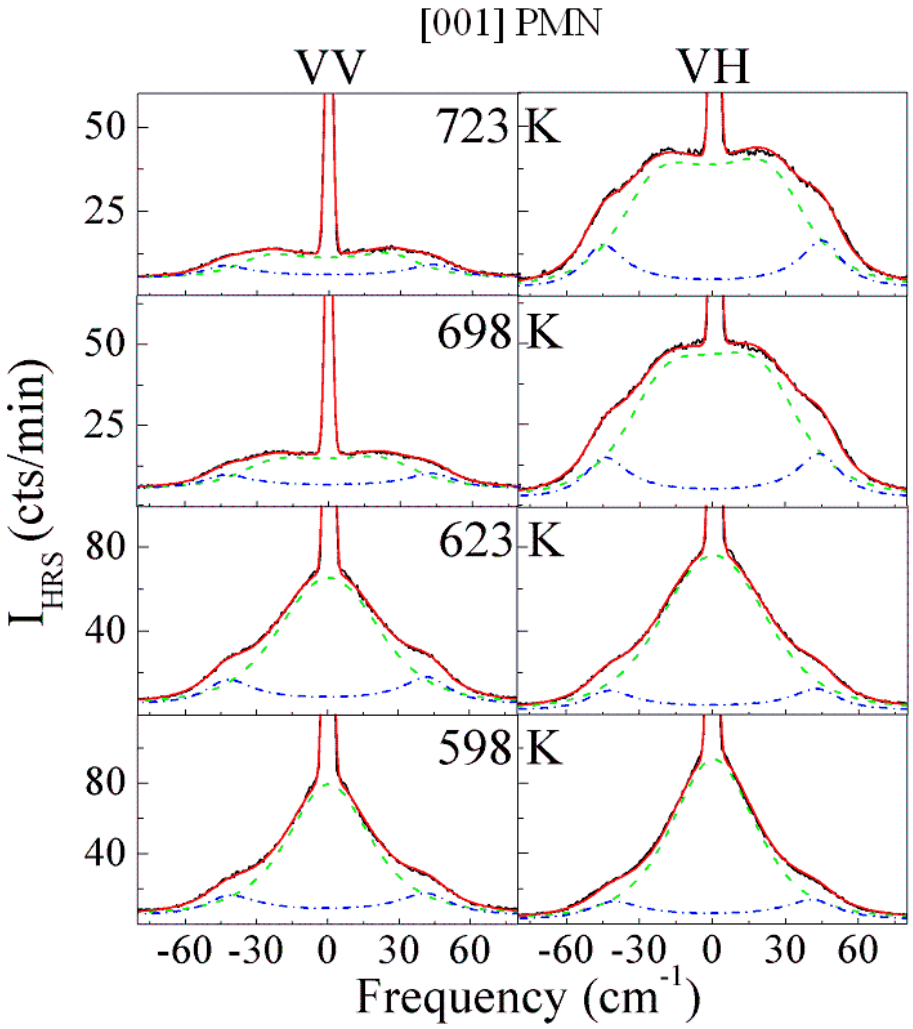


Figure 6.13: VV (left) and VH (right) hyper-Raman spectra of [001] PMN at various temperatures fitted to the model described in the text (red full lines). Green dashed and blue dash-dotted lines show DHO components corresponding to the E_1 and the A_1 modes, respectively.

$\sim 500\,\mathrm{K}$. The instrumental function scaled on top of the HRS spectra at 473 K and 423 K is shown in Figure 6.12, emphasizing the excess intensity in the wing arising for the highly overdamped soft mode. Unfortunately, the exponential rise of the hyper-Rayleigh signal prevented measurements below $\sim 420\,\mathrm{K}$.

The doublet appears both in VV and VH polarized HRS spectra (Figure 6.13). This supports the assumption that both modes are related to the F_{1u} mode, active in both geometries, rather than to the F_{2u} [139], which should be absent in the VV spectrum [136]. Therefore, it is natural, in the spirit of Ref. [153], to associate the upper- and lower-frequency bands with the A_1 and E_1 components of the F_{1u}(TO1) mode, respectively (see Figure 6.10).

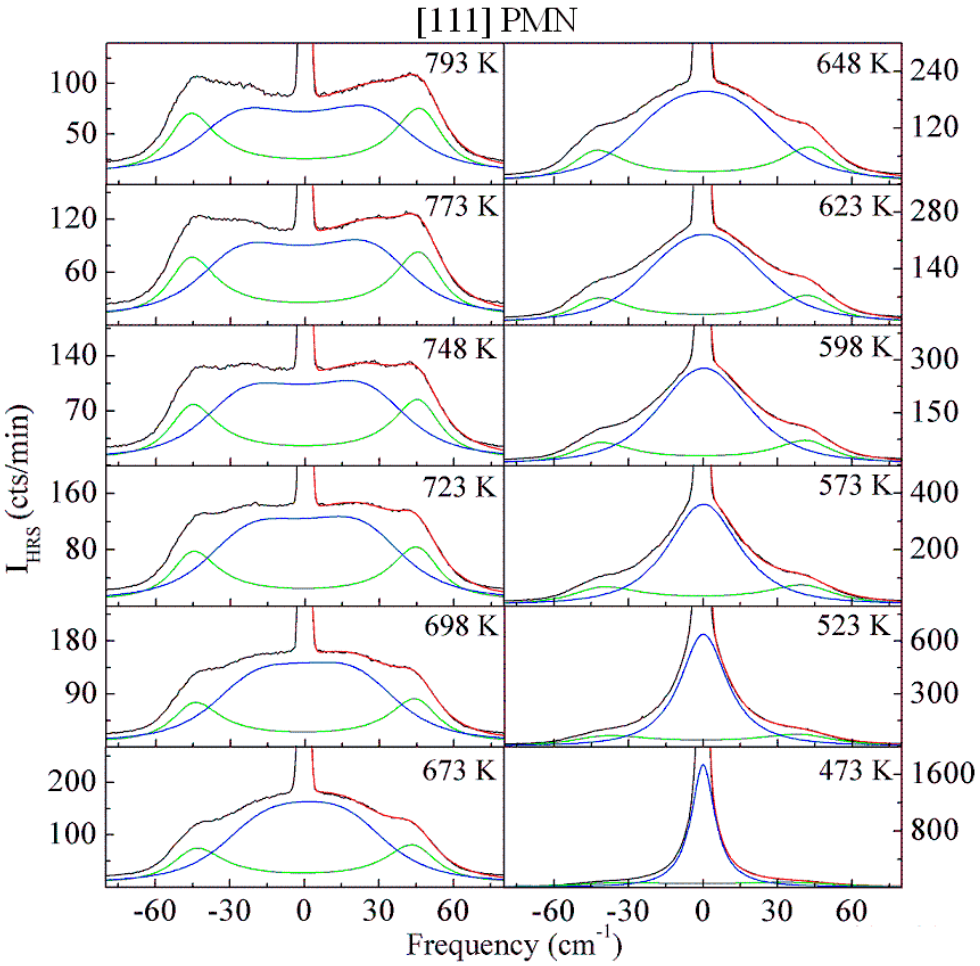


Figure 6.14: The fitting (red lines) of the Stokes part of unpolarized hyper-Raman spectra of [111] PMN. Blue and green lines show DHO components corresponding to the E_1 and the A_1 modes, respectively.

The spectra were fitted to a model including a flat background, a narrow Gaussian function accounting for the SHG elastic scattering and two damped harmonic oscillators (DHO) for the E_1 and the A_1 modes, each described by $F(\omega) = (2\omega/\pi)\,\mathrm{Im}[1/(\omega_0^2 - \omega^2 - i\Gamma\omega)]$,

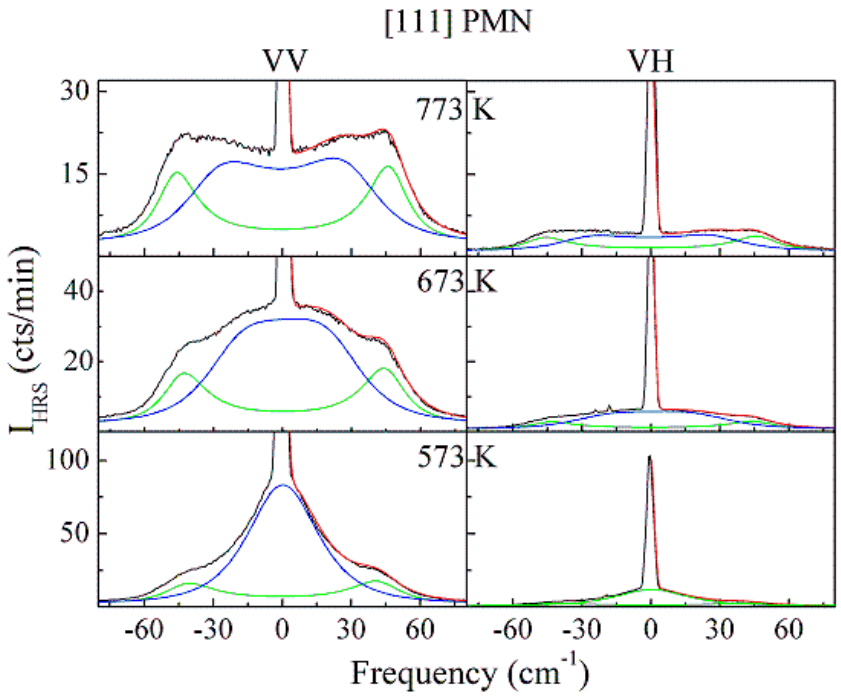


Figure 6.15: VV (left) and VH (right) hyper-Raman spectra of [111] PMN at 773 K, 673 K and 573 K with the fitting of the Stokes part shown in red. Blue and green lines show DHO components corresponding to the E_1 and the A_1 modes, respectively.

where ω_0 and Γ are the DHO frequency and damping, respectively. The model nicely reproduces the experimental data over the full temperature range explored, as shown in Figure 6.13 (VV and VH, $q \parallel [001]$) and in Figures 6.14 and 6.15 (unpolarized and polarized spectra, $q \parallel [111]$). For the [111] spectra, only the Stokes part was fitted because in that case a slight misalignment of the spectrometer led to an asymmetry between the Stokes and the anti-Stokes sides of the spectra. However, we checked that the fitting results are not strongly affected by this effect.

One notes that in our model, the DHO associated with the E_1 mode plays the dominant role. It describes the main scattering intensity and it shows a pronounced softening on cooling. In fact, its peak frequency is zero below T_d (Figure 6.13). In usual terms [175], such a mode is *overdamped*, as opposed to an *underdamped* mode peaking at a nonzero frequency. The observed overdamping-underdamping cross-over suggests that the E_1 mode is responsible for the difficulties in the analysis of the INS spectra between T_f and T_d. The peak frequency of the E_1 mode could not be resolved in early INS data. At the same time, it is the A_1 mode frequency which coincides with the soft-mode frequency proposed for the INS spectra taken above T_d [146]. Hence the A_1 mode probably corresponds to the vibration previously assigned to the soft mode of PMN [146]. In contrast, our data indicate that this mode does not show any signature of overdamping below T_d.

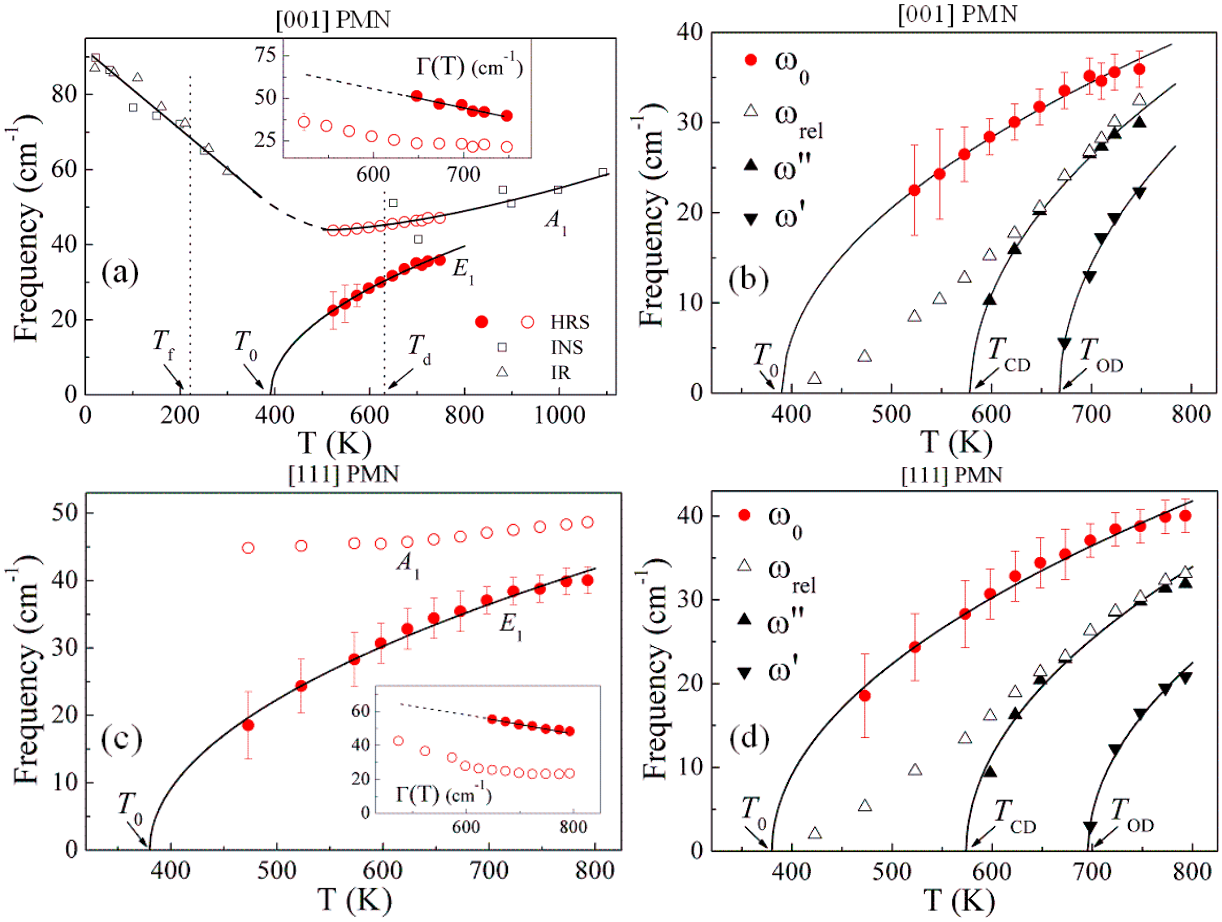


Figure 6.16: (a) Temperature dependence of E_1 and A_1 frequencies ω_0 and damping (in the inset) obtained from [001] PMN data compared to the INS data of Refs. [146, 159] and IR of Ref. [160]. The lower line (E_1) corresponds to a fit with a Cochran law. (b) Temperature dependence of the E_1 mode frequencies ω_0, $\omega_{\rm rel}$, ω', and ω'', defined in the text. (c) Temperature dependence of E_1 and A_1 frequencies ω_0 and damping (in the inset) obtained from [111] PMN data. (d) Temperature dependence of the E_1 mode frequencies ω_0, $\omega_{\rm rel}$, ω', and ω''. The lines in (b), (c) and (d) stand for Cochran-like laws $\omega^2 \propto (T - T_0)$.

The values of ω_0 and Γ of the E_1 and A_1 modes are shown in Figures 6.16(a) and 6.16(c) for the [001] and [111] directions, respectively. These parameters exhibit the same behavior, emphasizing that we are measuring the same softening in both directions. Indeed, a fit of ω_0 with a Cochran law gives very similar values for T_0, $T_0 \cong 390 \pm 30\,\mathrm{K}$ for $q \parallel [001]$ (Figure 6.16(a)) and $T_0 \cong 380 \pm 30\,\mathrm{K}$ for $q \parallel [111]$ (Figure 6.16(c)). The DHO model is very useful for the description of lattice modes with relatively large damping parameters. In the high-temperature limit, the maxima of the one-phonon DHO scattering spectral function $S(\omega) = [n(\omega) + 1]\,\mathrm{Im}[1/(\omega_0^2 - \omega^2 - i\Gamma\omega)]$ are at $\omega' = \pm\sqrt{\omega_0^2 - \Gamma^2/2}$ if $\omega_0 > \Gamma/\sqrt{2}$ and there is only one maximum at $\omega = 0$ if $\omega_0 < \Gamma/\sqrt{2}$. A related quantity is the frequency $\omega'' = \pm\sqrt{\omega_0^2 - \Gamma^2/4}$, defining the periodic factor in the temporal response of the oscillator coordinate Q in the absence of driving forces $Q(t) = \exp^{-t\Gamma/2} \cos(\omega'' t + \phi)$ for $(\omega_0 > \Gamma/2)$. The frequencies ω' and ω'' calculated using the E_1 mode parameters tend to

zero at temperatures $T_{OD} = 670\,\mathrm{K}$ and $T_{CD} = 580\,\mathrm{K}$ (Figure 6.16(b)) from [001] data and $T_{OD} = 690\,\mathrm{K}$ and $T_{CD} = 575\,\mathrm{K}$ (Figure 6.16(d)) from [111] data, marking overdamping and critical damping of the E_1 mode, respectively. It is worth noting that T_{OD} and T_{CD} bracket $T_d \approx 620\,\mathrm{K}$.

It is well known that an independent experimental determination of ω_0 and Γ from the $S(\omega)$ lineshape of an overdamped mode is quite problematic. Therefore, the spectra *below* T_d were fitted with the E_1 mode damping fixed to the value obtained by linear extrapolation of $\Gamma(T)$ measured *above* T_d (see the insets of Figure 6.16(a) and 6.16(c)). However the most reliable spectral parameter of a strongly overdamped DHO is the relaxational frequency $\omega_{rel} = \omega_0^2/\Gamma$, corresponding to the half-width at half-maximum of $S(\omega)$. For points below 523 K, a fit with a lorentzian centered on zero gives a half width at half maximum equal to ω_0^2/Γ. The fit of [111] spectra at 473 K and 423 K can be seen in Figure 6.17. Since ω_{rel} of E_1 mode clearly tends to zero at about 400 K (Figures 6.16(b) and 6.16(d)), we are confident that also ω_0^2 does so. This is further supported by the fit of ω_0 with a Cochran law (Figures 6.16(a) and 6.16(c)). These observations are very strong indications that the E_1 mode observed here accounts for the Curie-Weiss temperature T_0 extrapolated from $\epsilon(T)$ at high temperature [44].

In fact, well above T_d, where one can rely on ω_0 value of the E_1 mode, the dielectric contribution of the soft doublet can be estimated directly. Equation (5.14) can be written as follows

$$\epsilon(0) = \epsilon_\infty + \sum_m \Delta\epsilon_m = \epsilon_\infty + \sum_m \frac{\Omega_m^2}{\omega_{\mathrm{T_m}}^2} \tag{6.6}$$

where Ω_m is the mode-plasma frequency given by [164]:

$$\Omega_m^2 = -\frac{2}{\pi}\int_0^\infty \omega\ \mathrm{Im}\left[\frac{S_m}{\omega_{\mathrm{T_m}}^2 - \omega^2 - i\omega\Gamma_m}\right] \tag{6.7}$$

where S_m is the oscillator strength.

Using the mode-plasma frequencies $\Omega[A_1] = 537\,\mathrm{cm}^{-1}$ and $\Omega[E] = 711\,\mathrm{cm}^{-1}$ for the A_1 and E components of the $PbTiO_3$ (PT) soft mode [164] and the ω_0 frequencies of the A_1 and E_1 components of the PMN soft mode at 748 K (47.2 and 35.9 cm^{-1}, respectively), one can estimate the average static dielectric contribution of these two modes as

$$\Delta\epsilon = \frac{1}{3}\left(\frac{\Omega[A_1]}{\omega_0[A_1]}\right)^2 + \frac{2}{3}\left(\frac{\Omega[E]}{\omega_0[E_1]}\right)^2 \approx 305\,. \tag{6.8}$$

This value is still much larger than the background permittivity $\epsilon_\infty \approx 25$ associated with the TO2 and TO3 polar modes and the electronic contributions [153]. The total static permittivity $\epsilon_\infty + \Delta\epsilon \approx 330$ is thus in an excellent agreement with the low frequency permittivity $C/(T - T_0) \approx 343$, evaluated at $T = 748\,\mathrm{K}$ using the Curie-Weiss temperature

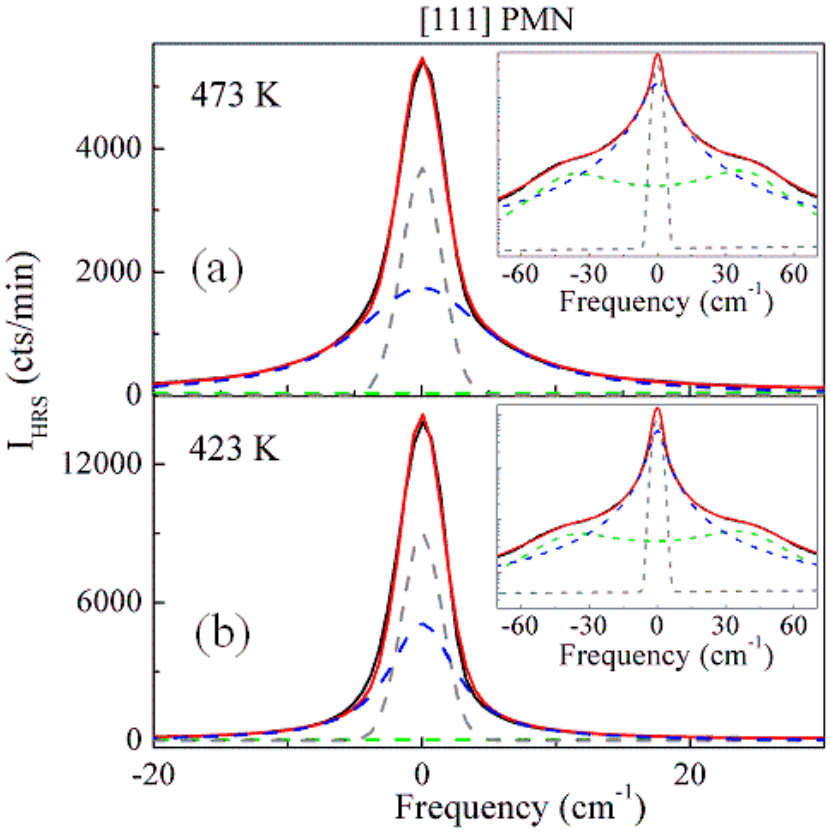


Figure 6.17: 473 K (a) and 423 K (b) spectra of [111] PMN together with the resulting fit (red lines) using a flat background, a gaussian, a lorentzian, and a DHO. Dashed grey, blue and green lines show individual components corresponding to the SHG, the E_1 mode and the A_1 mode respectively. For clarity, insets show the figure in log scale.

$T_0 = 398\,\mathrm{K}$ and Curie constant $C = 1.2 \times 10^5\,\mathrm{K}$ from Ref. [44].

The PT plasma frequencies were used in our estimate instead of the PMN plasma frequencies. Indeed, the phonon modes of PMN are quite broad and the determination of the plasma frequencies from IR reflectivity requires several approximations that are not needed when dealing with a classical ferroelectric material such as PT. In particular, the lack of reliable IR data below 20 cm^{-1} implies that the parameters of the heavily damped soft mode may not be very precise [164]. At the same time, the soft mode for both PT and PMN happens to involve primarily lead cation vibrations (it has a Last-type eigenvector). Therefore, it is quite natural to expect that the soft mode plasma frequencies, directly related to the "moving charge" of the mode, are quite similar in these two compounds. So it is completely reasonable to use the PT phonon mode parameters. Also, the temperature dependence of the plasma frequency is certainly smaller than the uncertainties in the analysis of the IR experimental data and they can be neglected here. This is why we rather use the room-temperature plasma frequencies of PT in equation 6.8. However, similar results can be obtained using plausible plasma frequencies inferred from room-temperature reflectivity spectra of PMN. The use of $\Omega[A_1] = 761\,\mathrm{cm}^{-1}$ and $\Omega[E_1] = 693\,\mathrm{cm}^{-1}$ of A_1 and E_1

components of PMN soft mode [164] in equation 6.8 give $\Delta\epsilon \approx 335$ close to 305 obtained with PT plasma frequencies.

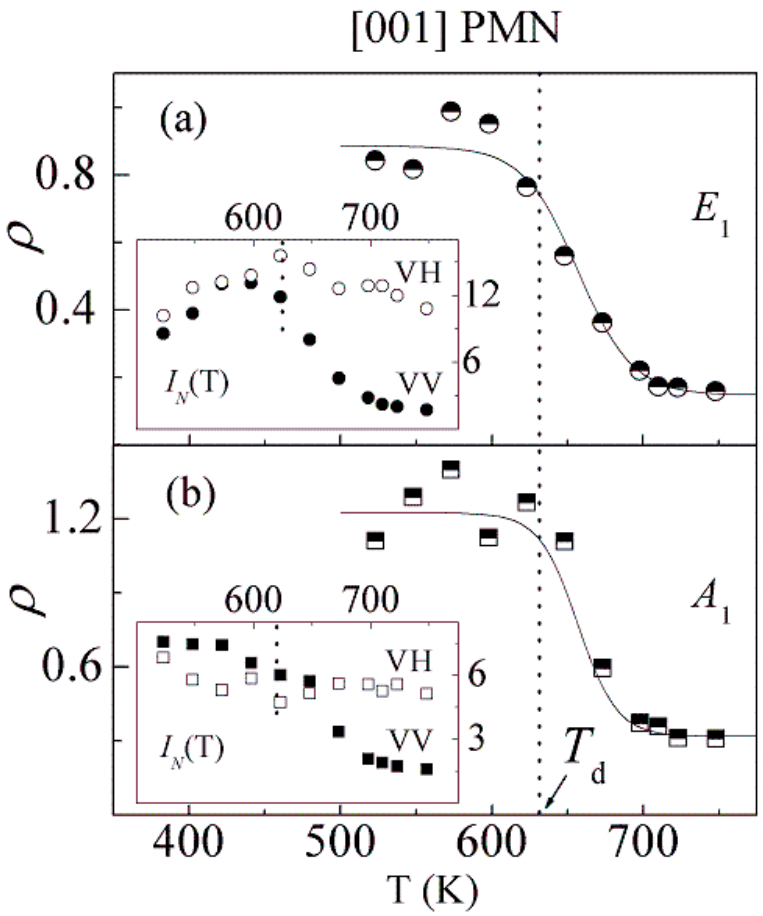


Figure 6.18: (a) and (b) show the polarization ratio ρ of the normalized HRS intensities of the E_1 and A_1 components, respectively. The lines are guides for the eyes. Insets show $I_N(VV)$ (full symbols) and $I_N(VH)$ (open symbols) for the two components separately.

The pairs of VH and VV spectra were recorded under identical conditions. Slight intensity drifts during temperature changes were corrected using the Bose-factor-corrected VH intensity of the very stable F_{2u} mode at $\sim 248\,\mathrm{cm}^{-1}$[136]. Therefore, we can extract for each mode its relative intensity factor I_N, proportional to the sum of squares of the HRS tensor components given in the right hand of equation (5.25).

$$I_N = \int \frac{\omega \times S_{HR}}{n(\omega)+1} d\omega = R^2 \int F(\omega) d(\omega) \tag{6.9}$$

Hence I_N is simply the area of the mode under consideration. Since E_1 and A_1 modes are both derived from the F_{1u} mode, their I_N factors should roughly be given by the two independent HRS tensor elements of the $F_{1u}(TO1)$ mode: $R^2_{111} = a^2$ and $R^2_{122} = b^2$ for the A_1 *singlet* in VV and VH spectra and $2R^2_{111} = 2a^2$ and $2R^2_{122} = 2b^2$ for the E_1 *doublet* in VV and VH spectra, respectively [136]. The results show that indeed the E_1 mode has a

twice as large I_N than the A_1 mode, as expected for a doublet-singlet pair derived from the same parent F_{1u}(TO1) mode (ratios $I_N^{E_1}(VV)/I_N^{A_1}(VV)$ and $I_N^{E_1}(VH)/I_N^{A_1}(VH)$ in the insets of Figure 6.18).

At the same time, the polarization ratios $\rho = I_N(VV)/I_N(VH)$ are much enhanced for both phonon modes near T_d (Figure 6.18). Inspection of the individual contributions (see the insets of Figure 6.18) suggests that the enhancement is related to I_N factors of VV spectra while those of VH spectra are rather temperature independent, implying that the diagonal tensor element $a(T)$ of the parent F_{1u}(TO1) mode is particularly sensitive to a local structural change while the off-diagonal element b is not. These observations might relate to the growth of a local-polarization-related order parameter near T_d.

The temperature dependence of the depolarization ratios for $q \parallel [111]$ is completely different from that for $q \parallel [001]$. From Table 6.2 one expects ρ to have a constant value 9 (ratio between lines 9 and 11), thus independent of a and b. The results show an almost constant value, between 4.6 and 6.9, in fairly agreement with the calculation (Figure 6.19). Moreover, it seems that contrary to $q \parallel [001]$, the depolarization ratio of E_1 and A_1 modes are the same, meaning that VV and VH spectra between $\sim$ -60 and 60 cm^{-1} are similar apart from an intensity factor (inset of Figure 6.19).

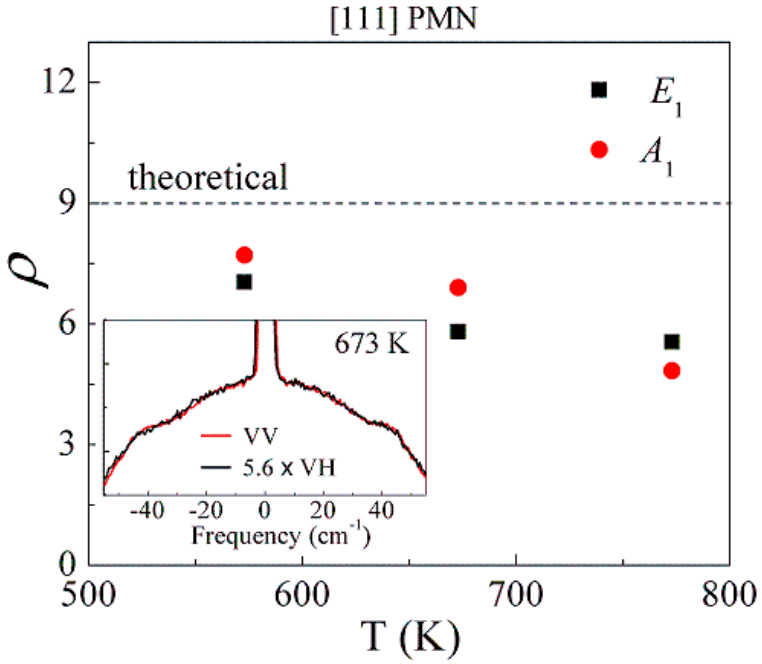


Figure 6.19: The polarization ratio ρ of the normalized HRS intensities of the E_1 and A_1 components, respectively. The inset shows the VV and 5.6×VH spectra at 673 K emphasizing that both E_1 and A_1 modes have the same depolarization ratio.

Knowing $\eta(t) = a/b$ of E_1 and A_1 from $q \parallel [001]$ experiments, it is possible to predict the

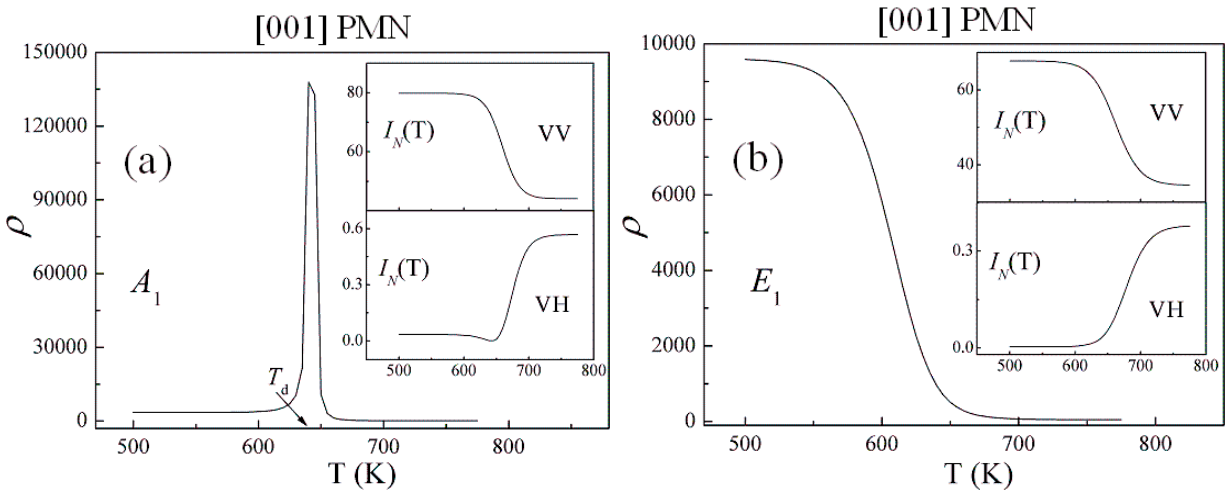


Figure 6.20: The polarization ratio ρ of the normalized HRS intensities of the A_1 (a) and E_1 (b) components obtained along $z(x'x')\bar{z}$ and $z(x'y')\bar{z}$ directions with $q \parallel [001]$. Insets show both $I_N(VV)$ and $I_N(VH)$ for the two components.

temperature dependence of the intensity in VV and VH for all other scattering geometries of Table 6.2. Figure 6.20 shows the result for the scattering with $q \parallel [001]$, $z(x'x')\bar{z}$ (VV) and $z(x'y')\bar{z}$ (VH). $I_N(t)$ in VH is very small ($I_N < 1$, insets of Figure 6.20) revealing that the low frequency HRS spectra is free from the TO-doublet in that case. This could provide a unique possibility to investigate the hyper Rayleigh component as well as the HRS central peak of PMN. The second important information is the very intense narrow peak in the depolarization ratio of the A_1 mode close to T_d, as well as the very strong increase of ρ_{E_1} below T_d. These expectations clearly deserve to be confirmed experimentally. The strong intensity anomalies of the TO1 doublet around T_d constitutes key information which originates from the local structural (polar ?) ordering of PMN below T_d. Based on these observations, structural models could be tested. This can be the subject for a future work.

6.3.2 PMT

To see whether the low frequency dynamics of PMN is a general feature of simple ferroelectric relaxors, we complemented the previous set of data with experiments performed on a PMT single crystal with $q \parallel [001]$.

The spectra have been recorded with a grating of 600 grooves/mm and a 150 μm entrance slit leading to a resolution of $\sim 9\,\mathrm{cm}^{-1}$. Unpolarized HRS spectra measured between 373 K and 773 K are shown in Figure 6.21. Similarly to PMN, two bands are present over the whole temperature interval investigated. The upper-frequency band peaks near $50\,\mathrm{cm}^{-1}$ while the lower-frequency band exhibits a clear soft-mode behavior on cooling. Below 473 K, it transforms from a vibrational to a relaxational mode. Since the temperature dependence of the low frequency doublet is similar to the scenario in PMN, we associate the upper- and

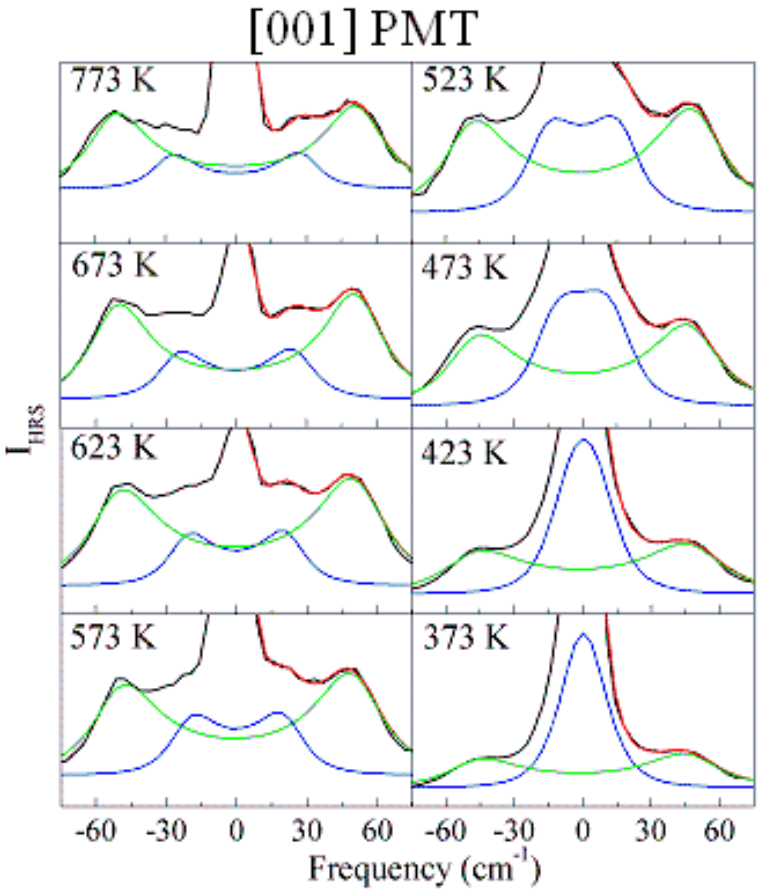


Figure 6.21: Unpolarized HRS spectra of PMT at various temperatures.

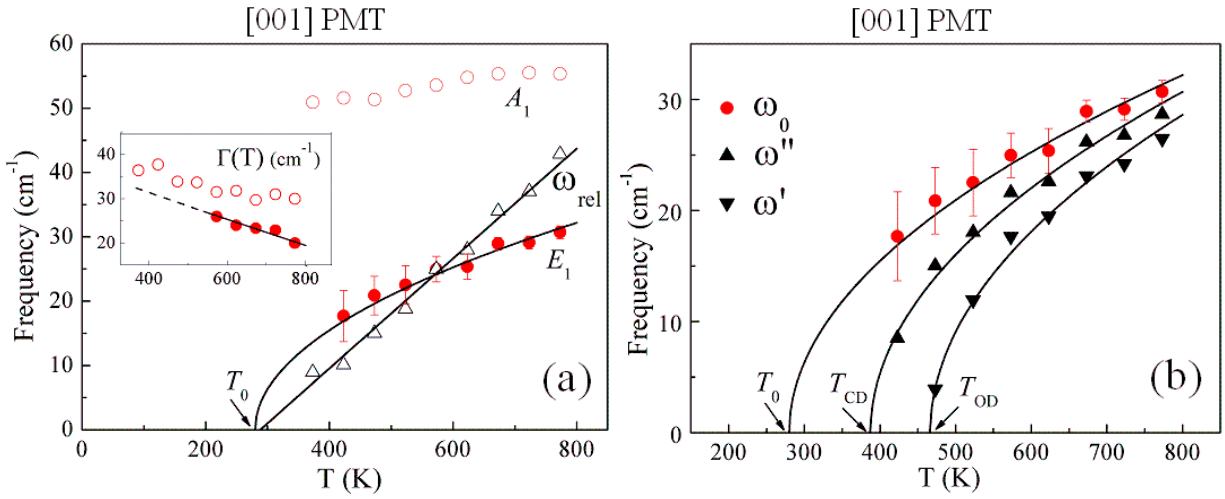


Figure 6.22: Temperature dependence of E_1 and A_1 frequencies ω_0 and damping (in the inset) obtained from PMT data. The open triangles represent the variation of ω_{rel}. (b) Temperature dependence of the E_1 mode frequencies ω_0, ω', and ω'', defined in the text. The lines are Cochran-like laws $\omega^2 \propto (T - T_0)$.

lower-frequency band to A_1 and E_1 components of the F_{1u}(TO1) mode, respectively. The same model was used to fit the spectra. Owing to optical-abberation-induced asymmetry on the anti-Stokes side, only the Stokes components have been fitted. The model reproduces the experimental data over the full temperature range. The damping of the E_1 mode in the overdamped region was fixed to the value obtained by linear extrapolation of $\Gamma(T)$ measured in the underdamped region (see the inset of Figure 6.22(a)).

The frequeny and damping of both modes are shown in Figure 6.22(a). The fit of ω_0 with a Cochran law gives $T_0 \cong 280 \pm 30\,\mathrm{K}$. This value is consistent with T_0 obtained from the extrapolation of the Curie-Weiss law used to fit high-temperature points of the inverse of the dielectric constant [78]. Using the values of ω_0 and Γ of the E_1 mode, we calculate the relaxational frequency $\omega_{rel} = \omega_0^2/\Gamma$ and the two frequencies ω' and ω''. ω_{rel} tends to zero at about 290 K (near T_0), while ω' and ω'' tend to zero at temperatures $T_{OD} = 470\,\mathrm{K}$ and $T_{CD} = 380\,\mathrm{K}$ (Figure 6.22(b)) marking overdamping and critical damping of the E_1 mode, respectively. These values of T_{OD} and T_{CD} are quite close to 420 K that corresponds to the temperature at which both the lattice parameter a [75] and the inverse of the dielectric constant ϵ^{-1} [78] show a deviation from their linear behavior. The compararison with PMN suggests that the Burns temperature of PMT is $\sim 420\,\mathrm{K}$ rather than 570 K as it is sometimes presented [55].

6.3.3 Conclusion

In summary, the current HRS experiment helped to elucidate ferroelectric order-parameter dynamics in the paraelectric phase of PMN and PMT single crystals. In particular, our data are well described by a model where (i) the scattering response has two components over a broad temperature range both below and above the Burns temperature, (ii) the E_1 mode becomes underdamped above the Burns temperature, (iii) the critical damping temperature T_{CD} and the overdamped temperature T_{OD} surrounds the Burns temperature T_d and (iv) the observed doublet is responsible for the high-temperature Curie-Weiss law. The E_1 mode clearly softens toward the anticipated random field transition [176] T_0. These findings seem to generalize to other simple ferroelectric relaxors. We hope that these results will help to reconcile the apparently contradictory reports on the nature of the PMN soft mode and to approach a more coherent picture of the dynamical polarization correlations in relaxors in general. Finally, the intensity of the low frequency TO doublet exhibits strong anomalies near T_d. Understanding these features will likely bring deep insight into the evolution of the polar nano-structure of these systems.

6.4 LO Modes

Longitudinal optic (LO) modes usually dominate the HRS spectra of mixed lead-based perovskites [139, 140, 141]. This is particularly true in PMN [136, 141] and PMT, in which the LOs almost completely mask the signal arising from the TOs, even in backscattering where the former are forbidden by symmetry (section 5.2). If one wants to get information on the intensity of the LOs, it is preferable to perform HRS using a geometry where they are allowed by symmetry, as for example near-forward scattering. In that case, the ratio between the LO mode strength observed in HRS and the intensity of the corresponding bands in the -Im[$1/\varepsilon$] spectrum determined from far-infrared reflectivity experiment is the same for all three main LO bands [153]. This leads to the conclusion that the HRS intensity of the LOs in relaxors mainly arises from the electro-optic (EO) coupling term of the HRS tensor (second term in equation (5.29)) rather from the deformation-potential contribution (first term in equation (5.29)). This strong EO coupling in relaxors provides HRS as an extremely useful tool for direct experimental observation of the polar LO modes (with their relative strength), otherwise only accessible via fitting or Kramers-Kronig analysis of IR reflectivity spectra. Figure 6.23 summarizes the HRS results on the temperature dependence of the modes in PMN and PMT, as well as in PZN which exhibits a paraelectric-ferroelectric transition near 400 K. It shows unpolarized HRS (V+H) spectra of PMN ($q \parallel$ [001]), PMT ($q \parallel$ [001]) and PZN ($q \parallel$ [001]) single crystals obtained with the setup in its low resolution mode (FWHM $\sim$ 9 cm^{-1}). The PMN spectra, the PZN spectra and the low temperature PMT spectra (below 230 K) were collected in near-forward scattering while the PMT spectra above room temperature were recorded in backscattering. The different experimental geometries used to perform this study prevent for a comparison of the intensities of the HRS bands with temperatures. The ferroelectric transition in PZN induces a growing second harmonic generation (SHG) signal on cooling below T_f. This strong green light induces a Raman scattering signal which superposes to the HRS one leading to a structured background at low temperatures. As stated before, the three LO bands are clearly seen in all the spectra: one weak and asymmetric line around 110 cm^{-1} (LO1), a double peak structure around 400 cm^{-1} (LO2) and a broad Lorentzian-like peak centered around 700 cm^{-1} (LO3). The subsections below describe the temperature behavior of these bands.

6.4.1 LO3

The LO3 mode near 700 cm^{-1} can be fitted with a lorentzian function (inset of Figure 6.24(b)) meaning that we access the homogeneous width of the vibration. A gaussian function centered near 600 cm^{-1} is also used to fit the tail in the low frequency side of LO3. This spectral component likely associates with the high frequency A_1 mode of the TO3 doublet which is indeed expected in that frequency range [153]. The fit sometimes

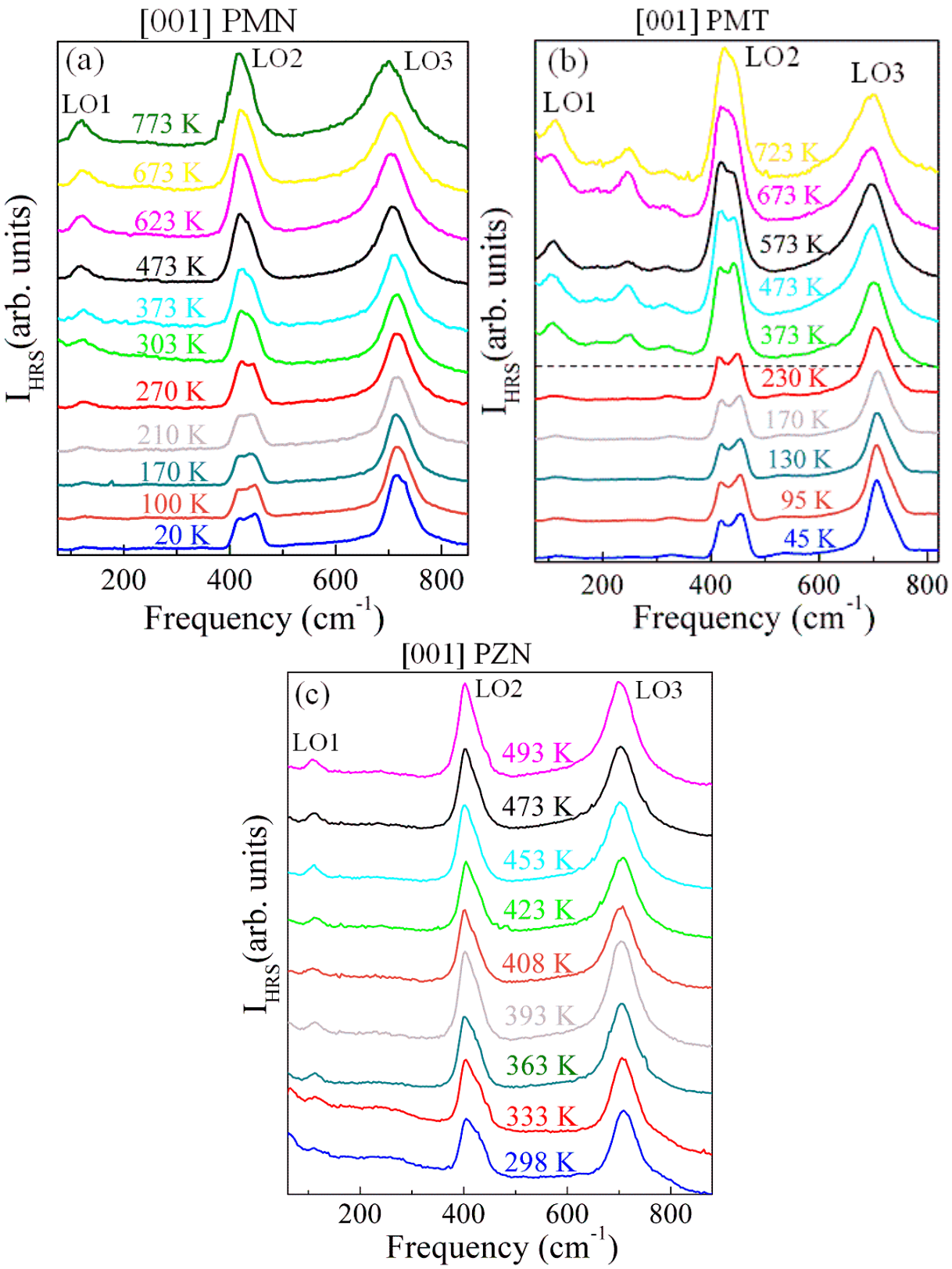


Figure 6.23: HRS spectra of PMN (a), PMT (b) and PZN (c) at various temperatures. Experiments were performed in forward-scattering except for the high temperature PMT spectra which were collected in backscattering geometry.

requires a weak additional contribution centered at ~ 780 cm^{-1}, suggesting that the band near ~ 700 cm^{-1} likely corresponds to the E_1 component of the LO3 doublet while the weak contribution ~ 780 cm^{-1} could eventually correspond to the A_1 component as proposed by IR reflectivity [153] (Figure 6.4). The temperature dependence of the frequency ω and the full width at half maximum of LO3 in PMN and PMT are shown in Figure 6.24. The dashed lines are guides for the eyes. They mimic standard monotonous behaviors. In PZN, the growth of the Raman signal underneath LO3 below T_f prevents for an accurate determination of these quantities.

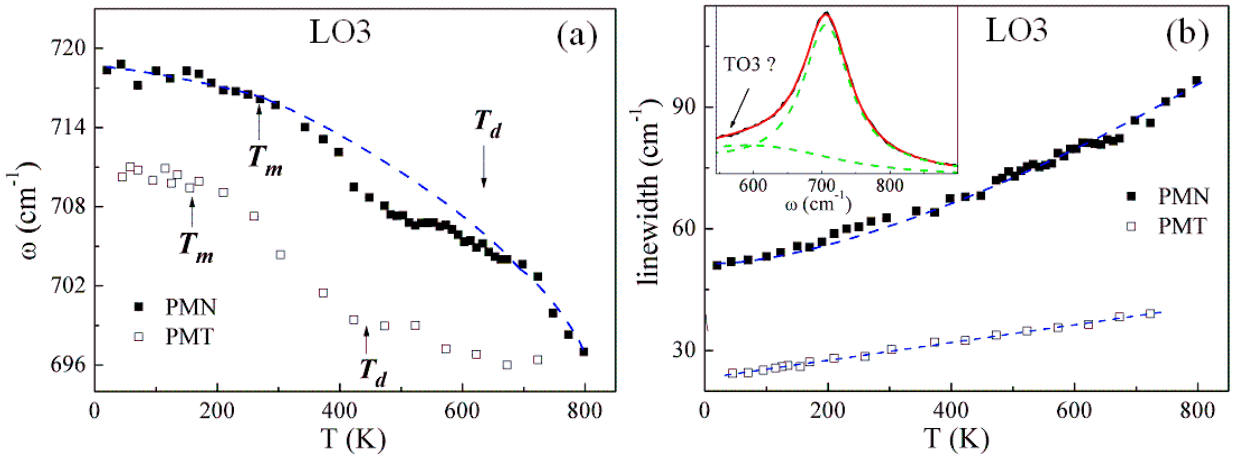


Figure 6.24: Temperature dependence of the frequency ω (a) and the linewidth (b) of the LO3 mode. The inset shows the fitting of the LO3 mode using a lorentzian function with a gaussian function for the tail.

One observes from Figure 6.24 that the linewidth of LO3 in PMT is smaller than that in PMN. It is worth noting here that the same observation applies for almost all the HRS active bands. No observable anomaly can be seen within the full temperature range explored. The temperature dependence of the frequency is more complicated. In PMN where the spectroscopy has been performed in more details, one can eventually see three inflection points (change in the sign of the second derivative of $\omega(T)$). The first one around T_d, the second one around 500 K (T^* in PMN) and the last one at T_m. This qualitative observation should be taken cautiously as we do not have any physical model that could explain these effects. Although the dispersion of the points is larger, the same behavior seems to apply in PMT. In any case, these anomalies are very weak (less than 1%) at least compared to those on LO1 and LO2 (see below).

6.4.2 LO2

The low resolution HRS spectra in Figure 6.23 show a clear splitting of the LO2 band in the three materials. This splitting increases as the temperature decreases. To obtain a better observation, high resolution HRS in PMN was performed. The obtained spectra zoomed on the LO2 region, together with those of PMT are shown in Figure 6.25. For sake

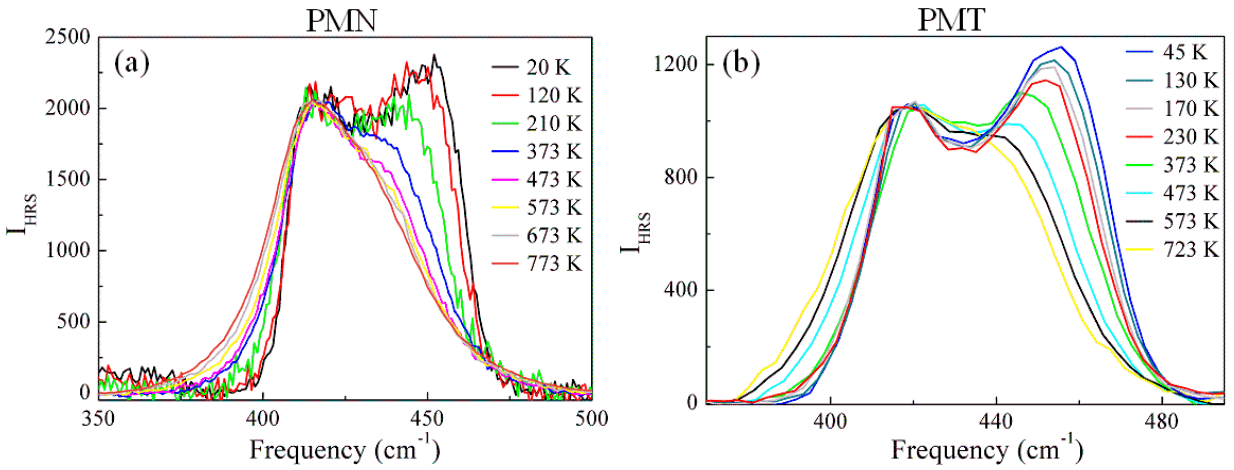


Figure 6.25: Temperature dependence of LO2 in (a) PMN (forward-scattering, high resolution) and (b) PMT (spectra reproduced from Figure 6.23). For sake of clarity, the spectra are normalized on top of low-frequency component.

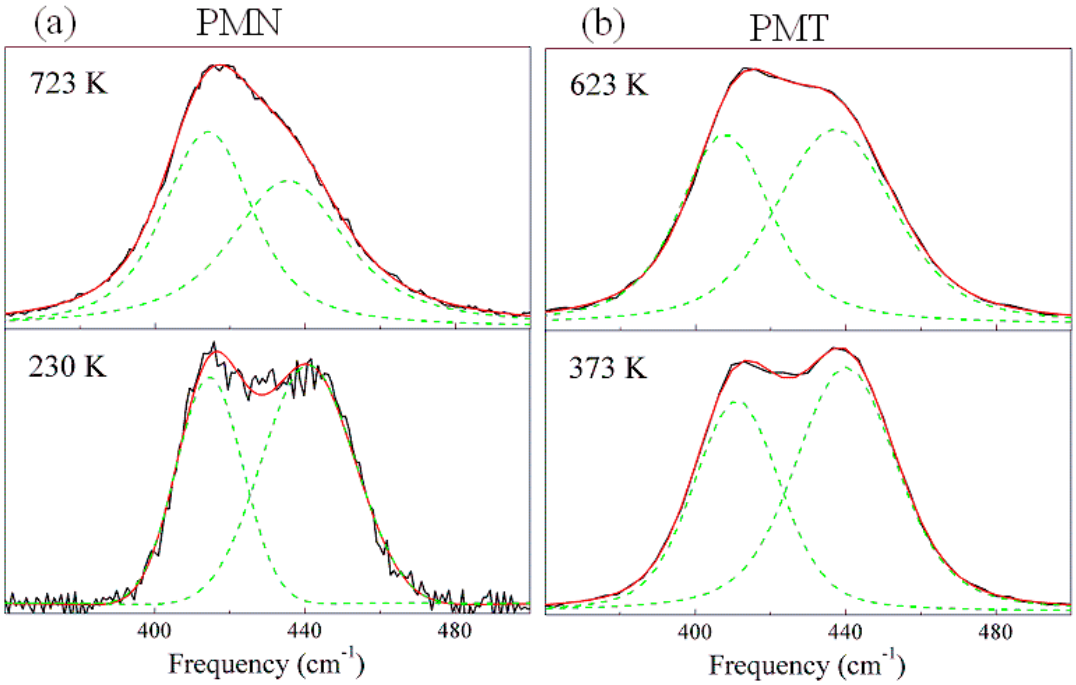


Figure 6.26: (a) PMN spectrum at 723 K (top) and at 230 K (bottom). (b) PMT spectra at 623 K (top) and at 373 K (bottom). The red line is fit resulting from the model described in the text. Dashed lines show the individual contributions corresponding to the E_1 and A_1 components.

of clarity, the spectra have been normalized on top of the low-frequency component.

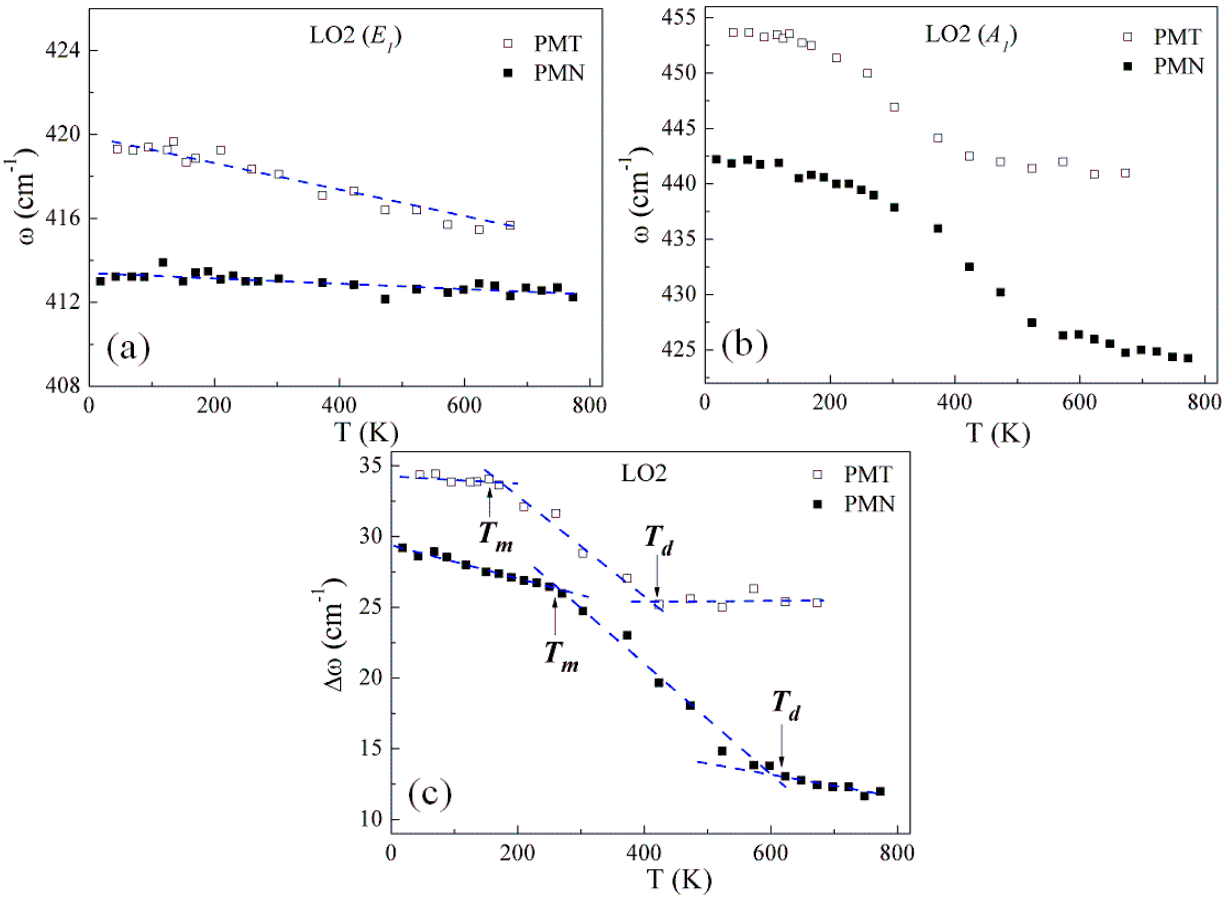


Figure 6.27: Temperature dependence of the E_1 (a) and A_1 (b) frequencies together with $\Delta\omega = \omega(A_1) - \omega(E_1)$ (c) for both PMN and PMT. The dashed lines are guides for the eyes.

It is impossible to reproduce the shape of the LO2 doublet with two lorentzians. The best fit is obtained with two Voigt functions in addition to a sloping background (Figure 6.26). This emphasizes an inhomogeneous broadening of the bands due to the structural disorder. The frequencies resulting from the fit are shown in Figure 6.27. The low-frequency component (Figure 6.27(a)) exhibits a linear temperature dependence in both materials with a larger slope for PMT. As directly evidenced by the raw data (Figure 6.25), the frequency of the higher band is much more affected by the temperature. It exhibits in both materials a stiff increase between T_m and T_d. This effect is more clear when one plots the frequency shift between the two lines, $\Delta\omega = \omega(A_1) - \omega(E_1)$ (Figure 6.27(c)). This representation has the advantage of avoiding the errors due to slight frequency drifts of the spectrometer. According to the anisotropic dielectric constant model developed by Hlinka *et al.* [153], we associated the low- and high-frequency lines of the LO2 doublet to the E_1 and A_1 modes, respectively. Similarly to the soft mode, the splitting of LO2 persists well above T_d, suggesting that the local structural disorder remains up to very high temperature as already proposed [149].

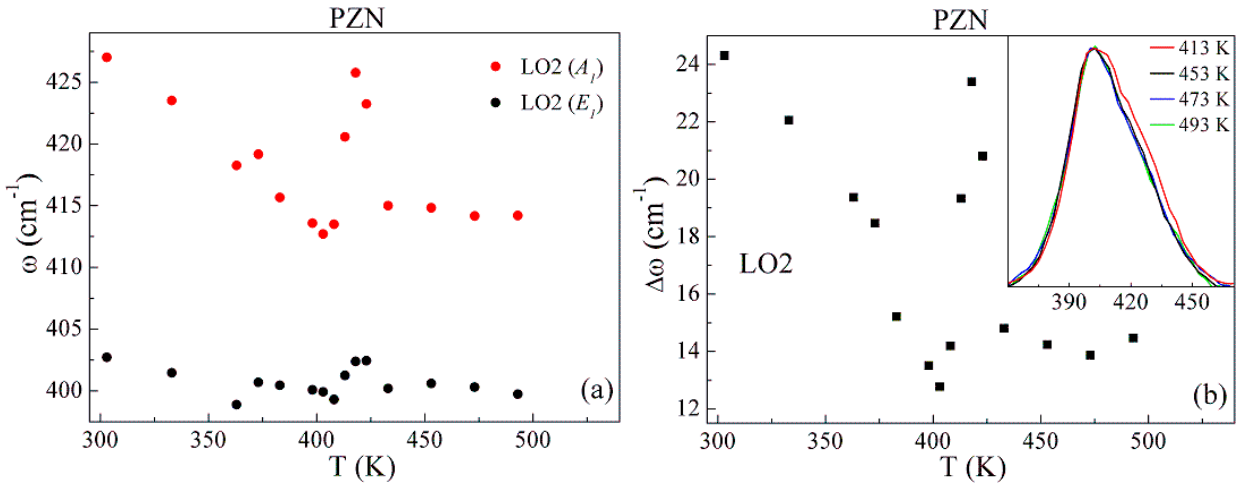


Figure 6.28: Temperature dependence of the E_1 and A_1 (a) and $\Delta\omega = \omega(A_1) - \omega(E_1)$ (b) for PZN. The inset shows the evolution of the A_1 component near T_m.

The data analysis in PZN was done exactly the same way as that for PMN and PMT (same fitting functions and same fitting procedure). Similarly to PMN and PMT, the E_1 component behaves normally (Figure 6.28(a)). However, and contrary to the cubic relaxors, a sharp but reliable anomaly is observed in the temperature dependence of the A_1-component at $T_m \approx 415\,\mathrm{K}$ where the long range transition from paraelectric to ferroelectric state takes place [73]. This transition-like feature is also clearly visible in a plot of $\Delta\omega = \omega(A_1) - \omega(E_1)$ (Figure 6.28(b)). Unfortunately, owing to possible sample damage, we stop our experiments at $\sim 500\,\mathrm{K}$ and thus did not reach $T_d \approx 740\,\mathrm{K}$. However, a quick observation on the raw data shows that the spectra above T_m are all very similar and that the splitting rather develops around T_m or slightly above (inset of Figure 6.28(b)). This situation is clearly different from that of PMN and PMT where the A_1 component starts to increase around T_d and is clearly visible between T_d and T_m. This probably means that the structural disorder is weaker in PZN, thus limiting frustration effect, and consequently favoring a long range order transition near T_m.

6.4.3 LO1

The last longitudinal band to be discussed in Figure 6.23 is the LO1 at low frequency. This band is clearly asymmetric in the three samples and cannot be fitted by a single l"'orentzian or gaussian. This asymmetry likely arises from a superposition of the E_1 and A_1 components of the LO1 doublet which cannot be resolved in our experiment. It follows that the frequency of the peak maximum of the band constitutes a measurement of the E_1 component. Indeed the frequency compares very well to that extracted from IR reflectivity [153], at least in PMN.

Owing to the above, we used a Breit-Wigner-Fano (BWF) formula [169, 170] defined in

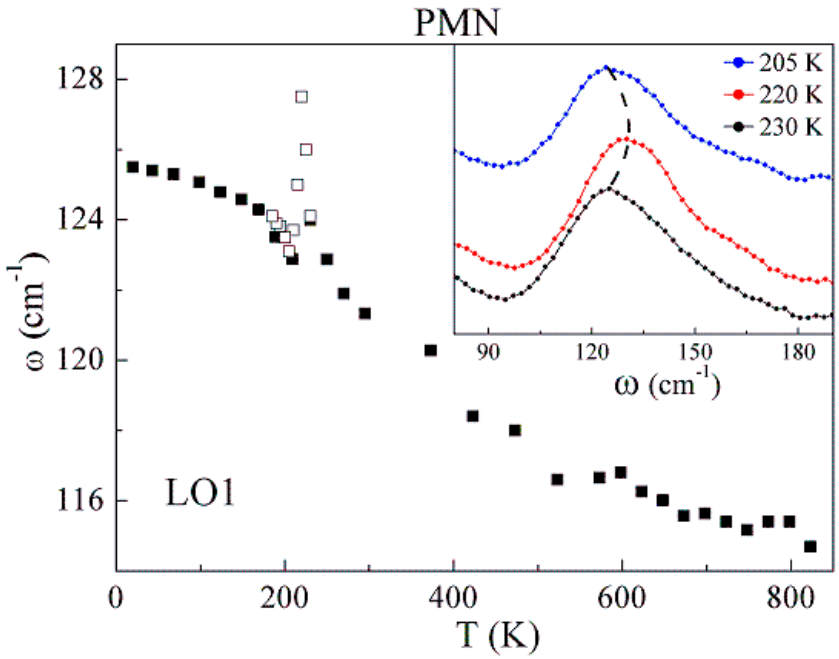


Figure 6.29: Temperature dependence of the frequency of the E_1-component of LO1 in PMN. The inset shows the HRS spectra at three different temperatures surrounding $T_f \approx 220\,\mathrm{K}$.

equation (6.5) and a sloping background to fit the data in PMN. In order to avoid dispersion in the fitting parameters, the asymmetry factor α was kept constant for all temperatures. This asymmetric function reproduces well the data over the whole investigated temperature range and the resulting frequencies at the maximum of the band (full symbols) are plotted in Figure 6.29. A weak anomaly is seen near the freezing temperature T_f that is, the temperature at which a ferroelectric phase transition is observed under an applied electric field[1]. To confirm this observation, another high resolution set of data was performed on the same PMN sample in the temperature interval between 185 and 230 K with a 5 K step. The same fitting model was used to extract the peak maximum and the results are shown by the open symbols in Figure 6.29. The two sets of data overlap at identical temperatures ensuring that these results are reproducible. The frequency of the E_1 component of LO1 exhibits a sharp transition-like feature near $T_f \approx 220\,\mathrm{K}$. This effect can be directly seen from the raw data presented in the inset of Figure 6.29.

To fit the LO1 mode in PMT and PZN, it is preferable to use a gaussian-asymmetric function

[1]In our experiments, no external field was applied but the strong light source incoming onto the sample could eventually induce displacements and thus acts as an applied external electric field. However, our HRS spectra are so similar to those extracted from IR-reflectivity at zero field [153] that this effect, if exists, can be neglected.

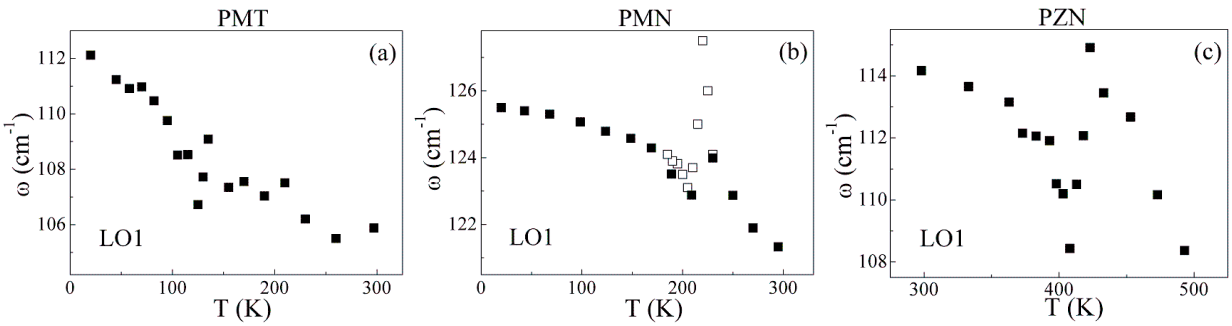


Figure 6.30: Temperature dependence of the frequency of the E_1-component of the LO1 mode of PMT (a), PMN (b) and PZN (c).

$$I(\omega) = I_0 \exp^{-\frac{1}{2}\left(\frac{\omega-\omega_0}{\sigma+\alpha\sqrt{\omega-\omega_0}}\right)^2} \times[n(\omega)+1] \quad , \tag{6.10}$$

where ω_0 is the peak frequency, σ is the gaussian width, I_0 the peak intensity, and α a coefficient relating to the degree of asymmetry of the line. This function provides better fits than the BWF function used previously in PMN. Similar results (although more dispersed) can be obtained by a simple fit of the points around the maximum with a polynomial function. The results for the three samples are summarized in Figure 6.30. A transition-like feature on LO1(E_1) is observed in PMN and PZN, but not in PMT. In PZN, the anomaly is similar to that observed on LO2 and most likely associates with the long-range paraelectric-ferroelectric phase transition. Finally in PMT, no field-induced ferroelectric phase transition has been reported near the temperature corresponding to the maximum of ϵ ($\approx 170\,\mathrm{K}$), and our results on LO1 does not show any anomaly in that temperature range (Figure 6.30(a)).

6.4.4 Conclusion

The eigenvectors for the three F_{1u} modes shown in Figure 6.1 apply for the three TOs, but it is not clear whether this picture is true for the LOs. However, it is tempting to relate the sharp anomaly on LO1(E_1) in PMN at $T_f \approx 220\,\mathrm{K}$ to the hardening of the soft TO1 mode observed in Raman scattering below T_f [171]. In addition, we have shown in previous section that the non-polar F_{2u} vibration has a normal temperature behavior. It probably means that the oxygen atoms play a minor role in the structural modifications of cubic relaxors. As LO3 exhibits the weakest anomalies with temperature, its eigenvectors likely involve preferentially the oxygen atoms. This corresponds to the Axe mode in Figure 6.1 which associates to the hardest F_{1u}-symmetry vibration (TO3). These general considerations suggest that TO$_i$ associates with LO$_i$ (i = 1,2,3) in cubic lead-based relaxors. Contrary to PZN, there is no long range order transition at T_f in PMN. This is probably the reason why the sharp anomaly observed at T_f in the latter is not reproduced by any other LO

mode (nor F_{2u}). From our simple eigenvectors description (Figure 6.1), the lead atoms have the major weight in the low-frequency F_{1u}-vibration (Last mode in Figure 6.1). It is thus likely that this transition-like anomaly relates to a local peculiar behavior (in the PNRs ?) at the A-site keeping the average structure unchanged. Indeed, the long range ordering in PZN translates into a sharp maximum of the SHG signal around $T_f \approx 385\,\mathrm{K}$ (Figure 6.31(b)). On the contrary, the continuous increase of the SHG in PMN (Figure 6.31(a)) rather supports the idea of local distortions in the disordered PNRs. Still, within our simple eigenvector description, LO2 should associate to the Slater mode (Figure 6.1). Assuming that oxygens are weakly involved in the structural process, the hardening and

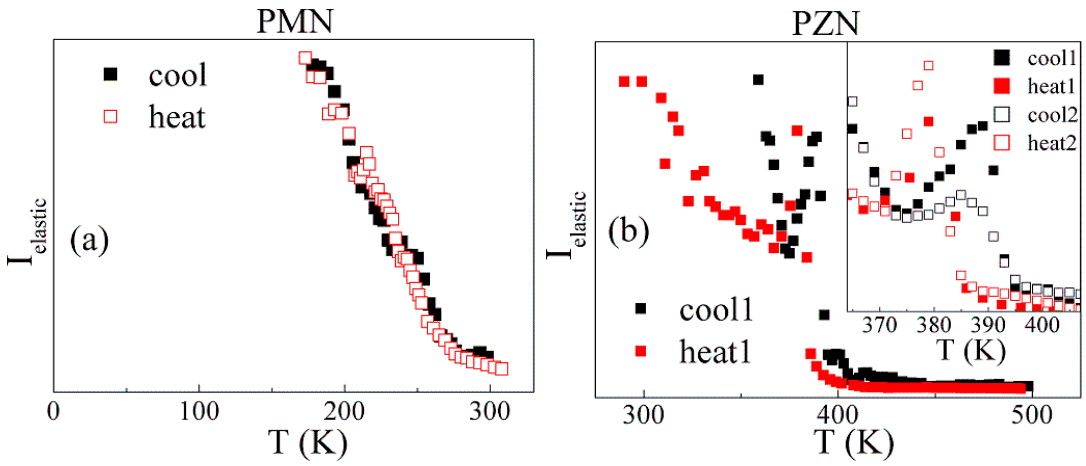


Figure 6.31: The SHG (elastic contribution in HRS) as a function of temperature in PMN (a) and PZN (b) emphasizing a sharp maximum at $T_f \approx 385\,\mathrm{K}$ in the latter. The inset shows the hysteresis behavior of the SHG signal in PZN.

the strong intensity increase of the LO2(A_1)-component in PMN and PMT (Figure 6.25 and 6.27) could thus be related to either a growth of a polarization component on the B-site between T_d and T_m or to an increase of the polar ordering of the B-atoms within the PNRs, or both. In PMN and PMT, the splitting remains well above T_d showing that the structural disorder persists up to the highest temperature measured ($\sim 750\,\mathrm{K}$). It is more pronounced in PMT than in PMN, and very weak in PZN. We conclude that the shape of the LO2-doublet could provide an indirect way to get information on the local structural disorder (most likely at the B-site). It seems from these results that the bigger the splitting, the higher the structural distortions and frustration, and the lower the value of the dielectric constant at T_m (At 100 kHz, $\epsilon_{PMT} \approx 5000$ [55], $\epsilon_{PMN} \approx 12000$ [43] and $\epsilon_{PZN} \approx 45000$ [69]).

6.5 Summary of HRS modes

6.5.1 Assignment of the modes

The results of the mode assignment of the HRS spectra of PMN and PMT are shown in Figure 6.32. In case of PMN, we choose three spectra obtained in three different scattering geometries which compile the full set of vibrations. The soft TO1(E_1) mode below 50 cm^{-1} is not shown. For the two other TOs, some interrogations remain because these modes are

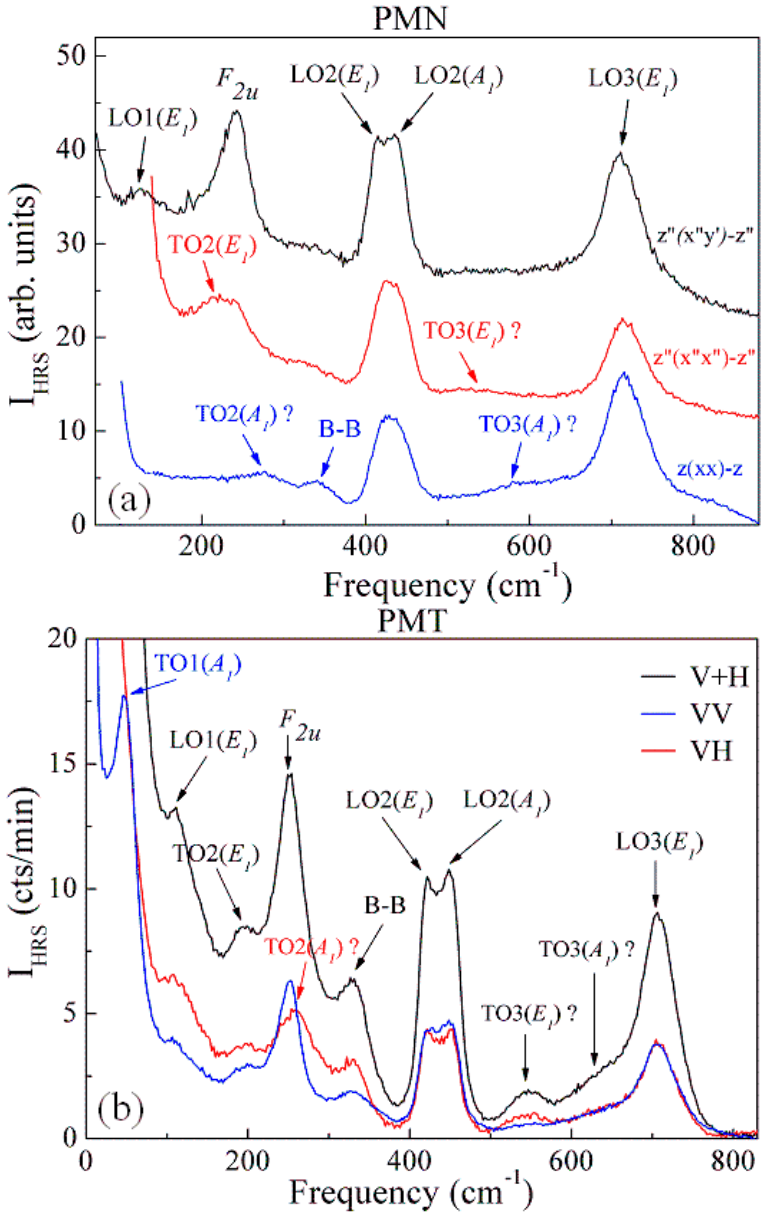


Figure 6.32: The full set of HRS vibrations in PMN (a) and PMT (b).

weak and/or broad, and often hidden by the strong LOs or F_{2u} vibrations. The unknown vibration (U-mode) discussed in section 6.2 has been tentatively associated to TO2(A_1), because its frequency matches with IR-reflectivity expectations. Same for TO3 (E_1 and A_1 components) whose observation is very difficult in HRS. Finally, the A_1-component of LO1

was not directly observed but we presume it lies on the high frequency wing of the LO1 asymmetric line. In PMT, the polar modes are narrower than in PMN, and the HRS spectra are easier to describe. Figure 6.32(b) shows the spectra with $q \parallel [001]$ with and without polarization analysis. The TO2 (A_1 and E_1) and TO3(E_1) are clearly visible. The broad feature centered around 625 cm^{-1} is tentatively assigned to TO3(A_1). In both samples, we did not see the high frequency component (A_1) of the third longitudinal mode (LO3).

It appears from these results that the three F_{1u}-modes of the cubic phase are splitted into two components. This constitutes a vibrational evidence of the local structural distortions from the average cubic phase, which characterize these materials. The splitting into two modes is also compatible with the anisotropic dielectric constant model developed in [153]. Within this framework, the existence of a local electrical polarization lifts the cubic selection rules leading to vibrations whose eigenvectors are either $\parallel$ (singly-degenerated A_1 component) or $\perp$ (doubly-degenerated E_1 component) to the polarization axis.

6.5.2 Relation to dielectric properties

Table 6.4: Frequencies and damping parameters of PMN and PMT modes obtained from HRS spectra at room temperature. The PMN parameters are compared with the corresponding values obtained from the fit of the IR reflectivity spectra [153].

		PMN					PMT		
		IR		HRS			HRS		
		ω (cm^{-1})	Γ (cm^{-1})	ω (cm^{-1})	Γ (cm^{-1})	$\Delta\epsilon_\sigma$	ω (cm^{-1})	Γ (cm^{-1})	$\Delta\epsilon_\sigma$
TO1	E_1			**35.9***	39.7*		**30.7***	20*	
	A_1	63.8	32.5	**47.1***	21.4*	328.7	**55.45***	30.5*	318.5
LO1	E_1	120.4	19.8	**121.3**	33.5		**105.9**	34.4	
	A_1	**166.6**	95.1				**146****		
TO2	E_1	221.4	53.9	**224**	47		**191.6**	23	
	A_1	284	53.8	**274**	55.3	15.8	**258.6**	41.2	18.0
LO2	E_1	409.7	15.1	**413.1**	26.7		**418.1**	26.9	
	A_1	461.5	4.8	**437.8**	35.1		**446.9**	31.6	
TO3	E_1	**545.8**	80.5	530?			**543.8**	38.6	
	A_1	**603.8**	117.3	590?		2.0	**626.3**	73.5	1.2
LO3	E_1	714.6	35.8	**715.7**	125.4		**704.4**	60.4	
	A_1	**757.2**	160.1						
B-B		335	55	340	47.1		332.9	32	
F_{2u}				247	40		250.9	31.8	

* Values at 748 K.
** From [155].
The values in bold are the most reliable ones.

Table 6.4 summarizes the frequency and damping of the HRS modes of PMN and PMT. In PMN, the IR-reflectivity results are also shown for comparison. All the values correspond to room temperature data except for TO1 taken at 748 K. Assuming no temperature

dependence for all the modes but TO1, the oscillator strengths $\Delta\epsilon_\sigma$ of the three polar vibrations at 748 K given in Table 6.4 are deduced from the TO-LO splittings with the formula [177]

$$\Delta\epsilon_\sigma = \frac{1}{3}\epsilon_\infty \left[\frac{\omega_{\sigma LO}^2 - \omega_{\sigma TO}^2}{\omega_{\sigma TO}^2} \prod_{i\neq\sigma} \frac{\omega_{iLO}^2 - \omega_{\sigma TO}^2}{\omega_{iTO}^2 - \omega_{\sigma TO}^2}\right]_{A_1} + \frac{2}{3}\epsilon_\infty \left[\frac{\omega_{\sigma LO}^2 - \omega_{\sigma TO}^2}{\omega_{\sigma TO}^2} \prod_{i\neq\sigma} \frac{\omega_{iLO}^2 - \omega_{\sigma TO}^2}{\omega_{iTO}^2 - \omega_{\sigma TO}^2}\right]_{E_1}, \tag{6.11}$$

with $\epsilon_\infty = 5.75$ for PMN and 4.75 for PMT.

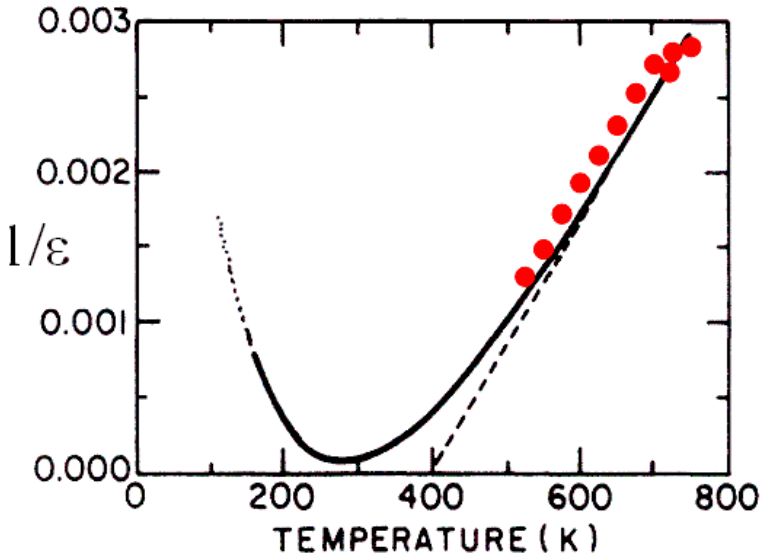


Figure 6.33: Temperature dependence of the inverse of the dielectric constant in PMN. The circles represents the values of $1/\epsilon$ calculated from the HRS polar modes.

Table 6.5: Frequencies and damping parameters of the E_1 and A_1 modes of the TO1 doublet of PMN obtained from HRS spectra at different temperatures.

	E_1		A_1	
T (K)	ω (cm^{-1})	Γ (cm^{-1})	ω (cm^{-1})	Γ (cm^{-1})
748	35.9	39.7	47.1	21.4
723	35.6	42.1	47.1	22.9
710	34.6	42.4	46.5	21.6
698	35.1	46.2	46.4	23.5
673	33.5	46.7	46	23.4
648	31.7	49	45.5	23.6
623	30	51	45	25.7
598	28.4		44.6	27.7
573	26.5		44.3	30.7
548	24.3		43.8	33.8
523	22.5		43.8	36.1

The value of $\Delta\epsilon_1$ in PMN is very close to that calculated in section 6.3, (305) as well as the static dielectric constant $\epsilon(0) = 353$ which should be compared to 330. Figure 6.33 shows $1/\epsilon(0)$ calculated from Table 6.4 and the temperature dependence of TO1 (Table

6.5). The data from dielectric measurements at 100 kHz [44] are also shown for comparison. Our data reproduces very well the dielectric ones at least in that temperature range within few % error, emphasizing the good accuracy of the HRS measurements. In PMT, the comparison with dielectric measurement is more difficult owing to differences on the values and temperature dependence of $\epsilon(0)$ reported in literature.

6.5.3 Comparison with Raman

The comparison between HRS and Raman spectra is shown in Figure 6.34. The broad Ra-

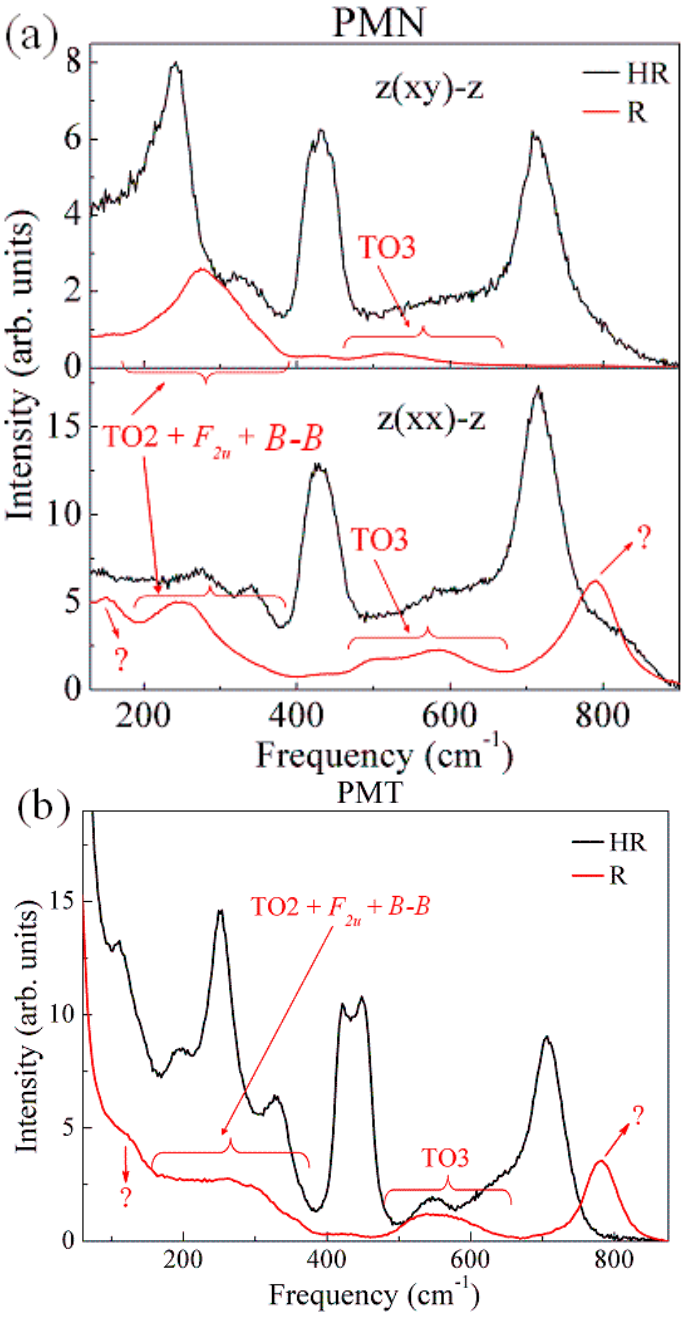


Figure 6.34: (a) Polarized HRS and RS spectra of [001] PMN crystal. (b) Unpolarized HRS and RS spectra of [001] PMT crystal.

man feature centered around 250 cm^{-1} corresponds to the frequency domain where TO2(E_1 and A_1), F_{2u}, and the B-$B_¡$ mode dominate the HRS spectra. However, it is impossible to account for the shape of this feature (in VV, VH and V+H) taking into consideration four modes, fixing their frequencies to that given by the HRS analysis. Therefore, the Raman signal cannot be explained by a simple superposition of these modes. The region between 500 - 650 cm^{-1} corresponds to that of TO3 vibrations. However, the HRS data in that region are very poor and do not allow any quantitative description of the Raman spectra. Interestingly, LO2 and LO3(E_1) translate into a minimum intensity in the Raman spectra, as expected from mutual exclusion rule in centro-symmetric situations. The Raman bands around 150 cm^{-1} and 800 cm−1 (pointed with interrogation marks) could eventually be assigned to LO1(A_1) and LO3(A_1). However, their strong intensity in RS is hard to be explained and the possibility that they correspond to additional vibrations only active in Raman cannot be excluded.

Conclusions and Perspectives

1) Conclusions:

In this PhD work, different experimental techniques are used to study the structural and dynamical properties of lead-based relaxors and ferroelectric materials at different scales. Starting from neutron diffraction which investigates long range order in the crystal structure to XAFS which can probe the local environment of a chosen atom in the perovskite and finally hyper-Raman scattering which is a powerful spectroscopic technique to study the lattice vibrations.

The first experimental part discusses the results obtained at large scale facilities (ILL and ESRF). High temperature and high pressure neutron powder diffraction experiments were performed to study the P-T phase diagram of the prototype material lead titanate PT. A high temperature high pressure XAFS experiment was performed in transmission geometry at the Zr K edge to study the ferroelectric-paraelectric phase transition at the atomic scale in $PbZr_{0.52}Ti_{0.48}O_3$. Another XAFS study was performed to characterize the effect of applied external electric field on the piezoelectric properties of PZN single crystal. These experiments yield the following conclusions:

- The disappearance of particular reflections, $(h, k, 2l)$ with h and k odd, at the F-P transition temperature $T_C \approx 763\,\mathrm{K}$ and at the transition pressure (~ 13 GPa) of PT. The high pressure phase is cubic with space group $Pm\bar{3}m$.

- In PZT, the static contribution of the Debye-Waller factor at Zr K edge disappears near 6-7 GPa at 300 K and around 5 GPa at 450 K. This suggests that pressure suppresses the disorder at the Zr-site. The decrease in σ^2_{Zr} is accompanied with the disappearance of the dipolar contribution in the PEFS region.

- Below the coercive field E_C of PZN, the Debye-Waller factor σ^2_{Zn} of the large Zn atom increases with the applied electric field while σ^2_{Nb} of the small Nb atom shows a decrease with the applied field. The increase in the DWF of the large cation occupying the B-site can be related to the increase in the distortion of the oxygen octahedra. The decrease in σ^2 of the small Nb cation is related to the alignment of the strong Nb-O dipole moments by the external applied electric field.

The second experimental part concerns hyper-Raman scattering in relaxors. This spectroscopy was widely used in the 80's and the 90's, mostly by H. Vogt and K. Inoue, to follow the temperature dependence of the soft modes and the central peak of ferroelectric materials. HRS in relaxors became possible recently owing to the advances in charge-coupled-device cameras and pulsed-laser technology. Still, HRS in relaxors remains a time-

demanding experiment. This arises from the very low damage threshold of these systems, which strongly limits the power of the incident beam into the sample. However, it appeared from the work presented in this manuscript that this spectroscopy, when it is feasible, it very nicely complements IR-Reflectivity and Raman scattering data on the vibrations. HRS was performed in PMN, PMT, and to a smaller extent, in PZN. We found that LO modes and silent modes are very efficient and thus rather easy to observe. TO modes are usually broad, which means that they are probably more affected by the disorder. Their intensities are weaker and they are sometimes hidden by the more intense contributions. Luckily, the scattering strength of the soft TO-mode benefits from a favorable population factor at low frequency (Bose-Einstein factor) and is easier to follow. These results lead to the following conclusions:

- In PMN, the spectroscopy allowed us to unambiguously identify the F_{2u}-symmetry vibration (silent mode) around 248 cm^{-1}. This mode shows no softening in the whole investigated temperature range from 20 K up to about 750 K.

- The local disorder traduces in the vibrational spectra by splitting into doublets of the three F_{1u} polar modes. The doublet structure remains up to the highest temperature investigated ($\sim$ 750 K) indicating that distortions from the cubic symmetry persist well above the Burns temperature.

- Soft mode splitting is clearly observed in both PMN and PMT. The lowest E_1 mode transforms from a vibrational mode (underdamped) above T_d to a relaxational feature (overdamped) below T_d. It softens towards the random field transition T_0 and reproduces the behavior of the dielectric constant. The temperature dependence of the soft mode intensity is compatible with the cubic selection rules, with however a particular temperature dependence of the diagonal tensor element a indicating that the latter is particularly sensitive to local structural changes.

- LO_i is linked to TO_i, with $i = 1$ to 3 and the Last, Slater, and Axe eigenvector pictures are consistent with our observations on LO1, LO2, and LO3, respectively. Within this framework, the splitting of LO2 would mostly be linked to disorder on the B-site. In addition, the more pronounced the splitting, the more important the disorder.

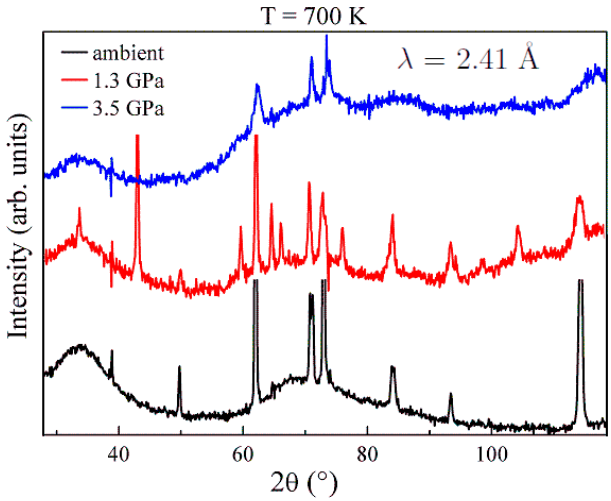
- In PZN, the long range order paraelectric-ferroelectric transition is seen by sharp anomalies at T_m in the temperature dependence of LO1 and LO2 (and most likely LO3). In PMN, this transition-like anomaly is only observed for LO1 at T_f. A possible explanation could be that local distortions involving (mainly) the lead atoms develop in the PNRs below T_f. The other modes are not (or at least much less) affected because this effect does not translate into a long-range order state and the PNRs

remain randomly oriented. This observation, together with that of a ferroelectric transition under electric field at T_f, suggests that at zero field, PMN is very close to instability. In PMT where the local distortions are larger (see discussion on LO2), there is no T_f (no evidence for a field-induced ferroelectric phase transition) and no transition-like anomaly on the LO modes was evidenced.

Hyper-Raman spectroscopy thus appears to be very powerful for the study of complex perovskites. The technique allows the soft polar modes to be followed down to very low frequency in the paraelectric phase. The local structural distortions give rise to departure from the HRS cubic selection rules, such as splitting of the polar modes and deviations from the calculated intensity ratios. These structural distortions strongly increase on cooling below T_d in PMN and PMT, but not in PZN. Depending on their amplitude near T_m (weak in PZN, larger in PMN and PMT), they are able to prevent the material from undergoing a ferroelectric transition. A deeper understanding of the origin of these vibrational behaviors and their relation to structure would deserve further theoretical and experimental investigations. Some ideas are summarized in the following part.

2) Perspectives:

- Perform high pressure high temperature neutron diffraction experiments to determine the P-T phase diagram of PT and PZT. Such experiments require the synthesis of special types of gaskets. Exploratory results obtained on PZT are shown in the Figure below



- Study the effect of applied electric field on X-ray diffraction patterns in PZT, lead free based materials and multiferroics.

- Intensity variations of the bands probed by vibrational spectroscopies are strongly correlated to structural changes. Hence, it would be highly desirable to develop a

structural model which could explain the very particular temperature dependence of the HRS intensities of the soft mode of PMN (Figure 6.18). A detailed understanding of the HRS selection rules (dependence on q and polarization of the scattered intensities) will likely shed light on the local structure of this material. Our experiments also suggest that the HRS selection rules of the low-frequency TO doublet are different in PMT (preliminary results are not shown in the manuscript) than in PMN (Figure 6.13). It would thus be interesting to perform HRS in an oriented single crystal of PMT and to compare with the situation in PMN.

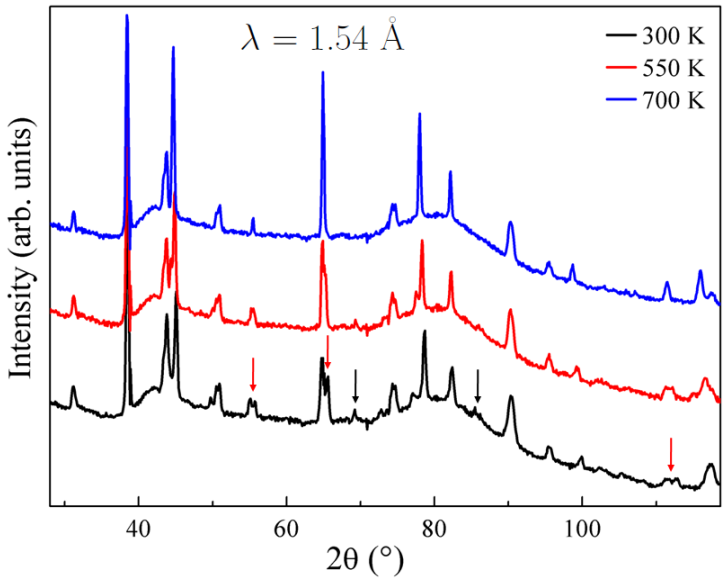
- Intensity calculations in PMN revealed that for measurements along [001] with $z(x'x')\bar{z}$ (VV) and $z(x'y')\bar{z}$ (VH), the components E_1 and A_1 of the soft mode are both almost inactive (Figure 6.20). This very peculiar situation provides a unique way to extract the temperature dependence of the second harmonic signal (SHG) and of the quasi-elastic component, otherwise hidden by the soft-mode. The measurement of the static and the relaxational components, will complement the available set of low-frequency HRS data. All these results will provide detailed information on the nature of the diffuse transition, as well on the dynamics of the PNRs below T_d.

- We found that the observation of the TOs (except the soft mode) is very difficult in complex perovskites. One possibility to circumvent the problem is to perform HRS under electric field. For sufficiently high electric field, we could also study the symmetry of the ferroelectric phase below T_f. For this experiment, it is not sure that one can access the soft mode, because the loss of a center of symmetry induced by the electric field translates into a strong second harmonic signal at zero frequency.

- Finally, HRS seems to be sensitive to the disorder on the B-site (LO2), and it could be interesting to perform the spectroscopy at very high temperature to see whether such a disorder disappears. However, HRS experiments above 800 K are usually difficult owing to the blackbody radiation which gives rise to a strong background. There exist technological solutions to reduce this contribution, and technical developments on the spectrometer are currently in progress.

Appendix

A High-Tempertaure Neutron Diffraction of $PbZr_{0.52}Ti_{0.48}O_3$

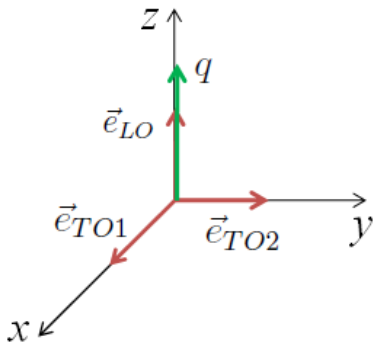


The black arrows correspond to the $(2h, 2k, l)$ reflections with l odd, which disappear above $T_C = 664\,\mathrm{K}$.

B Hyper-Raman Selection Rules in Cubic Relaxors: Detailed Calculations

The calculation of $R^2_{TO}(F_{1u})$, $R^2_{LO}(F_{1u})$, and $R^2(F_{2u})$ for different polarization geometries.

1) $q \parallel [001]$



$\vec{e}_{LO} \parallel [001] \Rightarrow R^{e_{LO}} = R^z$;
$\Rightarrow R^2_{LO} = |e^S R^z e^L e^L|^2$

$$\begin{cases} \vec{e}_{TO1} \parallel [100] \Rightarrow R^{e_{TO1}} = R^x; \\ \vec{e}_{TO2} \parallel [010] \Rightarrow R^{e_{TO2}} = R^y; \end{cases}$$

$\Rightarrow R^2_{TO} = |e^S R^x e^L e^L|^2 + |e^S R^y e^L e^L|^2$

a) For $z(xx)\bar{z}$, $e^S = e^L = [100]$.

$$R^2_{TO}(F_{1u}) = \left| \begin{pmatrix} 1 \\ 0 \\ 0 \end{pmatrix} R^x \begin{pmatrix} 1 \\ 0 \\ 0 \end{pmatrix} \begin{pmatrix} 1 \\ 0 \\ 0 \end{pmatrix} \right|^2 + \left| \begin{pmatrix} 1 \\ 0 \\ 0 \end{pmatrix} R^y \begin{pmatrix} 1 \\ 0 \\ 0 \end{pmatrix} \begin{pmatrix} 1 \\ 0 \\ 0 \end{pmatrix} \right|^2 = (R^x_{111})^2 + (R^y_{111})^2 = a^2$$

$$R^2_{LO}(F_{1u}) = \left| \begin{pmatrix} 1 \\ 0 \\ 0 \end{pmatrix} R^z \begin{pmatrix} 1 \\ 0 \\ 0 \end{pmatrix} \begin{pmatrix} 1 \\ 0 \\ 0 \end{pmatrix} \right|^2 = (R^z_{111})^2 = 0$$

$$R^2(F_{2u}) = \left| \begin{pmatrix} 1 \\ 0 \\ 0 \end{pmatrix} (R^x) \begin{pmatrix} 1 \\ 0 \\ 0 \end{pmatrix} \begin{pmatrix} 1 \\ 0 \\ 0 \end{pmatrix} \right|^2 + \left| \begin{pmatrix} 1 \\ 0 \\ 0 \end{pmatrix} (R^y) \begin{pmatrix} 1 \\ 0 \\ 0 \end{pmatrix} \begin{pmatrix} 1 \\ 0 \\ 0 \end{pmatrix} \right|^2$$
$$+ \left| \begin{pmatrix} 1 \\ 0 \\ 0 \end{pmatrix} (R^z) \begin{pmatrix} 1 \\ 0 \\ 0 \end{pmatrix} \begin{pmatrix} 1 \\ 0 \\ 0 \end{pmatrix} \right|^2 = 0$$

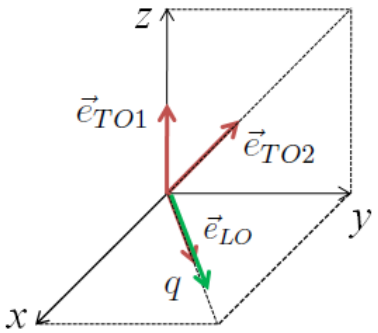
b) For $z(x'y')\bar{z}$, $e^S = [1\bar{1}0]$ and $e^L = [110]$.

$$R^2_{TO}(F_{1u}) = \left| \tfrac{1}{2\sqrt{2}} \begin{pmatrix} 1 \\ \bar{1} \\ 0 \end{pmatrix} R^x \begin{pmatrix} 1 \\ 1 \\ 0 \end{pmatrix} \begin{pmatrix} 1 \\ 1 \\ 0 \end{pmatrix} \right|^2 + \left| \tfrac{1}{2\sqrt{2}} \begin{pmatrix} 1 \\ \bar{1} \\ 0 \end{pmatrix} R^y \begin{pmatrix} 1 \\ 1 \\ 0 \end{pmatrix} \begin{pmatrix} 1 \\ 1 \\ 0 \end{pmatrix} \right|^2$$
$= \frac{1}{8}(R^x_{111} + R^x_{112} + R^x_{121} + R^x_{122} - R^x_{211} - R^x_{212} - R^x_{221} - R^x_{222})^2 + \frac{1}{8}(R^y_{111} + R^y_{112} + R^y_{121} + R^y_{122} - R^y_{211} - R^y_{212} - R^y_{221} - R^y_{222})^2 = \frac{1}{8}(a + b - 2b')^2 + \frac{1}{8}(a + b - 2b')^2 = (\frac{a+b-2b'}{2})^2$

$$R^2_{LO}(F_{1u}) = \left| \tfrac{1}{2\sqrt{2}} \begin{pmatrix} 1 \\ \bar{1} \\ 0 \end{pmatrix} R^z \begin{pmatrix} 1 \\ 1 \\ 0 \end{pmatrix} \begin{pmatrix} 1 \\ 1 \\ 0 \end{pmatrix} \right|^2$$
$$= \tfrac{1}{8}(R^z_{111} + R^z_{112} + R^z_{121} + R^z_{122} - R^z_{211} - R^z_{212} - R^z_{221} - R^z_{222})^2 = 0$$

$$R^2(F_{2u}) = \left| \tfrac{1}{2\sqrt{2}} \begin{pmatrix} 1 \\ \bar{1} \\ 0 \end{pmatrix} (R^x) \begin{pmatrix} 1 \\ 1 \\ 0 \end{pmatrix} \begin{pmatrix} 1 \\ 1 \\ 0 \end{pmatrix} \right|^2 + \left| \tfrac{1}{2\sqrt{2}} \begin{pmatrix} 1 \\ \bar{1} \\ 0 \end{pmatrix} (R^y) \begin{pmatrix} 1 \\ 1 \\ 0 \end{pmatrix} \begin{pmatrix} 1 \\ 1 \\ 0 \end{pmatrix} \right|^2$$
$$+ \left| \tfrac{1}{2\sqrt{2}} \begin{pmatrix} 1 \\ \bar{1} \\ 0 \end{pmatrix} (R^z) \begin{pmatrix} 1 \\ 1 \\ 0 \end{pmatrix} \begin{pmatrix} 1 \\ 1 \\ 0 \end{pmatrix} \right|^2 = \tfrac{1}{8}(c - 2c')^2 + \tfrac{1}{8}(c - 2c')^2 + 0 = \tfrac{1}{4}(c - 2c')^2$$

2) $q \parallel [110]$



$\vec{e}_{LO} \parallel [110] \Rightarrow R^{e_{LO}} = \frac{1}{\sqrt{2}}(R^x + R^y)$;
$\Rightarrow R^2_{LO} = \frac{1}{2}|e^S(R^x + R^y)e^L e^L|^2$

$$\begin{cases} \vec{e}_{TO1} \parallel [001] \Rightarrow R^{e_{TO1}} = R^z; \\ \vec{e}_{TO2} \parallel [1\bar{1}0] \Rightarrow R^{e_{TO2}} = \frac{1}{\sqrt{2}}(R^x - R^y); \end{cases}$$
$\Rightarrow R^2_{TO} = |e^S R^z e^L e^L|^2 + \frac{1}{2}|e^S(R^x - R^y)e^L e^L|^2$

a) For $x'(zz)\bar{x}'$, $e^S = e^L = [001]$.

$$R^2_{TO}(F_{1u}) = \left| \begin{pmatrix} 0 \\ 0 \\ 1 \end{pmatrix} R^z \begin{pmatrix} 0 \\ 0 \\ 1 \end{pmatrix} \begin{pmatrix} 0 \\ 0 \\ 1 \end{pmatrix} \right|^2 + \tfrac{1}{2} \left| \begin{pmatrix} 0 \\ 0 \\ 1 \end{pmatrix} (R^x - R^y) \begin{pmatrix} 0 \\ 0 \\ 1 \end{pmatrix} \begin{pmatrix} 0 \\ 0 \\ 1 \end{pmatrix} \right|^2$$
$$= (R^Z_{333})^2 + \tfrac{1}{2}(R^x_{333} - R^y_{333})^2 = a^2$$

$$R^2_{LO}(F_{1u}) = \tfrac{1}{2} \left| \begin{pmatrix} 0 \\ 0 \\ 1 \end{pmatrix} (R^x + R^y) \begin{pmatrix} 0 \\ 0 \\ 1 \end{pmatrix} \begin{pmatrix} 0 \\ 0 \\ 1 \end{pmatrix} \right|^2 = \tfrac{1}{2}(R^x_{333} + R^y_{333})^2 = 0$$

$$R^2(F_{2u}) = \left| \begin{pmatrix} 0 \\ 0 \\ 1 \end{pmatrix} (R^x) \begin{pmatrix} 0 \\ 0 \\ 1 \end{pmatrix} \begin{pmatrix} 0 \\ 0 \\ 1 \end{pmatrix} \right|^2 + \left| \begin{pmatrix} 0 \\ 0 \\ 1 \end{pmatrix} (R^y) \begin{pmatrix} 0 \\ 0 \\ 1 \end{pmatrix} \begin{pmatrix} 0 \\ 0 \\ 1 \end{pmatrix} \right|^2$$
$$+ \left| \begin{pmatrix} 0 \\ 0 \\ 1 \end{pmatrix} (R^z) \begin{pmatrix} 0 \\ 0 \\ 1 \end{pmatrix} \begin{pmatrix} 0 \\ 0 \\ 1 \end{pmatrix} \right|^2 = 0$$

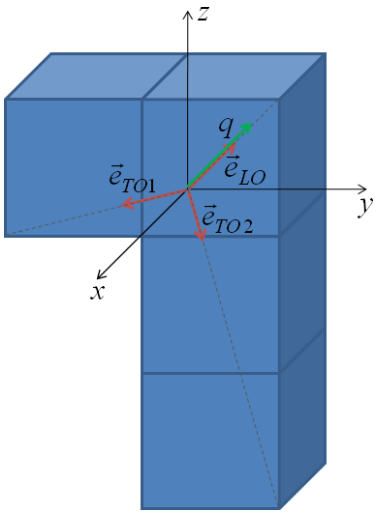
b) For $x'(y'y')\bar{x'}$, $e^S = [1\bar{1}0]$ and $e^L = [1\bar{1}0]$.

$$R^2_{TO}(F_{1u}) = \left| \tfrac{1}{2\sqrt{2}} \begin{pmatrix} 1 \\ \bar{1} \\ 0 \end{pmatrix} R^z \begin{pmatrix} 1 \\ \bar{1} \\ 0 \end{pmatrix} \begin{pmatrix} 1 \\ \bar{1} \\ 0 \end{pmatrix} \right|^2 + \tfrac{1}{2} \left| \tfrac{1}{2\sqrt{2}} \begin{pmatrix} 1 \\ \bar{1} \\ 0 \end{pmatrix} (R^x - R^y) \begin{pmatrix} 1 \\ \bar{1} \\ 0 \end{pmatrix} \begin{pmatrix} 1 \\ \bar{1} \\ 0 \end{pmatrix} \right|^2$$
$$= \tfrac{1}{8}(R^z_{111} - R^z_{112} - R^z_{121} + R^z_{122} - R^z_{211} + R^z_{212} + R^z_{221} - R^z_{222})^2$$
$$+ \tfrac{1}{2} \times \tfrac{1}{8}[(R^x_{111} - R^x_{112} - R^x_{121} + R^x_{122} - R^x_{211} + R^x_{212} + R^x_{221} - R^x_{222}$$
$$- (R^y_{111} - R^y_{112} - R^y_{121} + R^y_{122} - R^y_{211} + R^y_{212} + R^y_{221} - R^y_{222})]^2$$
$$= 0 + \tfrac{1}{2} \times \tfrac{1}{8}\left[(a+b+2b') - (-a-b-2b')\right]^2 = (\tfrac{a+b+2b'}{2})^2$$

$$R^2_{LO}(F_{1u}) = \tfrac{1}{2} \left| \tfrac{1}{2\sqrt{2}} \begin{pmatrix} 1 \\ \bar{1} \\ 0 \end{pmatrix} (R^x + R^y) \begin{pmatrix} 1 \\ \bar{1} \\ 0 \end{pmatrix} \begin{pmatrix} 1 \\ \bar{1} \\ 0 \end{pmatrix} \right|^2$$
$$= \tfrac{1}{2} \times \tfrac{1}{8}[(R^x_{111} - R^x_{112} - R^x_{121} + R^x_{122} - R^x_{211} + R^x_{212} + R^x_{221} - R^x_{222}$$
$$+ (R^y_{111} - R^y_{112} - R^y_{121} + R^y_{122} - R^y_{211} + R^y_{212} + R^y_{221} - R^y_{222})]^2$$
$$= \tfrac{1}{2} \times \tfrac{1}{8}\left[(a+b+2b') + (-a-b-2b')\right]^2 = 0$$

$$R^2(F_{2u}) = \left| \tfrac{1}{2\sqrt{2}} \begin{pmatrix} 1 \\ \bar{1} \\ 0 \end{pmatrix} (R^x) \begin{pmatrix} 1 \\ \bar{1} \\ 0 \end{pmatrix} \begin{pmatrix} 1 \\ \bar{1} \\ 0 \end{pmatrix} \right|^2 + \left| \tfrac{1}{2\sqrt{2}} \begin{pmatrix} 1 \\ \bar{1} \\ 0 \end{pmatrix} (R^y) \begin{pmatrix} 1 \\ \bar{1} \\ 0 \end{pmatrix} \begin{pmatrix} 1 \\ \bar{1} \\ 0 \end{pmatrix} \right|^2$$
$$+ \left| \tfrac{1}{2\sqrt{2}} \begin{pmatrix} 1 \\ \bar{1} \\ 0 \end{pmatrix} (R^z) \begin{pmatrix} 1 \\ \bar{1} \\ 0 \end{pmatrix} \begin{pmatrix} 1 \\ \bar{1} \\ 0 \end{pmatrix} \right|^2 = \tfrac{1}{8}(c+2c')^2 + \tfrac{1}{8}(c+2c')^2 + 0 = \tfrac{1}{4}(c+2c')^2$$

3) $q \parallel [111]$



$\vec{e}_{LO} \parallel [111] \Rightarrow R^{e_{LO}} = \frac{1}{\sqrt{3}}(R^x + R^y + R^z)$;
$\Rightarrow R^2_{LO} = \frac{1}{3}|e^S(R^x + R^y + R^z)e^L e^L|^2$

$$\begin{cases} \vec{e}_{TO1} \parallel [1\bar{1}0] \Rightarrow R^{e_{TO1}} = \frac{1}{\sqrt{2}}(R^x - R^y); \\ \vec{e}_{TO2} \parallel [11\bar{2}] \Rightarrow R^{e_{TO2}} = \frac{1}{\sqrt{6}}(R^x + R^y - 2R^z); \end{cases}$$

$\Rightarrow R^2_{TO} = \frac{1}{2}|e^S(R^x - R^y)e^L e^L|^2 + \frac{1}{6}|e^S(R^x + R^y - 2R^z)e^L e^L|^2$

a) For $z''(y'y')\bar{z''}$, $e^S = [1\bar{1}0]$ and $e^L = [1\bar{1}0]$.

$$R^2_{TO}(F_{1u}) = \tfrac{1}{2}\left|\tfrac{1}{2\sqrt{2}}\begin{pmatrix}1\\ \bar{1}\\ 0\end{pmatrix}(R^x - R^y)\begin{pmatrix}1\\ \bar{1}\\ 0\end{pmatrix}\begin{pmatrix}1\\ \bar{1}\\ 0\end{pmatrix}\right|^2 + \tfrac{1}{6}\left|\tfrac{1}{2\sqrt{2}}\begin{pmatrix}1\\ \bar{1}\\ 0\end{pmatrix}(R^x + R^y - 2R^z)\begin{pmatrix}1\\ \bar{1}\\ 0\end{pmatrix}\begin{pmatrix}1\\ \bar{1}\\ 0\end{pmatrix}\right|^2$$
$$= \tfrac{1}{2}\times\tfrac{1}{8}\left[(a+b+2b') - (-a-b-2b')\right]^2 + \tfrac{1}{6}\times\tfrac{1}{8}\left[(a+b+2b') + (-a-b-2b') + 0\right]^2$$
$$= (\tfrac{a+b+2b'}{2})^2$$

$$R^2_{LO}(F_{1u}) = \tfrac{1}{3}\left|\tfrac{1}{2\sqrt{2}}\begin{pmatrix}1\\ \bar{1}\\ 0\end{pmatrix}(R^x + R^y + R^z)\begin{pmatrix}1\\ \bar{1}\\ 0\end{pmatrix}\begin{pmatrix}1\\ \bar{1}\\ 0\end{pmatrix}\right|^2$$
$$= \tfrac{1}{3}\times\tfrac{1}{8}\left[(a+b+2b') + (-a-b-2b') + 0\right]^2 = 0$$

$$R^2(F_{2u}) = \left|\tfrac{1}{2\sqrt{2}}\begin{pmatrix}1\\ \bar{1}\\ 0\end{pmatrix}(R^x)\begin{pmatrix}1\\ \bar{1}\\ 0\end{pmatrix}\begin{pmatrix}1\\ \bar{1}\\ 0\end{pmatrix}\right|^2 + \left|\tfrac{1}{2\sqrt{2}}\begin{pmatrix}1\\ \bar{1}\\ 0\end{pmatrix}(R^y)\begin{pmatrix}1\\ \bar{1}\\ 0\end{pmatrix}\begin{pmatrix}1\\ \bar{1}\\ 0\end{pmatrix}\right|^2$$
$$+ \left|\tfrac{1}{2\sqrt{2}}\begin{pmatrix}1\\ \bar{1}\\ 0\end{pmatrix}(R^z)\begin{pmatrix}1\\ \bar{1}\\ 0\end{pmatrix}\begin{pmatrix}1\\ \bar{1}\\ 0\end{pmatrix}\right|^2 = \tfrac{1}{8}(c+2c')^2 + \tfrac{1}{8}(c+2c')^2 + 0 = \tfrac{1}{4}(c+2c')^2$$

b) For $z''(y'x'')\bar{z''}$, $e^S = [11\bar{2}]$ and $e^L = [1\bar{1}0]$.

$$R^2_{TO}(F_{1u}) = \tfrac{1}{2}\left|\tfrac{1}{2\sqrt{6}}\begin{pmatrix}1\\ 1\\ \bar{2}\end{pmatrix}(R^x - R^y)\begin{pmatrix}1\\ \bar{1}\\ 0\end{pmatrix}\begin{pmatrix}1\\ \bar{1}\\ 0\end{pmatrix}\right|^2 + \tfrac{1}{6}\left|\tfrac{1}{2\sqrt{6}}\begin{pmatrix}1\\ 1\\ \bar{2}\end{pmatrix}(R^x + R^y - 2R^z)\begin{pmatrix}1\\ \bar{1}\\ 0\end{pmatrix}\begin{pmatrix}1\\ \bar{1}\\ 0\end{pmatrix}\right|^2$$
$$= \tfrac{1}{2}\times\tfrac{1}{24}\left[(a+b-2b') - (a+b-2b')\right]^2 + \tfrac{1}{6}\times\tfrac{1}{24}\left[(a+b-2b') + (a+b-2b') - 2(-2b-2b)\right]^2$$
$$= (\tfrac{a+5b-2b'}{6})^2$$

$$R^2_{LO}(F_{1u}) = \tfrac{1}{3}\left|\tfrac{1}{2\sqrt{6}}\begin{pmatrix}1\\ 1\\ \bar{2}\end{pmatrix}(R^x + R^y + R^z)\begin{pmatrix}1\\ \bar{1}\\ 0\end{pmatrix}\begin{pmatrix}1\\ \bar{1}\\ 0\end{pmatrix}\right|^2$$
$$= \tfrac{1}{3}\times\tfrac{1}{24}\left[(a+b-2b') + (a+b-2b') - 4b\right]^2 = \tfrac{1}{2}(\tfrac{a-b-2b'}{3})^2$$

$$R^2(F_{2u}) = \left|\tfrac{1}{2\sqrt{6}}\begin{pmatrix}1\\ 1\\ \bar{2}\end{pmatrix}(R^x)\begin{pmatrix}1\\ \bar{1}\\ 0\end{pmatrix}\begin{pmatrix}1\\ \bar{1}\\ 0\end{pmatrix}\right|^2 + \left|\tfrac{1}{2\sqrt{6}}\begin{pmatrix}1\\ 1\\ \bar{2}\end{pmatrix}(R^y)\begin{pmatrix}1\\ \bar{1}\\ 0\end{pmatrix}\begin{pmatrix}1\\ \bar{1}\\ 0\end{pmatrix}\right|^2$$
$$+ \left|\tfrac{1}{2\sqrt{6}}\begin{pmatrix}1\\ 1\\ \bar{2}\end{pmatrix}(R^z)\begin{pmatrix}1\\ \bar{1}\\ 0\end{pmatrix}\begin{pmatrix}1\\ \bar{1}\\ 0\end{pmatrix}\right|^2 = \tfrac{1}{24}(c+2c')^2 + \tfrac{1}{24}(-c-2c')^2 + \tfrac{1}{24}(-2c+2c)^2 = \tfrac{1}{12}(c+2c')^2$$

Publications

1. **Soft Mode Doublet in $PbMg_{1/3}Nb_{2/3}O_3$ Relaxor Investigated with Hyper-Raman Scattering**
   A. Al-Zein, J. Hlinka, J. Rouquette, and B. Hehlen, *Phys. Rev. Lett.* ***105****, 017601 (2010).*

2. **Zr-shift at the origin of the exceptional piezoelectric properties in $PbZr_{0.52}Ti_{0.48}O_3$**
   A. Al-Zein, G. Fraysse, J. Rouquette, Ph. Papet, J. Haines, G. Aquilanti, B. Hehlen, C. Levelut, and Y. Joly, *Phys. Rev. B* ***81****, 174110 (2010).*

3. **High-Pressure Induced Structural Transition in $LuFe_2O_4$: Towards a New Charge Ordered State**
   J. Rouquette, J. Haines, A. Al-Zein, Ph. Papet, F. Damay, J. Bourgeois, A. Maignan, M. Hervieu, Ch. Martin, *Phys. Rev. Lett. (2010) accepted.*

4. **Polarized hyper-Raman scattering study of the silent F_{2u} mode in $PbMg_{1/3}Nb_{2/3}O_3$**
   A. Al-Zein, B. Hehlen, J. Rouquette, and J. Hlinka, *Phys. Rev. B* ***78****, 134113 (2008).*

5. **High-pressure structural and vibrational study of $PbZr_{0.4}Ti_{0.6}O_3$**
   J. Rouquette, J. Haines, G. Fraysse, A. Al-Zein, V. Bornand, M. Pintard, Ph. Papet, S. Hull, F. A. Gorelli, *Inorganic Chemistry* ***47*** *(2008) 9898-9904.*

6. **PIXE and RBS analysis of Tl-1223 superconducting phase Substituted by Scandium**
   M. Roumie, R. Awad, I.H. Ibrahim, A. Zein, K. Zahraman, and B. Nsouli, *Nucl. Instr. and Meth. B* ***266*** *(2008) 133-139.*

7. **Magnetoresistance Studies of Tl-1223 Phase Substituted by Scandium**
   R. Awad, I. H. Ibrahim, E. M. E. Mansour, M. Roumie, and A. Zein, *Journal of Physics: Conference Series* ***97*** *(2008) 012323.*

8. **Probing the Giant Piezoelectric Effect in $PbZn_{1/3}Nb_{2/3}O_3$ by X-ray Absorption Spectroscopy**
   A. Al-Zein, J. Rouquette, Ph. Papet, J. Haines, C. Levelut, B. Hehlen, H. Dammak, and O. Mathon, *In preparation.*

Bibliography

[1] D. Damjanovic, Rep. Prog. Phys **61**, 1267-1324 (1998).

[2] M. E. Lines and A. M. Glass, Principles and Applications of Ferroelectrics and Related Materials (Clarendon, Oxford, 1977).

[3] J. F. Nye, Physical Properties of Crystals (Oxford: Oxford University Press, 1985).

[4] R. E. Newnham, Proc. Chemistry of Electronic Ceramic Materials (National Institute of Standards and Technology, Jackson, WY). Special Publication 804 (1990).

[5] Y. Xu, Ferroelectric Materials and Their Applications (North-Holland, Amsterdam, 1991).

[6] H. Thurnaurer and J. Deaderick, U. S. Patent No. 2,429,588, Oct. 21, 1947; filed (1941).

[7] B. Wul and J. M. Goldman, C. R. Acad. Sci URSS **46**, 139 (1945).

[8] H. D. Megaw, Nature **155**, 484 (1945).

[9] S. Miyake and R. Ueda, J. Phys. Soc. Jap. **1**, 32 (1946).

[10] N. Orlovskaya, N. Browning, and A. Nicholls, Acta Materialia **51**, 5063 (2003).

[11] R. J. Cava, A. Santoro, D. W. Johnson, and W. W. Rhodes, Phys. Rev. B **35**, 6716 (1987).

[12] J. M. Tarascon, L. H. Greene, W. R. Mckinnon, G. W. Hull, and T. H. Geballe, Science **235**, 1373 (1987).

[13] C. W. Chu, P. H. Hor, R. L. Meng, L. Gao, and Z. J. Huang, Science **235**, 567 (1987).

[14] R. V. Helmolt, J. Wecker, B. Holzapfel, L. Schltz, and K. Samwer, Phys. Rev. Lett. **71**, 2331 (1993).

[15] J. Barrett, Phys. Rev. **86**, 118 (1952).

[16] E. O. Wollan and W. C. Koehler, Phys. Rev. **100**, 545 (1955).

[17] N. Hur, S. Park, P. A. Sharma, J. S. Ahn, S. Guha, and S-W. Cheong, Nature **429**, 392 (2004).

[18] H. D. Megaw, Crystal Structures, London: W. B. Saunders, 216-282 (1973).

[19] G. A. Samara, J.Phys.:Condens.Matter **15**, R367-R411 (2003).

[20] A. M. Glazer, Acta Cryst. **B28**, 3384-3392 (1972).

[21] A. M. Glazer, Acta Cryst. **A31**, 756-762 (1975).

[22] C. J. Howarda and H. T. Stokes, Acta Cryst. **B54**, 782-789 (1998).

[23] V. M. Goldschmidt, Skifter Norske Videskpas-Akad, Oslo, I. Mat. Nat. Kl. 8 (1926).

[24] I. M. Reaney, E. L. Colla, and N. Setter, Jpn. J. Appl. Phys. **33**, 3984 (1994).

[25] A. F. Wells, Structural Inorganic Chemsitry, Oxford Science publications, (1995).

[26] U. Müller, Inorganic Structural Chemistry, Wiley and Sons Ltd, (1993).

[27] W. Cochran, Adv. Phys **9**, 387 (1960).

[28] J. Fousek and V. Janovee, J. Appl. Phys. **40**, 135 (1969).

[29] K. Matsuura, Y. Cho, and R. Ramesh, Appl. Phys. Lett. **83**, 2650 (2003).

[30] J. C. Burfout and G. W. Taylor, Polar Dielectrics and Their Applications (London: Macmillan, 1979).

[31] R. E. Newnham, Structure-Property relations (Berlin: springer, 1975).

[32] H. F. Kay and P. Vousden, Phil. Mag. **40**, 1019 (1949).

[33] G. Shirane and R. Pepinsky, Phys. Rev. **91**, 812 (1953).

[34] L. E. Cross, Ferroelectirc ceramics: tailoring properties for specific applications *Ferroelectirc Ceramics* (Basel: Birkhäuser p1, 1993).

[35] R. W. Whatmore, Rep. Prog. Phys. **49**, 1335 (1986).

[36] H. Fu and R. E. Cohen, Nature (London) **403**, 283 (2000).

[37] G. A. Samara, Solid State Physics **56** (2001) (New York: Academic p240).

[38] A. A. Bokov and Z.-G. Ye, Journal of Materials Science **41**, 31 (2006).

[39] G. Burns and F. H. Dacol, Solid State Commun. **48**, 853 (1983).

[40] P. Bonneau, P. Garnier, G. Calvarin, E. Husson, J. R. Gavarri, A. W. Hewat, and A. Morell, J. Solid State Chem. **91**, 350 (1991).

[41] G. Schmidt, H. Arndt, J. Voncieminski, T. Petzsche, H. Voigt, and N. N. Krainik, Krist. Tech. **15**, 1415 (1980).

[42] L. E. Cross, Ferroelectrics **76**, 241 (1987).

[43] V. Bovtun, S. Veljko, S. Kamba, J. Petzelt, S. Vakhrushev, Y. Yakymenko, K. Brinkman, and N. Setter, J. of European Ceramic Society **26**, 2867 (2006).

[44] D. Vieland, S. J. Jang, L. E. Cross, and M. Wuttig, Phys. Rev. B **46**, 8003 (1992).

[45] E. Dul'kin, M. Roth, P.-E. Janolin, and B. Dkhil, Phys. Rev. B **73**, 012102 (2006).

[46] E. A. Dul'kin, Mat Res Innovat **2**, 338 (1999).

[47] B. Dkhil, P. Gemeiner, A. Al-Barakaty, L. Bellaiche, E. Dul'kin, E. Mojaev, and M. Roth, Phys. Rev. B **80**, 064103 (2009).

[48] E. Dul'kin, M. Roth, B. Dkhil, and J. M. Kiat, Journal of Applied Physics **98**, 023520 (2005).

[49] A. A. Bokov, X. Long, and Z.-G. Ye, Phys. Rev. B **81**, 172103 (2010).

[50] A. Sani, M. Hanfland, and D. Levy, J.Phys.:Condens.Matter **14**, 10601 (2002).

[51] B. Noheda, D. E. Cox, G. Shirane, J. A. Gonzalo, L. E. Cross, and S.-E. Park, Appl. Phys. Lett. **74**, 2059 (1999).

[52] J. Rouquette, J. Haines, V. Bornand, M. Pintard, Ph. Papet, R. Astier, J. M. Léger, and F. Gorelli, Phys. Rev. B **65**, 214102 (2002)

[53] J. Rouquette, J. Haines, V. Bornand, M. Pintard, Ph. Papet, W. G. Marshall, and S. Hull, Phys. Rev. B **71**, 024112 (2005).

[54] A. M. Glazer, P. A. Thomas, K. Z. Baba-Kishi, G. K. H. Pang, and C. W. Tai, Phys. Rev. B **70**, 184123 (2004).

[55] J.-H. Ko, S. Kojima, and S. G. Lushnikov, Appl. Phys. Lett. **82**, 4128 (2003).

[56] G. Shirane, S. Hushino, and K. Suzuki, Phys. Rev. **80**, 1105 (1950).

[57] J. Kwapuliński, J. Kusz, H. Böhm, and J. Dec, J.Phys.:Condens.Matter **17**, 1825 (2005).

[58] N. Sicron, B. Ravel, Y. Yacoby, E. A. Stern, F. Dogan, and J. J. Rehr, Phys. Rev. B **50**, 13 168 (1994).

[59] J. A. Sanjurjo, E. López-Cruz, and G. Burns, Solid State Commun. **48**, 221 (1983).

[60] P.-E. Janolin, P. Bouvier, J. Kreisel, P. A. Thomas, I. A. Kornev, L. Bellaiche, W. Chrichton, M. Hanfland, and B. Dkhil, Phys. Rev. Lett. **101**, 237601 (2008).

[61] N. Jaouen, A. C. Dhaussy, J. P. Itiè, A. Rogalev, S. Marinel, and Y. Joly, Phys. Rev. **75**, 224115 (2007).

[62] B. Noheda, L. Wu, and Y. Zhu, Phys. Rev. B **66**, 060103(R) (2002).

[63] B. Jaffe, W. R. Cook, and H. Jaffe, Piezoelectric Ceramics (Academic, London, 1971).

[64] B. Noheda, J. A. Gonzalo, L. E. Cross, R. Guo, S.-E. Park, D. E. Cox, and G. Shirane, Phys. Rev. B **61**, 8687 (2000).

[65] B. Noheda, D. E. Cox, G. Shirane, R. Guo, B. Jones, and L. E. Cross, Phys. Rev. B **63**, 014103 (2000).

[66] R. Guo, L. E. Cross, S-E. Park, B. Noheda, D. E. Cox, and G. Shirane, Phys. Rev. Lett. **84**, 5423 (2000).

[67] L. Bellaiche, A. Garcia, and D. Vanderbilt, Phys. Rev. Lett. **84**, 5427 (2000).

[68] K. Aizu, Phys. Rev. B **2**, 754 (1970).

[69] A. Lebon, Thèse de doctorat, "Influence de la Direction de Polarisation sur la Coexistence de Phases du Ferroelectrique-Relaxeur $PbZ_{1/3}Nb_{2/3}O_3$: Une Etude sur Monocristal par Diffraction des Rayons X et diffusion Raman", Ecole Centrale de Paris (2002).

[70] Y.-H. Bing, A. A. Bokov, Z.-G. Ye, B. Noheda, and G. Shirane, J.Phys.:Condens.Matter **17**, 2493 (2005).

[71] Y. Yokomizo, T. Takahashi, and S. Nomura, J. Phys. Soc. Japan **28**, 1278 (1970).

[72] S. Nomura, M. Endo, and F. Kojima, Japan. J. Appl. Phys. **13**, 2004 (1974).

[73] A. Lebon, H. Dammak, G. Calvarin, and I. O. Ahmedou, J.Phys.:Condens.Matter **14**, 7035 (2002).

[74] S. N. Gvasaliya, V. Pomjakushin, B. Roessli, T. Straessle, S. Klotz, and G. S. Lushnikov, Phys. Rev. B **73**, 212102 (2006).

[75] S. N. Gvasaliya, B. Roessli, D. Sheptyakov, S. G. Lushnikov, and T. A. Shaplygina, Eur. Phys. J. B **40**, 235 (2004).

[76] S. G. Lushnikov, J.-H. Ko, and S. Kojima, Appl. Phys. Lett. **84**, 4798 (2004).

[77] S. G. Lushnikov, A. I. Fedoseev, S. N. Gvasaliya, and S. Kojima, Phys. Rev. B **77**, 104122 (2008).

[78] Y. L. Wang, S. S. N. Bharadwaja, A. K. Tagantsev, and N. Setter, J. of European Ceramic Society **25**, 2521 (2005).

[79] H. Dachs, Topics in Current Physics, Neutron Diffraction (Springer, 1978).

[80] F. Hippert, E. Geissler, J. L. Hodeau, E. Lelièvre-Berna, and J. R. Regnard, Neutron and X-ray Spectroscopy (Springer, 2006).

[81] J. R. D. Copley, The Fundamentals of Neutron Powder Diffraction (Materials Science and Engineering Laboratory, 2001).

[82] http://www.ill.eu/instruments-support/instruments-groups/instruments/d1b/.

[83] T. C. Hansen, P. F. Henry, H. E. Fischer, J. Torregrossa, and P. Convert, Meas. Sci. Technol. **19**, 034001 (2008).

[84] http://www.ill.eu/instruments-support/instruments-groups/instruments/d20/.

[85] A. Sani, M. Hanfland, and D. Levy, Journal of Solid State Chemistry **167**, 446 (2002).

[86] L. B. McCusker, R. B. Von Dreele, D. E. Cox, D. Louër, and P. Scardi, J. Appl. Cryst. **32**, 36 (1999).

[87] J. Rodriguez-Carvajal, An introduction to the program FullProf 2000 (2001).

[88] G. Burns and B. A. Scott, Phys. Rev. Lett. **25**, 167 (1970).

[89] G. A. Samara, T. Sakuda, and K. Yoshimitsu, Phys. Rev. Lett. **35**, 1767 (1975).

[90] J. A. Sanjurjo, E. López-Cruz, and G. Burns, Phys. Rev. B **28**, 7260 (1983).

[91] C. M. Foster, Z. Li, M. Grimsditch, S.-K Chan, and D. J. Lam, Phys. Rev. B **48**, 14 (1993).

[92] I. A. Kornev, L. Bellaiche, P. Bouvier, P.-E. Janolin, B. Dkhil, and J. Kreisel, Phys. Rev. Lett. **95**, 196804 (2005).

[93] H. T. Stokes and D. M. Hatch, Isotropy Subgroups of the 230 Crystallographic Space Groups (World Scientific (1988)).

[94] J. Frantti, S. Ivanov, S. Eriksson, H. Rundlöf, V. Lantto, J. Lappalainen, and M. Kakihana, Phys. Rev. B **66**, 064108 (2002).

[95] J. P. Rameika and A. M. Glazer, Mater. Res. Bull **5**, 37 (1970).

[96] R. M. Hazen and R. T. Downs, High-Temperature and High-Pressure Crystal Chemistry (Virginia (2000)).

[97] A. Ahart, M. Somayazulu, R. E. Cohen, P. Ganesh, P. Dera, H. K. Mao, R. J. Hemley, Y. Ren, P. Liermann, and Z. Wu, Nature **451**, 545 (2008).

[98] J. J. Rehr and R. C. Albers, Rev. Mod. Phys. **72**, 621 (2000).

[99] M. Newville, Fundamentals of XAFS (University of Chicago, 2008).

[100] R. V. Vedrinskii, E. S. Nazarenko, M. P. Lemeshko, V. Nassif, O. Proux, A. A. Novakovich, and Y. Joly, Phys. Rev. B **73**, 134109 (2006).

[101] http://www.esrf.eu/UsersAndScience/Experiments/ElectStructMagn/BM29.

[102] M. Newville, J. synchrotron Rad. **8**, 322 (2001).

[103] Y. Joly, Phys. Rev. B **63**, 125120 (2001).

[104] R. V. Vedrinskii, V. L. Kraizman, A. A. Novakovich, Ph. V. Demekhin, and S. V. Urazhdin, J. Phys.: Condens. Matter **10**, 9561 (1998).

[105] R. E. Cohen, Nature **358**, 136 (1992).

[106] I. Grinberg, V. R. Cooper, and A. M. Rappe, Nature **419**, 909 (2002).

[107] A. M. George, J. Iniguez, and L. Bellaiche, Nature **413**, 54 (2001).

[108] K. Hirota, S. Wakimoto, and D. E. Cox, J. Phys. Soc. Jpn **75**, 111006 (2006).

[109] J. Rouquette, J. Haines, V. Bornand, M. Pintard, Ph. Papet, C. Bousquet, L. Konczewicz, F. A. Gorelli, and S. Hull, Phys. Rev. B **70**, 014108 (2004).

[110] K. A. Schönau, L. A. Schmitt, M. Knapp, H. Fuess, R.-A. Eichel, H. Kungl, and M. J. Hoffmann, Phys. Rev. B **75**, 184117 (2007).

[111] S. Takahash and M. Takahash, Jpn. J. Appl. Phys. **11**, 31 (1972).

[112] X.-h Du, J. Zheng, U. Belegundu, and K. Uchino, Appl. Phys. Lett. **72**, 2421 (1998).

[113] R. D. Shannon, Acta Cryst. **A32**, 751 (1976).

[114] D. Cao, I.-K. Jeong, R. H. Heffner, T. Darling, J.-K. Lee, F. Bridges, J.-S. Park, and K.-S. Hong, Phys. Rev. B **70**, 224102 (2004).

[115] W. Dmowski, T. Egami, L. Farber, and P. K. Davies, Fundamental Physics of Ferroelectrics (AIP conference proceedings) **582**, 33 (2001).

[116] W. Cochran, Adv. Phys. **10**, 401 (1961).

[117] A. M. Glazer, K. Roleder, and J. Dec, Acta Cryst. **B49**, 846 (1993).

[118] C. Laulhé, F. Hippert, J. Kreisel, M. Maglione, A. Simon, J. L. Hazemann, and V. Nassif, Phys. Rev. B **74**, 014106 (2006).

[119] D. Cao, F. Bridges, G. R. Kowach, and A. P. Ramirez, Phys. Rev. Lett. **89**, 215902 (2002).

[120] N. L. Ross, J. Zhao, and R. J. Angel, J. Solid State Chem. **177**, 3768 (2004).

[121] G. Xu, Z. Zhong, Y. Bing, Z.-G. Ye, C. Stock, and G. Shirane, Phys. Rev. B **67**, 104102 (2003).

[122] G. Xu, Z. Zhong, Y. Bing, Z.-G. Ye, C. Stock, and G. Shirane, Phys. Rev. B **70**, 064107 (2004).

[123] E. H. Kisi and J. S. Forrester, J.Phys.:Condens.Matter **17**, L381-L384 (2005).

[124] A. Lebon, H. Dammak, and G. Calvarin, J. Phys.: Condens. Matter **15**, 3069 (2003).

[125] G. Xu, Z. Zhong, Y. Bing, Z.-G. Ye, and G. Shirane, Nat. Mat. **5**, 134 (2006).

[126] S. Park and T. R. Shrout, J. Appl. Phys. **82**, 1804 (1997).

[127] E. Prouzet, E. Husson, N. Demathan, and A. Morell, J. Phys.: Condens. Matter **5**, 4889 (1993).

[128] V. N. Denisov, B. N. Marvin, and V. B. Podobedov, Phys. Rep. **151**, 1 (1987).

[129] S. J. Cyvin, J. E. Rauch, and J. C. Decius, J. Chem. Phys. **43**, 4083 (1965).

[130] H. Vogt, Phys. Rev. B **24**, 3086 (1981).

[131] H. Vogt, Phys. Rev. B **36**, 5001 (1987).

[132] H. Vogt, Phys. Rev. B **38**, 5699 (1988).

[133] W. Hays and R. Loudon, Scattering of Light by Crystals (Dover Publications, New York (1978)).

[134] L. D. Landau and E. M. Lifshitz, Statistical Physics (Oxford: Pergamon (1969)).

[135] W. Cochran and R. A. Cowley, J. Phys. Chem. Solids **23**, 447 (1962).

[136] A. Al-Zein, B. Hehlen, J. Rouquette, and J. Hlinka, Phys. Rev. B **78**, 134113 (2008).

[137] G. Simon, B. Hehlen, R. Vacher, and E. Courtens, Phys. Rev. B **76**, 054210 (2007).

[138] G. Simon, B. Hehlen, R. Vacher, and E. Courtens, J. Phys. Cond. Mat. **20**, 155103 (2008).

[139] H. Hellwig, A. Sehirlioglu, D. A. Payne, and P. Han, Phys. Rev. B **73**, 094126 (2006).

[140] H. Hellwig, Appl. Phys. Lett. **87**, 051104 (2005).

[141] B. Hehlen, G. Simon, and J. Hlinka, Phys. Rev. B **75**, 052104 (2007).

[142] K. Watanabe, K. Inoue, and F. Minami, Phys. Rev. B **46**, 2024 (1992).

[143] K. Inoue and K. Watanabe, Phys. Rev. B **39**, 1977 (1989).

[144] B. Chu, Laser Light Scattering (Academic Press, 1974).

[145] A. Naberezhnov, S. Vakhrushev, B. Dorner, D. Strauch, and H. Moudden, Eur. Phys. J. B **11**, 13 (1999).

[146] P. M. Gehring, S. Wakimoto, Z.-G. Ye, and G. Shirane, Phys. Rev. Lett. **87**, 277601 (2001).

[147] S. N. Gvasaliya, B. Roessli, R. A. Cowley, P. Huber, and S. G. Lushnikov, J. Phys.: Condens. Matter **17**, 4343 (2005).

[148] S. N. Gvasaliya, S. G. Lushnikov, and B. Roessli, Crystallography Reports **49**, 108 (2004).

[149] O. Svitelskiy, J. Toulouse, G. Yong, and Z.-G. Ye, Phys. Rev. B **68**, 104107 (2003).

[150] J.-H. Ko, D. H. Kim, and S. Kojima, Phys. Rev. B **77**, 104110 (2008).

[151] J. Toulouse, F. Jiang, O. Svitelskiy, W. Chen, and Z.-G. Ye, Phys. Rev. B **72**, 184106 (2005).

[152] S. Lushnikov, S. Gvasaliya, and R. S. Katiyar, Phys. Rev. B **70**, 172101 (2004).

[153] J. Hlinka, T. Ostapchuk, D. Noujni, S. Kamba, and J. Petzelt, Phys. Rev. Lett. **96**, 027601 (2006).

[154] S. A. Prosandeev, E. Cockayne, B. P. Burton, S. Kamba, J. Petzelt, Yu. Yuzyuk, R. S. Katiyar, and S. B. Vakhrushev, Phys. Rev. B **70**, 134110 (2004).

[155] S. Kamba, D. Nuzhnyy, S. Veljko, V. Bovtun, J. Petzelt, Y. L. Wang, N. Setter, J. Levoska, M. Tyunina, J. Macutkevic, and J. Banys, Journal of Applied Physics **102**, 074106 (2007).

[156] E. Husson, L. Abello, and A. Morel, Mater. Res. Bull. **25**, 539 (1990).

[157] N. N. Krainik, L. A. Markova, and A. A. Karamjan, Ferroelectrics **143**, 179 (1993).

[158] S. G. Lushnikov, S. N. Gvasalia, and I. G. Siny, Physica B **263-264**, 286 (1999).

[159] S. Wakimoto, C. Stock, R. J. Birgeneau, Z.-G. Ye, W. Chen, W. J. L. Buyers, P. M. Gehring, and G. Shirane, Phys. Rev. B **65**, 172105 (2002).

[160] V. Bovtun, S. Kamba, A. Pashkin, M. Savinov, P. Samoukhina, J. Petzelt, I. P. Bykov, and M. D. Glinchuk, Ferroelectrics **298**, 23 (2004).

[161] S. Kamba, M. Kempa, V. Bovtun, J. Petzelt, K. Brinkman, and N. Setter, J. Phys.: Condens. Matter **17**, 3965 (2005).

[162] G. Burns and B. A. Scott, Solid State Commun. **13**, 423 (1973).

[163] E. Dul'kin, I. P. Raevskii, and S. M. Emel'yanov, Phys. Solid State **45**, 158 (2003).

[164] J. Hlinka, J. Petzelt, S. Kamba, D. Noujni, and T. Ostapchuk, Phase Transitions **79**, 163 (2006).

[165] I. M. Reaney, J. Petzelt, V. V. Voitsekhovskii, F. Chu, and N. Setter, J. Appl. Phys. **76**, 2086 (1994).

[166] M. El. Marssi, R. Farhi, and Yu. Yuzyuk, J. Phys.: Condens. Matter **10**, 9161 (1998).

[167] H. Ohwa, M. Iwata, H. Orihara, N. Yasuda, and Y. Ishibashi, J. Phys. Soc. Jpn. **70**, 3149 (2001).

[168] A. Slodczyk, P. Daniel, and A. Kania, Phys. Rev. B **77**, 184114 (2008).

[169] J. F. Scott, Rev. Mod. Phys. **46**, 83 (1974).

[170] M. R. Dresselhaus and G. Dresselhaus, Adv. Phys. **30**, 139 (1981).

[171] D. Fu, H. Taniguchi, M. Itoh, S.-Y. Koshihara, N. Yamamoto, and S. Mori, Phys. Rev. Lett. **103**, 207601 (2009).

[172] J. Hlinka and M. Kempa, Phase Transitions **81**, 491 (2008).

[173] S. B. Vakhrushev and S. M. Shapiro, Phys. Rev. B **66**, 214101 (2002).

[174] H. Presting, J. A. Sanjurjo, and H. Vogt, Phys. Rev. B **28**, 6097 (1983).

[175] M. DiDomenico, Jr., S. H. Wemple, S. P. S. Porto, and R. P. Bauman, Phys Rev. **174**, 522 (1968).

[176] R. A. Cowley, S. N. Gvasaliya, and B. Roessli, Ferroelectrics **378**, 53 (2009).

[177] J. L. Servoin, Y. Luspin, and F. Gervais, Phys. Rev. B **22**, 5501 (1980).

Ordre et Désordre des Matériaux Ferroélectriques et Relaxeurs: Etudes Structurales et Vibrationnelles

Parmi les matériaux piézo-électriques, les pérovskites ferroélectriques à base de plomb sont connus pour avoir les meilleurs coefficients piézo-électriques et couplage électromécanique. Ils sont largement utilisés dans diverses applications industrielles et technologiques. Les "ferroélectrique relaxeurs" appartiennent à cette famille. Leur structure est caractérisée par la présence de nanoregions polaires orientées de faon aléatoire. Dans cette thèse, nous nous sommes intéressés à l'étude des propriétés structurales et dynamiques de matériaux ferroélectriques et relaxeurs tels que $PbTiO_3$, $PbZr_{0.52}Ti_{0.48}O_3$, $PbMg_{1/3}Nb_{2/3}O_3$ (PMN), $PbZn_{1/3}Nb_{2/3}O_3$, et $PbMg_{1/3}Ta_{2/3}O_3$ (PMT). La structure à longue et courte portée a été étudiée par diffraction de neutrons et spectroscopie d'absorption des rayons X (XAFS), alors que la spectroscopie hyper-Raman (HR) est utilisée pour sonder les vibrations. L'analyse de la structure locale de matériaux pérovskites complexes $AB'B''O_3$ montre que la pression diminue le désordre statique des gros cations occupant le site B, tandis que le champ électrique appliqué a un effet opposé. Cette distortion induite sous champ pourrait être l'origine des forts coefficient piézoélectrique dans ces matériaux. La diffusion HR dans PMN et PMT a permis d'observer pour la première fois le "mode mou" responsable de la dépendance en température de la constante diélectrique. L'analyse des règles de sélection et la description en modes propres des vibrations actives en HR, permet de rendre compte de l'implication de chaque atome dans le comportement structural en température des ferroélectriques relaxeurs.

Mots clé: Relaxeur, pérovskite, matériau ferroélectrique, structure, vibrations, transition de phase, température, pression, champ électrique, diffraction des neutrons, absorption des rayons X, hyper-Raman.

Order and Disorder of Relaxor and Ferroelectric Materials: Structural and Vibrational Studies

Among piezoelectric materials, lead-based ferroelectric perovskites are known to have the largest piezoelectric coefficients and electromechanical coupling. They are widely used in different industrial and technological applications. The so-called "relaxors" belong to this family. Their structure is characterized by the presence of randomly oriented polar nanoregions. In this thesis, we are interested in studying the structural and dynamical properties of prototypical ferroelectric materials and relaxors such as $PbTiO_3$, $PbZr_{0.52}Ti_{0.48}O_3$, $PbMg_{1/3}Nb_{2/3}O_3$ (PMN), $PbZn_{1/3}Nb_{2/3}O_3$, and $PbMg_{1/3}Ta_{2/3}O_3$ (PMT). The long and short range structure has been investigated by neutron diffraction and X-ray absorption fine structure (XAFS), while hyper-Raman scattering (HRS) is used to probe the vibrations. The local structure analysis of complex perovskite materials $AB'B''O_3$ shows that pressure reduces the static disorder of the large cation occupying the B-site, while an applied electric field has an opposite effect. This field-induced distortion might relate to the large piezoelectric coefficient in such materials. HRS in PMN and PMT allows the first observation of the "primary" soft mode responsible for the temperature dependence of the dielectric constant. The selection rule analysis reveals the nature of the HRS active vibrational bands and enables us to get insights about the involvement of each atom in the structural modifications upon temperature.

Key words: Relaxor, perovskite, ferroelectric material, structure, vibration, phase transition, temperature, pressure, electric field, neutron diffraction, X-ray absorption, hyper-Raman.

Ecole Doctorale: Sciences Chimiques et Physiques
Discipline: Physico-Chimie des Matériaux

"Institut Charles Gerhardt Montpellier, Equipe C2M, UMR 5253 CNRS"
et "Laboratoire des Collodes Verres et Nanomatériaux, UMR 5253 CNRS"
Université Montpellier II, place Eugène Bataillon, 34095 Montpellier, France